BAND GAP TUNING AND STRUCTURAL ENGINEERING OF TiO_2 FOR PHOTOCATALYSIS AND SOLAR CELLS

QUANRONG DENG

A thesis submitted in partial fulfilment of the requirements of the University of Bolton for the degree of Doctor of Philosophy

This research programme was carried out in collaboration with Hubei University

August 2012

Abstract

To tackle with the energetic and environmental problems for sustainable development, titanium dioxide (TiO_2) has attracted extensive scientific interests for its outstanding performances in photocatalytic decomposition of organic molecules and its application in solar cells.

This work aims at a fundamental break through towards significant reduction of TiO_2 band gap via doping, since the functionality for pure TiO_2 can be excited only by ultraviolet (UV) light that only accounts for less than 5% of solar irradiance because of the wide band gaps (3.2 eV for anatase and 3.0 eV for rutile), as well as structural engineering of TiO_2 thin films, in order to pave a technological basis for truly sustainable technologies for visible light photocatalytic applications for cleaner environment and novel photovoltaic (PV) cells.

By using the technique of pulse laser deposition, pure and ions doped TiO_2 thin films were successfully synthesized. The microstructure and optical absorption properties of doped thin films were systematically characterized and compared with pure one. Through involving Fe, Mn, V-Ga, the band gap of TiO_2 thin films were extensively narrowed, amazingly making the absorption edges shift well into visible region or even infrared region. Contrarily, rare earth dopants Gd, Er, Sm could hardly address the band gap of TiO_2 thin film.

Fe doped TiO_2 nanocatalysts were prepared using a hydrothermal method at low temperature. Fe doping induces significant red shift in the optical absorption edge of TiO_2 by introducing secondary absorption edges, extending the optical absorption edge well into the visible light region. Accordingly the visible light photocatalytic activity of TiO_2 increased on account of visible light absorption by Fe doped TiO_2, resulting in improved degradation rate of methylene blue (MB) under visible light irradiance.

Mn doped TiO_2 nanocatalysts were successfully prepared by means of a sol–gel method using ethanol–water as a solvent. A remarkable red shift of the absorption edge was achievable through Mn doping, giving rise to gigantically narrowed energy

gap to permit absorption well into the infrared spectral region. The Mn doped anatase powders exhibited considerable high visible light photocatalytic activity, leading to greatly enhanced degradation rate of MB under visible light irradiance.

Single rutile TiO_2 nanorod and nanofibre thin films with preferred [002] orientation were successfully synthesized on fluoride doped tin dioxide (FTO) coated substrate. Through adjusting the reaction duration, alcohol substitution of water as solvent, reaction temperature and tetrabutyl titanate ($Ti(OBu)_4$) concentration, TiO_2 thin films of different packing density and thickness were well controlled for various potential applications. By employing the nanorod TiO_2 thin film in hybrid solar cell, considerable efficiencies were obtained and expected to improve furthermore.

Table of contents

List of figures

List of tables

List of symbols

A	absorbance
ab initio	from the beginning
ALD	atomic layer deposition
B	full width of half maximum
BF	bright field
C	concentration
C_0	initial concentration
CB	conduction band
CBM	conduction band minimum
CDF	central dark field
CVD	chemical vapour deposition
D	crystalline size
d	thickness
d^*	planar distance of crystal lattice
DFT	density functional theory
DOS	density of state
DSSC	dye sensitized solar cell
E_b	binding energy
EDX	energy dispersive X-ray spectroscope
E_g	band gap
E_{kin}	kinetic energy
FE-SEM	field-emission-gun scanning electron microscope
Ff	fill factor
FFT	fast Fourier transformation
FLAPW	full potential linearized augmented plane wave method
FTO	fluoride-doped tin oxide covered glass
G	generation rate
GGA	generalized gradient approximation
h	Planck's constant
HBHJ	hybrid bulk hetero junction

HOMO	highest occupied molecular orbital
HRTEM	high resolution TEM
I	output current (amperes)
I^*	Intensity of light
I_0^*	intensity of reference light
I_D	diode current (amperes)
I_L	photogenerated current (amperes)
I_{sc}	short circuit current (amperes)
I_{SH}	shunt current (amperes)
J	output current density
J_{sc}	short circuit current density
k	the Boltzmann constant
K	Scherrer's constant
k_{et}	recombination rate
LDA	local density approximation
L_n	electron diffusion length
LOMO	lowest unoccupied molecular orbital
L_p	hole diffusion length
MB	methylene blue
MDMO−PPV	poly[2-methoxy-5-(3',7'-dimethyloctyloxy)-1,4-phenylenevinylene]
$M(OR)_n$	metal alkoxides
n	number
n_0	electron density on the conduction band of the semiconductor in the dark
N719	bis(tetrabutylammonium) dihydrogen bis(isothiocyanato)bis(2,2'-bipyridyl-4,4'-dicarboxylato)ruthenium(II), $C_{58}H_{86}N_8O_8RuS_2$
P3HT	poly(3-hexylthiophene), $(C_{10}H_{14}S)_n$
PAW	projector augmented wave
PCBM	phenyl-C61-butyric acid methyl ester, $C_{72}H_{14}O_2$
PCPDTBT	poly[2,1,3-benzothiadiazole-4,7-diyl[4,4-bis(2-ethylhexyl)-4H-cyclopenta[2,1-b:3,4-b']dithiophene-2,6-diyl]]
PPV	poly(*p*-phenylenvinylene)

PLD pulsed laser deposition

P_nR_m TiO_2 particle layer by using sputtering for *n* hours and TiO_2 rod layer by employing hydrothermal for *m* hours

q magnitude of the electron charge

QD quantum dot

R alkyl group

R_S series resistance (ohms)

SAED selected area electron diffraction

SEM scanning electron microscopy/ scanning electron microscope

T absolute temperature

TEM transmission electron microscopy/ transmission electron microscope

TTIP titanium tetraisopropoxide

$Ti(OBu)_4$ tetrabutyl titanate

TCO transparent conducting oxide

U Hubbard U correction

UV ultra violet

VASP Vienna *Ab initio* simulation package

VB valency band

VBM valence band maximum

V_j voltage across both diode and resistor R_{SH} (volts)

V_{oc} open voltage (volts)

X-OH nucleophilic molecules

XPS X-ray photoelectron spectroscopy/X-ray photoelectron spectrometer

XRD X-ray diffraction analysis

Y Young's modulus

Greek symbols

α absorption coefficient

α_0 a constant

θ Bragg angle (degree)

λ wavelength

ν frequency of photon

μ	stored elastic energy per unit area
σ	the internal stress
ϕ_{sp}	work function
η	energy conversion efficiency
Φ_0	incident photon flux

Acknowledgements

I would like to express my sincere grateful to my supervisors, Prof. Guosheng Shao at University of Bolton, United Kingdom and Prof. Yun Gao at Hubei University, China, for offering me the opportunity to start this research project, as well as their invaluable guidance, support and encourage throughout my years of research project. I am deeply impressed by their profound knowledge in research and attitude to science. Undoubtedly, I shall benefit from this experience in my future work and life.

My sincere thanks must also go to Dr Xiaohong Xia in Hubei University, China, Prof. Jack Luo and Dr Zan Bian in University of Bolton for their generous help and technical suggestions regarding this work, Dr Xiaoping Han in University of Bolton for carrying out theoretical simulation with regard to this work.

My grateful are also extended to all my friends, especially my group mates in University of Bolton, including Yonglong Shen and Liu Lu for solving technical problems, Le Zhu for providing theoretical suggestion in terms of solar cells, Muhammad Faruq, Chukwunonso Anajemba, Dheeraj Singh, Anand Arcot Narasimulu, for their kind help in laboratory and office, as well as group mates in Hubei University, including Lin Wan and Yong Zhang for assisting me to do part experiments in chapter 5 and Chapter 6, Meilan Guo and Rushan Chen for helping to do some sample characterization, Guowen Jiang, Haowen Liu, for their kind support in my daily work. Thank you all for making my PhD life so enjoyable. I am also grateful for Shirley Hankers for her helpful proof reading of the manuscript.

Particularly, I would like to dedicate my deepest grateful to my lovely family, my parents and my sisters. Thank you all for the endless love and support for the pursuit of my PhD. Lastly, I want to thank my boyfriend friend, Lin Huang, for giving me understanding and courage throughout this process. Thank you for always being there.

Sample characterization from external institutes are all acknowledged, including Institute of Nanoscience and Nanotechnology of Huazhong Normal University for providing X-ray diffraction (XRD), scanning electron microscopy (SEM) and UV-

visible absorption spectroscopy characterization, School of Physics and Technology of Wuhan University for offering high resolution transmission electron microscopy (TEM) and X-ray photoelectron spectroscopy (XPS) testing, Department of Physics in The Chinese University of Hong Kong, China, for providing UV-visible absorption spectroscopy and high resolution TEM characterization.

This project was supported by the UK Technology Strategy Board with Grant TP11/LCE/6/I/AE142J, the National Science Foundation of China (No. 50702019 and No. 11174256).

Chapter 1 Introduction

1.1 Introduction and motivation

The global developing and human activities have brought out a tremendous set of environmental problems related to a variety of hazardous wastes, toxic air contaminants and contaminated ground water. Likewise, the ever rising in world population and global energy demand has given rise to serious energy shortage which is considered to be another environmental issue, and the worldwide energy consumption is expected to double in the next three decades. In addition, consumption carbon based fossil energy that is commonly used now has yet resulted in global warming and devastating climate change due to the emission of CO_2. Therefore, the challenge in this day and age is how to tackle the energetic and environmental issues to keep the sustainable developing and provide the quality of living environment with higher expectations. To resolve these problems, developing environmental cleaning materials and renewable energy that can replace the inevitably vanishing fossil fuel supplies, nowadays, have been paid worldwide attention. It is worth noting that the availability of renewable resources should avoid negative effects from the current energy system on climate, environment and health. These have promoted the extensive exploration of titanium dioxide (TiO_2) material, since it is the most promising candidate to address both environmental problems, owing to its great potential applications such as photocatalysis [1,2] water splitting for H_2 production [3]; self cleaning or anti-microbial coating; gas sensors [4,5] and low cost but clean solar cells [6,7], together with the benefit in terms of its low-cost, high stability, low biological toxicity, and environmental compatible. The wide applications of TiO_2 materials are the main motivation of this project.

When TiO_2 is illuminated under ultraviolet (UV) light, two phenomena would happen: one is the widely studied photocatalytic phenomenon, the second is super hydrophilicity phenomenon [8]. In 1972, the strong oxidation and reduction potential of photoexcited TiO_2 was realized from the first discovering of photocatalytic splitting of water on titanium dioxide by Fujishima and Honda [9]. Since then, this property has triggered tremendous research on heterogeneous photocatalysis,

including photocatalytic decomposition of organic compounds, photocatalytic sterilization [10,11] and cancer treatment [12,13]. On the other hand, according to Wang [14,15], the illumination of UV light could give rise to the conversation of Ti^{4+} to Ti^{3+} ions on the surface of TiO_2, and then the typical charge transfer between Ti atoms and adsorbents such as oxygen, H_2 and hydroxyl can be changed, under illumination, leading super hydrophilicity of TiO_2. The longer illumination time the smaller contact angle for water on TiO_2 surface, this means the water can totally spread on the surface after a period of illumination time so that they can be used as self cleaning and anti fogging coating on substance.

However, the functionality for pure TiO_2 can be excited only by UV light that only accounts for less than 5% of solar irradiance because of the wide band gaps (3.2 eV for anatase and 3.0 eV for rutile). This wide gap nature of TiO_2 phases seriously limits, in most circumstances, their practical applications including photocatalysis, photo induced hydrophilicity and production of hydrogen, because the UV light can be readily absorbed even by pure water vapour and clear glass. Therefore, it is very important and urgent to fabricate modified TiO_2 thin films and powders with a narrowed band gap to utilize the visible light from solar irradiance. This has attracted great interest of tuning the optical absorption properties of TiO_2 by ions doping, compositing TiO_2 with narrower band gap semiconductors or dyes.

Up to now, intense efforts have been made in order to tune the band structure of the semiconductor TiO_2 phases and thereby extend the light absorption spectrum toward the visible light range. The most feasible modification method seems to be doping them with metallic and non-metal atoms. Even though TiO_2 materials have been widely explored by doping with a variety of metal ions such as Fe [16], Cr [17], Co [18], Mn [19], V [20], Ni [21] and non-metal ions such as N [22], C [23], S [24], F [25], B [26], few was able to narrow its band gap effectively since the chemical states of doping ions played a crucial role on the doping effect.

Recently, on the ground of widely studied mono-doping, reports on two ions co-doping have attracted extensive attention, including nonmetal and metal co-doping, e.g. N-W [27] and N-Ta [28], N-Pt [29], S-Bi [30], C-Mo [31], B-V [32] or two nonmetal ions co-doping, e.g. C-H [33], N-H [33], C-N [34,35], N-S [36]. By employing suitable

dopants, the band structure could be conceivably narrowed. For example, Gai and co-workers [31] have found C-Mo co-doped dramatically shifted the band gap from 3.2 eV to 2.26 eV, apparently much more than mono-doping did. The same phenomenon was also observed in C-H and N-H co-doping TiO_2 materials [33]. However, to our knowledge band gap properties of two metal ions co-doped TiO_2 materials have been relatively seldom carried out, though mono metal ions doping has been widely studied and has been proven to be one of the most impressive way to address optical drawback [37, 38].

On the other hand, as a semi-conducting metal oxide, the conductivity of TiO_2 may charge up on gas absorption, such as H_2, CO, O_2 and ethanol vapour etc, promoting its use for gas sensing to monitor and control environmental pollution [39]. When gas or vapour is chemisorbed on TiO_2 surface, charges would transfer from gas to TiO_2 or from TiO_2 to gas, depending on which kind of gas and TiO_2 is being used. The transfer of electrons to TiO_2 makes the conductivity enhanced while the reverse transfer of electrons to adsorbed gas leads to conductivity decrease. Consequently, one would expect to measure the resistance or capacity of TiO_2 to detect gas.

Moreover, TiO_2 materials has been also widely investigated due to its increasing uses in photovoltaic (PV) cells such as the dye-sensitised solar cells (DSSC), polymer solar cells, organic-inorganic hybrid solar cells and the recently developed extremely thin absorber (ETA) solar cells, which is based on a hetero-junction formed between TiO_2 and another semiconducting material. In most TiO_2 based solar cells, various kinds of TiO_2 nanostructures are combined with a p type photo active layer, forming a barrier to dissociate photogenerated carriers at interface and at the same time block the passing through of holes into TiO_2. The detail will be reviewed in next chapter.

For the application of gas sensors and PV cells, the central factor to functionality is carrier conductivity. As it is known, the carrier mobility of single crystal TiO_2 is as low as 1~10 $cm^2\ V^{-1}\ s^{-1}$, which is incomparable to most of semiconductors. Of polycrystalline nanomaterials, the mobility is even worse owing to interface scattering and defects trapping. Therefore, the microstructures of TiO_2 phases play very important roles for their functional performances. While nanopowders are

excellent for photocatalysis, self assembled TiO_2 nanoarrays in the form of well aligned nanorods or nanowires are expected to offer improved properties in gas sensors and thin-film PV cells, owing to the longer electron diffusion lengths through their one dimensional channel for carrier transportation, unique electric properties and low recombination rate of carriers [40]. Adopting these structures in turn may increase electron transportation rate and improve the performance of functional devices.

1.2 Objectives of the present study

This work aims at a fundamental break-through towards significant reduction of TiO_2 band gap via doping and structural engineering of TiO_2 thin films, in order to pave a technological basis for truly sustainable technologies for visible light photocatalytic applications for cleaner environment and novel PV cells. This would be achieved via the realisation of the following objectives:

(1) Synthesis of pure and doped materials using various methods to produce different structural and optical characteristics including nanocrystalline powders, thin films.

(2) Correlation of the microstructures and compositions to the associated optical properties of pure, doped or alloyed TiO_2 nanopowders. Measurement of photocatalytic activities of doped TiO_2 materials under visible light and optimization of visible light photocatalytic activity with doping.

(3) Investigation of growth mechanism of structured TiO_2 nanorod thin films. Synthesis of structured TiO_2 nanoarrays of controlled packing density and growth orientations.

(4) Applications of effectively structural engineered TiO_2 nanoarrays to PV cells.

References

[1] A. Fujishima, T. N. Rao, D. A. Tryk. Titanium dioxide photocatalysis. Journal of Photochemistry and Photobiology C: Photochemistry Reviews 1 (2000) 1-21.

[2]T. Yamaki, T. Sumita, S. Yamamoto, A. Miyashita. Preparation of epitaxial TiO_2 films by PLD for photocatalyst applications. Journal of Crystal Growth 237–239 (2002) 574–579.

[3]M. Ni, M. K. H. Leung, D. Y. C. Leung, K. Sumathy. A review and recent developments in photocatalytic water-splitting using TiO_2 for hydrogen production. Renewable and Sustainable Energy Reviews 11 (2007) 401-425.

[4]H. Lin, C. Keng, C. Tung. Gas-sensing properties of nanocrystalline TiO_2. Nanostructured Materials 9 (1997) 747–750.

[5]G. Eranna. Metal Oxide Nanostructures as Gas Sensing Devices. Taylor and Francis (2011).

[6]M. Gratzel. Dye-sensitized solar cells. Journal of Photochemistry and Photobiology C: Photochemistry Reviews 4 (2003) 145–153.

[7]M. Grarzel. Recent Advances in Sensitized Mesoscopic Solar Cells. Accounts of Chemical Reseach. 42 (2009) 1788-1798.

[8] A. Fujishima. T. N. Rao, D. A. Tryk. Titanium dioxide photocatalysis. Journal of Photochemistry and Photobiology C: Photochemistry Reviews 1 (2000) 1–21.

[9]K. Honda, A. Fujishima. Electrochemical photolysis of water at a semiconductor electrode. Nature 238 (1972) 37-38.

[10]Y. Kikuchi, K. Sunada, T. Iyoda. K. Hashimoto, A. Fujishima. Photocatalytic bactericidal effect of TiO_2 thin films: dynamic view of the active oxygen species responsible for the effect. Journal of Photochemistry and Photobiology. A, Chemistry 106 (1997) 51-56.

[11]N. M. Mahmoodi, M. Arami, N. Y. Limaee, N. S. Tabrizi. Kinetics of heterogeneous photocatalytic degradation of reactive dyes in an immobilized TiO_2 photocatalytic reactor. Journal of Colloid and Interface Science 295 (2006) 159-164.

[12] R. Cai, K. Hashimoto, K. Itoh, Y. Kubota, A. Fujishima. Photokilling of malignant cells with ultra-fine TiO_2 powder. Bulletin of the Chemical Society of Japan 64 (1991) 1268-1273.

[13] H. Sakai, R. Baba, K. Hashimoto, Y. Kubota, A. Fujishima. Selective killing of a single cancerous T_{24} cell with TiO_2 semiconducting microelectrode under irradiation. Chemistry Letters 24 (1995) 185-186.

[14] R. Wang, K. Hashimoto, A. Fujishima, M. Chikuni, E. Kojima, A. Kitamura, M. Shimohigoshi, T. Watanabe. Light-induced amphiphilic surfaces. Nature 388 (1997) 431-432.

[15]R. Wang, K. Hashimoto, A. Fujishima, M. Chikuni, A. Kitamura,M. Shimohigoshi, T. Watanabe, Photogeneration of highly amphiphilic TiO_2 surfaces. Advanced Materials 10 (1998) 135-138.

[16] M. Wang, H. Lin, T. Characteristics and optical properties of iron ion (Fe^{3+})-doped titanium oxide thin films prepared by a sol-gel spin coating. Journal of Alloys and Compounds 473 (2009) 394–400.

[17]G. H. Takaoka, T. Nose, M. Kawashita. Photocatalytic properties of Cr-doped TiO_2 films prepared by oxygen cluster ion beam assisted deposition. Vacuum 83 (2008) 679–682.

[18]M. A. Barakat, H. Schaeffer, G. Hayes, S. Ismat-Shah. Photocatalytic degradation of 2-chlorophenol by Co-doped TiO_2 nanoparticles. Applied Catalysis B: Environmental 57 (2005) 23–30.

[19]L. Devi, S. Kumar, B. Murthy, N Kottam. Influence of Mn^{2+} and Mo^{6+} dopants on the phase transformations of TiO_2 lattice and its photo catalytic activity under solar illumination. Catalysis Communications 10 (2009) 794–798.

[20]L. Li, C. Liu, Y. Liu. Study on activities of vanadium (IV/V) doped TiO_2 (R) nanorods induced by UV and visible light. Materials Chemistry and Physics 113 (2009) 551–557.

[21]H. Yu, X. Li, S. Zheng, W. Xu. Photocatalytic activity of TiO_2 thin film non-uniformly doped by Ni, Materials Chemistry and Physics 97 (2006) 59-63.

[22]S. Sato. Photocatalytic activity of NO_x-doped TiO_2 in the visible light region. Chemical Physics Letters 123 (1986) 126–128.

[23]H. Li, D. Wang, H. Fan, P. Wang, T. Jiang, T. Xie. Synthesis of highly efficient C-doped TiO_2 photocatalyst and its photo-generated charge-transfer properties. Journal of Colloid and Interface Science 354 (2011) 175–180.

[24]T. Ohno, M. Akiyoshi, T. Umebayashi, K. Asai, T. Mitsui, M. Matsumura. Preparation of S-doped TiO_2 photocatalysts and their photocatalytic activities. Applied Catalysis A: General 265 (2004) 115–121.

[25]X. Dong, J. Tao, Y. Li, H. Zhu. Enhanced photoelectrochemical properties of F-containing TiO_2 sphere thin film induced by its novel hierarchical structure. Applied Surface Science 255 (2009) 7183–7187.

[26]Y. Huang, W. Ho, Z. Ai, X. Song, L. Zhang, S. Lee. Aerosol-assisted llow synthesis of B-doped, Ni-doped and B–Ni-codoped TiO_2 solid and hollow microspheres for photocatalytic removal of NO. Applied Catalysis B: Environmental 89 (2009) 398–405.

[27]R. Long, N. J. English. First-principles calculation of nitrogen-tungsten codoping effects on the band structure of anatase titania. Applied Physics Letters 94 (2009) 132102-132104.

[28]R. Long, N. J. English. Band gap engineering of (N, Ta)-codoped TiO_2: A first-principles calculation. Chemical Physics Letters 478 (2009) 175–179.

[29]S. Kim, S. K. Lee. Visible light-induced photocatalytic oxidation of 4-chlorophenol and dichloroacetate in intrided Pt-TiO_2 aqueous suspensions. Journal of Photochemistry and Photobiology A Chemistry 203 (2009) 145-150.

[30]Y. Wang, Y. L. Meng, H. M. Ding, Y. K. Shan, X. Zhao, X.Z. Tang. A highly efficient visible-light-activated photocatalyst based on bismuth- and sulfur-codoped TiO_2. The Journal of Physical Chemistry C 112 (2008) 6620-6626.

[31]Y. Gai, J. Li, S. Li, J. Xi, S. Wei. Design of narrow-gap TiO_2: a passivated codoping approach for enhanced photoelectrochemical activity. Physical Review Letters 102 (2009) 036402-03646.

[32]M. Bettinelli, V. Dallacasa, D. Falcomera, P. Fornasiero, V. Gombac, T. Montini, L. Romano, A. Speghini. Photocatalytic activity of TiO_2 doped with boron and vanadium. Journal of Hazardous Materials 146 (2007) 529-534.

[33]X. Han, G. Shao. Electronic properties of rutile TiO_2 with nonmetal dopants from first principles. The Journal of Physical Chemistry C 115 (2011) 8274–8282.

[34]C. Yu, J. C. Yu. A simple way to prepare C–N-codoped TiO_2 photocatalyst with visible-light activity. Catalysis Letters 129 (2009) 462-470.

[35]J. Yang, H. Bai, Q. Jiang, J. Lian. Visible-light photocatalysis in nitrogen–carbon-doped TiO_2 films obtained by heating TiO_2 gel–film in an ionized N_2 gas. Thin Solid Films 516 (2008) 1736-1742.

[36]Y. W. Sakai, K. Obata, K. Hashimoto, H. Irie. Enhancement of visible light-induced hydrophilicity on nitrogen and sulfur-codoped TiO_2 thin films. Vacuum 83 (2008) 683-687.

[37]E. Thimsen, S. Biswas, C. S. Lo, P. Biswas. Predicting the Band Structure of Mixed Transition Metal Oxides: Theory and Experiment. The Journal of Physical Chemistry C 113 (2009) 2014-2021.

[38]T. Umebayashi, T. Yamaki, H. Itoh, K. Asai. Analysis of electronic structures of 3d transition metal-doped TiO_2 based on band calculations. Journal of Physics and Chemistry of Solids 63 (2002) 1909-1920.

[39]G. Sberveglieri. Gas sensors: principles, operation, and development. Kluwer Academic Publishers (1992).

[40]B. Liu, E. Aydil. Growth of oriented single-crystalline rutile TiO_2 nanorods on transparent conducting substrates for dye-sensitized solar cells. Journal of the American Chemical Society 131 (2009) 3985-3990.

Chapter 2 Literature review

2.1 Structures of TiO_2 phases

2.1.1 The crystal structures of intrinsic TiO_2 phases

TiO_2 materials naturally occur in three available crystal forms, known as anatase, rutile and brookite, in which well crystallized anatase and rutile have been widely studied owing to their practical uses. Both anatase and rutile phase of TiO_2 crystal structures are comprised of TiO_6^- octahedrons that each Ti atom is surrounded octahedrally by six oxygen atoms, as that presented in Fig. 2.1.1. Actually, the octahedrons in both structures are more or less distorted leading to two kinds of bonds between titanium and oxygen atoms in TiO_6^- octahedron no matter the phases, marked as Ti-O_1 and Ti-O_2 in Fig. 2.1.1. In rutile, the distortion of octahedron only stretches the Ti-O_2 bonds along diagonal direction, resulting in longer TiO_2 bonds along diagonal direction than the other four Ti-O_1 bonds in lateral plane, the angles between Ti-O_1 and Ti-O_2 bonds are still 90^o. While in anatase structure, except for the stretching of Ti-O_2 bonds, Ti-O_1 bonds are deviated from lateral plane therefore the angles between TiO_1 and TiO_2 are not now 90^o. Ti-O_2 bonds in both structures have the same distance of 0.198 nm while the Ti-O_1 bond in anatase is shorter than that in rutile, with distances of 0.1934 nm versus 0.1949 nm [1].

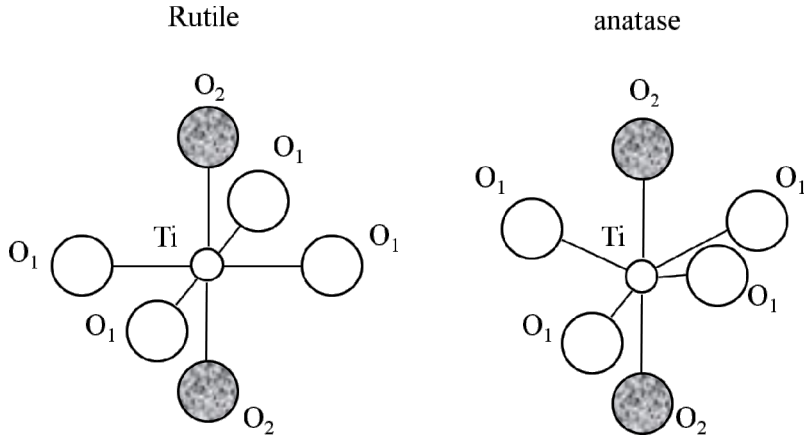

Figure 2.1.1 The octahedrons of rutile and anatase structure.

The connecting manners with different lattice distortion lead to different crystal structures with corresponding chemical and physical properties though both of them have tetragonal lattice structure. As shown in Fig. 2.1.2, each distorted octahedron in rutile contacts with ten neighbour octahedrons, in which two share edge oxygen pairs and eight share corner oxygen atoms forming a liner chain. Each octahedron in anatase is connecting with eight neighbours, four sharing edges and four sharing corners, to form a zig-zag chain [2]. The difference in distortion and connecting manner results in distinctive Ti-Ti distances, 0.379 nm and 0.304 nm in anatase versus 0.357 nm and 0.296 nm in rutile. Therefore, anatase phase is considered to have a more open structure with corresponding higher specific surface.

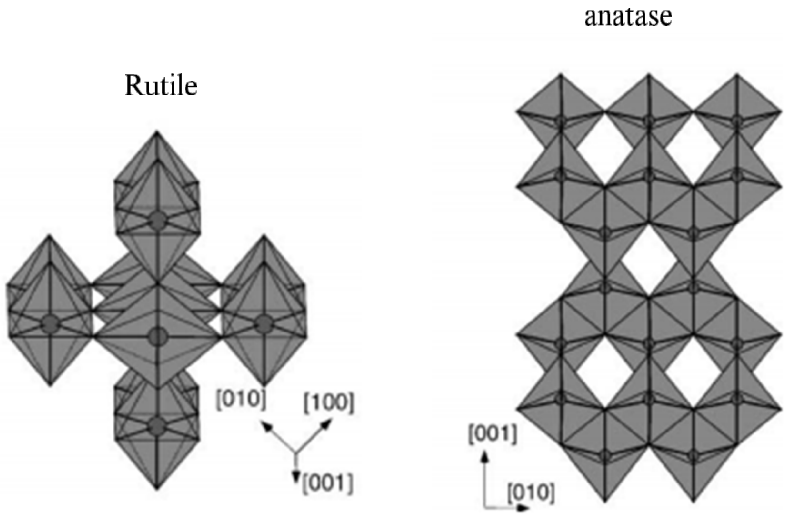

Figure 2.1.2 Crystal structures of rutile and anatase [3].

Ramamoorthy and Wanderbilt [4] studied surface energies of four low index surfaces (110), (100), (001), (011) of rutile structure, using first principle total energy calculation combined with a self consistent ab initio method. On the basis of calculating surface stabiltiy and counting the density of dangling bonding on each surface, the studies predicted that (110) surface has the lowest surface energy, followed by (100), (011) and (001) surface has the highest surface energies, which was in accord with experimental results [5]. The calcualted surface energy are listed in Table 2.1. Although the accurate value of surface energy is hard to obtain by theoretical calculation, the relative surface energies are still meaningful. According

to the calculated energies, a equilibrium Wuff shape of rutile TiO_2 crystal at zero temperature was proposed, as shown in Fig. 2.1.3(a). In Waff structure [6], the lower surface energy of a facet corresponding to the shorter length the facet to the centre of the crystal and the greater surface area of the facet. If the surface energy is high, the distance between the facet and centre of the crystal would be very long and the corresponding surface area would be small in the construction [7]. If the surface energy of one facet is too high, the distance between the facet to centre of the crystal wounld be greater than the size of the crystal in that direction, and that facet would not appear in the Wulff shape. This means the facet of high surface energy decreases its surface area and the facet of lower surface energy increases its surface area, to decrease the total surface energy per area. Therefore, the Wolff construnction obey the principle of lowest energy. In rutile TiO_2 crystal, energy of (001) facet of very high surface energy is not expected to apear at 0 K as that shown in Fig. 2.1.3(a). Among four low index sufaces, (110) surface is the predomint facet in rutile phase TiO_2 materials, though other surface are also found.

Table 2.1 Calculated surface energy vs. surface for relaxed rutile TiO_2 crystal [4].

Surface	Surface Ti Coordination	Surface O coordination	Surface Energy (unrelexed) J/m^2	Surface Energy (relexed) J/m^2
(110)	5, 6	2, 3	1.751	0.889
(010)	5	2	1.928	1.118
(011)	5	2, 3	2.104	1.392
(001)	4	2	2.931	1.648

The calculated surface energies of low index surfaces of anatase structure are listed in Table 2.2 by using a self consistent ab initio method [8,9,10]. (101) surface was calculated to be the most thermaldynamic stable surface with lowest surface energy among different low index surfaces, followed by (100), (001) and (110). Based on the relative value of surface energies of facets, the Wulff shape of anatase structure was proposed, as shown in Fig. 2.1.3(b), being in excellent agreement with shape of matrually grown samples. In anatase, (101) plane is the predominent facet in anatase phase TiO_2 materials and other planes are also observed.

Table 2.2 Calculated surface energy vs. surface for relaxed anatase TiO_2 crystal.

Surface	Surface Energy (relexed) J/m^2
(101)	0.44
(100)	0.53
(001)	0.90
(110)	1.09

Since bulk rutile is more stable thermodynamically than anatase at all temperatures and pressure due to its lower total free energy (bulk and surface), metastable anatase phase can easily transfer to rutile upon heating accompanied by a thermal generation [11,12]. Comparing Table 2.1 and 2.2, however, we can see the average surface energy of equilibrium shape anatase crystal is lower than that of rutile crystal. In the case of crystallites of extremely small sizes below a critical value, anatase has a lower total free energy on account of their correspondingly high surface areas [13,14]. This means the nanometre sized TiO_2 particles could be more stable in anatase phase compared to rutile.

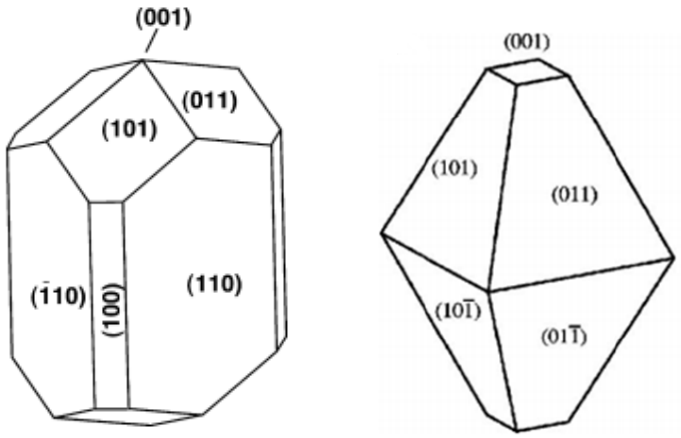

(a) (b)

Figure 2.1.3 The equilibrium shape of TiO_2 in rutile crystal (a) [4] and anatase crystal (b) [9,10].

2.1.2 The electronic structures of intrinsic TiO_2 materials

In the energy view, electrons in the crystalline semiconductors are confined to certain energy levels, which are also known as electron movement orbitals, and forbidden from other region, as shown in Fig. 2.1.4. The highest range of energy levels which electrons occupy at absolute zero degree is called valence band and the range of energy levels, higher than that, is called conduction band. Each energy band has a large number of quantum states. The valence band describes a state of electrons tightly bound to the atomic nuclei and the conduction band reflects the electrons escaped from the materials to move entirely free in crystal lattice. As for TiO_2, the bottom of the conduction band (CB) is dictated by the Ti 3d electron states and the top of the valence band (VB) is dominated by the oxygen 2p electron states. The energy difference between the top of valence band and the bottom of conduction band is dubbed as band gap (E_g). Therefore, the band gap determines the specific minimum amount of energy in order for an electron to jump from valence band to conduction band. When a semiconductor is illuminated with light of energy higher than the band gap, electrons receive the energy from incident photons and jump from the valence band to the conduction band leaving as many positive holes in the valance band. This process is equivalent to the movement of electrons from bonding orbital to anti-bonding orbital. In most cases, the excited electrons are unstable and can easily jump back into the valence band and recombine with holes quickly with the release of heat. There are two kinds of band gaps, direct band gap which means carriers at the highest point of valence band and the lowest point of conduction band have the same momentum and electrons can directly jump into conduction band without changing momentum, and indirect band gap which means electrons must pass through an intermediate state to reach conduction band and transfer momentum to crystal lattice. Rutile phase TiO_2 has a direct band gap of 3.0 eV while anatase phase has an indirect band gap of 3.2 eV.

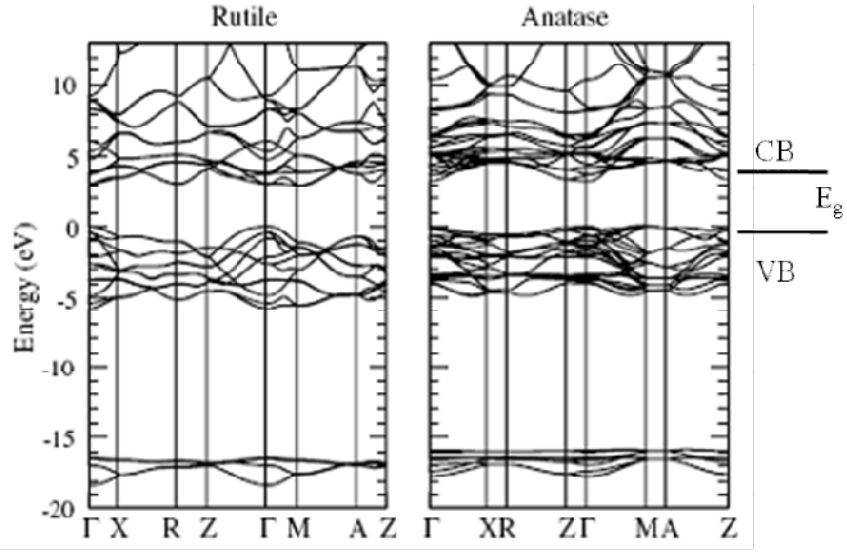

Figure 2.1.4 Energy band structures of TiO_2.

The differences in crystals and energy band structures of rutile and anatase phases result in different properties of TiO_2 bulk materials as shown in Table 2.3.

Table 2.3 Parameters of rutile and anatase phases TiO_2 bulk materials.

Atomic radius (nm)	O	0.066 [15]
	Ti	0.146 [8]
Ionic radius (nm)	O (-2)	0.14
	Ti (4+)	0.064
Crystal structure	Rutile	anatase
System	Tetragonal	Tetragonal [16]
Space group	D^{14}_{4h}-$P4_2/mnm$	D^{14}_{4h}-$I4_1/amd$ [17,18]
Lattice constants(nm)	a=b=0.4594	a=b= 0.3785
	c=0.2959	c=0.9514 [17,19]
Electron mobility at 500 K μ ($cm^2 V^{-1} s^{-1}$)	~1 [20]	~10 [21]
Band gap (eV)	~3.0 (direct)	~3.2 (indirect) [22,23,24]
Absorption edge (nm)	413	387
Density (g cm^{-3})	4.2-4.3	3.8-3.9 [25]

The properties of TiO_2 materials mean it can be used as white pigment, in ceramics, as UV or corrosion protective coating, in electric devices [26,27], in antifogging on account of photo induced hydrophilicity [28,29,30,31], as heterogeneous photocatalyst to clean the environment [32,33,34,35], in water splitting for the production of hydrogen [36,37,38], as gas sensor [39, 40] and in solar cells for electric power [41,42,43,44] and so on.

2.2 Band gap engineering of TiO_2

As it was mentioned, the functionality for pure TiO_2 can be excited only by ultraviolet (UV) light that only accounts for less than 5% of solar irradiance because of the wide band gaps (3.2 eV for anatase and 3.0 eV for rutile). This wide gap nature of TiO_2 phases seriously limits their practical applications in most circumstances including photocatalysis, photo induced hydrophilicity and production of hydrogen, as the UV light can be readily absorbed even by pure water vapour and clear glass. It is very important and urgent therefore to fabricate modified TiO_2 thin films and powders with a narrowed band gap to utilize the visible light from solar irradiance.

To extend the light absorption spectrum toward the visible light range, intense efforts have been made in order to modify the optical absorption properties of TiO_2 phases, including ions doping, compositing TiO_2 with semiconductors of narrower band gaps. The most feasible modification method seems to be doping TiO_2 with metal and non-metal atoms to tune the band structures [45,46,47,48]. Although TiO_2 materials have been widely explored by doping with a variety of metal ions and nonmetal ions, the extensive exploration of TiO_2, especially experimental research, has never been concluded because the practical application of TiO_2 under visible light is nevertheless restricted.

2.2.1 Single metal ions doped TiO_2

The main objective of single metal ions doping on band gap narrowing is to shift up valence band or shift down conduction band of intrinsic TiO_2 or create shallow intermediate band levels into forbidden band through substituting Ti atoms by

dopants in TiO_2 lattice, since deep intermediate band levels would predicatively act as recombination centre and thereby arouse significant electron and hole recombination. On the ground of this, various single metal ions have been widely studied to address the optical limitation of TiO_2 materials, including transition metal such as V [49,50,51,52], Cr [53,54,55,56,57], Mn [58,59], Fe [60,61,62,63,64,65], Co [66], Ni [67], Cu [68], Zn [69], Zr [70], Mo [58], Ru [71], Rh [72], Ag [71,73], W [74,70], Pt [75], rare earth metals [76,77,78, 79, 80], such as Ce [81,82], Pr, Sm [83], Eu [84], Gd [85] and Er [86], other metals such as Mg [87], Sr [88], Ba [89], Ca [90], Pb [91] and so on. Albeit a great deal of theoretical and experimental works have been focused on doping TiO_2 with single metal ions, the exploitation of TiO_2 with doping still has profound prospective because the chemical states of doping ions determined by fabrication method play a crucial role on the doping effect.

Among these, transition metal ions, especial 3d transition metal ions has merited extensive attention, since substituting Ti atoms by these ions would result in mixing of intrinsic energy bands of TiO_2 with partial occupied d orbitals of dopants, and thus being expected to effectively alter the electronic structure of TiO_2. Another attractive reason for the extensive studies on 3d transition ions doping is their comparable ionic size to Ti^{4+}, which is not expected to introduce serious lattice distortion and defect states into TiO_2 crystal and would be much easier to be incorporated into TiO_2 matrix. At the initial stage, ions implantation was utilized to implant ions into TiO_2 bulk materials to achieve ions doped TiO_2. For instance, Anpo and co-workers [92,93,94,95,96,97,98,99,100] have implanted TiO_2 bulk material with various metal ions, including V, Cr, Mn, Fe, Co, Ni, Cu, Rh, Nb, Mg and Ti, by using a high voltage acceleration ion implantation method. The metal ions were injected into the deep bulk of TiO_2 with high acceleration energy of 150-200 keV, and then subsequently calcined in O_2 at around 723 K to produce visible light response. The implantation of transition metal ions into TiO_2 materials, such as V, Cr, Mn, Fe, Co, Ni, and Cu ions, was found to effectively shift the absorption edge of TiO_2 to visible light region, making doped TiO_2 materials be capable to absorb visible light. These indicated that the implantation of these transition metal ions could alter the intrinsic band energy structure of TiO_2. The order of the effective on band gap narrowing and corresponding red shift was found to be

V>Cr>Mn>Fe>Ni>Cu in their work, partial absorption properties were depicted in Fig. 2.2.1. By implanting V ions into P25 TiO_2 pellet, the absorption edge was red shifted gradually with increased V amount [50], to about 500 nm with 2.2×10^{-6} mol g^{-1} cat^{-1} V implantation, owing to the intermediate band level within the forbidden band. While the implantation of Mg or Ti ions into TiO_2 materials was not effective to shift the optical absorption edge to make any visible light response, indicating that the shift is not caused by high energy implantation process, but by the interaction of metal ions with host ions in TiO_2.

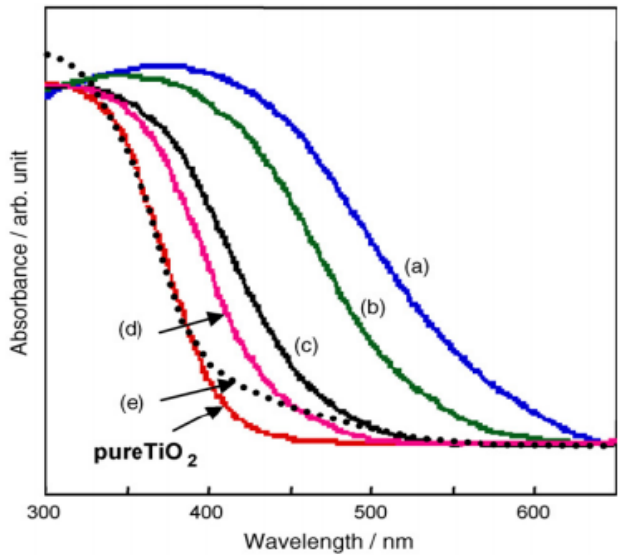

Figure 2.2.1 Diffuse reflectance UV-visible spectra of TiO_2 implanted with (a) V, (b) Cr, (c) Fe, (d) Ni ions [50].

Similarly, Klosek et al. [101] synthesized V doped TiO_2 by a simple chemical process and found that V doped TiO_2 was able to absorb light in the energetic range of 2.5-2.7 eV, corresponding to the wavelength from 450 nm to 500 nm. Likewise, Wu [51] and Bhattacharyya [52] also observed promoted red shift in UV visible absorption spectra through increasing the doping concentration of V. Dvoranova [102] prepared Cr, Mn, Co, doped TiO_2 nanoparticle by hydrolysis of $TiCl_3$ or $TiCl_4$ together with dopants sources. The UV visible light spectra indicated that all of Cr, Mn and Co caused slight absorption shift into visible region by introducing second absorption

shoulders located in the region of 400-600 nm. Choi [103] synthesized V, Cr and Ni doped TiO_2 by standard sol-gel method via adding metal precursors into distilled water prior the hydrolysis titanium tetraisopropoxide (TTIP) to a given doping concentration. All three dopants gave rise to slight red shift in order of V>Cr>Ni, being in good agreement with the results of Anup.

Shao [59] carried out a theoretical calculation, using a molecular design approach, of Mn doped rutile TiO_2 on the grounds of the density function theory combined with Hubbard U correction (DFT+U). The results suggested that Mn substitution of Ti site in TiO_2 matrix could remarkably reduce the energy band gap of TiO_2 via introducing quality intermediate bands into forbidden band. It was emphasized that giving a particular high doping concentration of Mn could widen the intermediate band enough to join the conduction band. As a consequence, the energy band gap was continuously reduced through substituting Ti lattice site by increasing Mn doping concentration. Devi et al. [58] fabricated Mn solely doped TiO_2 powders by sol-gel method by adding Mn precursors as sources of Mn^{2+}. Under optimal doping concentration, the absorption edge of Mn doped TiO_2 was shifted to 454 nm corresponding to the band gap of 2.73 eV.

Fe doped TiO_2 materials have been mostly studied experimentally and theoretically, not only owing to its effect band gap narrowing effect but also on account of its nontoxic and inexpensive property. Theoretical calculation of Fe doped rutile TiO_2 based on density function theory was also carried out by Shao [61]. Calculated results suggested that Fe substitution of Ti site in TiO_2 matrix could significantly reduce the energy band gap of TiO_2 via introducing quality intermediate bands into forbidden band; inducing a secondary absorption edge well below the major optical band gap. Experimentally, Teoh et al. [104] Fe doped TiO_2 nanopowders through flame spray pyrolysis technique, making the optical absorption edge shift to 460 nm.

Nevertheless, controversial doping effects on optical properties of TiO_2 materials were observed by different processing techniques and conditions. Different results were typically obtained by Ghasemi [105], via a sol-gel method employing ionic liquid in precursor to synthesize transition metal ions doped TiO_2, as shown in Fig. 2.2.2. Discernibly, the order of shifting levels that Co was the most effective doping on

absorption shifting and Fe doping was more effective than Cr were not in consistent with the results of Anup. This was mainly attributed to the completely different fabrication methods since the nature of doping states depends strongly on fabrication methods, in which other distinctive results were also revealed [106].

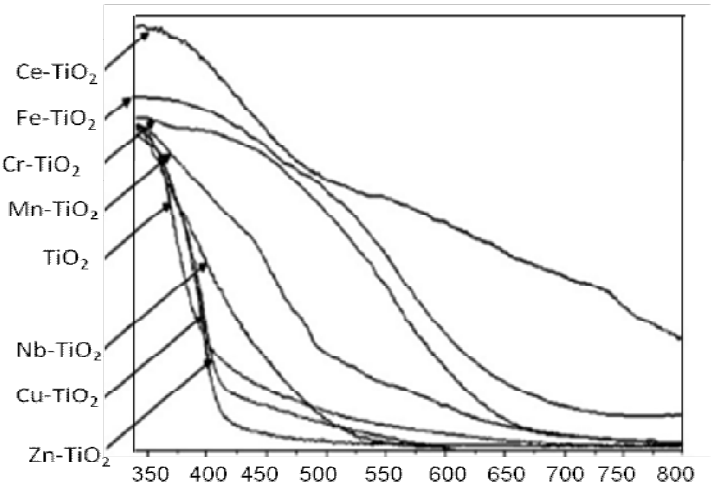

Figure 2.2.2 Diffuse reflectance spectra of TiO_2 doped with transition metal ions obtained by Ghasemi [106].

Therefore, to systematic compare the doping effect of 3D transition metals and give an instructional road for effective doping formulation, Shao [69] has carried out a series theoretical calculation on 3d transition metals doped TiO_2 based on DFT. The electronic structures of 3d transition metal doped rutile TiO_2 were shown in Fig. 2.2.3, in which the band gap of virgin TiO_2 was marked by vertical bar with band gap of 2.03 eV. Discernibly, one can realize that most of dopants introduced intermediate states or bands within the forbidden band of TiO_2 by substituting Ti atoms in TiO_2 matrix. In addition, despite most could give rise to effective red shift of absorption edge according to the energy band structures, it was suggested that Mn has the biggest potential as dopant among 3d transition metals not only on account of the significant band gap narrowing effect, but also because the intermediate bands in forbidden band were overlapping with each other to avoid isolated states in Mn-TiO_2. It was stressed therefore that the recombination caused by isolated states were conceivably avoided, making co-doped TiO_2 more efficient as photoelectronic or photocatalytical materials.

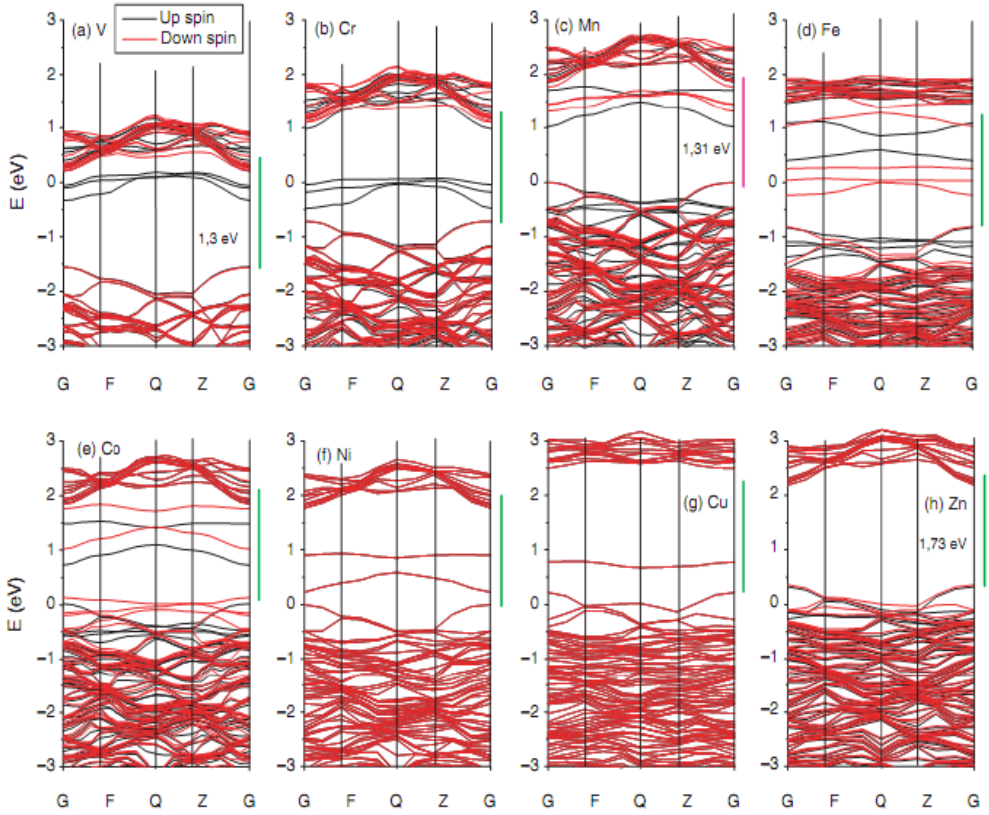

Figure 2.2.3 Calculated band structure of rutile TiO_2 doped with 3d transition metals, with one Ti atoms substituted in each 2×2×2 supercell [69].

Except for 3d transition metal ions, other transition metals have also been widely attempted. Devi et al. [57], for example, fabricated Mo solely doped TiO_2 powders by sol-gel method via adding Mo precursors as sources of Mo^{6+}. Under optimal doping concentration, the absorption edge of Mo doped TiO_2 was shifted to 480 nm corresponding to the band gap of 2.58 eV. By using standard sol-gel method, Chie [103] tried 13 different metal ions doped TiO_2, including Ni, Co, Cu, V, Fe, Rb, Ru, Os, U, La, Pt at doping concentrations ranging from 0.1 to 1.0 at%. The UV-visible diffuse reflectance spectroscopy reflected that Ni, Co, Cu, V, Fe and Pt doping resulted in varying degrees of red shift into visible region while Ag, Rb, Y and La could hardly cause any red shift of the absorption spectrum of TiO_2. In addition, it was reported by Nagaveni [70] that W doping introduced intermediate states into

forbidden band of TiO_2 locating under the bottom of conduction band, leading to TiO_2 sensible to visible light, while Zr doping contrarily extended band gap of TiO_2.

Besides transition metals ions, rare earth metal has also been paid considerable attention, not only in view of the band gap shift effect upon doping, but also on account of their ability to form complexities with various Levies bases in the reaction of 4f orbitals of rare earth metals with these functional compounds, including acids, amines, aldehydes, alcohols and so on. Thus incorporation of rare earth dopants into TiO_2 matrix is expected to be a predominant way to improve the photocatalytic property. Accordingly, 17 kinds of rare earth ions, including La, Ce, Pr, Nd, Sc, Dy, Eu, Ho, Gd, Tb, Er, Tm, Yb, Lu, Sm Y, Pm, doped rutile TiO_2 were calculated by using DFT [76], wherein nearly all of these rare earth doping, except Lu, Y, Yb and Sc, could reduce the band gap width of rutile, though in a lesser extent compared to 3d transition metal doping. Experimentally, absorption of rare earth doped TiO_2 in visible light region was realized in a large number of publications and considered to be attributable to the charge transfer between f orbital of rare earth and the valence band or conduction band of TiO_2 [77,86]. However, in some cases, the absorption in visible region came from new absorption peaks corresponding to the electronic transitions between I, H and F orbitals [79,80,86]. The main draw back of rare earth doping is their huge ionic sizes compared to Ti^{4+}, making it is difficult to incorporate these dopants into TiO_2 lattice as much higher formation energy is required.

Other metals have also been studied though there seldom can produce red shift in optical absorption edge [87,88,89]. Long and co-workers [107,108] performed theoretical calculations on Ge Sn Pb doped rutile and anatase TiO_2 via replacing Ti atoms by dopants. Based on the optimized structures of ions doped TiO_2, the band gap of Ge doped anatase TiO_2 were reduced by 0.15 eV whereas broadened by 0.05 and 0.02 eV with Sn and Pb doping. Mg doped TiO_2 was reported elsewhere to show a blue shift in optical absorption edge compared to undoped TiO_2 [87] and the same phenomenon was likewise observed in Sr doped TiO_2 [88].

2.2.2 Single nonmetal ions doped TiO_2

Nonmetal ions were also extensively studied as a means to address the absorption edge towards long wavelength region by substituting oxygen with various kinds of nonmetal ions in TiO_2 lattice [109]. For nonmetal ions doped TiO_2, the p states of dopants were either mixed with O 2p to shift the valence band edge upwards or located above valence band to act as stepping stones to relay electrons from valence band to conduction band, making the absorption edge is shifted into visible region. Among all nonmetal dopants, N [110,111,112,113,114] has been most studied since the first report by Sato in 1986. In addition to this, C [115,116,117], S [118,119], F [120], B [121], P were also widely exploited as nonmetal dopants.

Asahi et al. [109] calculated the electronic structure of nonmetal ions doped anatase TiO_2 crystal by replacing O with C, N, S, F or P, using the full potential linearized augmented plane wave method (FLAPW) in the framework of local density approximation (LDA). Based on the total density of state (DOS) of doped TiO_2 as shown in Fig. 2.2.4 (a), they proposed that replacing O by N in anatase TiO_2 was the most effective way since its 2p states was mixing with O 2p states to contribute to the band gap narrowing. Fig. 2.2.4(b) shows the comparison of absorption of N doped TiO_2 with pure TiO_2 thin film synthesized by sputtering. Discernable visible absorption ability was seen from $TiO_{2-x}N_x$, being in line with theoretical results.

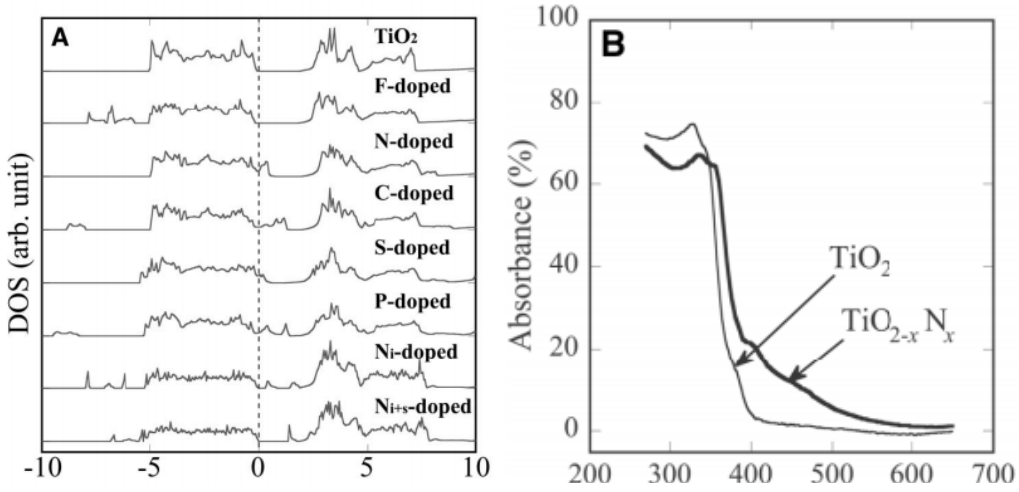

Figure 2.2.4 (a) Total density of states (DOSs) of doped anatase TiO_2 and (b) experimental measured optical absorption spectra of $TiO_{2-x}N_x$ and TiO_2 film [109].

However, it was also reported that only TiO_2 with high substitutional N level (>=2 at%) can effectively narrow the band gap, whereas low doping level resulted in shallow isolated states located above valence band instead of band gap narrowing since the mixing of N 2p and O 2p was incompletely [122]. This was in agreement with most experimental results that N doped TiO_2 exhibited visible light absorption with a shoulder in the range of 400 nm to 600 nm [123, 113, 124]. Similar to this, calculation based on DFT+U suggested N doping in rutile crystal introduced a shallow isolated band states above the O 2p states of valence band, which was mainly from N 2p [125], whereas the overall band gap of rutile TiO_2 was to be slightly broadened. The shallow isolated state here could take the role as stepping stones to transfer photo excited carriers into conduction band, making optical absorption edge red shifted into visible region.

In Asahi's study [109], S doping had the same band gap narrowing effect as N doping by mixing S 2p with O 2p states. However, it was emphasized that it would be difficult to incorporate S into TiO_2 crystal owing to its big ionic size compared to O ion, as large formation energy was required for the substitution of S than the substitution of N. In an attempt to modify electronic structure of TiO_2, Umebayashi [126] successfully synthesized S doped TiO_2 powder by oxidation annealing of titanium disulfide (TiS_2) in air, with absorption edge shifted to longer wavelength region due to the substitution of O atoms by S in TiO_2 lattice. Besides this, S ions were considered to be able to either substitute Ti atoms or O atoms in TiO_2 lattice in some experimental cases, which principally depended on synthesis methods and conditions. With regard to S doping as cation, DOS calculation results revealed that replacing of Ti by S ions atoms gave rise to a localized S 3s states in forbidden band and could stretch absorption edge into a longer wavelength region via acting as stepping stone to relay electrons from valence band to conduction band [127]. Therefore, distinctive shift degrees of band edge were achieved experimentally as the doping states and degree were determined by disparate fabrication methods [128, 129, 130].

What's more, according to Asahi, the states introduced by C and P in forbidden band were too deep to helpfully transfer photoexcited carriers from valence band to conduction band, whereas the F 2p states were localized below valence band edge

without any gap in forbidden gap or mixing with valence band or conduction band [109]. Nevertheless, some studies proposed distinctive issue that substitutional doping C in TiO_2 resulted in significant overlap between C states and O 2p states near the top of valence band [131]. Apart from N, S, C, F and P, other nonmetal ions doping into TiO_2 have been exploited likewise but with less extent.

2.2.3 Ions co-doped TiO_2

Recently, on the ground of widely studied mono-doping, reports on two ions co-doping have attracted extensive attention in attempt to conquer visible light absorption of TiO_2 materials, including nonmetal and metal co-doping [132], e.g. N-Fe [133,134], N-Cr [135], C-Mo [136, 137], N-W [138], N-Ta [139], N-Pt [140], S-Bi [141], B-V [142], N-V [143], two nonmetal ions co-doping, e.g. C-N [144,145], N-S [146], C-S [147], N-H [125], C-H [125], two metal ions doping, such as Fe-Ho [148], Sc-V [149,150], Fe-Co[151], Sm-Eu [152]. By employing suitable dopants, the electronic structure could be conceivably modified compared to single ions doping. For example, in the study of N-Fe co-doping, co-doped TiO_2 powders, prepared by using homogeneous precipitation hydrothermal method, showed apparent red shifted absorption region and abrupt stronger absorption intensity with corresponding to ones that of N or Fe solely doped [133]. As shown in Fig. 2.2.5, the probable mechanism was that N dopant introduced shallow intermediate states above valence band while Fe dopant introduced shallow intermediate states under conduction band, leading to obvious red shift of absorption edge.

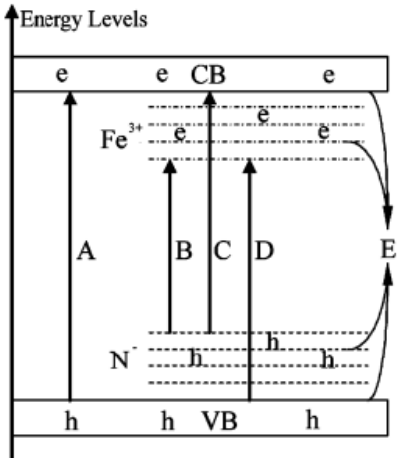

Figure 2.2.5 The schematic diagram of mechanism of the N-Fe co-doped TiO_2 [133].

Gai and co-workers [136] found C-Mo co-doped dramatically shifted the band gap from 3.2 eV to 2.26 eV, apparently much more than mono-doping. It was impressive that the isolated states induced by mono-doping were annihilated via co-doping, and thereby would be helpful to avoid electron and hole recombination due to gap states. On the ground of spin polarized calculation using GGA formalism, Long [138] proposed that N-W co-doping not only introduced a continuous band to the top of valence band owing to the hybridization of N 2p and W 5d states, but also brought W 5d orbitals to the bottom of conduction band. Such combined effect helped to narrow the band gap significantly. The same phenomenon was also observed in N-Ta co-doped TiO_2, by using the same calculation method, that hybridization of N 2p and Ta 5d gave rise to formation of continuum states above the top of valence band together with Ta 5s orbitals located at the bottom of conduction band, leading to remarkable band gap narrowing [139].

Apart from such metal-nonmetal doping effect due to p-d hybridization, it was shown that the addition of H together with N in TiO_2 matrix helped to reduce the band gap without introducing mid-gap states, making the co-doped material intrinsic in nature due to donor-acceptor annihilation [125]. Similarly, the C-H co-doping also induced significant reduction in band gap with reduced number of gap states [125].

2.3 Visible light photocatalysis of TiO_2 on organic compounds

2.3.1 Photocatalysis mechanism

Photocatalysis is defined as 'capture of the sun light or any incident light to turn organic matter to carbon dioxide and water' by the presence of as semiconductor photocatalyst. To better understand the mechanism of photocatalysis, oxidative and reductive reaction procedures of TiO_2 are depicted in Fig. 2.3.1, in which the energy band diagram of TiO_2 in PH 7 solution is proposed by Fujishima [153], together with redox potential of various radials and molecules versus standard hydrogen electrode (SHE). The photocatalytic mechanism starts from the absorption of photons with

energy equal to or greater than the band gap value of TiO_2. Then electrons in valence band would be ejected into conduction band leaving an equal amount of positive holes in valence band. When TiO_2 is in contact with electrolyte solution, the thermodynamic equilibrium of Fermi level occurs at the interface. This would result in the formation of space charge region, normally of the order of 1-3 nm, in which the energy level is bent upwards or downwards. In this space charge region, photogenerated electrons and holes are separate and move in a different way on account of band bending. Therefore, upon the absorption of photons, electron and hole pairs are generated in TiO_2 and one portion diffuses to the surface of the photocatalyst taking part in the chemical reaction with adsorbed molecules on the surface of TiO_2 [154]. The oxidative potential of photogenerated hole is as high as 2.53 V, which is positive enough to not only oxidize some organic and inorganic matters straightly but also react with water and hydroxyl ion to generate highly oxidative compound (·OH).

$$TiO_2 + hv \rightarrow TiO_2 + e^- + h^+ \quad (2.1)$$

$$h^+ + OH^- \rightarrow \cdot OH \quad (2.2)$$

$$h^+ + H_2O \rightarrow \cdot OH + H^+ \quad (2.3)$$

On the other hand, the reducing potential for photogenerated electrons is as negative as – 0.52 V, which is in principle enough to extract H from water to decompose water into H_2 and O_2 [153]. Once it diffuses to the surface of TiO_2, electrons can reduce the adsorbed oxygen to form charged super oxide anion. In high PH solution, the charged super oxide anion desorbs and can directly oxidize adjacent organic molecules. In low PH solution, the charged super oxide anion reacts with H^+ to form a perhydroxyl radical $\cdot HO_2$, which is an oxidative agent to be able to decompose hydrocarbons.

$$e^- + O_2 \rightarrow O_2^- \quad (2.4)$$

$$O_2^- + H^+ \rightarrow HO_2 \cdot \quad (2.5)$$

It was also advocated that the formed perhydroxyl could directly react with absorbance or react with super oxide anion again to produce oxidative compound (·OH) or be further decomposed to oxygen and oxidative oxyful [155].

$$2HO_2 \cdot \rightarrow O_2 + H_2O_2 \qquad (2.6)$$

$$H_2O_2 + O_2^- \rightarrow \cdot OH + OH^- + O_2 \qquad (2.7)$$

Apparently, photogenerated electrons and holes are consumed through oxidation and reduction process thus the total reaction cycle is completed, resulting in the back of TiO_2 to original state. At the same time, organic molecules absorbed on the surface of TiO_2 have been decomposed relying on the above described process. Then another excitation happens again until organic molecules are decomposed completely into CO_2 and H_2O. From Fig. 2.3.1, one can see that the oxidative potential of the formed oxidative hydroxyl radical (·OH) is extremely high as 2.27 V, much higher than most of oxidants such as O_3, H_2O_2, and thus can decompose most of organic compounds completely into CO_2 and H_2O [156,157].

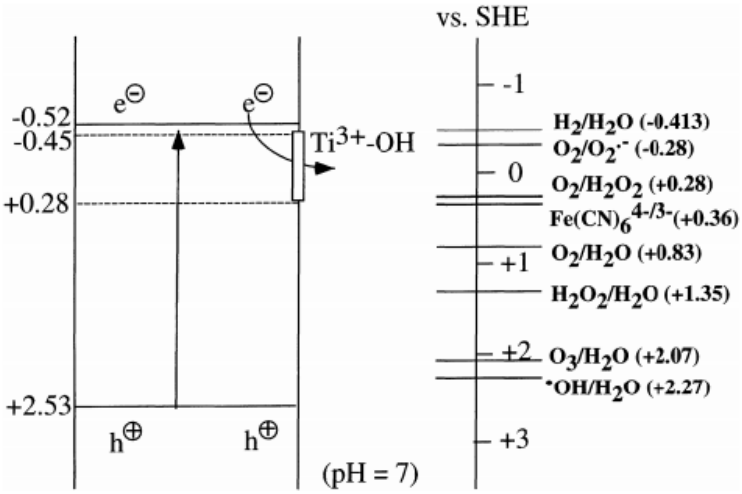

Figure 2.3.1 Schematic diagram of photocatalysis process of TiO_2 [153].

In effect, apart from TiO_2, a variety of semiconductor materials have been identified and studied experimentally; including ZnO, CdS, SnO_2, WO_3, CuO, Fe_2O_3 and so on. However compared to these semiconductor materials, TiO_2 has incontrovertibly been the most studied photocatalyst partly, on account of it being extremely stable in the presence of aqueous solution, while other types of semiconductor could be easily dissolved in acidic or alkaline solution. What is more, TiO_2 also has sufficient positive valence band edge making photogenerated positive holes can react with

water and organic molecules adsorbed on semiconductor surface. As mentioned previously, in most case the photogenerated carriers recombine quickly, but in TiO_2 the recombination is much slower than that of most semiconductors. The main drawback of TiO_2 is the wide band gap meaning TiO_2 can only absorb the light with wavelength shorter than 380 nm, in other words, only UV part that possesses 5% of the whole energy of the sun can be used by pure TiO_2, though the absorption coefficient of TiO_2 in this region is in the order of 10^5 cm^{-1}.

2.3.2 Photocatalytic activity of doped TiO_2 with visible light absorption

As it was mentioned above, the band gap of TiO_2 can be tuned through suitable doping to shift valence band up or conduction band down; or introduce intermediate states for effective absorption under visible light illumination. Nevertheless, photocatalytic activities, of some doped catalysts, were hardly improved despite red shift of optical absorption edges was indeed observed.

The photocatalytic activity of TiO_2 materials is largely affected by the following factors. The first critical factor is the light absorption properties of TiO_2 materials, including absorption region and coefficient, which decide the maximum amount of photons that can be converted into electrons and holes from incident light. Larger absorption region and coefficient leads to more excitation of carriers. Conceivably, the doping not only narrows the electronic band gap but simultaneously alters the oxidative and redox potential of photogenerated carriers, leading to contradictory influence on photocatalytic activity. Another factor is the surface area of TiO_2 photocatalyst, the larger surface area means more molecules can adsorb onto TiO_2, leading to faster photocatalytic rates. In addition, the electron and hole recombination rate, normally determined by defect levels, is also central to the photocatalytic activity. The interface is generally a defective site for carriers to recombine, as the lifespan of photogenerated carriers are approximately 10 ns [158]. One can improve the crystalline degree of TiO_2 photocatalyst to avoid defects. However, this in turn may cause undesirable aggregation of TiO_2 nanomaterials and decrease the relative surface area. In doped TiO_2, high doping level could induce electronic defect states, crystal defects or even ions oxides separated out from TiO_2 crystal, to act as carrier recombination centres, whereas low doping level could act as

charge transfer mediator to prolong lifespan, when carriers migrated from the inside of the photocatalyst to the surface [159].

Therefore, the relationship between the photocatalytic activity of doped TiO_2 and the physical properties is complicated. Optimum conditions for a specific case should be pursued by taking all of these factors into consideration and may be disparate from one case to another. Generally, in ideally doped TiO_2 materials for visible light photocatalysis, the doping should avoid deep isolated states in forbidden band together with extending absorption region, to maintain or prolong carrier diffusion length before they are recombined, and thus offer good photocatalytic activity under visible light illumination [160].

Choi et al [161] have systematically studied doping effects of 21 transition metal ions on the photocatalytic activity of TiO_2 prepared from the controlled hydrolysis of titanium tetraisopropoxide. According to their work, the presence of metal ion dopants in TiO_2 matrix significantly influenced its photocatalytic activity in the degradation of $CHCl_3$. Doping TiO_2 with suitable ions such as Fe, V, Mo, Ru, Os, Re, and Rh at optimum concentration of 0.1-0.5 at% effectively improved the photo reactivity for both oxidation and reduction. In contrary, doping TiO_2 with Co and Al decreased the photocatalytic activity. It was deduced that the photocatalytic activity was predominantly dependent on the distribution of dopants within TiO_2 particles together with the electronic band structures of doped TiO_2, which determined the role of dopants states, including mixing with intrinsic energy band, shallow acceptor/donor states for effective trap, or deep isolated states leading recombination.

Teoh and co-workers [104] investigated the photocatalytic activity of Fe doped TiO_2 that prepared via flame paralysis technique, by dissociating oxalic acid under visible light with wavelength longer than 400 nm. Although the increasing of Fe doping level resulted in gradually extended absorption region, the optimum ratio of Fe/Ti for visible light photocatalytic activity was 0.05, as a balance existed between charge excitation and charge recombination. With respect to the same ion doping, the optimum conditions of doped TiO_2 for the application in visible light photocatalysis were mainly determined by synthesis methods and varied from case to case. As an example, Li et al. [159] similarly synthesized Fe doped TiO_2 particles by a

hydrothermal process with conceivable red shift of absorption edge. The photocatalytic activities of doped TiO_2 particles were even worse compared to that of pure TiO_2 particle upon the degradation of methylene blue (MB) under a 300 W highly pressure mercury vapour lamp.

Likewise, controversial results were also reported in terms of doped TiO_2 with nonmetal dopants. Liu et al. [114] studied N doped TiO_2 powders with different ratios of anatase to rutile phases via milling the mixture of P25 TiO_2 and $C_6H_{12}N_4$ in air or gaseous NH_3 atmosphere respectively. It was found that N doped TiO_2 with higher rutile phase had higher photocatalytic activity regardless of light absorption ability, being in contrast with reported results of pure TiO_2. Optimum doping level and corresponding photocatalytic activity were discriminative on account of diverse techniques.

2.4 Structural engineering of TiO_2 thin films

One dimensional TiO_2 nanostructures are of great interest in today's research in nanotechnology on account of their unique electrical pathways for photogenerated charge carriers, high surface to volume ratio, as well as tuneable size and morphology. To date, most of the reported one-dimensional TiO_2 nanostructures were synthesized in the forms of oriented nanotubes on conductive substrates by anodization synthesis technique [162, 163], or disoriented TiO_2 nanorods/wires on nonconductive and opaque substrates using various distinct synthesis techniques. Through employing different electrolyte and tailoring electrochemical conditions, uniform TiO_2 nanotube arrays of controlled length, pore diameter and wall thickness can be easily synthesized. With reference to literatures, oriented TiO_2 nanotube arrays have been proven by a variety of studies to have improved unique properties, especially lower recombination rate, compared with other form of structures for the application of solar cells, photocatalysis, gas sensing, and etcetera. Nonetheless, the electron diffusion coefficient in each nanotube is several magnitude orders lower than that in single crystal TiO_2, supposable owing to grain boundary scattering and trapping in polycrystalline nanotubes.

Recently, hydrothermal methods have been developed to fabricate heterogeneous growth of oriented single-crystalline TiO_2 nanorods/wires on substrates of transparent conducting oxide (TCO) glass or without supporting substrate. Thin films, made of self-assembled and vertically aligned TiO_2 nanorods or nanowires that can provide uninterrupted pathway for the transportation of carriers compared with nanotubes, meriting great attention for their potential application in dye- and quantum-dot-sensitized solar cells, or as photocatalysts. It was demonstrated that the use of well aligned TiO_2 single crystal nanorods in dye sensitized TiO_2 solar cells resulted in significantly improved energy conversion efficiency [164]. On the other hand, TiO_2 nanorods were also shown to have enhanced photocatalytic activity due to their improved charge transfer [165]. Typically, electron mobility in single crystalline rutile is about 1 $cm^2\ V^{-1}\ s^{-1}$, being nearly two orders of magnitude larger than that in nanoparticle TiO_2 thin film [20].

In 2004, Hosano [166] reported a structured morphology of TiO_2 films consisting of highly crystalline rectangular rutile TiO_2. In this work, single crystalline TiO_2 was successfully synthesized on borosilicate glass slide via hydrothermal reaction of aqueous $TiCl_3$ solutions containing a large amount of NaCl. As it can be seen in Fig. 2.4.1, nucleation of rutile crystals started from some spots on the surface of glass substrate, and then crystal growth occurred and proceeded radically from theses nucleation spots in the direction towards bulk solution. The crystal structure of nano rod was determined by using a high resolution transmission electron microscope to be single rutile crystal with [001] growth direction. It was emphasized that addition of NaCl was central to achieve the morphology and absence of NaCl resulted in TiO_2 powders precipitated in solution, since adsorption of Cl^- onto (110) plane inhibited the growth along [110] direction. Accordingly, TiO_2 had grown along [001] direction which is perpendicular to [110]. The wettability of TiO_2 thin films consisting of this kind of nanorods on glass substrate were evaluated by contact angle measurement [167]. A remarkable and controllable surface wettability, with super hydrophobicity and illuminated reversible super hydrophobicity, was observed on the nanorod thin film.

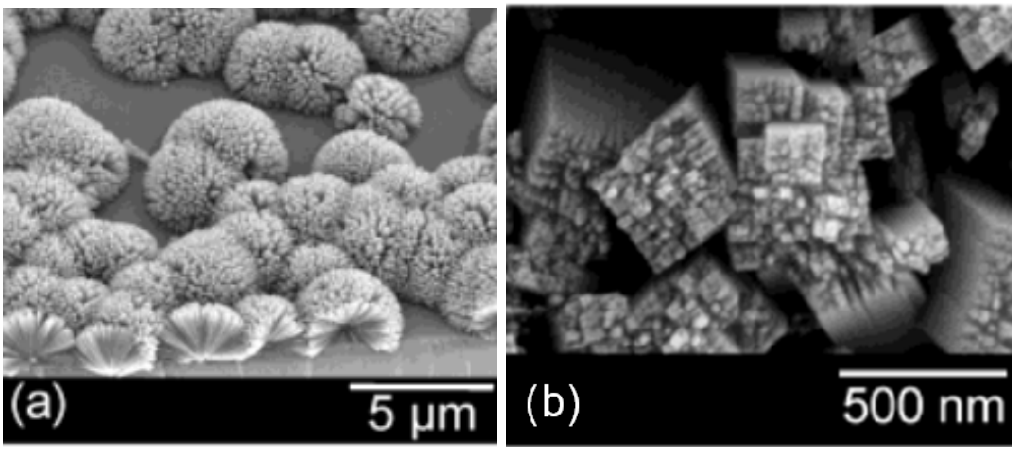

Figure 2.4.1 (a) Surface SEM image and (b) top SEM image of films under high magnification of TiO_2 films synthesized by Hosano [166].

However, as it was mentioned, the growth of these TiO_2 nanorods were started from some unpredictable spots on glass substrate, resulting in incompletely covered thin film on nonconductive substrate which limited their application in solar cell, gas sensing and so on. In order to form the most desirable, aligned, oriented and density packed single crystal nanorod or nanowire array on conductive substrate, a variety of synthesis techniques were attempted, including chemical vapour deposition (CVD) [168], hydrothermal method [169]. By using peroxotitanate complex ions in the starting solution, density packed rutile TiO_2 thin film with preferred [001] direction was successfully synthesized on conductive fluoride-doped tin oxide covered glass (FTO) substrate, as shown in Fig. 2.4.2(a). This method enabled dense films fabricated on a big substrate with the potential to be used in photo electrical devices, though the packing density was extremely dense and uncontrollable with low specific surface area. Besides this, Feng and co-workers [170] successfully synthesized densely packed single crystal TiO_2 nanowire arrays on FTO substrates, as can be seen from Fig. 2.4.2(b), via hydrolysis reaction by using mixture of toluene, tetrabutyl titanate, titanium tetrachloride and hydrochloric acid solution as precursor. With the increase of temperature during reaction process, water was inclined to diffuse away from the high energy water and toluene interface and aggregate on the hydrophilic FTO surface to minimize system energy, resulting in hydrolysis of Ti^{4+} on the surface of

FTO. Then, TiO_2 was formed on top of FTO substrate and new hydrolysis occurred on hydrophilic TiO_2 surface, giving rise to continuous crystal growth. It was demonstrated that the presence of HCl promoted [001] growth direction leading to single crystal rutile TiO_2 nanowire thin film formed perpendicular to FTO substrate. On the other hand, FTO substrate also played critical role as it had the same tetragonal rutile structure and tiny lattice mismatch with rutile TiO_2. The light to chemical conversion efficiency of the nanowire thin film was measured to be 75%, indicating an excellent charge separation ability and low recombination in TiO_2 nanowire.

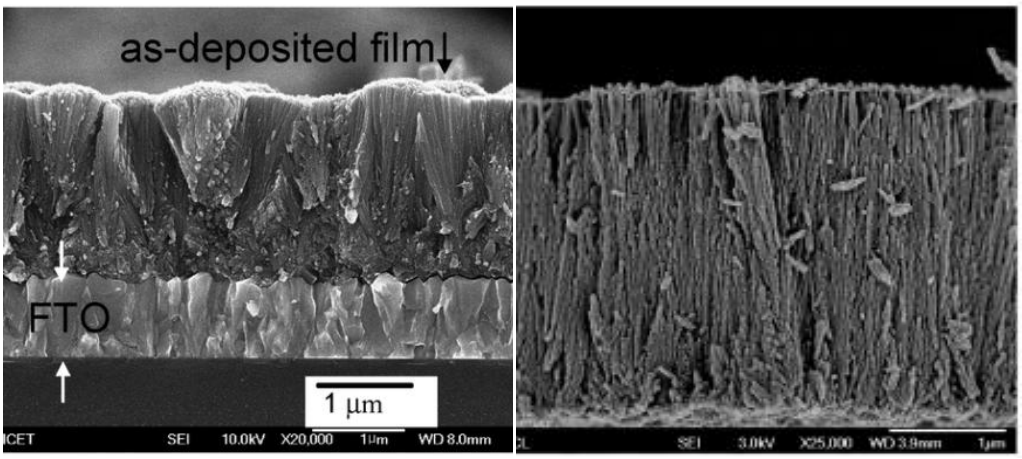

(a) (b)

Figure 2.4.2 Cross sectional SEM images of (a) aligned rutile TiO_2 synthesized using peroxotitanate complex ions [169], (b) aligned rutile TiO_2 synthesized in water and toluene solution [170].

Most recently, by using an extremely facile hydrothermal method, Liu and Aydil [171] have succeeded in synthesizing oriented single crystalline rutile TiO_2 nanorod films on FTO substrate, rather than glass or silicon. Fig. 2.4.3 shows a representative sample grown on FTO, in which the nanorods, being in tetragonal shape of [001] preferred growth direction and nearly perpendicular to substrate, uniformly cover the substrate. By adjusting the synthesis conditions, including initial concentration of reactants, growth temperature, growth time, PH value, additives, the packing density

and length of TiO_2 nanorod thin films were varied. It was emphasized that the existence of Cl^- played a key role on the growth of single rutile crystal along [001] direction. This facile and inexpensive hydrothermal technique has provided us a fresh start for application in photocatalysis and photo voltaic devices, even though more refined control is expected.

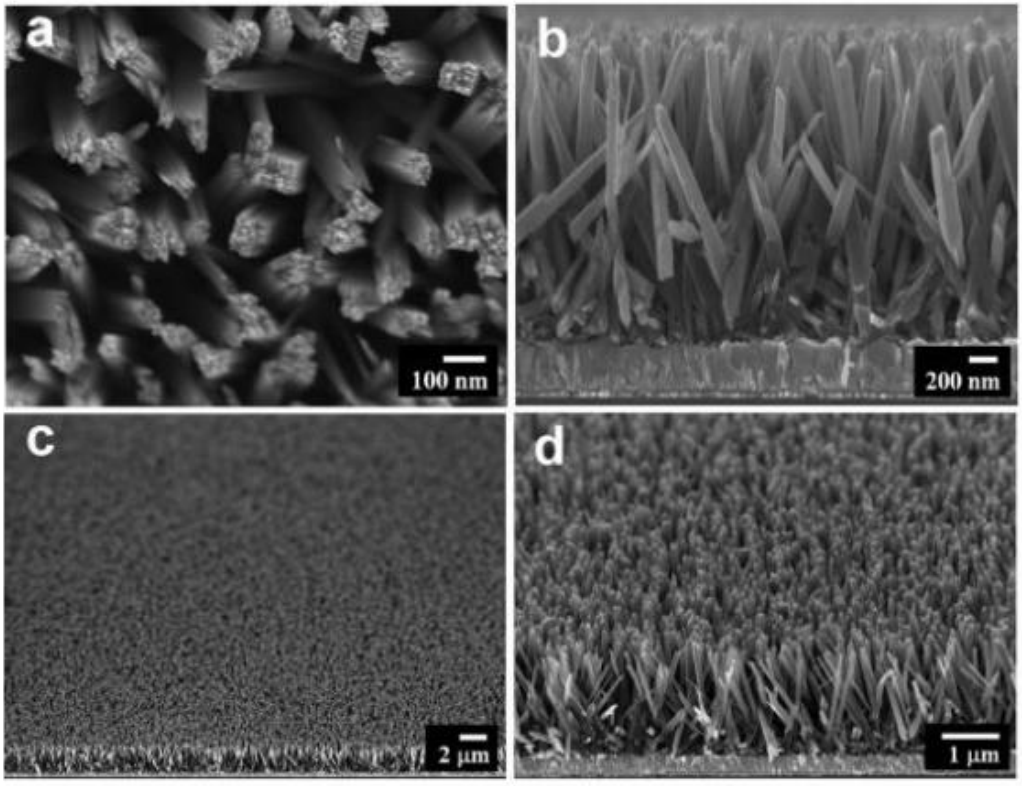

Figure 2.4.3 SEM images of one representative oriented rutile nanorod film grown on FTO in Liu's work, (a) top view, (b) Cross view, (c) and (d) cross sectional views [171].

2.5 Application of structural engineered TiO_2 in solar cells

The development of solar cell technology originated from the discovery of photovoltaic effect which refers to the creation of voltage and electric current in materials absorbing photons of light. Since in most photovoltaic application the irradiate light is sunlight, photovoltaic cells are also known as solar cells. The solar cell has to fulfil two fundamental functions, photogeneration of charge carriers in

light absorbing material and separation of the carriers to electrodes to transmit electricity [172]. This effect was first discovered in 1839 by French physicist Becquerel that the electricity generation between two electrodes placed in a conductive solution increased when exposed to light [173]. In 1954, Bell Laboratories announced the invention of the first reasonably efficient modern silicon solar cell [174], which was made of diffused silicon p-n junction with impressive efficiency up to 6%. To date, after years of development, silicon based solar cells have became the most dominating type of solar cells used commercially with the highest 27.6% efficiency in laboratory [173].

However, from a materials point of view, the indirect semiconductor is not an ideal material for photovoltaic application, since light absorption coefficient is much lower in an indirect band gap semiconductor than a direct semiconductor. For example, for a 90% light absorption it takes only 1 um of GaAs versus 100 um of Si [175]. Therefore it is necessary for silicon solar cells to be unparalleled thick, meaning they are extremely consuming materials. On the other hand, the photogenerated carriers have to pass through a long distance to reach the electrodes. Thus the material has to be of a very high purity and of high crystalline perfection to avoid carrier recombination and scattering, resulting in an extremely high manufacturing fee. This therefore has led to the development of the second generation of solar cell, thin film solar cells with the highest efficiency of 43.5% to date have been achieved by multi-junction cells via utilizing III-V semiconductor materials [173]. The multi-junction cells are also too expensive to allow practical use outside, mainly due to the complex fabrication process and high price of materials.

2.5.1 Dye sensitized solar cells

Compared to silicon solar cells and multi-junction thin film solar cells, TiO_2 based dye-sensitized solar cells (DSSCs) have many advantages such as low production cost and diversity of manufacture, making DSSCs promising as the third generation photovoltaic cells.

DSSCs have been extensively studied since the first report of regenerative photo-electrochemical process by Gratzel in 1991 [176, 177]. The technology of DSSCs is totally different from semiconductor devices that rely on a traditional p-n junction to

separate photogenerated charge carriers [178]. In the case of original DSSCs, the cell has three primary parts [179], as depicted in Fig. 2.5.1. On top is a transparent electrode made of FTO glass plate. Attached to this conductive layer is a thin layer of electron conducting material, typically being a wide band gap semiconductor, which forms into a highly porous structure with high surface area and, at the same time, connects together to allow electronic conduction to take place [180]. This layer of semiconductor is sensitized by a dye to absorb incident light. Photo excitation of the dye results in the injection of electrons into the conduction band of the oxide. Subsequently, the original state of the dye is restored by electron donation from the organic electrolyte, which is usually the iodide/tri-iodide containing redox couple [181]. The electrolyte is then oxidized by contact with second electrode. The voltage generated under illumination is determined by the difference between the Fermi level of the electron in the solid and the redox potential of the electrolyte [182].

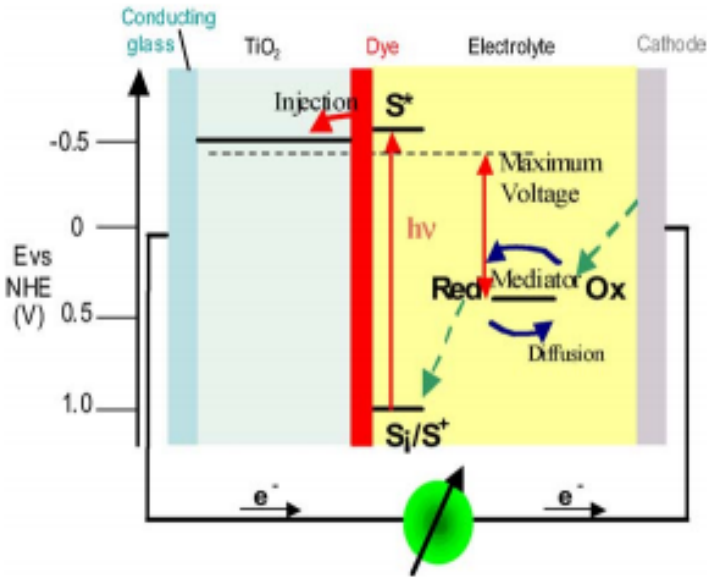

Figure 2.5.1 Band diagram of dye sensitized solar cell composed of TiO_2 [183].

The semiconductor material of choice is normally TiO_2, though alternative wide band gap metal oxides such as ZnO [184,185,186], V_2O_5, SnO_2 and Nb_2O_5 have also been investigated. Compared with others, TiO_2 oxide is a very promising semiconductor for use on dye sensitized solar cells because of its abundance; low

cost; nontoxicity and easily prepared to be nanostructured electrodes such as nanotubes and nanorods. In addition, TiO_2 is extremely stable and has strong interaction with carboxylate group of the dye while the out layer of ZnO surface could be easily dissolved by the acidic carboxylate group to form Zn^{2+}-dye compound at interface, resulting in higher charge separation on the interface of TiO_2 and dye. Employing 2 μm long oriented ruitle TiO_2 nanowire film as electron conducting material and N719 (Bis(tetrabutylammonium) Dihydrogen Bis(isothiocyanato)bis(2,2'-bipyridyl-4,4'-dicarboxylato)ruthenium(II), $C_{58}H_{86}N_8O_8RuS_2$) as dye in DSSC, Feng and co-workers [170] obtained a high light to electricity conversion efficiency of 4.83%, which was even higher than that of rutile particle films with thickness more than 5 μm, being mainly attributed to efficient vertical charge transport in TiO_2 nanowires. Through comparing solar cells made up of TiO_2 with ZnO, it was found that DSSC composed of single crystalline ZnO nanorod arrays of 20 μm in length exhibited lower efficiencies even though it had superiorly higher carrier mobility [187]. Similarly, in Liu' work [171], an efficiency of 3% was reached by using a 4 μm long single crystalline rutile TiO_2 nanorod thin film in DSSC.

However, the requirement of liquid electrolytes in dye sensitized solar cell is still a very challenging issue to be resolved for commercial applications, due to the temperature stability problems [188]. At high temperature the electrolyte could expand, making sealing the panels a serious problem while lower temperature causes the liquid to freeze, ending power production and potentially leading to physical damage. Another major drawback is that the electrolyte solution contains volatile organic compounds and solvent, being hazardous to human health and environment, and thus must be carefully sealed. Therefore, getting rid of liquid electrolyte now has been a major ongoing field of research as the developing of third generation of solar cells.

2.5.2 Polymer solar cells

The unavoidable draw backs of silicon solar cells and dye sensitized solar cells have promoted tremendous effort to develop polymer solar cells since the first observation of photovoltaic effect in tetracene-water system in 1966 [189]. Polymer solar cells are typically thin film devices based on a self assembling of electrons donors

(semiconducting polymers) and acceptors (fullerene) to convert sunlight to electrical power, by splitting photogenerated excitons across interface between electron donor and electron acceptor [190]. When the excitons meet the interface of electron donor and acceptor, it will be separated in the time scale of femto second [191]. Transparent and conductive ITO or FTO on flexible plastic substrate are often used as one side electrode to let incident light pass through, while metal electrodes are normally deposited onto the other side of optical active layer.

Polymer solar cells are a type of flexible solar cells obtained by various coating methods in range of laboratory spinning coating to large scale printing or spray coating [192], yet hold advantages of inexpensive to fabricate, light weight, potentially disposable and have lower negative impacts on environmental, thus supposed to be competitive substantial candidates to substitute silicon solar cells and DSSCs [193]. On the other hand, polymer solar cells could be very thin as the result of strong absorption coefficients (normally $>10^5$ cm^{-1}) [194] of organic semiconducting polymers, 300 nm is thick enough to absorb most of incident light from the sun.

The molecules used as the electron donor are generally conjugated polymers possessing delocalized π electrons owing to carbon p orbit hybridization. These π electrons can be excited from molecule's highest occupied molecular orbital (HOMO) to the lowest unoccupied molecular orbital (LOMO), by light in or near visible part of spectrum [195]. The energy band gaps of most conjugated polymers are around 2 eV, leading to the absorption peaks of typical conjugated polymers match the solar spectra better than that of Si [196], as that can be seen from Fig. 2.5.2. Among these p type conducting polymers, P3HT (Poly(3-hexylthiophene), $(C_{10}H_{14}S)_n$) is the most promising hole transport material with relative high hole mobility of up to 0.2 cm^2 V^{-1} s^{-1} [197,198] compared to 10^{-1}-10^{-7} cm^2 V^{-1} S^{-1} of most polymers [199] together with its suitable band gap of 1.9 eV that can absorb the main part of solar spectrum.

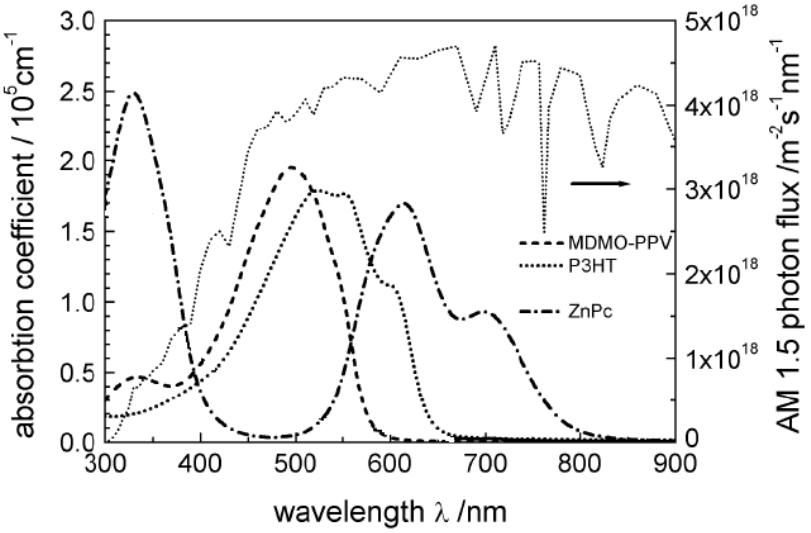

Figure 2.5.2 Optical absorption spectra of typical conjugated polymers [193].

The extremely localized electronic wave functions in organic molecules give rise to strong electrostatic attraction to keep electron and hole together as exciton, and thus cause strongly bound excitons in organic solar cells with energy between 0.1 and 1.4 eV. Therefore an electric field is required to separate strongly bound electrons and holes [195]. As shown in Fig. 2.5.3, in polymer solar cells, accepter materials are employed to separate photogenerated excitons, and the material acquiring the electron, such as PCBM (phenyl-C61-butyric acid methyl ester, $C_{72}H_{14}O_2$), is called acceptor. Electron donor has high ionization energy and electron acceptor has high electron affinity. When exciton diffuses to the donor-acceptor interface, the chemical potential of electrons decreases and then electron and hole dissociation happens at the interface.

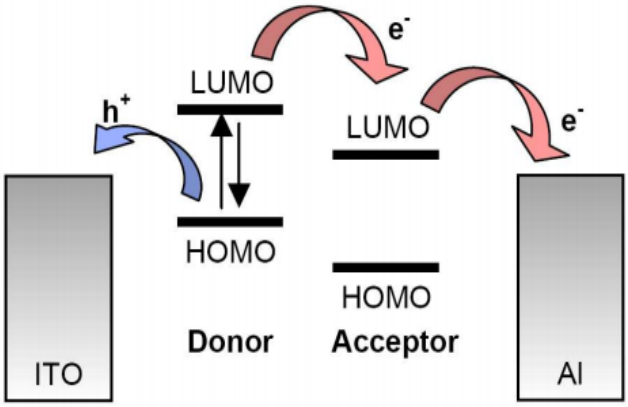

Figure 2.5.3 Band diagram of polymer solar cell [200].

In organic semiconducting polymers, charge transport proceeds by hopping between localised states, rather than transport with in a band. Therefore they suffer from generally poor charge carrier mobility, orders of magnitudes lower than inorganic semiconductors, and relatively small diffusion length of excitons, typically less than 20 nm [201,202]. These make exitons easily to recombine or decay via thermalization before they reach the electrodes [203]. To address these drawbacks, bulk heterojunction was designed via blending electron donor and electron accepter together, which provided adequate interface area for charge dissociation. In addition, structured n type inorganic semiconductor films, especially vertical aligned nanotube or nanorod films were employed as one side of electrode offering direct pathways to export photogenerated electrons. Takanezawa [204] observed that the efficiency of devices was improved by introducing ZnO as electron conductor into P3HT/PCBM bulk heterojunction devices, suggesting that ZnO behaved as a better charge conductor than PCBM. By employing oriented TiO_2 nanotubes into P3HT/PCBM bulk heterojunction devices, an improved efficiency of 3.32% was obtained [205], implying better electron transfer in TiO_2 nanotube despite that the conductivity characteristic of nanotube is uncomparable to single oriented nanorod.

2.5.3 Organic-inorganic hybrid solar cells

To combine the high carrier mobility of inorganic semiconductor [206] and strong absorption coefficients of organic semiconducting polymer (normally $>10^5$ cm^{-1}) [207]

together, polymer-inorganic hybrid solar cells have been designed. They are of particular interest by using inorganic semiconductors as electron acceptors in solar cells to dissociate excitons formed in conjugated absorption materials, resulting from their physical and chemical stability and facile fabrication properties. A wide range of nanomaterials were employed as n type inorganic semiconductors, including TiO_2 [208,209], ZnO [210], CdSe [211,212,213], PbS [214, 215], and so on. In organic-inorganic hybrid solar cells, wide band gap semiconductors such as TiO_2 and ZnO act as electron conducting medium, while narrow band gap semiconductors CdSe and PbSe are both light absorber and electron transporter [216,217].

Same as polymer solar cells, the so called organic-inorganic hybrid solar cells also consist of photoactive layer between two electrodes of different work functions. It can be built from bilayer structure, blends of inorganic nanoparticles and conjugated polymers (hybrid bulk hetero junctions HBHJs), as well as from nanostructured inorganic semiconductors fabricated on transparent electrode and impregnated with conjugated polymer, as seen in Fig. 2.5.4.

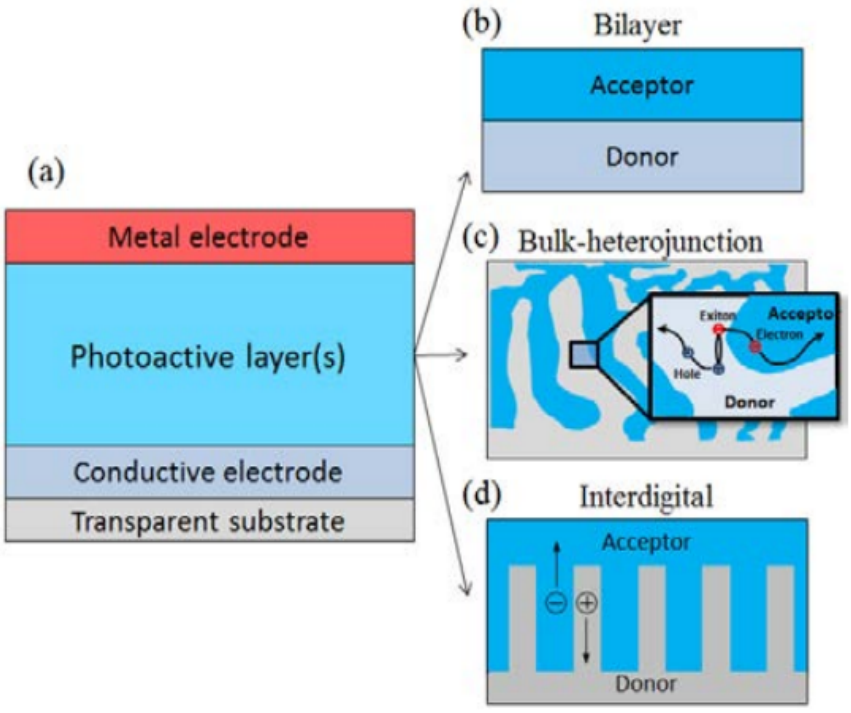

Figure 2.5.4 Structures of organic-inorganic devices [218].

The bilayer structure is the most straightforward approach via depositing a second layer on top of the first. This geometry can guarantee directional transfer of photogenerated charges across the donor and acceptor interface. Since both positive and negative charges travel to their respective electrodes in p type or n type layers, the chances for recombination losses are significantly reduced. However, as discussed previously, the efficiency of this structure is still limited by the short charge diffusion length in donor material. In addition, the interfacial area for charge separation is extensively restricted [219]. As an example, dense nanoparticle TiO_2 and P3HT bilayer structure fabricated by Wu and co-workers only achieved an efficiency of 0.26% [220].

Hybrid bulk heterojunction solar cells, which are the most studied structure in organic polymer solar cells, are also widely studied here by blending inorganic semiconductor materials with organic polymer due to their obvious advantages compared to bilayer structure. Sun et al. [213] have demonstrated solar cells with respectable efficiencies up to about 2.8% by blending CdSe tetrapods with the poly(*p*-phenylenvinylene) (PPV) derivative OC1C10-PPV. Recently, the highest efficiency of 3.2% was achieved by using the lower band gap polymer Poly[2,1,3-benzothiadiazole-4,7-diyl[4,4-bis(2-ethylhexyl)-4H-cyclopenta[2,1-b:3,4-b']dithiophene-2,6-diyl]] (PCPDTBT) together with CdSe nanoparticles [221]. Although CdSe is comparative effective, the most studied semiconductors used in hybrid solar cells are TiO_2 and ZnO as the undesirable use of toxic CdSe material should be avoided. Beek [222] reported that bulk heterojunction photovoltaic devices based on blends of a conjugated polymer poly[2-methoxy-5-(3‘,7‘-dimethyloctyloxy)-1,4-phenylenevinylene] (MDMO−PPV) as electron donor and crystalline ZnO nanoparticles (nc-ZnO) as electron acceptor had achieved the efficiency of 1.6%, with incident photon to current conversion efficiency up to 50%. By using P3HT as light absorber material together with 50 wt% ZnO nanoparticles in polymer matrix, the efficiency was optimized up to 2% by Oosterhout [223]. Kwong [208] reported a P3HT/TiO_2 composite solar cell, which had a power conversion efficiency of 0.42%.

The sizes of domains and the continuity of network are important parameters in determining the power conversion efficiency of the hybrid bulk heterojunction

devices. The main point is the domains should be continuous in the vertical direction so that the separated electrons and holes can move easily to their respective electrodes without interruption. But unfortunately, the unconnected islands are unavoidable in hybrid bulk heterojunction devices. High surface tension of small inorganic nanocrystals together with the low solubility of inorganic in the same organic solvent that organic material use, make inorganic materials very easy to self-assemble together [224]. Therefore, nanostructured inorganic semiconductors combined with p type polymer has attracted extensive attention since it not only has much higher interfacial area than bilayer structure but also can overcome the recombine problem of bulk heterojunction devices [225]. Moreover, the carrier mobility is several orders of magnitude higher in single crystal as compared to nanoparticle devices [226], thus higher power conversion efficiencies are expected to achieve by solar cells composed of single crystal materials.

The short exciton diffusion length of p type polymer means the interval of inorganic nanorods should be below 20 nm [201,202], and on the other hand, should be big enough for polymer to infiltrate into. So the dimensional optimization of nanostructured materials is an ideal way to improve the performance of the device. ZnO material has been most studied in structured inorganic-polymer heterojunctions owing to the ease of synthesizing crystalline at low temperature and high surface area of nanorod arrays [227,228]. Hybrid inorganic-polymer solar cells using ZnO nanorod arrays instead of planar films as electron transport layer exhibited significant improved performance. For example, effective infiltration of P3HT into ZnO nanorod resulted in an efficiency of 0.28% [229]. Greene [230] fabricated ZnO-TiO_2 core shell nanorod/P3HT solar cells by depositing thin shells of TiO_2 on top of ZnO nanorods by atomic layer deposition (ALD) method. By comparing them with ZnO nanorod/P3HT solar cells without shells, they found the introduction of TiO_2 thin shells showed significantly increased open voltage and fill factor, along with an improved efficiency of 0.29%, indicating TiO_2 /P3HT interface had more efficient charge separation than that of ZnO/P3HT interface, being in good agreement with that in DSSCs. Vertical aligned nanotube TiO_2 based organic-inorganic hybrid devices with high power conversion efficiency of 3.8% have been successfully obtained by uniformly infiltrating with P3HT and another unsymmetrical squaraine

dye [231]. To the best of author's knowledge, aligned nanorod TiO_2 based organic-inorganic hybrid devices were seldom reported as the fabrication technique was newly realized. Therefore, hybrid devices based on one dimensional TiO_2 nanorod thin films are necessary and urgent to be systemically studied.

References

[1]L. Vayssieres. On solar hydrogen and nanotechnology. Wiley (2011).

[2] A. Khataee, G. A. Mansoori. Nanostructured titanium dioxide materials: properties, preparation and applications. World Scientific Publishing Company (2011).

[3]U. Diebold. The surface science of titanium dioxide. Surface Science reports 48 (2003) 53-229.

[4]M. Ramamoorthy, D. Vanderbilt, R K. Smith. First principle calculations of energetics of stoichiometric TiO_2 surfaces. Physic Review B 49 (1994) 16721-16727.

[5]Y. W. Chung, W. J. Lo, G. A. Somorjai. Low energy electron diffraction and and electron spectroscopy studies of the clean (110) and (100) titanium dioxide (rutile) crystal surfaces. Surface Science 64 (1977) 588-602.

[6]A. Zangwill. Physics at surfaces. Cambridge University Press (1988).

[7]J. B. Lowekamp. The anisotropy of the surface energy and photochemical activity of rutile. Carnegie Mellon University. (1999).

[8]U. Diebold. The surface science of TiO_2. Surface Science Reports 48 (2003) 53-229.

[9]M. Lazzeri, A. Vittadini, A. Selloni. Structure and energetics of stoichiometric TiO_2 anatase surfaces. Physical Review B 63 (2001) 1-9.

[10] M. Lazzeri, A. Vittadini, A. Selloni. Erratum: Structure and energetics of stoichiometricTiO_2 anatase surfaces. Physical Review B 65 (2002) 155409-155409.

[11] J. M. G. Amores, V. S. Escribano, G. Busca. Anatase crystal growth and phase transformation to rutile in high-area TiO_2, MoO_3–TiO_2 and other TiO_2 supported oxide catalytic systems. Journal of Materials Chemistry 5 (1995) 1245-1249.

[12]Z. Zhang, C. Wang, R. Zakaria, J. Ying. Role of particle size in nanocrystalline TiO_2-based photocatalysts. Journal of Materials Chemistry B 102 (1998) 10871.

[13]H. Zhang, J. F. Banfield. Thermodynamic analysis of phase stability of nanocrystalline titania. Journal of Materials Chemistry 8 (1998) 2073-2076.

[14]D. J. Reidy, J. D. Holmes, M. A. Morris. The criticalsizemechanism for the anatase to rutiletransformation in TiO_2 and doped-TiO_2. Journal of the European Ceramic Society 26 (2006) 1527-1534.

[15] C. V. Samsonov. The oxide hand book. IFI/Plenum Press (1982).

[16] J. Fisher, T. Egerton. Titanium compounds, inorganic, Kirk-Othmer encyclopaedia of chemical technology. Wiley (2001)

[17] G. Peters, V. Vill. Index of modern inorganic compounds. Subvolume A. Landolt-Bornstein numerical data and functional relationships in science and technology. Verlag (1989)

[18]T. Hahn. International tables for crystallography. Reidel (1988)

[19]J. K. Burdett, T. Hughbanks, G. J. Miller, J. W. Richardson, J. V. Smith. Structural-electronic relationships in inorganic solids: powder neutron diffraction studies of the rutile and anatase polymorphs of titanium dioxide at 15 and 295 K. Journal of the American Chemical Society 109 (1987) 3639-3646.

[20]E. Hendry, M. Koeberg, B. O'Regan, M. Bonn. Local field effects on electron transport in nanostructured TiO_2 revealed by terahertz spectroscopy. Nano Letters (2006) 755-759.

[21]L. Kavan, M. Gratzel, S. E. Gilbert, C. Klemenz, and H. J. Scheel. Electrochemical and photoelectrochemical investigation of single-crystal anatase. Journal of the American Chemical Society 118 (1996) 6716–6723.

[22] A. Beltran, L. Gracia, and J. Andres. Density functional theory study of the brookite surfaces and phase transitions between natural titania polymorphs. The Journal of Physical Chemistry B 110 (2006) 23417–23423.

[23]N. Daude, C. Gout, C. Jouanin. Electronic band structure of titanium dioxide. Physical Review B 15 (1977) 3229–3235.

[24]D. Mardarea, M. Tascab, M. Delibasa, G. I. Rusu. On the structural properties and optical transmittance of TiO_2 r.f. sputtered thin films. Applied Surface Science 156 (2000) 200–206.

[25]J. Winkler. Titanium dioxide. Vincentz Network (2003).

[26] Y. Matsumoto, T. Shono, T. Hasegawa, T. Fukumura, M. Kawasaki, P. Ahmet, T. Chikyow, S. Koshihara, H. Koinuma. Room-temperature ferromagnetism in transparent transition metal-doped titanium dioxide. Science 291 (2001) 854-856.

[27] S. A. Chambers, S. Thevuthasan, R. F. C. Farrow, R. F. Marks, J. U. Thiele, L. Folks, M. G. Samant, A. J. Kellock, N. Ruzycki, D. L. Ederer, U. Diebold. Epitaxial growth and properties of ferromagnetic co-doped TiO_2 anatase. Applied Physics Letters 79 (2001) 3467-3469.

[28] N. Sakai, R. Wang, A. Fujishima, T. Watanabe, K. Hashimoto. Langmuir. Effect of ultrasonic treatment on highly hydrophilic TiO_2 surfaces. Langmuir 14 (1998) 5918–5920.

[29] M. Miyauchi, A. Nakajima, A. Fujishima, K. Hashimoto, T. Watanabe. Photoinduced surface reactions on TiO_2 and $SrTiO_3$ films: photocatalytic oxidation and photoinduced hydrophilicity. Chemistry Materials 12 (2000) 3– 5.

[30] N. Sakai, A. Fujishima, T. Watanabe, K. Hashimoto. Quantitative evaluation of the photoinduced hydrophilic conversion properties of TiO2 thin film surfaces by the reciprocal of contact angle. The Journal of Physical chemistry B 107 (2003) 1028–1035.

[31] W. Y. Gan, S. W. Lam, K. Chiang, R. Amal, H. Zhao, M. P. Brungs. Novel TiO_2 thin film with non-UV activated superwetting and antifogging behaviours. Communication. Journal of Materials Chemistry 17 (2007) 952-954.

[32] A. Fujishima, K. Hashimoto, T. Watanabe. TiO_2 photocatalysis. BKC Inc (1999).

[33] T. N. Obee, R. T. Brown. TiO_2 photocatalysis for indoor air applications: effects of humidity and trace contaminant levels on the oxidation rates of formaldehyde, toluene, and 1,3-butadiene. Environmental Science & Technology 29 (1995) 1223–1231.

[34] P. Pichat, J. Disdier, C. H. Van, D. Mas, G. Goutailler, C. Gaysse. Purification/deodorization of indoor air and gaseous effluents by TiO_2 photocatalysis. Catalysis Today 63 (2000) 363–369.

[35] P. A. Pekakis, N. P. Xekoukoulotakis, D. Mantzavinos. Treatment of textile dyehouse wastewater by TiO_2 photocatalysis. Water Research 40 (2006) 1276–1286

[36] G. Bamwenda. Photoassisted hydrogen production from a water-ethanol solution: a comparison of activities of Au-TiO_2 and Pt-TiO_2. Journal of Photochemistry and Photobiology A Chemistry 89 (1995) 177–189.

[37] F. Boccuzzia, A. Chiorinoa, M. Manzolia, D. Andreevab, T. Tabakovab, L. Ilievab, V. Iadakiev. Gold, silver and copper catalysts supported on TiO_2 for pure hydrogen production. Catalysis Today 75 (2002) 169–175.

[38] M. Ni, M. K.H. Leung, D. Y. C. Leung, K. Sumathy. A review and recent developments in photocatalytic water-splitting using TiO_2 for hydrogen production. Renewable and Sustainable Energy Reviews 11 (2007) 401–425.

[39] H. Lin, C. Keng, C. Tung. Gas-sensing properties of nanocrystalline TiO_2. Nanostructured Materials 9 (1997) 747–750.

[40] G. Eranna. Metal Oxide Nanostructures as Gas Sensing Devices. Taylor and Francis (2011).

[41] K. Kalyanasundaram, M. Gratzel. Applications of functionalized transition metal complexes in photonic and optoelectronic devices. Coordination Chemistry Reviews 77 (1998) 347–414.

[42]A. J. Frank, N. Kopidakis, J. V. D. Lagemaat. Electrons in nanostructured TiO_2 solar cells: transport, recombination and photovoltaic properties. Coordination Chemistry Reviews 248 (2004) 1165–1179.

[43]U. Bach, D. Lupo, P. Comte, J. E. Moser, F. Weissortel, J. Salbeck, H. Spreitzer, M. Gratzel. Solid-state dye-sensitized mesoporous TiO_2 solar cells with high photon-to-electron conversion efficiencies. Nature 395 (1998) 583-585.

[44]B. ORegan, F. Lenzmann, R. Muis, J.Wienke. A solid-state dye-sensitized solar Cell fabricated with pressure-treated P25−TiO_2 and CuSCN: analysis of pore filling and IV characteristics. Chemistry of Materials 14 (2002) 5023–5029.

[45]O. Carp, C. L. Huisman, A. Reller. Photoinduced reactivity of titanium dioxide. Progress in Solid State Chemistry 32 (2004) 33–177.

[46]M. Kitano, M. Matsuoka, M. Ueshima, M. Anpo. Recent developments in titanium oxide-based photocatalysts. Applied Catalysis A: General 325 (2007) 1–14.

[47]X. Chen, S. S. Mao. Titanium dioxide nanomaterials: synthesis, properties, modifications, and applications. Chemical reviews 107 (2007) 2891-2959.

[48]Y. Cui, H. Du, L. Wen. Doped-TiO_2 photocatalysts and synthesis methods to prepare TiO_2 films. Journal of Materials Science and Technology 24 (2008) 675-689.

[49]L. Li, C. Liu, Y. Liu. Study on activities of vanadium (IV/V) doped TiO_2 (R) nanorods induced by UV and visible light. Materials Chemistry and Physics 113 (2009) 551–557.

[50]J. Zhou, M. Takeuchi, A. K. Ray, M. Anpo, X. S. Zhao. Enhancement of photocatalytic activity of P25 TiO_2 by vanadium-ion implantation under visible light irradiation. Journal of Colloid and Interface Science 311 (2007) 497–501

[51]J. C. Wu, C. Chen. A visible-light response vanadium-doped titania nanocatalyst by sol–gel method. Journal of Photochemistry and Photobiology A: Chemistry 163 (2004) 509–515.

[52]K. Bhattacharyya, S. Varma, A. K. Tripathi, A. K. Tyagi. Synthesis and photocatalytic activity of nano V-doped TiO_2 particles in MCM-41 under UV–visible irradiation. Journal of Materials Research 25 (2010) 125-133

[53]M. Takeuchi, H. Yamashita, M. Matsuoka, M. Anpo, T. Hirao, N. Itoh, N. Iwamoto. Photocatalytic decomposition of NO under visible light irradiation on the Cr-ion-implanted TiO_2 thin film photocatalyst. Catalysis letters 67 (2000) 135-137.

[54]B. Sun, E. P. Reddy, P. G. Smirniotis. Effect of the Cr^{6+} concentration in Cr-incorporated TiO_2-loaded MCM-41 catalysts for visible light photocatalysis. Applied Catalysis B: Environmental 57 (2005) 139–149.

[55]J. Zhu, Z. Deng, F. Chen, J. Zhang, H. Chen, M. Anpo, J. Huang, L. Zhang. Hydrothermal doping method for preparation of Cr^{3+}-TiO_2 photocatalysts with concentration gradient distribution of Cr^{3+}. Applied Catalysis B: Environmental 62 (2006) 329–335.

[56]G. H. Takaoka, T. Nose, M. Kawashita. Photocatalytic properties of Cr-doped TiO_2 films prepared by oxygen cluster ion beam assisted deposition. Vacuum 83 (2008) 679–682.

[57]H. Zhu, J. Tao, X. Dong. Preparation and photoelectrochemical activity of Cr-Doped TiO_2 nanorods with nanocavities. The Journal of Physical Chemistry C 114 (2010) 2873–2879.

[58]L. Devi, S. Kumar, B. Murthy, N Kottam. Influence of Mn^{2+} and Mo^{6+} dopants on the phase transformations of TiO_2 lattice and its photo catalytic activity under solar illumination. Catalysis Communications 10 (2009) 794–798.

[59]G. Shao. Electronic structures of manganese-doped rutile TiO_2. The Journal of Physical Chemistry C. 112 (2008) 18677-18685.

[60]M. Wang, H. Lin, T. Yang. Characteristics and optical properties of iron ion (Fe^{3+})-doped titanium oxide thin films prepared by a sol-gel spin coating. Journal of Alloys and Compounds 473 (2009) 394–400.

[61]G. Shao. Red shift in manganese- and iron-doped TiO_2: a DFT+U analysis. The Journal of Physical Chemistry C 113 (2009) 6800–6808.

[62]T. Tong, J. Zhang, B. Tian, F. Chen, D. He. Preparation of Fe^{3+}-doped TiO_2 catalysts by controlled hydrolysis of titanium alkoxide and study on their photocatalytic activity for methyl orange degradation. Journal of Hazardous Materials 155 (2008) 572–579.

[63]S. George, S. Pokhrel, Z. Ji, B. L. Henderson, T. Xia, L. Li, J. I. Zink, A.E. Nel, L. Madler. Role of Fe doping in tuning the band gap of TiO_2 for the photo-oxidation-induced cytotoxicity paradigm. Journal of the American Chemical Society 133 (2011) 11270–11278.

[64]X. Wang, J. Li, H. Kamiyama, M. Katada, N. Ohashi, Y. Moriyoshi, T. Ishigaki. Pyrogenic Iron(III)-doped TiO_2 nanopowders synthesized in RF thermal plasma: phase formation, defect Structure, band Gap, and magnetic properties. Journal of the American Chemical Society 127 (2005) 10982–10990.

[65]Z. Li, W. Shen, W. He, X. Zu. Effect of Fe-doped TiO_2 nanoparticle derived from modified hydrothermal process on the photocatalytic degradation performance on methylene blue. Journal of Hazardous Materials 155 (2008) 590–594.

[66]M. A. Barakat, H. Schaeffer, G. Hayes, S. Ismat-Shah. Photocatalytic degradation of 2-chlorophenol by Co-doped TiO_2 nanoparticles. Applied Catalysis B: Environmental 57 (2005) 23–30.

[67]H. Yu, X. Li, S. Zheng, W. Xu, Photocatalytic activity of TiO_2 thin film non-uniformly doped by Ni. Materials Chemistry and Physics 97 (2006) 59-63.

[68]G. Colon, M. Maicu, M. C. Hidalgo, J. A. Navio. Cu-doped TiO_2 systems with improved photocatalytic activity. Applied Catalysis B: Environmental 67 (2006) 41–51.

[69]G. Shao, Q. Deng, L. Wan, M. Guo, X. Xia, Y. Gao. Molecular design of TiO_2 for gigantic red shift via sublattice substitution. Journal of Nanoscience and Nanotechnology 10 (2010) 1–5.

[70]K. Nagaveni, M. S. Hegde, G. Madras. Structure and photocatalytic activity of $Ti_{1-x}M_xO_{2\pm\delta}$ (M = W, V, Ce, Zr, Fe, and Cu) synthesized by solution combustion method. The Journal of Physical Chemistry B 108 (2004) 20204–20212.

[71]J. Choi, H. Park, M. R. Hoffmann. Effects of single metal-Ion doping on the visible-light photoreactivity of TiO_2. The Journal of Physical Chemistry C 114 (2010) 783–792.

[72]F. E. Oropeza, R. G. Egdell. Control of valence states in Rh-doped TiO_2 by Sb co-doping: A study by high resolution X-ray photoemission spectroscopy. Chemical Physics Letters 515 (2011) 249-253.

[73]S. Sen, S. Mahanty, S. Roy, O. Heintz, S. Bourgeois, D. Chaumon. Investigation on sol–gel synthesized Ag-doped TiO_2 cermet thin films. Thin Solid Films 474 (2005) 245–249.

[74]H. Tiana, J. Ma, K. Li, J. Li. Photocatalytic degradation of methyl orange with W-doped TiO_2 synthesized by a hydrothermal method. Materials Chemistry and Physics 112 (2008) 47–51.

[75]S. Kim, S.Hwang, W. Choi. Visible light active platinum-ion-doped TiO_2 photocatalyst. The Journal of Physical Chemistry B 109 (2005) 24260–24267

[76]L. Bian, M. Song, T. Zhou, X. Zhao, Q. Dai. Band gap calculation and photo catalytic activity of rare earths doped rutile TiO2. Journal of Rare Earths 27 (2009) 461-468.

[77]Y. Zhang, H. Zhang, Y. Xu, Y. Wang. Significant effect of lanthanide doping on the texture and properties of nanocrystalline mesoporous TiO_2. Journal of Solid State Chemistry 177 (2004) 3490–3498.

[78]A. Xu, Y. Gao, H. Liu. The preparation, characterization, and their photocatalytic activities of rare-earth-doped TiO_2 nanoparticles. Journal of Catalysis 207 (2002) 151–157.

[79]V. Stengl, S. Bakardjieva, N. Murafa. Preparation and photocatalytic activity of rare earth doped TiO_2 nanoparticles. Materials Chemistry and Physics 114 (2009) 217–226.

[80]C. Liang, F. Li, C. Liu, J. Lu, X. Wang. The enhancement of adsorption and photocatalytic activity of rare earth ions doped TiO_2 for the degradation of Orange I. Dyes and Pigments 76 (2008) 477-484.

[81]G. Li, C. Liu, Y. Liu. Different effects of cerium ions doping on properties of anatase and rutile TiO_2. Applied Surface Science 253 (2006) 2481–2486.

[82]F. Li, X. Li, M. Hou, K.. Cheah, W. Choy. Enhanced photocatalytic activity of Ce^{3+}–TiO_2 for 2-mercaptobenzothiazole degradation in aqueous suspension for odour control. Applied Catalysis A: General 285 (2005) 181–189.

[83] Q. Xiao, Z. Si, J. Zhang, C. Xiao, X. Tan. Photoinduced hydroxyl radical and photocatalytic activity of samarium-doped TiO_2 nanocrystalline. Materials Science and Engineering B (2007) 189-194.

[84] M. Saif, M. S. A. Abdel-Mottaleb. Titanium dioxide nanomaterial doped with trivalent lanthanide ions of Tb, Eu and Sm: Preparation, characterization and potential applications. Inorganica Chimica Acta 360 (2007) 2863–2874.

[85] J. Xu, Y. Ao, D. Fu, C. Yuan. Synthesis of Gd-doped TiO_2 nanoparticles under mild condition and their photocatalytic activity. Colloids and Surfaces A: Physicochem. Eng. Aspects 334 (2009) 107–111.

[86] C. Liang, M. Hou, S. Zhou, F. Li, C. Liu, T. Liu, Y. Gao, X. Wang, J. Lu. The effect of erbium on the adsorption and photodegradation of orange I in aqueous Er^{3+}-TiO_2 suspension. Journal of Hazardous Materials B 138 (2006) 471–478.

[87] C. Zhang, S. Chen, L. Mo, Y. Huang, H. Tian, L. Hu, Z. Huo, S. Dai, F. Kong, X. Pan. Charge recombination and band-edge shift in the dye-sensitized Mg^{2+}-doped TiO_2 solar cells. The Journal of Physical Chemistry C 115 (2011) 16418–16424.

[88] L. Kumaresan, M. Mahalakshmi, M. Palanichamy, V. Murugesan. Synthesis, characterization, and photocatalytic activity of Sr^{2+} doped TiO_2 nanoplates. Industrial and Engineering Chemistry Research 49 (2010) 1480–1485.

[89] N. Venkatachalam, M. Palanichamy, V. Murugesan. Sol–gel preparation and characterization of alkaline earth metal doped nano TiO_2: Efficient photocatalytic degradation of 4-chlorophenol. Journal of Molecular Catalysis A: Chemical 273 (2007) 177–185.

[90] N. I. Al-Salim, S. A. Bagshaw, A. Bittar, T. Kemmitt, A. J. McQuillan, A. M. Mills, M. J. Ryan. Characterisation and activity of sol–gel prepared TiO_2 photocatalysts modified with Ca, Sr or Ba ion additives. Journal of Materials Chemistry 10 (2000) 2358-2363.

[91] M. M. Rahmana, K. M. Krishnab, T. Sogac, T. Jimboc, M. Umeno. Optical properties and X-ray photoelectron spectroscopic study of pure and Pb-doped TiO_2 thin films. Journal of Physics and Chemistry of Solids 60 (1999) 201–210.

[92] M. Anpo. Photocatalysis on titanium oxide catalysts: Approaches in achieving highly efficient reactions and realizing the use of visible light. Catalysis Surveys from Japan 1 (1997) 169-171.

[93] M. Anpo, Y. Ichihashi, M. Takeuchi, H. Yamashita. Design of unique titanium oxide photocatalysts by an advanced metal ion-implantation method and photocatalytic reactions under visible light irradiation. Research on Chemical Intermediates 24 (1998) 143-149.

[94] M. Anpo, Y. Ichihashi, M. Takeuchi, H. Yamashita. Design and development of uniquetitaniumoxide photocatalysts capable of operating under visible light irradiation by an advanced metal ion-implantation method. Studies in Surface Science and Catalysis 121 (1999) 305-310.

[95] M. Takeuchi, H. Yamashita, M Matsuoka, T. Hirao, N. Itoh, N. Iwamoto, M. Anpo. Photocatalytic decomposition of NO on titanium oxide thin film photocatalysts prepared by an ionized cluster beam technique. Catalysis Letters 66 (2000) 185-187.

[96]M. Anpo. Use of visible light. Second-generation titanium oxide photocatalysts prepared by the application of an advanced metal ion-implantation method. Journal of Photochemistry and Photobiology A: Chemistry 148 (2002) 257–261.

[97]H. Yamashita, M. Harada, J. Misaka, M. Takeuchi, K. Ikeue, M. Anpo. Degradation of propanol diluted in water under visible light irradiation using metal ion-implanted titanium dioxide photocatalysts. Journal of Photochemistry and Photobiology A: Chemistry 148 (2002) 257–261.

[98] M. Anpo. Preparation, characterization, and reactivities of highly functional titanium oxide-based photocatalysts able to operate under UV–visible light irradiation: approaches in realizing high efficiency in the use of visible light. Bulletin of the Chemical Society of Japan 77 (2004) 1427-1442.

[99]K. Iino, M. Kitano, M. Takeuchi, M. Matsuoka, M. Anpo. Design and development of second-generation titanium oxide photocatalyst materials operating under visible light irradiation by applying advanced ion-engineering techniques. Current Applied Physics 6 (2006) 982–986.

[100]M. Kitano, M. Matsuoka, M. Ueshima, M. Anpo. Recent developments in titanium oxide-based photocatalysts. Applied Catalysis A: General 325 (2007) 1–14.

[101] S. Klosek, D. Raftery. Visible light driven V-doped TiO_2 photocatalyst and its photooxidation of ethanol. The Journal of Physical Chemistry B 105 (2001) 2815-2819.

[102] D. Dvoranova, V. Brezova, M. Mazur, M. A. Malati. Investigations of metal-doped titanium dioxide photocatalysts. Applied Catalysis B: Environmental 37 (2002) 91–105.

[103]J. Choi, H. Park, M. R. Hoffmann. Combinatorial doping of TiO_2 with platinum (Pt), chromium (Cr), vanadium (V), and nickel (Ni) to achieve enhanced photocatalytic activity with visible light irradiation. Journal of Materials Research 25 (2010) 149-158.

[104]W. Y. Teoh, R. Amal, L. Mädler, S. E. Pratsinis. Flame sprayed visible light-active Fe-TiO_2 for photomineralisation of oxalic acid. Catalysis Today 120 (2007) 203–213.

[105]S. Ghasemi, S. Rahimnejad, S. Rahman Setayesh, S. Rohani, M. R. Gholami. Transition metal ions effect on the properties and photocatalytic activity of nanocrystalline TiO_2 prepared in an ionic liquid. Journal of Hazardous Materials 172 (2009) 1573–1578.

[106] K. Lee, N. H. Lee, S. H. Shin, H. G. Lee, S. J. Kim. Hydrothermal synthesis and photocatalytic characterizations of transition metals doped nano TiO_2 sols. Materials Science and Engineering B 129 (2006) 109–115.

[107]R. Long, Y. Dai, G. Meng, B. Huang. Energetic and electronic properties of X- (Si, Ge, Sn, Pb) doped TiO_2 from first-principles. Physical Chemistry Chemical Physics 11 (2009) 8165-8172.

[108]R. Long, Y. Dai, B, Huang. Geometric and electronic properties of Sn-doped TiO_2 from first-principles calculations. The Journal of Physical Chemistry C 113 (2009) 650–653.

[109]R. Asahi, T. Morikawa, T. Ohwaki, K. Aoki, Y. Taga. Visible-light photocatalysis in nitrogen-doped titanium oxides. Science 293 (2001) 269-276.

[110]S. Sato. Photocatalytic activity of NOx-doped TiO_2 in the visible light region. Chemical Physics Letters 123 (1986) 126–128.

[111]J. Senthilnathan, L. Philip. Photocatalytic degradation of lindane under UV and visible light using N-doped TiO_2. Chemical Engineering Journal 161 (2010) 83–92.

[112]M. Sathish, B. Viswanathan, R. P. Viswanath, C. S. Gopinath. Synthesis, characterization, electronic structure, and photocatalytic activity of nitrogen-doped TiO_2 nanocatalyst. Chemical Materials 17 (2005) 6349–6353.

[113]Y. Nakano, T. Morikawa, T. Ohwaki, Y. Taga. Origin of visible-light sensitivity in N-doped TiO_2 films. Chemical Physics 339 (2007) 20–26.

[114]G. Liu, X. Wang, Z. Chen, H. Cheng, G. Lu. The role of crystal phase in determining photocatalytic activity of nitrogen doped TiO_2. Journal of Colloid and Interface Science 329 (2009) 331-338.

[115]H. Irie, Y. Watanabe, K. Hashimoto. Carbon-doped Anatase TiO_2 Powders as a Visible-light Sensitive Photocatalyst. Chemistry Letters 32 (2003) 772-773.

[116]J. H. Park, S. Kim, A. J. Bard. Novel carbon-doped TiO_2 nanotube arrays with high aspect ratios for efficient solar water splitting. Nano Letters 6 (2006) 24-28.

[117]H. Li, D. Wang, H. Fan, P. Wang, T. Jiang, T. Xie. Synthesis of highly efficient C-doped TiO_2 photocatalyst and its photo-generated charge-transfer properties. Journal of Colloid and Interface Science 354 (2011) 175–180.

[118]T. Umebayashi, T. Yamaki, S.Tanaka, K.Asai. Visible Light-Induced Degradation of Methylene Blue on S-doped TiO_2. Chemistry Letters 32 (2003) 330-331.

[119]T. Ohno, M. Akiyoshi, T. Umebayashi, K. Asai, T. Mitsui, M. Matsumura. Preparation of S-doped TiO_2 photocatalysts and their photocatalytic activities. Applied Catalysis A: General 265 (2004) 115–121.

[120]X. Dong, J. Tao, Y. Li, H. Zhu. Enhanced photoelectrochemical properties of F-containing TiO_2 sphere thin film induced by its novel hierarchical structure. Applied Surface Science 255 (2009) 7183–7187.

[121]Y. Huang, W. Ho, Z. Ai, X. Song, L. Zhang, S. Lee. Aerosol-assisted flow synthesis of B-doped, Ni-doped and B–Ni-codoped TiO_2 solid and hollow microspheres for photocatalytic removal of NO. Applied Catalysis B: Environmental 89 (2009) 398–405.

[122]M. Kitano, M. Matsuoka, M. Ueshima, M. Anpo. Recent developments in titanium oxide-based photocatalysts. Applied Catalysis A: General 325 (2007) 1–14

[123]G. Liu, X.Wang, Z. Chen, H. Cheng, G. Lu. The role of crystal phase in determining photocatalytic activity of nitrogen doped TiO_2. Journal of Colloid and Interface Science 329 (2009) 331–338.

[124]F. Dong, W. Zhao, Z. Wu, S. Guo. Band structure and visible light photocatalytic activity of multi-type nitrogen doped TiO_2 nanoparticles prepared by thermal decomposition. Journal of Hazardous Materials 162 (2009) 763–770.

[125]X. Han, G. Shao. Electronic properties of rutile TiO_2 with nonmetal dopants from first principles. The Journal of Physical Chemistry C 115 (2011) 8274–8282.

[126]T. Umebayashi, T. Yamaki, H. Itoh, K. Asai. Band gap narrowing of titanium dioxide by sulfur doping. Applied Physics Letters 81(2002) 454-456.

[127]T. Ohno, M. Akiyoshi, T. Umebayashi, K. Asai, T. Mitsui, M. Matsumura. Preparation of S-doped TiO_2 photocatalysts and their photocatalytic activities under visible light. Applied Catalysis A: General 265 (2004) 115–121.

[128]E. M. Rockafellow, L. K. Stewart, W. S. Jenks. Is sulfur-doped TiO_2 an effective visible light photocatalyst for remediation?. Applied Catalysis B: Environmental 91 (2009) 554–562.

[129]S. Liu, X. Chen. A visible light response TiO_2 photocatalyst realized by cationic S-doping and its application for phenol degradation. Journal of Hazardous Materials 152 (2008) 48–55.

[130]Y. Wang, J. Li, P. Peng, T. Lu, L. Wang. Preparation of S-TiO_2 photocatalyst and photodegradation of L-acid under visible light. Applied Surface Science 254 (2008) 5276–5280.

[131]H. Wang, J. P. Lewis. Effects of dopant states on photoactivity in carbon-doped TiO_2. Journal of Physics: Condensed Matter 17 (2005) L209–L213.

[132]Z. Liu, Y. Zhou, Z. Li, Y. Wang, C. Ge. Preparation and characterization of (metal, nitrogen)-codoped TiO_2 by $TiCl_4$ sol-gel auto-igniting synthesis. Rare Metals 26 (2007) 263–270.

[133]Y. Cong, J. Zhang, F. Chen, M. Anpo, D. He. Preparation, photocatalytic activity, and mechanism of nano-TiO_2 co-doped with nitrogen and iron (III). The Journal of Physical Chemistry C 11 (2007) 10618-10623.

[134]S. Yamazaki, M. Sugihara, E. Yasunaga, T. Shimooka, K. Adachi. Preparation and photocatalytic activity of TiO_2 powder codoped with iron and nitrogen. Journal of Photochemistry and Photobiology A Chemistry 23 (2007) 74-78.

[135]C. Liu, X. Tang, C. Mo, Z. Qiang. Characterization and activity of visible-light-driven TiO_2 photocatalyst codoped with nitrogen and cerium. Technology 181 (2008) 913-919.

[136]Y. Gai, J. Li, S. Li, J. Xi, S. Wei. Design of narrow-gap TiO_2: a passivated codoping approach for enhanced photoelectrochemical activity. Physical Review Letters 102 (2009) 036402-03646.

[137] K. Tan, H. Zhang, C. Xie, H. Zheng, Y. Gu, W. Zhang. Visible-light absorption and photocatalytic activity in molybdenum- and nitrogen-codoped TiO_2. Catalysis Communications 11 (2010) 2-6.

[138]R. Long, N. J. English. First-principles calculation of nitrogen-tungsten codoping effects on the band structure of anatase titania. Applied Physics Letters 94 (2009) 132102-132104.

[139]R. Long, N. J. English. Band gap engineering of (N, Ta)-codoped TiO_2: A first-principles calculation. Chemical Physics Letters 478 (2009) 175–179.

[140]S. Kim, S. K. Lee. Visible light-induced photocatalytic oxidation of 4-chlorophenol and dichloroacetate in intrided Pt-TiO_2 aqueous suspensions. Journal of Photochemistry and Photobiology A Chemistry 203 (2009) 145-150.

[141]Y. Wang, Y. L. Meng, H. M. Ding, Y. K. Shan, X. Zhao, X. Z. Tang. A highly efficient visible-light-activated photocatalyst based on bismuth- and sulfur-codoped TiO_2. The Journal of Physical Chemistry C. 112 (2008) 6620-6626.

[142]M. Bettinelli, V. Dallacasa, D. Falcomera, P. Fornasiero, V. Gombac, T. Montini, L. Romanò, A. Speghini. Photocatalytic activity of TiO_2 doped with boron and vanadium. Journal of Hazardous Materials 146 (2007) 529-534.

[143]Z. Zhao, Q. Liu. Designed highly effective photocatalyst of anatase TiO_2 codoped with nitrogen and vanadium under visible-light irradiation using first-principles. Catalysis Letters 124 (2008) 111-117.

[144]C. Yu, J. C. Yu. A simple way to prepare C–N-codoped TiO_2 photocatalyst with visible-light activity. Catalysis Letters 129 (2009) 462-470.

[145]J. Yang, H. Bai, Q. Jiang, J. Lian. Visible-light photocatalysis in nitrogen–carbon-doped TiO_2 films obtained by heating TiO_2 gel–film in an ionized N_2 gas. Thin Solid Films 516 (2008) 1736-1742.

[146]Y. W. Sakai, K. Obata, K. Hashimoto, H. Irie. Enhancement of visible light-induced hydrophilicity on nitrogen and sulfur-codoped TiO_2 thin films. Vacuum 83 (2008) 683-687.

[147]P. Xu, T. Xu, J. Lu, S. Gao, N .S. Hosmane, B. Huang, Y. Dai, Y. Wang. Visible-light-driven photocatalytic S- and C- codoped meso/nanoparous TiO_2. Energy Environmental Science 3 (2010) 1128.

[148]J. Shi, J. Zheng, Y. Hu, Y. Zhao. Photocatalytic degradation of organic compounds in aqueous systems by Fe and Ho codoped TiO_2. Kinetics and Catalysis 49 (2008) 279-284.

[149]D. Zhang, Y. Kim, Y. Kang. Synthesis and characterization of nanoparticle of TiO_2 co-doped with Sc^{3+} and V^{5+} ions. Current Applied Physics 6 (2006) 801-804.

[150]D. Zhang, Y. Kang. Synthesis and characterization of nanocrystalline TiO_2 doped with 2 at.% Sc^{3+} and V^{5+} ions. Solid State Phenomena 121-123 (2007) 41-44.

[151]Z. Wang, C. Chen, F. Wu, B. Zou, M. Zhao, J. Wang, C. Feng. Photodegradation of rhodamine B under visible light by bimetal codoped TiO_2 nanocrystals. Journal of Hazardous Materials 164 (2009) 615-620.

[152]W. Luo, R. Li, Y. Liu, X. Chen. Sensitized luminescence of Sm^{3+}, $Eu(^{3+})$-codoped TiO_2 nanoparticles. Journal of Nanoscience and Nanotechnology 10 (2010) 1693-1698.

[153] A. Fujishima. T. N. Rao, D. A. Tryk. Titanium dioxide photocatalysis. Journal of Photochemistry and Photobiology C: Photochemistry Reviews 1 (2000) 1–21.

[154] A. Zaleska. Doped-TiO_2: a review. Recent Patents on Engineering 2 (2008) 157-164.

[155]Y. Chen, Z. Sun, Y. Yang, Q. Ke. Heterogeneous photocatalytic oxidation of polyvinyl alcohol in water. Journal of Photochemistry and Photobiology A: Chemistry 142 (2001) 85–89

[156]M. Asilturka, F. S. lkan, E. Arpac. Effect of Fe^{3+} ion doping to TiO_2 on the photocatalytic degradation of Malachite Green dye under UV and vis-irradiation. Journal of Photochemistry and Photobiology A: Chemistry 203 (2009) 64–71.

[157]F. Dong, W. Zhao, Z. Wu, S. Guo. Band structure and visible light photocatalytic activity of multi-type nitrogen doped TiO_2 nanoparticles prepared by thermal decomposition. Journal of Hazardous Materials 162 (2009) 763–770.

[158]Y. Cui, H. Du, L. Wen. Doped-TiO_2 photocatalysts and synthesis methods to prepare TiO_2 films. Journal of Materials Science and Technology 24 (2008) 675-689.

[159] Z. Li, W. Shen. W. He, X. Zu. Effect of Fe-doped TiO_2 nanoparticle derived from modified hydrothermal process on the photocatalytic degradation performance on methylene blue. 155 (2008) 590-594.

[160]W. Hung, Y. Chen, H. Chu, T. Tseng. Synthesis and characterization of TiO_2 and Fe/TiO_2 nanoparticles and their performance for photocatalytic degradation of 1,2-dichloroethane. Applied Surface Science 255 (2008) 2205-2213.

[161]W. Choi, A. Termin, M. R. Hoffman. The role of metal Ion dopants in quantum-sized TiO_2: correlation between photoreactivity and charge carrier recombination dynamics. Journal of Physical Chemistry 98 (1994) 13669–13679.

[162]G. K. Mor, O. K. Varghese, M. Paulose, K. Shankar, C.A. Grimes. A review on highly ordered, vertically oriented TiO_2 nanotube arrays: Fabrication, material properties, and solar energy applications. Solar Energy Materials and Solar Cells 90 (2006) 2011–2075.

[163]K. Shankar, J. I. Basham, N. K. Allam, O. K. Varghese, G. K. Mor, X.Feng, M. Paulose, J. A Seabold, K. Choi, C. A. Grimes. Recent advances in the use of TiO_2 nanotube and nanowire arrays for oxidative photoelectrochemistry. The Journal of Physical Chemistry C 113 (2009) 6327-6359.

[164] B. Liu, E. S. Aydil. Growth of oriented single-crystalline rutile TiO_2 nanorods on transparent conducting substrates for dye-sensitized solar cells. Journal of the American Chemical Society 131 (2009) 3985-3990.

[165] Y. Yu, D. Xu. Single-crystalline TiO_2 nanorods: Highly active and easily recycled photocatalysts. Applied Catalysis B: Environmental 1-2 (2007) 166-171.

[166]E. Hosono, S. Fujihara, K. Kakiuchi, H. Imai. Growth of submicrometer-scale rectangular parallelepiped rutile TiO_2 films in aqueous TiCl3 solutions under hydrothermal conditions. Journal of the American Chemical Society 126 (2004) 7790–7791.

[167]X. Feng, J. Zhai, L. Jiang. The fabrication and switchable superhydrophobicity of TiO_2 nanorod films. angewandte chemie international edition 44 (2005) 5115 –5118.

[168]S. Jung, S. Kim, N. Imaishi, Y. Cho. Effect of TiO_2 thin film thickness and specific surface area by low-pressure metal–organic chemical vapour deposition on photocatalytic activities. Applied Catalysis B: Environmental 55 (2005) 253–257.

[169]Y. Gao, M. Nagai,W. S. Seo, K. Koumoto. Thick transparent rutile TiO_2 films crystallized in solution. Langmuir, 23 (2007) 4712–4714. Nano letters 8 (2008) 3781-3786.

[170]X. Feng, K. Shankar, O. K. Varghese, M. Paulose, T. J. Latempa, C. A. Grimes. Vertically aligned single crystal TiO_2 nanowire arrays grown directly on transparent conducting oxide coated glass: synthesis details and applications. Nano letters 8 (2008) 3781-3786.

[171] B. Liu, E. S. Aydil. Growth of oriented single-crystalline rutile TiO_2 nanorods on transparent conducting substrates for dye-sensitized solar cells. Journal of the American Chemical Society 131 (2009) 3985-3990.

[172]http://www.alternative-energy-news.info/technology/solar-power/photo-voltaics/.

[173]http://en.wikipedia.org/wiki/Solar_cells.

[174]K. A. Tsokos, Physics for the IB Diploma. Cambridge University Press (2008).

[175]J. Kruger. Interface engineering in solid-state dye-sensitized solar cells. Lausanne: EPFL (2003).

[176]B. Oregan, M. Gratzel. A low-cost, high-efficiency solar cell based on dye-sensitized colloidal TiO_2 films. Nature 333 (1991) 737-740.

[177] K. Kalyanasundaram, M. Gratzel. Applications of functionalized transition metal complexes in photonic and optoelectronic devices. Coordination Chemistry Reviews 77 (1998) 347–414

[178]A. Hagfeldt, M. Gratzel. Molecular photovoltaics. Accounts of Chemical Research 33 (2000) 269-277.

[179]M. Gratzel. Dye-sensitized solar cells. Journal of photochemistry and photobiology C: photochemistry reviews 4 (2003) 145–153.

[180]http://en.wikipedia.org/wiki/Dye-sensitized_solar_cell.

[181]M. Adachi, Y. Murata, F. Wang, J. Jiu. Synthesis of titania nanocrystals: application for dye-sensitized solar cells. Nanostructure Science and Technology (2006) 71-100 DOI: 10.1007/0-387-27976-8_2.

[182]M. Gratzel. Conversion of sunlight to electric power by nanocrystalline dye-sensitized solar cells. Journal of Photochemistry and Photobiology A: Chemistry 164 (2004) 3–14

[183] M. Gratzel. Photovoltaic performance and long-term stability of dye-sensitized meosocopic solar cells. Comptes Rendus Chimie 9 (2006) 578–583.

[184] G. Redmond, D. Fitzmaurice, M. Gratzel. Visible light sensitization by cis-Bis(thiocyanato)bis(2,2'-bipyridyl-4,4'-dicarboxylato)ruthenium(II) of a transparent nanocrystalline ZnO film prepared by sol-gel techniques. Chemistry Materials 6 (1994) 686-691.

[185]K. Keis,J. Lindgren, S. Lindquist, A. Hagfeldt. Studies of the adsorption process of Ru complexes in nanoporous ZnO electrodes. Langmuir 16 (2000) 4688-4694.

[186]M. Quintana, T. Edvinsson, A. Hagfeldt, G. Boschloo. Comparison of dye-sensitized ZnO and TiO_2 solar cells: studies of charge transport and carrier lifetime. Journal of Physical Chemistry B 111 (2007) 1035-1041.

[187]M. Law, L. E Greene, J. C. Johnson, R. Saykally, P. Yang. Nanowire dye-sensitized solar cells. Nature Materials 4 (2005) 455-459.

[188]H. Tributsch. Dye sensitization solar cells: a critical assessment of the learning curve. Coordination Chemistry Reviews 248 (2004) 1511-1530.

[189]N. Geacintov, M. Pope, H. Kallmann. Photogeneration of charge carriers in tetracene. The Journal of Chemical Physics 45 (1966) 2639–2649.

[190]G. Dennler, M. C. Scharber, C. J. Brabec. Polymer-fullerene bulk-heterojunction solar cells. Advanced Materials 21 (2009) 1323–1338.

[191]C. J. Brabec, G. Zerza, G. Cerullo, S. D. Silvestri, S. Luzzati, J. C. Hummelen, S. Sariciftci, Tracing photoinduced electron transfer process in conjugated polymer/fullerene bulk heterojunctions in real time. Chemical Physics Letters 340 (2001) 232–236.

[192]C. N. Hoth, S. A. Choulis, P. Schilinsky, C. J. Brabec. High photovoltaic performance of inkjet printed polymer: fullerene blends. Advanced Materials 19 (2007) 3973–3978.

[193]H. Hoppe, N. S. Sariciftci. Organic solar cells: an overview. Journal of Materials Research 19 (2004) 1924-1945.

[194]T. Ameri, G. Dennler, C. Waldauf, P. Denk, K. Forberich, M. C. Scharber, C. J. Brabec, K. Hingerl. Realization, characterization, and optical modeling of inverted bulk-heterojunction organic solar cells. Journal of Applied Physics 103 (2008) 0845061-0845066.

[195]http://en.wikipedia.org/wiki/Polymer_solar_cell

[196]H. Hoppe, M. Niggemann, C. Winder, J. Kraut, R. Hiesgen, A. Hinsch, D. Meissner, N. S. Sariciftci. Nanoscale morphology of conjugated polymer/fullerene-based bulk-heterojunction solar cells. Advanced Functional Materials 14 (2004) 1005-1011.

[197]G. Wang, S. James; D. Moses, A. J. Heeger. Increased mobility from regioregular poly(3-hexylthiophene) field-effect transistors. Journal of Applied Physics 93 (2003) 6137-6141.

[198]A. Dodabalapur, Z. Bao, A. Makhija, J. G. Laquindanum, V. R. Raju, Y. Feng, H. E. Katz, J. Rogers. Organic smart pixels. Applied Physics Letters 73 (1998) 142-144.

[199]K. M. Coakley, M. D. McGehee. Conjugated polymer photovoltaic cells. Chemistry Materials 16 (2004) 4533-4542.

[200]H. Spanggaard, F. C. Krebs. A brief history of the development of organic and polymeric photovoltaics. Solar Energy Materials and Solar Cells 83 (2004) 125–146.

[201]H. Hoppe, N. S. Sariciftci. Polymer solar cells. Advances in Polymer Science 214 (2008) 1–86.

[202]P. Peumans, A. Yakimov, S. R. Forrest, S. R. Small molecular weight organic thin-film photodetectors and solar cells. Journal of Applied Physics 93 (2003) 3693-3723.

[203]W. Cai, X. Gong, Y. Cao. Polymer solar cells: Recent development and possible routes for improvement in the performance. Solar Energy Materials and Solar Cells 94 (2010) 114–127.

[204] K. Takanezawa, K. Tajima, K. Hashimoto. Efficiency enhancement of polymer photovoltaic devices hybridized with ZnO nanorod arrays by the introduction of a vanadium oxide buffer layer. Applied Physics letters 93 (2008) 063308.

[205]S. Yodyingyong, X. Zhou, Q. Zhang, D. Triampo, J. Xi, K. Park, B. Limketkai, G. Cao. Enhanced photovoltaic performance of nanostructured hybrid solar cell using highly oriented TiO_2 nanotubes. Society 114 (2010) 21851-21855.

[206]W. J. E. Beek, M. M. Wienk, R. A. J. Janssen. Hybrid Solar Cells from Regioregular polythiophene and ZnO nanoparticles. Advanced Functional Materials 16 (2006) 1112-1116.

[207]Y. Qin, X. Wang, Z. Wang. Microfibre – nanowire hybrid structure for energy scavenging. Nature 451 (2008) 809-813.

[208]C. Y. Kwong, W. C. H. Choy, A. B. Djurisi, P. C. Chui, K. W. Cheng, W. K. Chan. Poly(3 hexylthiophene):TiO_2 nanocomposites for solar cell applications. Nanotechnology 15 (2004) 1156–1161.

[209]K. Shankar, G. K. Mor, H. E. Prakasam, O. K. Varghese, C. A. Grimes. Self-assembled hybrid polymer TiO_2 nanotube array heterojunction solar cells. Langmuir 23 (2007)12445-12449.

[210]W. J. E. Beek, M. M. Wienk, R. A. J. Janssen. Efficient hybrid solar cells from zinc oxide nanoparticles and a conjugated polymer. Advanced Materials 16 (2004) 1009-1013.

[211]B. Sun, E. Marx, N. C. Greenham. Photovoltaic devices using blends of branched CdSe nanoparticles and conjugated polymers. Nano Letters 3 (2003) 961-963.

[212]W. U. Huynh, J. J. Dittmer, A. P. Alivisatos. Hybrid nanorod-polymer solar cells. Science 295 (2002) 2425-2427.

[213]B. Sun, H. J. Snaith, A. S. Dhoot, S. Westenhoff, N. C. Greenham. Vertically segregated hybrid blends for photovoltaic devices with improved efficiency. Journal of Applied Physics 97 (2005) 0149141-0149146.

[214]S. Zhang, P. W. Cyr, S. A. McDonald, G. Konstantatos, E. H. Sargent. Enhanced infrared photovoltaic efficiency in PbS nanocrystal/semiconducting polymer composites: 600-fold increase in maximum power output via control of the ligand barrier. Applied Physics Letters 87 (2005) 233101.

[215]S. A. McDonald, G. Konstantatos, S. Zhang, P. W. Cyr, E. J. D. Klem, L. Levina, E. H. Sargent. Solution-processed PbS quantum dot infrared photodetectors and photovoltaics. Nature Materials 4 (2005) 138.-142

[216]B. Sun, N. C. Greenham. Improved efficiency of photovoltaics based on CdSe nanorods and poly(3-hexylthiophene) nanofibers. Physical Chemistry Chemical Physics 8 (2006) 3557-3560.

[217]D. Cui, J. Xu, T. Zhu, G. Paradee, S. Ashok, M. Gerhold. Harvest of near infrared light in PbSe nanocrystal-polymer hybrid photovoltaic cells. Applied Physics Letters 88 (2008) 183111-183113.

[218]Y. Zhou, M. Eck, M. Kruger. Organic-Inorganic Hybrid Solar Cells: State of the Art, Challenges and Perspectives, Solar cells - new aspects and solutions. InTech (2011)

[219]L. C. Chen, D. Godovsky, O. Inganas, J. C. Hummelen, R. A. J. Janssens, M. Svensson, M. R. Andersson.Polymer photovoltaic devices from stratified multilayers of donor-acceptor blends. Advanced Materials 12 (2000) 1367–1370.

[220]C. Wu, H. Li, H. Fong, V. A. Pozdin, G. G. Malliaras, L. A. Estroff. Room-temperature preparation of crystalline TiO_2 thin films and their applications in polymer/TiO_2 hybrid optoelectronic devices. Organic Electronics 12 (2011) 1073–1079.

[221]S. Dayal, N. Kopidakis, D. C. Olson, D. S. Ginley, G. Rumbles. Photovoltaic devices with a low band gap polymer and CdSe nanostructures exceeding 3% efficiency. Nano Letters 10 (2010) 239-242.

[222]W. J. E. Beek, M. M. Wienk, M. Kemerink, X. Yang, R. A. J. Janssen. Hybrid zinc oxide conjugated polymer bulk heterojunction solar cells. The Journal of Physical Chemistry B 109 (2005) 9505–9516.

[223]S. D. Oosterhout, M. M. Wienk, S. S. Van Bavel, R. Thiedmann, L. Koster, J. Gilot, J. Loos, V. Schmidt, R. Janssen. The effect of three-dimensional morphology on the efficiency of hybrid polymer solar cells. Nature Materials 8 (2009) 818-824

[224]C. T. Black, C. B. Murray, R. L. Sandstrom, S. Sun. Spin-dependent tunneling in self-assembled cobalt-nanocrystal superlattices. Science 290 (2000) 1131-1134.

[225]K. M. Coakley, M. D. McGehee. Conjugated polymer photovoltaic cells. Chemistry of Materials 16 (2004) 4533-4542.

[226]L. Kavan, M. Grätzel, S. E. Gilbert, C. Klemenz, H. J. Scheel. Electrochemical and photoelectrochemical investigation of single-crystal anatase. Journal of the American Chemical Society 118 (1996) 6716-6723.

[227]Y. Lin, C. Chen, W. Yen, W. Su, C. Ku, J. Wu. Near-ultraviolet photodetector based on hybrid polymer/zinc oxide nanorods by low-temperature solution processes. Applied Physics Letters 92 (2008) 233301.

[228]Y. Lee, M. T. Lloyd, D. C. Olson, R. K. Grubbs, P. Lu, R. J. Davis, J. A. Voigt, J. W. P. Hsu. Optimization of ZnO nanorod array morphology for hybrid photovoltaic devices. The Journal of Physical Chemistry C 113 (2009) 15778-15782.

[229]D. C. Olson, Y. J. Lee, M .S. White, N. Kopidakis, S. E. Shaheen, D. S. Ginley, J. A. Voigt, J. W. P. Hsu. Effect of Polymer Processing on the Performance of Poly(3-hexylthiophene)/ZnO Nanorod Photovoltaic Devices. Journal of Physical Chemistry B 111 (2007) 16640-16645.

[230]L, E Greene, M, Law, B, D Yuhas, P.Yang. ZnO−TiO_2 core−shell nanorod/P3HT solar cells. Journal of Physical Chemistry C 111 (2007)18451-18456.

[231]G. K. Mor, S. Kim, M. Paulose, O. K. Varghese, K.Shankar, J. Basham, C, A. Grimes. Visible to near-Infrared light harvesting in TiO_2 nanotube array−P3HT based heterojunction solar cells. Nano Letters 9 (2009) 4250–4257.

Chapter 3 Methodology

3.1 Fabrication techniques

Various kinds of fabrication techniques have been extensively developed to synthesize ions doped and structural engineered TiO_2 materials. In terms of ions doped TiO_2 materials, both physical methods, such as magnetron sputtering deposition, pulsed laser deposition, and chemical methods, such as sol-gel, hydrothermal, chemical vapour deposition, are widely employed [1]. While both physical and chemical methods are suitable for the fabrication of ions doped TiO_2 materials, hydrothermal is the most feasible method to synthesize structured TiO_2, especially TiO_2 nanorods and nanowires. In this project, studies have been focused on doped TiO_2 materials by pulsed laser deposition, sol-gel and hydrothermal method, as well as structured TiO_2 thin films by hydrothermal method.

3.1.1 Pulsed laser deposition

The pulsed laser deposition (PLD) process is a conceptually simple physical vapour deposition process for thin film as illustrated in Fig. 3.1.1 and Fig. 3.1.2, where a short pulsed and high power laser beam is focused into a vacuum chamber through a set of optical components to strike a rotated solid target of material that is to be deposited. The material of target is vaporized in the form of a plume containing many energetic species which deposits as thin film on a substrate facing the target. It enables to deposit a variety of target materials on a wide range of substrates at designed temperature. However, the detailed mechanisms of PLD are extremely complicated in terms of laser–target ablation interaction; the absorption of energy and localized heating of materials; the generation of a plasma plume with high energetic species and the film growth itself on substrate [2,3]. Each step is central to the formation of high quality, uniform, thin film with slight surface roughness.

In the process of laser ablation, a short pulsed and high power laser is focused onto the target material and penetrates into the surface of material within the shallow penetration depth which depends on the laser wavelength and refraction index of the target material according to the laser wavelength. For most materials, the penetration

depth in which the energy of incident laser is absorbed by target material is typically in range of 10 nm. Then a quantum of incident laser energy is absorbed by an electron of target material. When the energy of laser is higher than the ablation threshold values, electrons are excited to higher energy states and then collide with lattice and thereby transferring some of the absorbed energy to lattice. This process happens within nanosecond. Then, being companied with chemical bound rupture the absorbed energy is converted into thermal, chemical and mechanical energy, resulting in the evaporation of materials from the target surface in the form of vapour with energetic species which is dubbed as plasma, typically being a mixture ions, molecules, electrons, clusters as well as neutral atoms. The kinetic energy of the ablated species is dependent, not only on the wavelength, but also on the fluence of incident laser. For ceramic target, it generally requires the laser pulse to be high in energy density by using short wavelength excimer operating in the ultraviolet region [4].

In the second stage, the evaporated plasma material expands in high vacuum or in the presence of a background gas along the vector of target surface towards substrate in plume shape according to the gas dynamic laws. The introduced gas molecules in the chamber can be used to react with the atoms or molecules from the plasma to deposit a film on the substrate with desired chemical composition. In a vacuum chamber, without background gas input, ions, molecules, electrons, clusters, neutral atoms travel at different velocities and the scattering of ablated material by back ground gas could be avoided, leading to extremely narrow and forward directed plume. Whereas under high background gas pressure, ablated material strongly interacts with the background gas, such as oxygen, nitrogen and hydrogen, giving rise to expansion of plume in various degrees, which depends on the background gas. Generally, chemical reaction and collision are the main interactions of ablated material and background gas, so all of the nature, mass and pressure of the background gas play important roles on the shape of plasma.

Then the ablated plasma with energetic species is striking onto the substrate surface and condenses on the surface of substrate. High energetic striking may cause damage to the surface of substrate by sputtering off atoms, so particles emitted from target and the sputtered spices from the substrate form a collision region on top of substrate

surface, serving as condensation source for thin film [5]. When the condensation rate is high enough, a thermal equilibrium can be reached and each pulse is likely to give rise to the formation of submonolayer of desired phase. In subsequence, persistent evaporation of target results in continuous growth of film on substrate surface as the consumption of target material. The deposition of energetic particles allows the formation of well crystallized phase and metastable phase, such as nanocrystalline, highly supersaturated solid solution or amorphous films over a vast composition range.

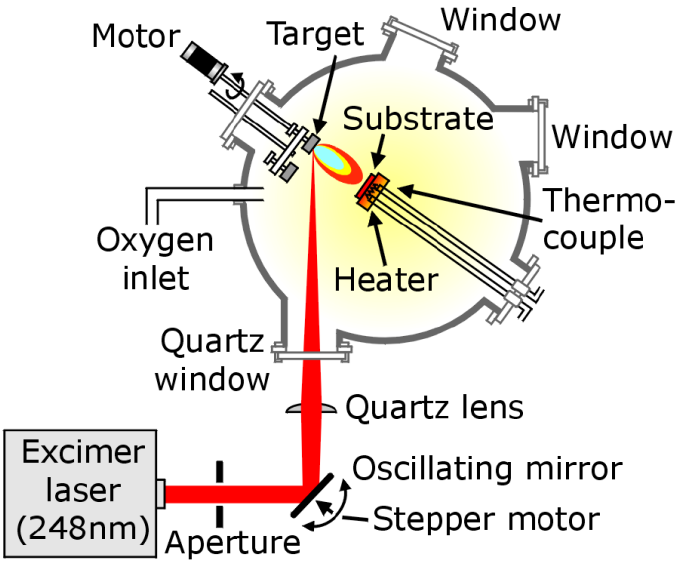

Figure 3.1.1 Illustration of pulsed laser deposition process [6].

Figure 3.1.2 Pulsed laser deposition system.

Vapour condensation on top of substrate is a nucleation and growth process similar to crystallization from melt [7]. Naturally, the super saturation property of plasma vapour will cause a large number of nucleation sites on top of substrate, and thereby growth can start from these nucleated sites. The nucleation process and growth kinetics of the film on substrate surface significantly rely on several growth parameters, including laser parameters such as laser wavelength; repetition rate; laser fluence which determine the deposition flux; preparation conditions such as target to substrate distance, substrate temperature, substrate surface and background pressure to strongly affect the properties of the thin films [8,9,10,11]. For example, generally both higher deposition flux and lower substrate temperature bring about higher nucleation density [12], whereas the effect of other parameters on the film properties are relatively complex.

Apart from nucleation, film growth also involves complex process. The ablated plasma of energetic species leads to complicated kinetic effects and large nucleation rate on top of substrate, resulting in the occurrence of various growth modes. Normally, arriving vapour atoms (called “adatoms”) striking on the top of substrate

or newly formed film will diffuse through, on average, several atomic distances before sticking to a stable position. Three markedly different possible growth modes as shown in Fig. 3.1.3 are proposed strongly relying on the mobility of surface adatoms, which is generally attributed to the type of materials to deposit and the substrate [13].

The simplest growth mode is Volmer–Weber mode, also dubbed as island growth. In the island growth mode, interactions between adjacent adatoms are stronger than those of adatoms with substrate surface. Adtoms landing on the surface of substrate move randomly until they meet another adtoms to nucleate as islands. Once the islands are formed, additional materials will nucleated on top of the existed islands, leading to 3 dimensional growths of the islands. Eventually, the separated islands will grow to become grains in the final film.

The second mode preferred in PLD deposition is Frank–Van der Merwe mode, also called as 'layer by layer', that a new layer only nucleates after the completion of the previous layer. During this mode, adtoms attach preferentially to the surface of substrate. Then when more material is deposited onto the surface, the adtoms diffuse into these nucleated islands to accomplish the layer prior to the start of subsequent layers. Layer by layer growth is always related to sufficient lateral surface diffusion of adtoms, which is also a thermally activated process determined by the substrate temperature except for the nature of material and substrate. Low temperature favours disordered, or even amorphous structure, on account that crystal growth may be inhibited by plasma impingement, whereas high temperature favours rapid and defect free crystal growth resulting in atomically smooth, fully formed layers.

Another mode is Stranski–Krastanov, also known as layer plus island growth, by which thin film initially grows in layer by layer up to several monolayer thick to complete substrate surface of adsorbates and then, when the thickness beyond the critical layer thickness, it grows continuously through the nucleation and coalescence of adsorbate islands [14].The critical layer thickness strongly depends on physical and chemical properties, including lattice parameters between the deposited material and substrate, chemical potential of the deposited material, and surface energies. This

growth mode has meriting increased attention as a means of fabricating epitaxial nanoscale structures, such as quantum dots (QDs) [15].

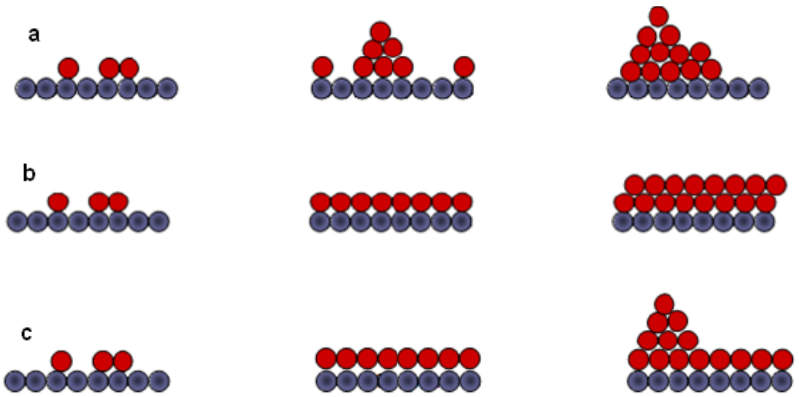

Figure 3.1.3 Illustrations of the basic growth modes including (a) Volmer–Weber mode (island growth), (b) Frank–Van der Merwe mode (layer by layer growth), and (c) Stranski–Krastanov mode (layer plus island growth) [16].

The most important factor in the successful use of PLD is the stoichiometric removal of material from solid target to substrate, keeping the stoichiometry of deposited thin film very close to that in target. However, stoichiometric remove does not necessarily transfer the materials exactly from the target into the thin film, since not all elements get the same volatile referred to sticking coefficient. If one of the elements is more volatile than others in target, this element is easier to be evaporated and the corresponding ratio of the element in plume is undoubtedly higher. On the other hand, re-evaporation of volatile component from growth surface may occur due to its lower sticking coefficient. Therefore, an initial pre-ablation process, by exposing the target surface to the laser ablation for a period of time, is necessary to obtain an equilibrium and steady state as well as to remove surface contamination when growing materials of different volatile. Moreover, the use of additional source can also be adopted to compensate for the componential loss. For example, oxygen gas is often introduced into the vacuum chamber when depositing oxide material to compensate oxygen loss caused by ablation process.

Besides the stoichiometric transfer, the pulsed nature of high energy laser makes it possible to utilize laser to precisely deposit almost any type of solid state materials via changing the laser conditions for distinct materials [17]. Moreover, it becomes possible to produce complex composite film of controlled composition gradients, alloys or super lattices and polymer-metal system, by using compound target. There has been tremendous success in synthesis of complex oxide materials with extremely high purity compared with chemical methods. Therefore, ions doped TiO_2 thin films are expected to be successfully fabricated by PLD by employing compound targets under specific conditions.

3.1.2 Sol-gel method

Compared with expensive physical methods carried out in high vacuum system, chemical methods are obviously relatively cheaper and easier to bring out. On the other hand, because of the high surface energy caused by chemical reactions, the obtained products are expected to need lower annealing crystallization temperature. Hence, as a wet chemical technique, sol-gel method has been widely employed in the field of materials science, especially in the fabrication of novel metal oxide materials through a chemical reaction at low temperature.

The most significant feature of this technique is the sol to gel process led by the transition from liquid into a solid. Fig. 3.1.4 shows a typical sol-gel process for the fabrication of pure TiO_2 powder materials which starts from a solution containing metal-organic compounds, alcohol as solvent, water as hydrolysis agent and acid or, base as catalyst. Then the hydrolysis and polycondensation of metal organic compounds in solution result in the formation of colloidal sol where partial fine particles and polymers suspend in [18]. Being different from a solution in which only single phase exists, the sol mentioned here is a colloidal suspension of one solid particle phase in another liquid phase [19]. Generally it is as stable as a solution, due to the extremely small size of dispersed particles that gravitational forces are negligible and interactions between suspended particles are dominated by short range forces, such as Van der Waals force and surface charges [20]. In sol-gel process, the sol gradually evolves towards the formation of a gel like diphasic system containing both a liquid phase and a solid phase whose morphologies range from discrete

particles to continuous chain like polymer networks [21,22]. After annealing, the gel like system transfers into powder metal oxide.

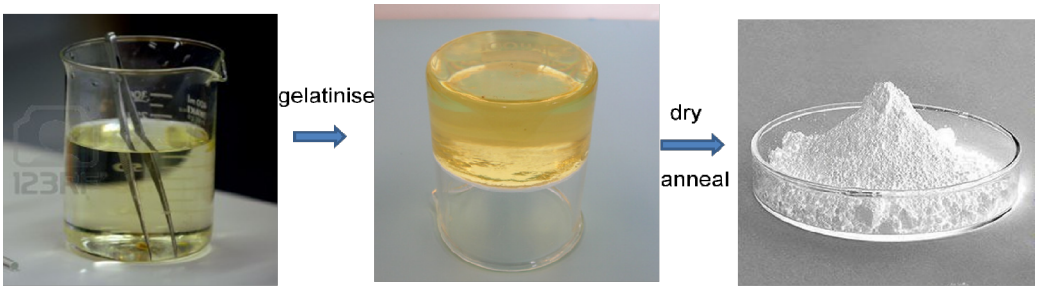

Figure 3.1.4 A typical sol-gel process.

Although the sol-gel method can be conceptually employed to fabricate various kinds of materials, it is preferentially to synthesize metal oxides through hydrolyzing metal salts or metal-organic compounds that contains metals and organic ligands. For instance, as a type of metal-organic compounds, metal alkoxides $M(OR)_n$ can react directly with nucleophilic molecules X-OH to form metal oxides via two chemical processes: hydrolysis and polycondensation process, which are fulfilled through the reaction as follows [23,24,25].

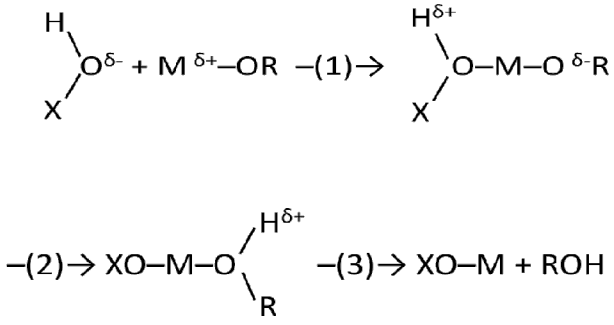

(3.1)

where R is an alkyl group. This process is known as bimolecular nucleophilic substitution. At first, negatively charged OH group is adsorbed onto positively charged metal atom due to nucleophilic reaction that positively charged metal atoms tend to accept electrons from nucleophilic ligand by their vacant orbitals to increase coordination number. At the same time, positively charged proton transfers to one negatively charged OR group. After transfer state, positively charged alkoxide ROH

tends to depart from original position, resulting in the replacement of OR group by OX group. This process can also be simply understood as:

$$M(OR)_n + mXOH \rightarrow M(OR)_{n-m}(OX)_m + mROH \quad (3.2)$$

or:

$$-M-OR + X-OH \rightarrow -M-OX + ROH \quad (3.3)$$

When X is H, the reaction is correlated with the hydrolysis of $M(OR)_n$ with water:

$$M(OR)_n + H-OH \rightarrow M(OR)_{n-m}(OH) + ROH \quad (3.4)$$

or

$$-M-OR + H-OH \rightarrow -M-OH + H_2O \quad (3.5)$$

Any intermediate species $M(OR)_{n-m}(OH)_m$ could be regarded as partial hydrolyzed products. Once the hydrolysis of metal alkoxide happens to form M-OH bonds, hydrolyzed molecules polymerize to link together by polycondensation process. When X is metal, the reaction directly corresponds to the polycondensation process to produce polymers comprising M-O-M bonds, and thereby the whole process is ended up as:

$$-M-OR + -M-OH \rightarrow -M-O-M- + ROH \quad (3.6)$$

$$-M-OH + -M-OH \rightarrow -M-O-M- + H_2O \quad (3.7)$$

The relative hydrolysis and polycondensation rate have strong influence on the final structure and properties of synthesized metal oxides, because the partially hydrolyzed molecules can link together to form various kinds of structures by polycondensation process. Generally, the produced M-O-M bonds are in the form of a three dimensional net work structure in solution because of polycondensation.

Sol-gel methods have been widely applied to fabricate various metal oxides in diverse forms of dense films, bulk ceramics, nanoparticles, fibres, all relying on different operating modes as that described in Fig. 3.1.5. Dip coating or spinning coating the sol onto diverse substrates under different coating parameters will result

in metal oxide thin films with distinct thickness after heating. Aging of gel, until the gel transforms into solid state, and followed by heating will give rise to metal oxides particles varying broadly in size and shape. Directly precipitating can produce ultra fine and uniform particles. By adjusting viscosity of a sol into a proper range, both transparent and opaque metal oxide fibres can be synthesized [26].

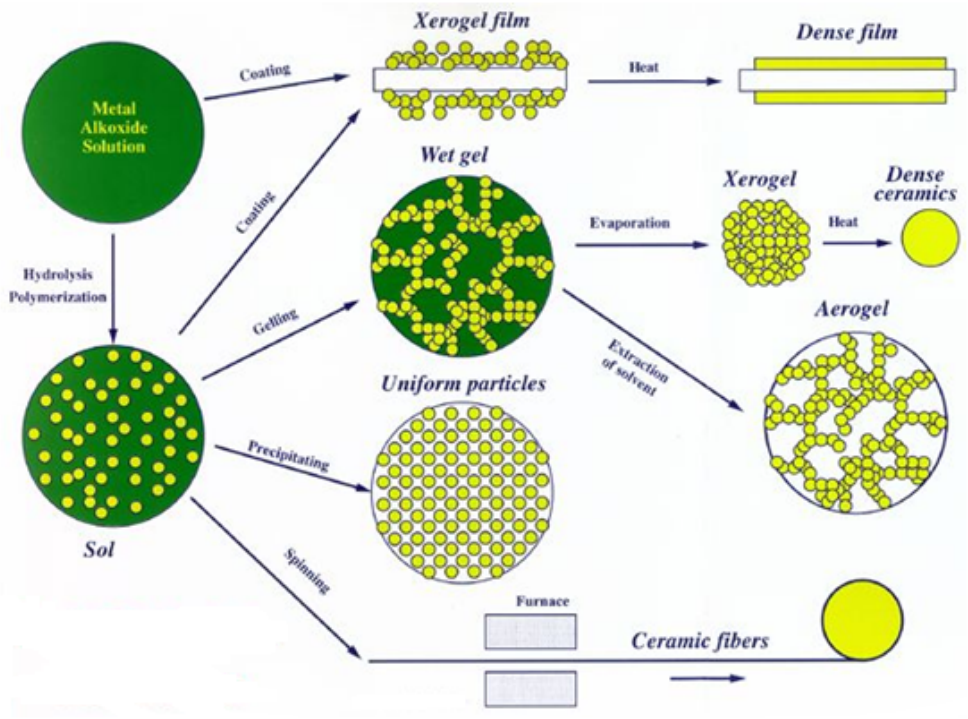

Figure 3.1.5 Simplified chart of sol-gel technologies and their application [27].

Typically, for the preparation of TiO_2 materials, $Ti(OR)_4$ are commonly used as a starting precursor to react with water directly on account of the high reactivity of titanium alkoxides with water. Thereby the hydrolysis reaction can be written as

$$Ti(OR)_4 + mH_2O \rightarrow Ti(OR)_{4-m}(OH)_m + mROH \quad (3.8)$$

$$2Ti(OR)_{4-m}(OH)_m \rightarrow [Ti(OR)_{4-m}(OH)_{n-1}] - O - [Ti(OR)_{4-m}(OH)_{n-1}] + H_2O \quad (3.9)$$

The final product titanium hydroxide groups are often in the form of white amorphous precipitates [28, 29]. However, the actual reaction is more complex than it is expected. Generally, the high reactivity of titanium alkoxides with water results in precipitation of particles rather than gelation, leading to inhomogeneous structure of final product. Therefore, additives such as solvent, acidic, basic catalyst or stabilizing agents are introduced to control the hydrolysis rate. For example, the introduction of nucleophilic molecules XOH can react with alkoixde generating a new molecular precursor. The hydrolysis and condensation of the modified precursor depends on the stability of the new ligands which can react differently with the nucleophilic agent [20]. Generally, less electronegative ligands are removed faster in hydrolysis process while more electronegative are mainly removed in condensation process [30,23,31]. As a consequence, modified ligands can give rise to less effective hydrolysis and polycondensation, resulting in a controlled and promoted gelation instead of aggregation of particles. The common used chemical modifiers for the fabrication of TiO_2 materials are acetic acid, alcohols, oxyful, acetylacetone and so on [32, 33, 34, 35].

In addition, polycondensation rate can also be inhibited by using titanium alkoxides with higher molecular weight alkyl groups. Moreover, adding acid catalysts, such as HCl, H_2SO_4, HNO_3 and CH_3COOH, into precursor are also employed to suppress the hydrolysis of titanium alkoxides to control the hydrolysis time and level via electrophilic substitution [36]. Then the polycondensation rate will be decreased once the hydrolysis is retarded. Therefore, high concentration of titanium alkoxide precursors can be prepared with the existence of acids.

The introducing of additives and acids can result in the generation of complicated intermediate molecules, so the structures and properties of final products could be extremely complex depending on various parameters such as temperature, solvent, concentration, type of acid, PH value and the steric hindrance of alkoxide groups.

It is worth mentioning that sol-gel technique makes it possible to incorporate dopants into TiO_2 lattice to produce ions doped TiO_2 materials, due to the homogeneous mixing of multi component system at molecular level [37]. Besides, there are a great deal of advantages compared to other conventional chemical production techniques

for the preparation of ions doped TiO_2 materials. For example, if not contaminated during fabrication process, the derived product is expected to be highly pure on account of the high purity of starting materials [38]. In addition, the desired sintering and calcination temperature could be much lower than physical methods resulted from the high surface energy of materials caused by the sol-gel technique. Post heat treatment is needed to not only make final product crystallized but also remove remaining solvent and organic by products. Furthermore, by varying the sol parameters together with operating modes, various kinds of structures in the shapes of homogeneous particles, dense or porous thin films can be realized. For the above mentioned reasons, ions doped TiO_2 powders are expected to be successfully fabricated via sol-gel method.

3.1.3 Hydrothermal method

Apart from sol-gel technique, hydrothermal is another attractive method that utilizes aqueous solution at high temperature and pressure to crystallize materials directly from solution [39]. The precursors used in hydrothermal process could be in forms of solutions, sols, and gels, which are typically located in an apparatus consisting of closed Teflon lined steel pressure vessel dubbed as autoclave (Fig. 3.1.6). The autoclave is generally put in an oven at elevated temperature, allowing for aqueous solutions to be heated over their boiling point and extremely high vapour pressures to be obtained. The inherent feature of this hydrothermal method is through controlling the solution and the temperature of autoclave to modify internal pressure of individual reaction, giving rise to crystal precipitation. In most cases, the obtained products are already well crystallized and therefore post annealing is avoided.

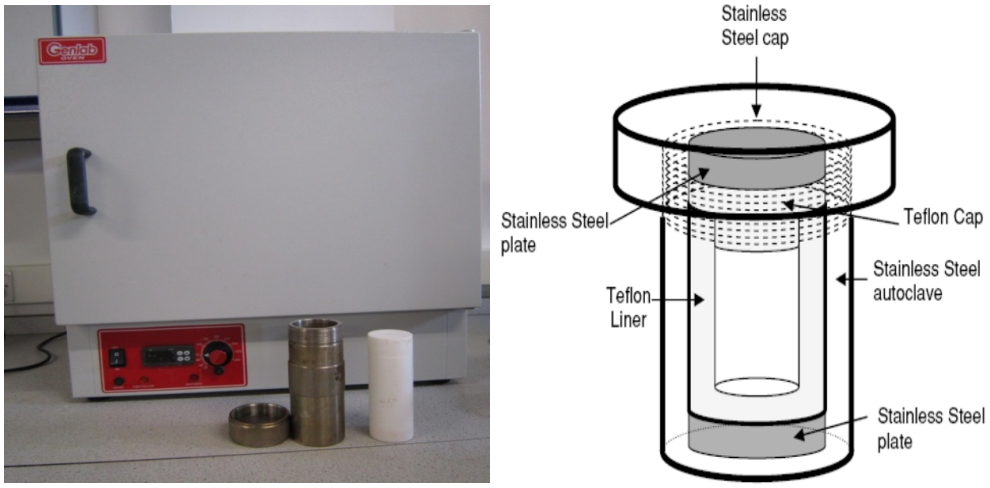

(a) (b)

Figure 3.1.6 Practical (a) and schematic diagram (b) of hydrothermal autoclave.

Hydrothermal method has been widely employed for the synthesis of TiO_2 materials, including pure and doped TiO_2 nanoparticles of diverse structures, such as powders and thin films on various kinds of substrate [40,41,42,43,44]. In the preparation of TiO_2 materials, titanium alkoixdes are normally used as nutrient along with water as precursor, together with other additives, such as ethanol and acid. Similar to sol-gel technique, the synthesis of TiO_2 materials by hydrothermal method is through a two-stage hydrolysis-condensation process that occurs in solution as the temperature elevates up. Different from the tender hydrolysis at the low temperature during sol-gel process, the reaction during hydrothermal is extremely energetic due to the high temperature and extremely relative high pressure in autoclave, leading to the formation of a large amount of TiO_2 crystals.

The hydrothermal method keeps most of advantages of sol-gel, such as high purity of product, uniform composition and narrow size distribution [45]. Besides these, it has been shown to favour a decrease in aggregation and be more effective in tuning the size and crystalline structures than other methods, by controlling processing parameters. Furthermore, hydrothermal method has become the most powerful and promising technique for preparing one dimensional TiO_2 nanostructures as the crystallization happens during hydrothermal process [46,47,43,44]. Therefore, both ions

doped TiO_2 nanopowder materials and structural engineered TiO_2 nanoarray are expected to be successfully synthesized by hydrothermal method under controlled conditions.

3.1.4 Fabrication of hybrid solar cells

For TiO_2 nanorod this film based hybrid solar cells without electrolyte, a thin layer of dense TiO_2 particle was deposited on FTO surface by magnetron sputtering as shown in Fig. 3.1.7, before fabrication of TiO_2 nanorod by hydrothermal method. Magnetron sputtering is a physical vapour deposition method which involves ionized argon to strike a target to deposit thin films on substrate in vacuum.

Figure 3.1.7 Magnetron sputtering system.

After hydrothermal process the as prepared TiO_2 thin films were treated by $TiCl_4$ 0.5 M solution to form a very thin TiO_2 layer or deposited by a thin layer of ZnO by using atomic layer deposition (ALD) as shown in Fig. 3.1.8, which is a thin film deposition technique based on the sequence use of gas phase chemical precursors. By exposing the precursors separately and repeatedly to the growth surface in vacuum chamber, a thin film is deposited slowly.

Figure 3.1.8 Atomic layer deposition system.

P3HT was spin coated in ambient atmosphere on top of TiO_2 layer by using a spin coating machine as shown in Fig. 3.1.9 and then annealed in N_2 atmosphere at various temperature. Then thick Cu dot electrodes were deposited on top of P3HT layer in vacuum chamber by using thermal evaporator as presented in Fig. 3.1.10.

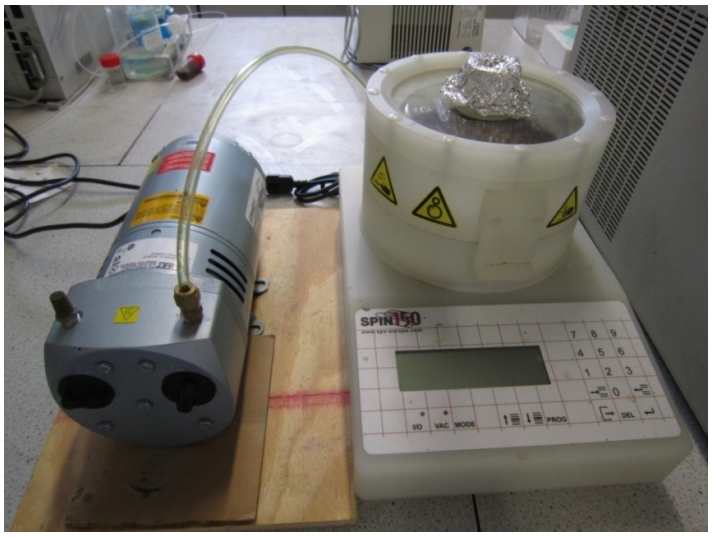

Figure 3.1.9 Spin coating machine.

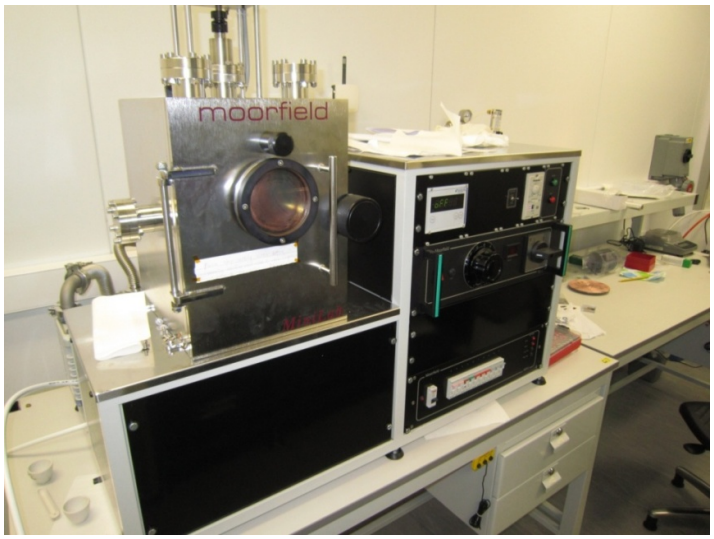

Figure 3.1.10 Thermal evaporator.

3.2 Characterization techniques

3.2.1 X-ray diffraction analysis (XRD)

X-ray diffraction analysis (XRD) is a powerful method to determine the crystal structure of a solid via a collimated X-ray beam of wavelength typically ranges from 0.7-2 Å. The wavelength of X-ray is on the geometrical length scales of three dimensional periodic crystal lattices. When a collimated X-rays irradiates on a specimen, diffraction effects will happen because of the interaction of the incident light and specimen according to Bragg's Law ($n\lambda=2dsin\theta$), where d is the planar distance of crystal lattice and λ is the wavelength of incident X-ray. The intensity of diffracted X-ray is detected as a function of incident angle 2θ, giving information about diffraction peak position and relative intensity to identify specimen's crystal phase and preferred orientation. Besides this, from the shift of peak position, one can calculate the change in d spacing resulted from the change of lattice constants [48]. If there is no change of crystal constant, the crystalline size, D can be estimated from the peak width with Scherrer's formula:

$$D = \frac{K\lambda}{B\cos\theta} \qquad (3.10)$$

where K is the Scherrer's constant and B is the full width of half maximum of diffraction peak. This method is very useful for estimating the average size of nanoparticles.

XRD measurements were performed with a Bruker-AXS Micro diffractometer (model D5005) with Cu Kα radiation (λ=1.54056Å) as presented in Fig. 3.2.1.

Figure 3.2.1 X-ray diffractometer.

3.2.2 UV-visible absorption and reflectance spectroscopy

The optical absorption edge of semiconductor is directly related to band gap where longer wavelength corresponding to bigger band gap, so optical absorption properties were the focus of interest throughout the whole work. The optical properties of transparent samples, including thin film and solution, are usually measured by UV-visible absorption spectrometer, in which one beam of light from ultraviolet or visible light source passes through the sample and then detected by an electronic detector. By comparing the intensity of measured light I^* with that of reference beam I_0^*, the spectrometer gives out the absorption ratio at specific wavelength, which is presented as transmittance ($T=I^*/I_0^*$) or absorbance ($A=-log(I^*/I_0^*)$). The spectrometer can automatically scan all wavelengths in a given range,

providing a curve of absorption versus wavelength of incident beam. For thin film, the absorption coefficient α is given by

$$\alpha = A/d \qquad (3.11)$$

where α is the absorption coefficient, A is the absorbance and d is the thickness of the thin film. If the sample to be measured is opaque, a reflectance spectrometer is necessary to be employed where the incident light is absorbed and reflected by the sample.

The edge of absorption spectra is directly connected with band gap of semiconductor, since the dependence of α on incident photon energy $h\nu$ for semiconductor is given by the relation [49]:

$$\alpha \propto \alpha_0 \left(h\nu - E_g\right)^n \qquad (3.12)$$

where α_0 is a constant which does not depend on $h\nu$, E_g is the optical band gap and n is a value dependent on the type of predominant electron transition (equals ½ for direct band gap and 2 for indirect band gap). In consequence, the band gaps of materials can be obtained from optical absorption spectra.

In this work, optical absorption spectra of the TiO_2 films were obtained by a Lambda UV-visible-infrared spectrometer (UV-2500, Japan) in the range of 326–1500 nm or a Lambda UV-visible spectrometer (UV-2550, Japan) in the range of 200–900 nm. Optical absorbance spectra of powders were obtained using a UV–visible diffuse reflectance spectrometer in range of 200-900 nm or 200-1500 nm. Fig. 3.2.2 is a typical UV-Visible spectrometer connected with computer to get optical absorption or transmission spectrum.

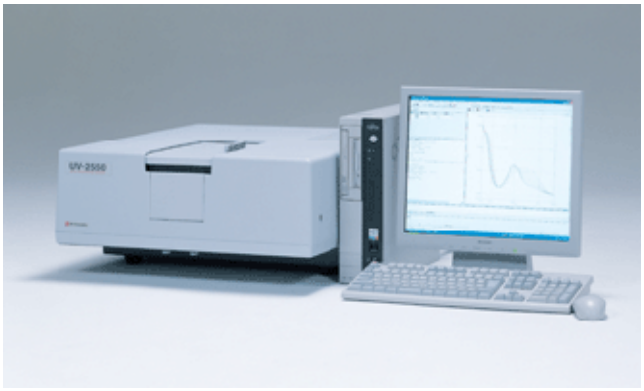

Figure 3.2.2 A typical UV-Visible spectrometer.

3.2.3 Scanning electron microscopy (SEM)

Scanning electron microscopy (SEM), which can produce high resolution images of the surface of a sample, is widely used to analyze the surface morphology of synthesized materials. It is a type of electron microscopy that images a sample by scanning it with a focused beam of high energy electrons. The primary incident electrons coming from electron gun strike the surface of the sample and interact with the surface atoms of the tested sample, giving rise to emitted electrons that reveal information about surface morphology, crystal structure, and electrical conductivity. Except for the emitted electrons, X-rays are also produced owing to electron-atom interaction. Detecting the X-rays by equipped energy dispersive X-ray spectroscope (EDX) can reveal chemical composition of the sample.

The planar and cross-sectional morphologies of the thin film samples were characterized by using field-emission-gun scanning electron microscope (FE-SEM, JSM-6700F) fitted with an EDX accessory, at an accelerating voltage of 20 kV, as presented in Fig. 3.2.3.

Figure 3.2.3 Scanning electron microscope (SEM).

3.2.4 Transmission electron microscopy (TEM)

In transmission electron microscopy (TEM), a beam of focused high energy electrons is transmitted through a very thin sample, interacting with the atoms in the sample when it passes through and giving information of inner structure of the sample. Therefore samples for TEM must be thin enough to allow electrons to transmit. The high accelerate voltage gives out extremely short wavelength of focused electrons, providing atomic scale image from the interaction of electrons with atoms in the sample. Except for the transmitted electrons, X-rays are also produced owing to electron-atom interaction. Generally, transmission electron microscope is also equipped with an EDX accessory to reveal chemical composition of samples.

Selected area electron diffraction (SAED) and transmission electron microscopy of thin films were conducted under a Philips CM200 transmission electron microscope (TEM) at an acceleration voltage of 200 kV.

The morphologies of the powders were observed using a Tecnai G20 transmission electron microscope (TEM) at an acceleration voltage of 200 kV, as shown in Fig.

3.2.4. SAED and EDX analysis were utilized for in situ determination of the crystalline structure and doping concentration. To prepare the TEM specimens, the powder samples were ultrasonically dispersed in ethanol and the suspension was collected by carbon supported copper grids.

Figure 3.2.4 Tecnai G20 transmission electron microscope (TEM).

3.2.5 X-ray photoelectron spectroscopy (XPS)

X-ray photoelectron spectroscopy (XPS) is a surface technique to analyze the chemical states of constituent elements in a sample. In XPS spectrometer, a beam of soft X-rays with specific high photon energies is utilized to strike a solid sample in a vacuum system, and thereby to eject electrons from inner shell orbitals. The theoretical foundation of XPS is Einstein photoelectronic equation $E_b = h\nu - E_{kin} - \phi_{sp}$, where E_b is the binding energy of the electron in the sample, $h\nu$ is the quantum energy of incident photon, E_{kin} is the kinetic energies of inner or valence electrons ejected by incident photons and ϕ_{sp} is the work function of the spectrometer [50]. By collecting and recording kinetic energy distribution of emitted electrons, it can easily calculate binding energy E_b, which is related to the energy of

ionization as one intrinsic characteristic of chemical bonds [51]. Thus, XPS is expected to give information about the elemental composition and the chemical state of each element. The chemical states of elements were determined by X-ray photoelectron spectrometer (XPS) using an Al Kα X-ray source (Kratos Ltd, XSAM800, as presented in Fig. 3.2.5), with the spectra calibrated in situ by the C 1s binding energy.

Figure 3.2.5 X-ray photoelectron spectrometer (XPS).

3.2.6 Visible light photocatalytic activity measurement

Under light illumination, TiO_2 materials can decompose organic dye in solution by light excited electron and hole, making it possible to measure the photocatalytic activity by measuring the intensity of optical absorption peak of specific molecule. For example, the absorption peak intensity of methylene blue (MB) at 665 nm is decreased as the degradation of MB molecule. By referring to an absorption–concentration standard curve that is established by measuring the optical absorption of MB at 665 nm the relative concentration of MB in the solutions is ascertained. Therefore, the degradation rate of photocatalytic activity of TiO_2 photocatalyst can

be estimated recording the absorption intensity as a function of time. The detailed procedures will be described in related chapters.

3.2.7 I-V measurement of solar cells

An ideal solar cell can be modelled by a current source in parallel with a diode. Considering no solar cell is ideal in practice, a series resistance and a shunt resistance are involved in the model, as shown in Fig. 3.2.6. Without light illumination to generate current, the solar cell behaves like a diode. When light is present, current is generated by the solar cell.

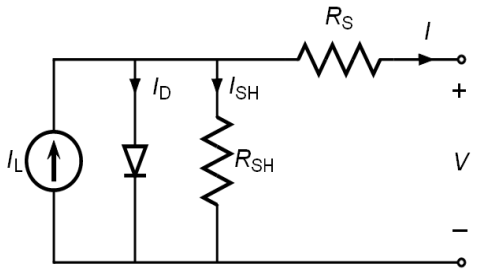

Figure 3.2.6 Simplified equivalent circuit model for a solar cell.

From the equivalent circuit it is evident that the current produced by the solar cell is equal to that produced by the current source, minus that which flows through the diode, minus that which flows through the shunt resistor:

$$I_{sc} = I_L - I_D - I_{SH} \qquad (3.13)$$

where

I_{sc} = short circuit current (amperes)

I_L = photogenerated current (amperes)

I_D = diode current (amperes)

I_{SH} = shunt current (amperes).

The open voltage is governed by:

$$V_{oc} = V_j - IR_S \qquad (3.14)$$

where

V_{oc} = open voltage (volts)

V_j = voltage across both diode and resistor R_{SH} (volts)

I = output current (amperes)

R_S = series resistance (ohms).

Therefore, solar cells show dark and illuminated curves as illustrated in Fig. 3.2.7. The performance of solar cells can be estimated through measuring the I-V curves which can give out I_{sc}, V_{oc} and η (energy conversion efficiency).

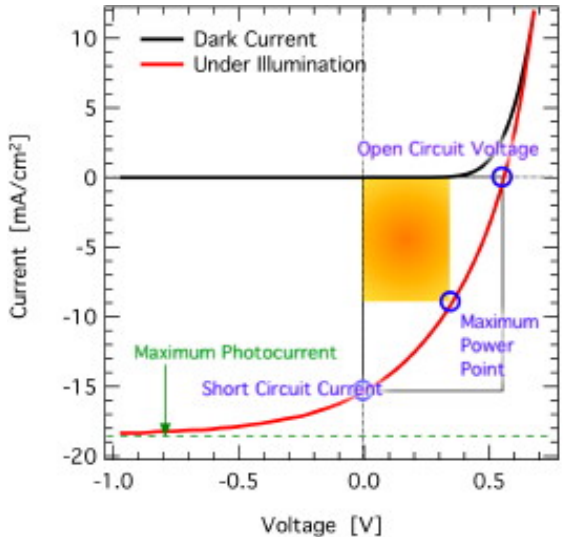

Figure 3.2.7 Dark and illuminated J-V curves of solar cell.

In this work, the dark and illuminated I-V curves of devices were measured by using Keithley 2700 source meter fitted with solar simulator AM 1.5 G (100 mV cm^{-2}), as shown in Fig. 3.2.8.

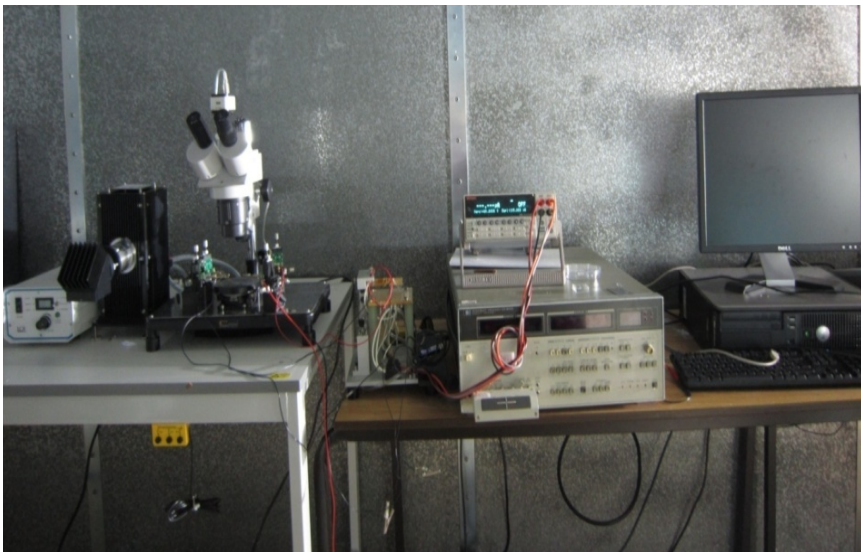

Figure 3.2.8 Solar cell measurement system.

3.3 Contributions

The ab initio DFT simulation results used in this thesis were done by author's supervisor and a post doctor mentioned in acknowledgement, and thus the detailed simulation theory was not presented in this thesis.

Pure and ions doped TiO_2 thin films fabricated by using PLD, Fe doped TiO_2 photocatalysts by using hydrothermal technique and Mn doped TiO_2 photocatalysts by using sol gel method were carried out in Hubei University. Experiments about TiO_2 nanorod thin films were carried out in both Hubei University, China and University of Bolton, UK. TiO_2 nanorod thin films based hybrid solar cells were prepared and tested in University of Bolton. Except for the sample preparation finished by author, the preparation of Fe doped TiO_2 photocatalyst and pure TiO_2 nanorods were achieved with some assistance from my colleague as shown in acknowledgement.

XRD, SEM, TEM and XPS characterization and analysis were accomplished under the cooperation of laboratory assistants (operating equipment) and author. Others without special mention were carried out on author's own.

References

[1] V. Augugliaro, M. Pagliaro, V. Loddo, G. Palmisano, L. Palmisano. Clean by Light Irradiation: Practical Applications of Supported TiO_2. Royal Society of Chemistry (2010).

[2] http://en.wikipedia.org/wiki/Pulsed_Laser_Deposition.

[3] Z. Wang, Y. Liu, Z. Zhang. Handbook of nanophase and nanostructured materials: synthesis. Springer (2002)

[4] R. Eason. Pulsed laser deposition of thin films: applications-led growth of functional materials. Wiley-Interscience (2006).

[5] S. Soltan. Interaction of superconductivity and ferromagnetism in YBCO/LCMO heterostructures. Cuvillier Verlag (2005)

[6] http://www.egr.msu.edu/erc-cleanroom/equipment/pld/.

[7] M. V. Allmen, A. Blatte. Laser-beam interactions with materials: physical principles and applications. Springer (1995).

[8] H. Krebs, M. Weisheit, J. Faupel, E. Suske, T. Scharf, C. Fuhse, M. Stormer, K. Sturm, M. Seibt, H. Kijewski, D. Nelke, E. Panchenko, M. Buback. Pulsedlaserdeposition - aversatiletechnique only for high-temperature superconductor thin-filmdeposition?. Applied Surface Science 1-4 (1993) 204-211.

[9] N. Stankova, I. Dimitrov, T. Stoyanchov, P. Atanasov, D. Kovacheva. Structure and optical anisotropy of pulsed-laser deposited TiO_2 films for optical applications. Applied Surface Science 255 (2009) 5275–5279.

[10] G. Shukla, P. K. Mishra, A. Khare. Effect of annealing and O_2 pressure on structural and optical properties of pulsed laser deposited TiO_2 thin films. Journal of Alloys and Compounds 489 (2010) 246–251.

[11] M. Walczak, E. Papadopoulou, M. Sanz, A. Manousaki, J. Marco, M. Castillejo. Structural and morphological characterization of TiO_2 nanostructured films grown by nanosecond pulsed laser deposition. Applied Surface Science 255 (2009) 5267–5270.

[12] J. D. Ferguson, G. Arikan, D. S. Dale, A. R. Woll, J. D. Brock, Measurements of surface diffusivity and coarsening during pulsed laser deposition. Physical Review Letters 103 (2009): 256103.

[13] H. Luth. Solid surfaces, interfaces and thin films. Springer (2010).

[14] J. Venables.. Introduction to surface and thin film processes. Cambridge University Press (2000).

[15] http://en.wikipedia.org/wiki/Stranski%E2%80%93Krastanov_growth#cite_ref-li2005_11-0.

[16]http://www.physics.uwo.ca/~lgonchar/courses/p9826/Chapter11_TFGrowth.pdf.

[17]A. Miotello, P. M. Ossi. Laser-surface interactions for new materials production. Springer (2010)

[18]S. Sakka. Handbook of sol-gel science and technology: applications of sol-gel technology. Springer(2005).

[19]L. C. Klei. Sol-gel optics: processing and applications. Springer (1994).

[20]C. J. Brinker, G. W. Schere. Sol-gel science: the physics and chemistry of sol-gel processing. Academic Press Inc (1990).

[21]http://en.wikipedia.org/wiki/Sol-gel#cite_note-3.

[22]L. C. Klein, G. J. Garvey. Kinetics of the sol-gel transition. Journal of Non-Crystalline Solids 38 (1980) 45-50.

[23]J. Livage, M. Henry, C. Sanchez. Sol-gel chemistry of transition metal oxides. Progress in Solid state Chemistry 18 (1988) 259-342.

[24]C. Sanchez, J. Livage, M. Henry, F. Babonneau. Chemical modification of alkoxide precursors. Chemical modification of alkoxide precursors 100 (1988) 65-76.

[25]J. Livage, C. Sanchez. Sol-gel chemistry. Journal of Non-Crystalline Solids 145 (1992) 11-19.

[26]S. Sakka. Handbook of sol-gel science and technology: Applications of sol-gel technology. Springer (2005)

[27]http://www.chemat.com/.

[28]Z. Tang, J. Zhang, Z.Cheng, Z Zhang. Synthesis of nanosized rutile TiO_2 powder at low temperature. Materials Chemistry and Physics 77 (2003) 314-317.

[29]D. A. H. Hanaor, C. C. Sorrell. Review of the anatase to rutile phase transformation. Journal of Materials Science 46 (2010) 855-874.

[30]C. Sanchez, J. Livage, M. Henry, F. Baboneau. Chemical modification of alkoxide precursors. Journal of Non-Crystalling Solids 100 (1988) 65-76.

[31]J. Livage, C. Sanchez, M. Henry. S. Doeuff. The chemistry of the sol-gel process. Solid state ionics 32-33 (1989) 633-638.

[32]I. Moriguchi, H. Maeda, Y. Teraoka, S. Kagawa. Preparation of TiO_2 ultra thin film by newly developed two-dimensional sol-gel Process. Journal of American chemical society 117 (1995) 1139–1140.

[33]H. Yang, K. Zhang, R. Shi, X. Li, X. Dong, Y. Yu. Sol–gel synthesis of TiO_2 nanoparticles and photocatalytic degradation of methyl orange in aqueous TiO_2 suspensions. Journal of Alloys and Compounds 413 (2006) 302–30.

[34]T. Zhang, B. Tian, J. Kong, P. Yang, B. Liu. A sensitive mediator-free tyrosinase biosensor based on an inorganic–organic hybrid titania sol–gel matrix. Analytica Chimica Acta 489 (2003) 199–206.

[35]X. Tang, J. Qian, Z. Wang, H. Wang, Q. Feng, G. Liu. Comparison of low crystallinity TiO_2 film with nanocrystalline anatase film for dye-sensitized solar cells. Journal of Colloid and Interface Science 330 (2009) 386–391.

[36] S. Doeuff, M. Henry, C. Sanchez, J. Licaje. Hydrolysis of titanium alkoxides : modification of molecular precursor by acetic acid. Journal of Non-Crystalline Solids 89 (1987) 206-216.

[37] Y. Kuroda, T. Mori, K. Yagi, N. Makihata, Y. Kawahara, M. Nagao, S. Kittaka. Preparation of Visible-Light-Responsive $TiO_{2-x}N_x$ Photocatalyst by a Sol−Gel Method: Analysis of the Active Center on TiO_2 that Reacts with NH_3. Langmuir 21 (2005) 8026–8034.

[38]M. Keshmiri. Composite sol gel process for photocatalytic titanium dioxde. The University of British Columbia (2004).

[39]K. Byrappaa, T. Adschirib. Hydrothermal technology for nanotechnology. Progress in Crystal Growth and Characterization of Materials. 55 (2007) 117-166.

[40]Q. Chena, Y. Qian, Z. Chen, G. Zhou, Y. Zhang. Preparation of TiO_2 powders with different morphologies by an oxidation-hydrothermal combination method. Materials Letters 22 (1995) 77-80.

[41]Y. Suzuki, S. Pavasupree, S. Yoshikawa, R. Kawahata. Natural rutile-derived titanate nanofibers prepared by direct hydrothermal processing. Journal of Materials Research 20 (2005) 1063-1070.

[42]S. S. Mali, P. S. Shinde, C. A. Betty, P. N. Bhosale, W. J. Lee, P. S. Patil. Nanocoral architecture of TiO_2 by hydrothermal process: synthesis and characterization. Applied Surface Science 257 (2011) 9737-9746.

[43]X. Feng, K. Shankar, O. K. Varghese, M. Paulose, T. J. Latempa, C.A. Grimes. Vertically aligned single crystal TiO_2 nanowire arrays grown directly on transparent conducting oxide coated glass: Synthesis Details and Applications. Nano letters 8 (2008) 3781-3786.

[44] B. Liu, E. S. Aydil. Growth of oriented single-crystalline rutile TiO_2 nanorods on transparent conducting substrates for dye-sensitized solar cells. Journal of the American Chemical Society 131 (2009) 3985-3990.

[45]K. A. Malingera, A. Maguerb, A.Thorelb, A. Gaunanda, J. Hochepied. Crystallization of anatase nanoparticles from amorphous precipitate by a continuous hydrothermal process. Chemical Engineering Journal 174 (2011) 445-451.

[46] F. Zhang, H. Li. Hydrothermal synthesis of TiO_2 nanofibres. Materials Science and Engineering C 27 (2007) 80–82.

[47] L. Dong, K. Cheng, W. Weng, C. Song, P. Du, G. Shen, G. Han. Hydrothermal growth of rutile TiO_2 nanorod films on titanium substrates. Thin Solid Films 519 (2011) 4634-4640.

[48] G. Cao, Y. Wang. Nanostructures and nanomaterials: synthesis, properties, and applications. Imperial College Press (2004).

[49] J. I. Pankove. Optical Processes in Semiconductors. Courier Dover Publications (1971).

[50] E. Mccafferty. Introduction to corrosion science. Springer (2010).

[51] V. I. Nefedov. X-ray photoelectron spectroscopy of solid surfaces. VSP (1988).

Chapter 4 Pure and doped TiO_2 thin films by PLD

4.1 Pure TiO_2 thin films synthesised by PLD

In PLD, various growth parameters have influence on properties of final film, including laser parameters such as wavelength, repetition rate, laser fluence, and preparation conditions such as target to substrate distance, substrate temperature, substrate surface and background pressure [1,2,3,4]. In terms of ions doped TiO_2 thin films, the important parameters are supposed to be background pressure and post annealing manner, thus the effects of oxygen partial pressure and post annealing on the properties of pure TiO_2 thin film were studied.

4.1.1 Experimental details

Pure TiO_2 thin films were grown on quartz substrates at room temperature by PLD using a KrF laser operated at a wavelength of 248 nm. A dense ceramic target was made from high-purity TiO_2 powder by pressing the powder into a pellet and then sintering it at 1200^{o}C in atmosphere. Quartz slices were chosen as substrates because of their high transparency in near-UV and visible light regions and their high thermal stability. The substrates were cleaned by acetone, ethanol and distilled water in ultrasonic bath before each deposition. The spacing between the parallel arranged target and substrate was 5 cm. The base pressure of the vacuum chamber was evacuated down to 3×10^{-4} Pa and then oxygen was introduced into to a specific oxygen partial pressure in range of 0 to 2 Pa. In order to avoid contamination on the target surface, the target was pre-irradiated by laser for 10-minutes with a shutter located between the target and substrate. The deposition duration was fixed at 1-hour with laser energy of 200-250 mJ per pulse and frequency of 5 Hz. Also, both the target and the substrate were rotated with a rate of 6 rpm during the deposition process to enhance thin firm uniformity. After deposition, samples were post annealed in different ways, including annealing at 1000^{o}C in ambient atmosphere or with oxygen introduction for 10-minutes by a rapid thermal furnace and annealing at 700^{o}C in PLD vacuum chamber for 30-minutes. The influences of oxygen partial

pressure on crystallinity, optical absorption and surface morphology properties were studied.

4.1.2 Results and discussion

4.1.2.1 Microstructures

The crystal properties of fabricated TiO_2 target and thin films were detected by XRD as shown in Fig. 4.1.1, with all peaks identified by comparing them with JCPDS cards for powered materials. Apparently, TiO_2 target well crystallized into rutile phase as identified in Fig. 4.1.1(a). Fig. 4.1.1(b) shows the indexed XRD patterns of pure TiO_2 thin films as-deposited and post sintered at 1000^{o}C in atmosphere. As-deposited thin film under 0 Pa showed no diffraction peak in the XRD pattern though the target had well crystallization of rutile phase. TiO_2 thin films deposited at oxygen pressure of 1 Pa crystallized into the anatase phase after annealing, with the XRD pattern showing only one characteristic peak corresponding to the (101) plane. While TiO_2 thin films deposited at oxygen pressure of 0 Pa crystallized into the rutile phase after annealing, with only one characteristic peak corresponding to the (110) plane. Apparently, crystal properties of the samples presented strong dependence on the oxygen pressure here.

The non-crystalline structure of the as-deposited films was attributable to high cooling rates involved in such a physical vapour deposition process. The fact that anatase and rutile peaks were detected in the samples annealed at high temperatures offers confirmation that the featureless diffraction pattern from the as-deposited films was not due to the limitation of sample quantity. It has been generally recognized that the kinetic process of phase formation upon annealing is temperature and time reliable [5] and the formation of crystal is mainly dominated by particle size, defects concentration [6, 7]. Crystallization of the amorphous pure TiO_2 undergoes anatase to rutile transition, at least at intermediate temperatures [8], so there is shorter time for the lastly formed rutile crystals to grow. Although 1000^{o}C was higher than the reported anatase into rutile transformation temperatures from 600 to 700^{o}C, the 10-minutes annealing in this work was inadequate to complete the phase transition and the thin film was still anatase for the one deposited at 1 Pa. When deposited in vacuum chamber without oxygen compensation (0 Pa), TiO_2 thin film conceivably

possessed plenty of deficiencies to facilitate favourable ionic rearrangement and structure reorganization for the formation of rutile phase during annealing process [9]. The presence of rutile phase in the samples deposited 0 Pa was suggestive that oxygen deficiencies facilitated the phase transformation, so that crystallization of the rutile crystals occurred in 10-minutes.

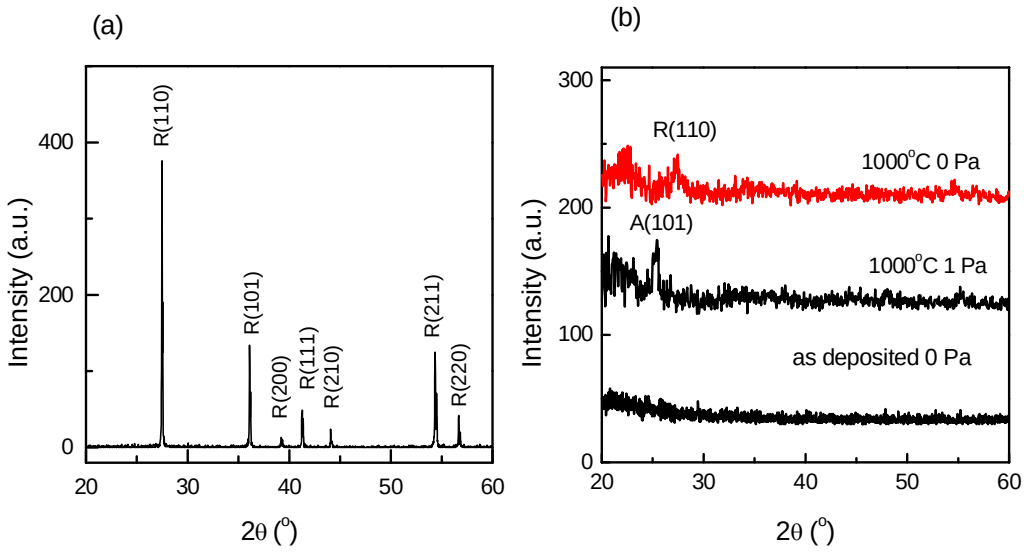

Figure 4.1.1 XRD patterns of synthesized (a) TiO_2 target; (b) TiO_2 thin films.

The effect of oxygen partial pressure on surface morphologies were observed under SEM. Fig. 4.1.2 presents two typical SEM pictures of sintered thin films grown at 0 Pa and 1 Pa. One can see that the TiO_2 film deposited at 1 Pa demonstrated a compact and smooth surface, while the film deposited at 0 Pa showed a slight coarser surface with appearance of cracks. Generally, high oxygen pressure favours the formation of condense and smooth layer during deposition, since the ablated particles with smaller size after collision with oxygen is advantageous to a homogeneously distribution of nano-structured layer [10, 11]. On the other hand, this is also mainly caused by the anatase to rutile phase transformation accompanied with growing up of crystals, leading to surface coarsening process. Such anatase to rutile transition has been widely reported to occur in pure TiO_2 films [12,13]. The cracks were conceivably contributed to lateral tension or stress along with crystal growing up during annealing process.

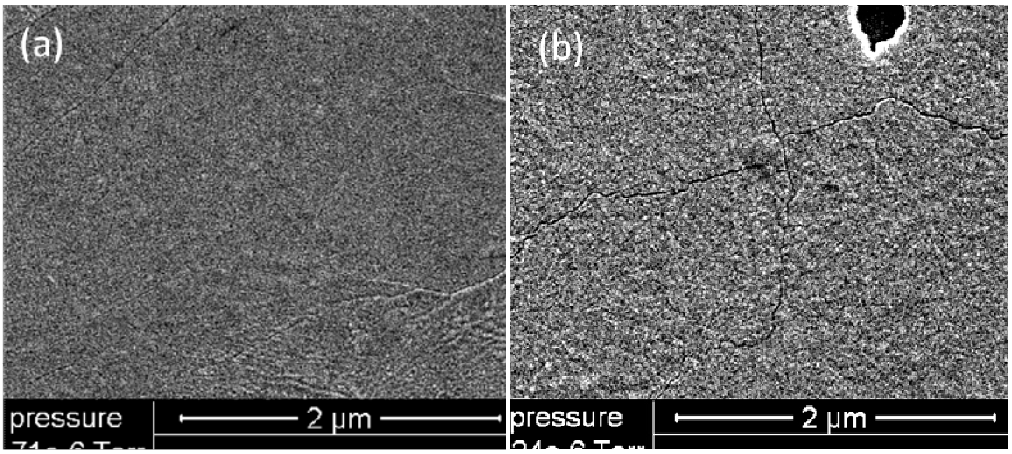

Figure 4.1.2 Surface SEM images of TiO_2 thin films deposited at (a) 1 Pa; (b) 0 Pa.

4.1.2.2 Optical absorption properties

Fig. 4.1.3 shows the optical absorption spectra of these prepared thin films deposited under different oxygen partial pressure from 0 Pa to 2 Pa, where vertical coordinate is the measured value of optical absorbance regardless thickness of thin film. As it can be seen, each absorption spectrum of TiO_2 film demonstrated a typical sharp drop at around 350 nm, resulting from intrinsic electron excitation from valence band to conduction band of semiconductor. The value of absorption edges around 350 nm were a bit smaller than 387 nm of bulk material, revealing a widening of band gaps which was mainly attributed to the low crystallization degree of thin films because of rapid thermal treatment, or the quantum effect of nanomaterial [14, 15].

Obviously, reducing oxygen partial pressure resulted in a slight red shift in the absorption curves, and a board secondary absorption shoulder located during 350-400 nm of the film deposited at 0 Pa in comparison with others. The XRD results had demonstrated that lower oxygen pressure was beneficial to the formation of stable rutile phase with narrower band gap. Therefore, the slight red shift is reasonable due to the different degree of crystallization and the band gap discrepancy between anatase and rutile. We know from density of states that the top valence band of TiO_2 is composed mainly of O 2P states while the bottom conduction band predominately consists of Ti 3d states [16]. Lacking of oxygen was supposed to bring in plenty of oxygen vacancies into TiO_2 matrix and the annealing in natural

atmosphere at high temperature could hardly eliminate all oxygen vacancies [17]. The oxygen vacancies consequently introduced intermediate energy bands into forbidden gap [18], serving as step stones to relay valence electrons into conduction band and resulting in a secondary absorption shoulder in optical absorption spectrum.

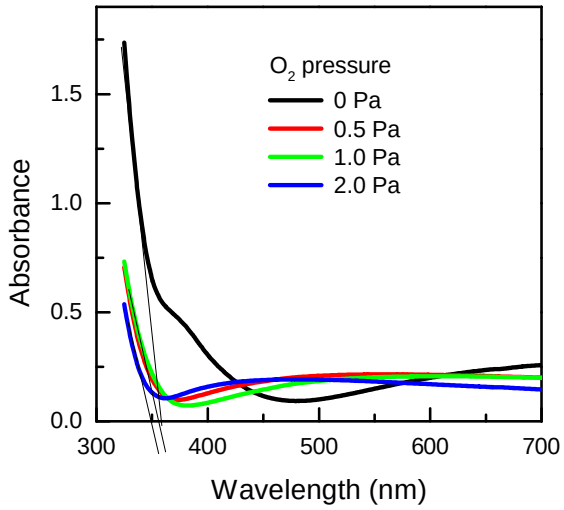

Figure 4.1.3 Optical absorption spectra of TiO_2 thin films deposited at different oxygen partial pressure.

Fig 4.1.4 depicts the optical absorption spectra of thin films deposited under 0 Pa but annealed in different ways. Comparing two spectra of thin films annealed at 1000°C, we find the secondary board absorption shoulder during 350-450 nm disappeared after annealed in oxygen atmosphere, while the intrinsic absorption edges were nearly the same in both spectra. This means annealing TiO_2 thin films in oxygen rich atmosphere helped to fill oxygen vacancies. In addition, the intrinsic absorption edge of thin film annealed at 700°C was smaller that that of thin films annealed at 1000°C, conceivably attributed to lower degree of crystallinity. On the other hand, a boarder secondary absorption shoulder located during 350-480 nm with respect to vacuum annealing, being likely attributed to more intermediate energy bands introduced by oxygen defects resulted from a great deal of oxygen vacancies in TiO_2 thin film when annealed in vacuum.

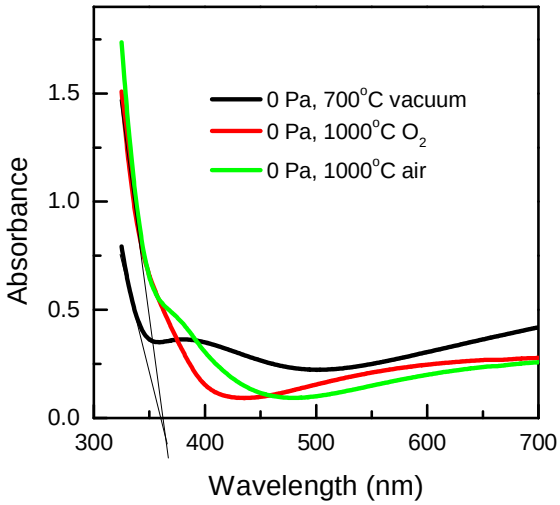

Figure 4.1.4 Optical absorption spectra of TiO_2 thin films annealed at 700°C in vacuum and at 1000°C in atmosphere or in oxygen.

4.1.3 Conclusions

Pure TiO_2 thin films under different oxygen partial pressure were successfully fabricated by using PLD method. It was demonstrated that lower oxygen partial pressure during deposition were responsible for facilitating phase transformation of anatase to rutile in post annealing process. Annealing manners also played important roles on the properties of TiO_2 thin film, in which lacking of oxygen during annealing gave rise to plenty of oxygen deficiency in thin film while introduction of oxygen during annealing compensated oxygen deficiency, leading to distinctive optical absorption properties.

4.2 Transition metal ions doped TiO_2 thin films by PLD

4.2.1 Fe doped TiO_2 thin films

Fe is a rather interesting candidate to enhance the visible absorption of TiO_2 for unique half field 3d electron configuration as transitional metal. Although theoretical calculation has definitely shown that the band gap could be effectively narrowed by Fe doping through the jointed effect of effect on band gap reduction and introduction of intermediate energy levels within forbidden gap of TiO_2 [19], there still is a debate regarding the effect of Fe doping on the reactivity of TiO_2 according to experimental results, as fabrication methods play critical roles on the chemical state of dopant which is central to actual doping effect. It has been reported that a proper concentration of Fe^{3+} is not only beneficial to electron-hole separation, but also narrows the band gap of TiO_2 to permit visible light excitation [20], whereas other works demonstrated an opposite trend [21]. In this work, a series of TiO_2 thin films with various Fe doping levels were prepared by PLD method that had seldom been studied.

4.2.1.1 Experimental details

Fe doped TiO_2 thin films were fabricated in the same way as preparation of pure TiO_2 thin films. The targets for doped materials were made by adding 1% - 7% F_2O_3 in weight into the pure TiO_2 powders before pressing powders into pellets. The deposition duration was fixed at 1-hour with laser energy of 250 mJ per pulse and frequency of 5 Hz. Considering the influence of oxygen partial pressure on the properties of pure TiO_2 thin films, the oxygen partial pressure was chosen as 0 Pa for the purpose of effective doping. Substrate temperature was set at room temperature or 700^oC. After deposition, thin films were post annealed at temperature in range from 1000^oC to 1100^oC in ambient atmosphere since a certain extent of oxygen vacancies are expected to be beneficial for ions doping. A tube furnace was used to post anneal samples at different temperatures instead of rapid thermal treatment.

Apart from these, other parameters without special mention remained the same as of pure TiO_2 as described previously.

4.2.1.2 Results and discussion

Fig. 4.2.1 shows the optical absorption spectra, plotted as the function of absorbance versus wavelength, of Fe doped TiO_2 thin films annealed at 1050^{o}C with different doping levels. As it can be seen, each sample possessed distinct value of absorbance in UV region, though the absorption coefficient α in UV region was hardly influenced by dopants, indicating each sample had different thickness d which can be calculated from the following equation:

$$d = A/\alpha \qquad (4.1)$$

However, the absorption edge is not dependant on the intensity of absorbance, and can be clearly deduced by extrapolating the liner drop of optical absorption spectra to horizontal coordinate. The absorption edge was firstly red shifted as the concentration of Fe increases, but then fall back when doping level was over 2%, being different from theoretical predictions and other experimental reports [22, 23] that band gap narrows as the doping level increases. The conceivable reasons responsible for this phenomenon is that impurities would aggregate together as metal oxide when the concentration of Fe is too high to excess its solubility in solid host, leading to extremely low doping level in TiO_2 matrix. The most suitable concentration was 2% that amazingly shifted the absorption edge of TiO_2 to 445 nm in visible light region, meaning the TiO_2 can be effectively excited by part of visible light with wavelength shorter than 445 nm. According to theoretical calculation [24], the red shift associated with Fe doping are largely ascribed to introduction of intermediate energy levels in forbidden gap caused by Fe 3d and O 2p hybridization, leading to relative charge transfer between intermediate energy levels and valence or conduction band.

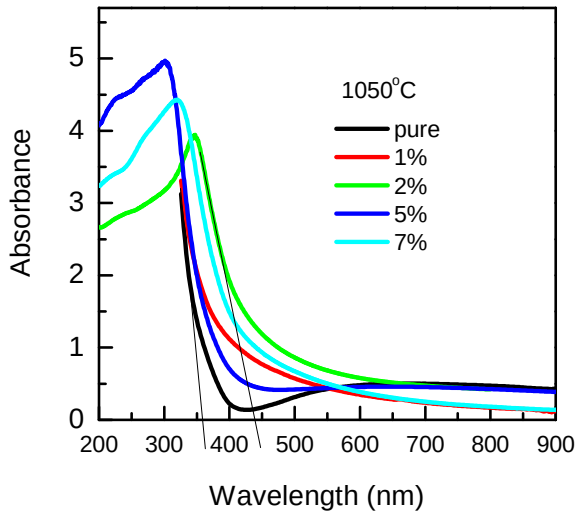

Figure 4.2.1 Optical absorption spectra of Fe-TiO_2 films annealed at 1050°C.

In addition to doping level, post annealing temperature after deposition was also supposed to be an important parameter affecting doping effect. To reveal the annealing effect, 2% Fe doped sample was selected to be annealed at different temperature in range from 1000°C to 1100°C. It is apparent, in Fig. 4.2.2, that elevating annealing temperature gave rise to bigger red shift of absorption edge, to 550 nm after 1100°C annealing in spite of the same doping concentration. As mentioned previously, crystallinity degree and states of dopants are central to band gap narrowing, so the discrepancy of red shift here were conceivably attributed to two feasible factors, which were higher level of Fe as substantial ions in TiO_2 lattice and better crystallinity degree caused by higher annealing temperature.

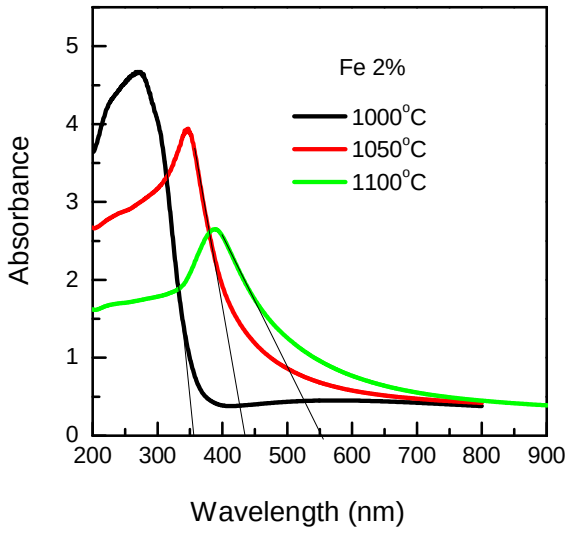

Figure 4.2.2 Optical absorption spectra of 2% Fe doped sample under different annealing temperature.

Thermal treating samples at high temperature over 1000°C are likely to cause extensive oxygen release accompanied with the formation of oxygen vacancies. High level of defects is fatal to PV cells by causing electrical leakage and carrier recombination during current transportation, making it important to lower the fabrication temperature. Thermal treating samples at 700°C during deposition were expected to be beneficial to lowering crystal growth temperature. Fig. 4.2.3(a) shows XRD pattern of one typical thin film with 2% Fe dopants deposited at 700°C. Discernibly, the film was still amorphous as no diffraction peak appeared, even though the substrate temperature was higher than phase transition temperature from anatase phase to rutile phase of bulk material. During PLD process the material of target was vaporized in form of a plume containing extraordinary small spices and then deposited onto substrate as thin film. This was confirmed by the corresponding SEM image in Fig. 4.2.3(b), in which thin film was composed of extremely fine and uniform nanoparticles. In consequence, small size effect raised the crystallization temperature resulting in amorphous phase under specific temperature.

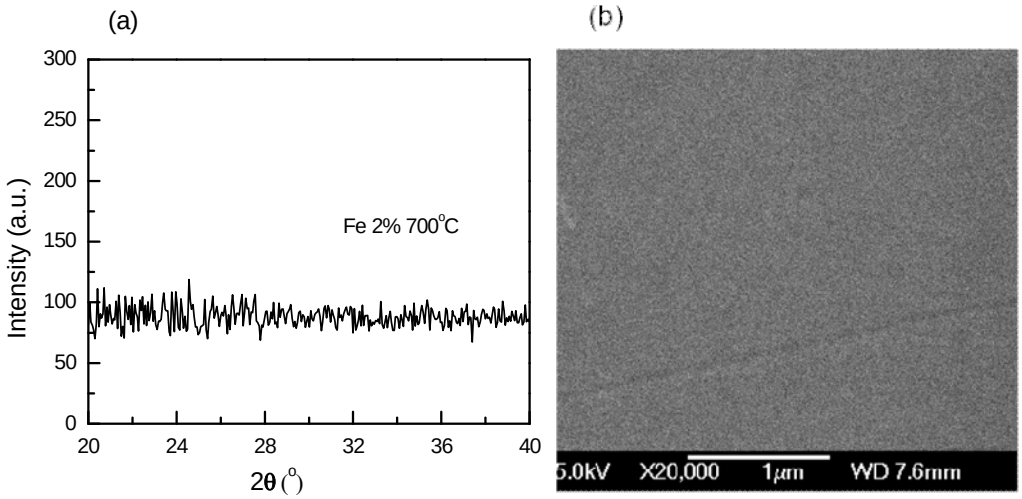

Figure 4.2.3 (a) XRD pattern; (b) SEM image of 2% Fe-TiO_2 thin film deposited at 700°C.

Fig. 4.2.4(a) shows the optical absorption spectra of Fe-TiO_2 deposited at 700°C, in which all samples have same absorption edge around 350 nm regardless the concentration of Fe. This is not hard to understand since all samples were amorphous and the atomic disorder thereby restricted doping effect. After post annealing at 1100°C, the 2% Fe-TiO_2 thin film deposited at 700°C had same absorption edge with the one deposited at room temperature as presented in Fig. 4.2.4(b), implying that the crystallization of TiO_2 thin film gave rise to the doping effect.

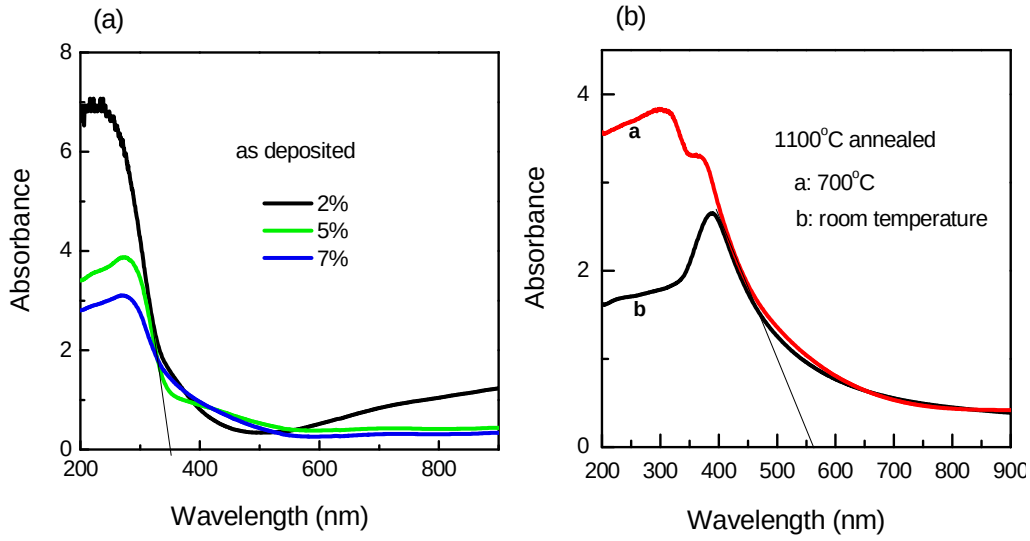

Figure 4.2.4 Optical absorption spectra of (a) Fe-TiO_2 films as-deposited at 700°C with different doping concentration; (b) 2% Fe-TiO_2 films post annealed at 1100°C with different deposition temperature (room temperature and 700°C).

4.2.1.3 Conclusions

Fe doped TiO_2 thin films with different doping levels were successfully fabricated. Substrate temperature of 700°C during deposition process showed no difference with respect to microstructure and optical absorption properties of Fe doped TiO_2 thin films compared with room temperature. Higher post annealing temperature gave rise to bigger red shift of absorption edge. It was shown that the optimized Fe doping concentration for band gap narrowing was 2%, with absorption edge red shifted to 550 nm, under the preparation parameters used in this work.

4.2.2 Mn doped TiO_2 thin films

Theoretical calculation has suggested that substitutional manganese doping can significant reduce band gap of TiO_2, with redshift significant enhanced by means of increasing Mn doping level, through reducing its intrinsic band gap together with introducing several intermediate energy levels originated from Mn 3d electrons [25].

In this work, TiO_2 thin films with different content of Mn doping were fabricated on the basis of theoretical calculation, with optical properties being the focus of interest.

4.2.2.1 Experimental details

Mn doped TiO_2 thin films were fabricated in the same way as preparation of pure TiO_2 thin films, by adding MnO_2 into TiO_2 powder before pressing the powders into targets, with weight concentration of MnO_2 in range of 1% to 5%. The deposition duration was fixed at 1-hour with laser energy of 250-300 mJ per pulse. All doped films were deposited under vacuum at room temperature and subsequently annealed in ambient atmosphere at different temperature for 10-minutes.

4.2.2.2 Results and discussion

The crystal structures of 1% Mn doped TiO_2 thin films, as well as the relative pure one, were analyzed by XRD as shown in Fig. 4.2.5(a), with peaks identified by comparing them with JCPDS cards. Unlike pure TiO_2 thin film that merely one dominant peak existed in the XRD pattern corresponding to the lattice plane of the lowest surface energy, other two peaks belonging to R(101) and R (211) appeared in Mn-TiO_2 thin films. This phenomenon implies that Mn doped TiO_2 thin films completely crystallized into rutile phase with random direction, agreeing well with powder diffraction pattern. The formation of rutile phase upon heating is generally considered as nucleation growth when the rutile nuclei are formed within the anatase phase, which is strongly temperature reliable. Even though difference was hardly seen from XRD patterns of thin films annealed at distinct temperature, the one annealed at higher temperature was expected to have better crystallization degree. Furthermore, on account of the sensitivity of XRD technology, no trace of manganese metal and oxides was detected from the doped samples.

Surface morphology of 1% Mn-TiO_2 thin film annealed at 1000^oC was taken by SEM as illustrated in Fig. 4.2.5(b), in which thin film was composed of extremely fine and uniform nanoparticles with big cracks existing. These cracks were conceivably contributed to lateral tension or stress along with crystal growing up during high temperature annealing process.

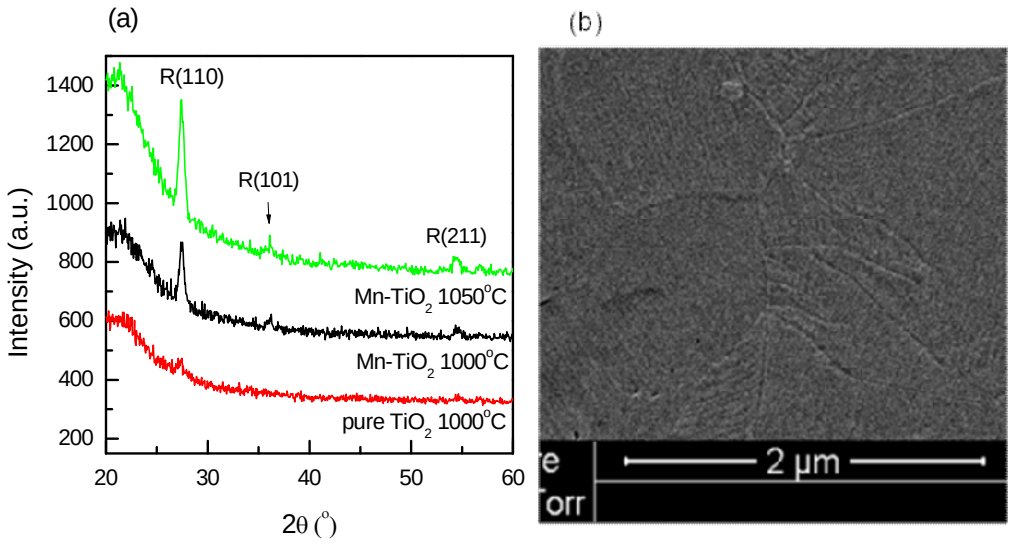

Figure 4.2.5 (a) XRD of Mn-TiO_2 and pure TiO_2 thin film annealed at different temperature; (b) SEM picture of 1% Mn-TiO_2 thin film annealed at 1000°C.

Fig. 4.2.6(a) shows the optical absorption spectra of Mn-TiO_2 thin films annealed at 1000°C. The primary absorptions edge for the thin films all located around 400 nm, being in good agreement with the absorption edge of pure rutile. Through comparing absorption edges of Mn-TiO_2 thin films with that of a pure one, we can see the absorption edge was marginally and randomly changed with different Mn concentration, being not in agreement with the theoretical prediction that band gap of TiO_2 monotonously narrows as the increasing of Mn doping level. Considering that higher doping concentration was supposed to have stronger influence on band gap narrowing of rutile phase, the uniformity of absorption edge was mainly attributed to the similar doping level. It is therefore supposed that only few partial Mn incorporated into TiO_2 lattice as substantial ions under this preparation condition.

Taking 1% Mn-TiO_2 thin film for example as revealed in Fig. 4.2.6(b), dramatic enhancement of red shift occurred depending on annealing temperature. After being annealed at 1050°C, the edge was shifted up to about 830 nm, in the infrared region. For the 1100°C annealed thin film, the absorption edge was extended amazingly beyond visible part into infrared region with absorption peak located at around 600

nm and primary edge shifted up to about 1200 nm, making Mn-TiO_2 extremely sensitive to the sun light.

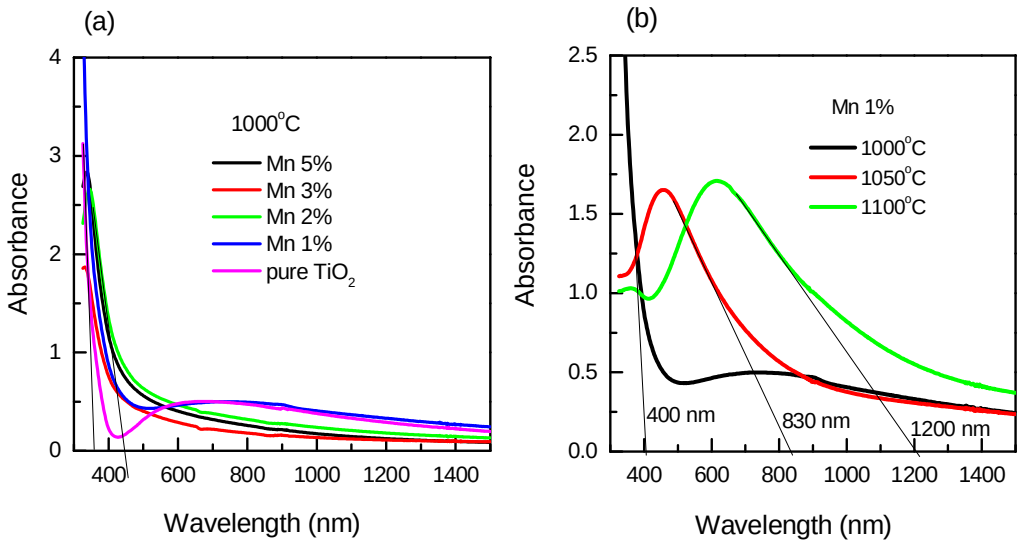

Figure 4.2.6 Optical absorption spectra of (a) Mn-TiO_2 films annealed at 1000°C; (b) Mn 1%-TiO_2 films annealed at different temperature.

The band gap of semiconductor can be obtained from its optical absorption spectrum, as the dependence of α on incident photon energy $h\nu$ is given by the expression [26]:

$$\alpha \propto \alpha_0 (h\nu - E_g)^n \qquad (4.1)$$

where n is a value dependent on the type of predominant electron transition (equals ½ for direct band gap and 2 for indirect band gap).

For rutile phase with direct band gap, the equation (4.1) can be written as

$$A = \alpha d \propto \alpha_0 d (h\nu - E_g)^{1/2} \qquad (4.2)$$

A is the absorbance, $\alpha_0 d$ is a constant and d is the thickness of sample.

Herein, Mn doped TiO_2 thin films had rutile phase with direct band gap when annealing temperature was higher than 1000°C. Therefore, the band gaps of the typical 1% doped TiO_2 thin films were estimated by extrapolating the linear part of the A^2 versus photon energy curve to the energy axis, as seen from Fig 4.2.7. The

band gap was gigantic narrowed from 3.2 eV to 1.2 eV as the annealing temperature increased form 1000°C to 1100°C, signifying that high temperature annealing was central to the substantial state of Mn dopants. Being in good agreement with theoretical prediction, this gigantic narrowing behaviour makes TiO_2 as a promising material to practical application under natural light for extensive absorption ability in visible and infrared region, making the energy gap continuously tuneable through replacing Ti lattice sites by increased Mn content.

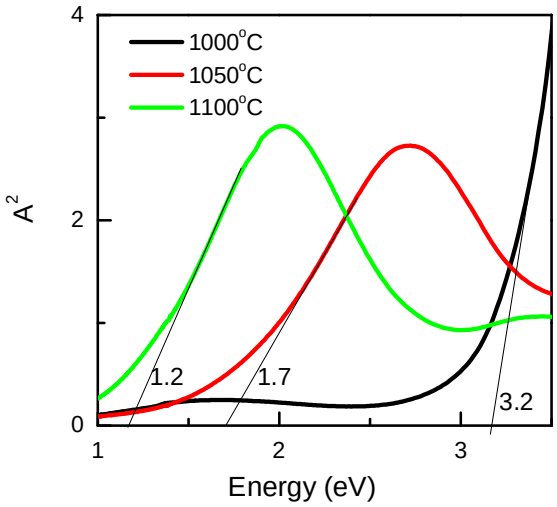

Figure 4.2.7 A^2 versus photo energy plots of 1% Mn-TiO_2 annealed at 1000°C, 1050°C and 1100°C.

4.2.2.3 Conclusions

Mn doping gigantically narrowed the band gap TiO_2 thin films fabricated by using PLD method. 1% Mn doping significantly shifted the absorption edge from 360 nm to 1200 nm after post annealed at 1100°C, corresponding to the band gap of 1.2 eV, making TiO_2 extremely sensible to visible light even infra red region.

4.3 Rare earth metal ions doped TiO_2 thin films by PLD

Rare earth metal has also been paid extensively attention for their ability to introduce various electron states into TiO_2 band gap to change its optical properties by 4f-orbital electrons [27,28]. In this part, optical properties of rare earth ions Gd, Sm and Er doped TiO_2 thin films fabricated by PLD were studied.

4.3.1 Experimental details

Gd, Sm and Er separately doped TiO_2 thin films were fabricated in the same way as preparation of pure TiO_2 thin films, by adding Gd_2O_3, Sm_2O_3 or Er_2O_3 into TiO_2 powders before pressed into targets, with different weight concentration. The deposition duration was fixed at 1-hour with laser energy of 300 mJ per pulse. All doped films were deposited under vacuum atmosphere at room temperature and subsequently annealed in ambient atmosphere at different temperature for 10-minutes.

4.3.2 Results and discussion

Optical absorption patterns of thin films post annealed under 1000^{o}C with different Gd concentration are described in Fig. 4.3.1(a). The absorption edges were gradually blue shifted to ultraviolet region referring to pure one, even though theoretical calculation has shown incorporation of Gd into TiO_2 crystal lattice introduced many Gd^{3+} 4f states in the forbidden gap. This phenomenon obviously implies Gd atoms did not take substantial sites of Ti atoms, since aggregation of rare earth oxide on TiO_2 surface can restrain its crystal growth and transformation of anatase to rutile phase leading to a blue shift of absorption edge [29]. It was mentioned in Mn-TiO_2 thin films, higher post annealing temperature was proved to be helpful for doping effect. Even though the optical absorption spectra also showed the same trend as the increasing of annealing temperature, the absorption edge of 0.5% Gd-TiO_2 thin film was still below 400 nm when the annealing temperature was as high as 1100^{o}C. Hua prepared rare earth doped TiO_2 powders by various methods, XRD results show that lattice parameters of TiO_2 does not change because of their big ionic radius referring to Ti^{4+} [30], confirming that it is hard to insert Gd into TiO_2 lattice because of its big ionic radius of 0.938 Å.

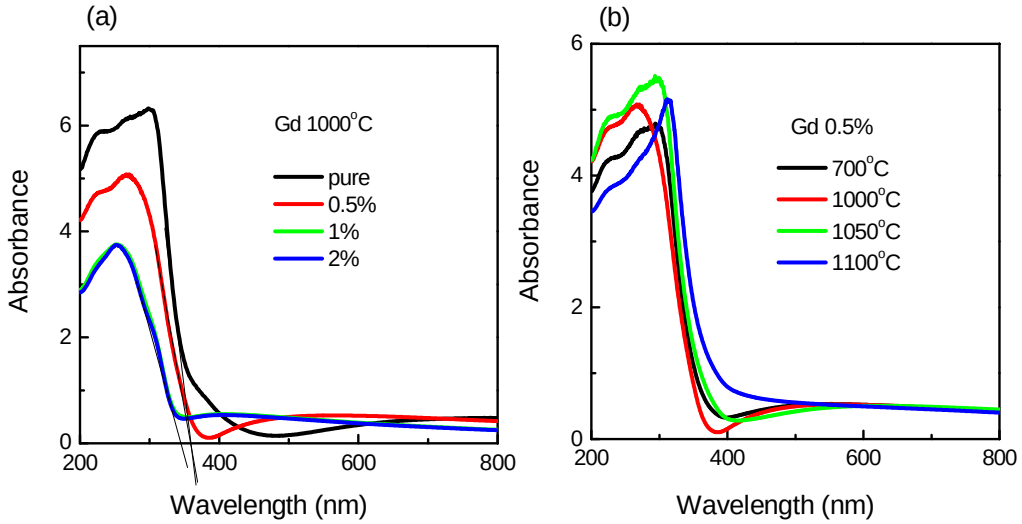

Figure 4.3.1 Optical absorption spectra of (a) Gd-TiO_2 films annealed at 1000°C; (b) 5% Gd-TiO_2 films annealed at different temperature.

The post annealing temperature for Sm and Er doping was 1100°C with the purpose of providing effective doping effect. Although blue shift of absorption edge was effectively restrained, theoretical expectations were still not realized on account of their big ionic sizes, Sm^{3+} (0.964 Å) and Er^{3+} (0.881 Å), making them was very hard to be inserted into the TiO_2 crystal lattice. So it is likely deduced that Sm and Er dopants segregated as metal oxides on the surface of TiO_2 crystal after annealing, hardly contributing to band gap narrowing.

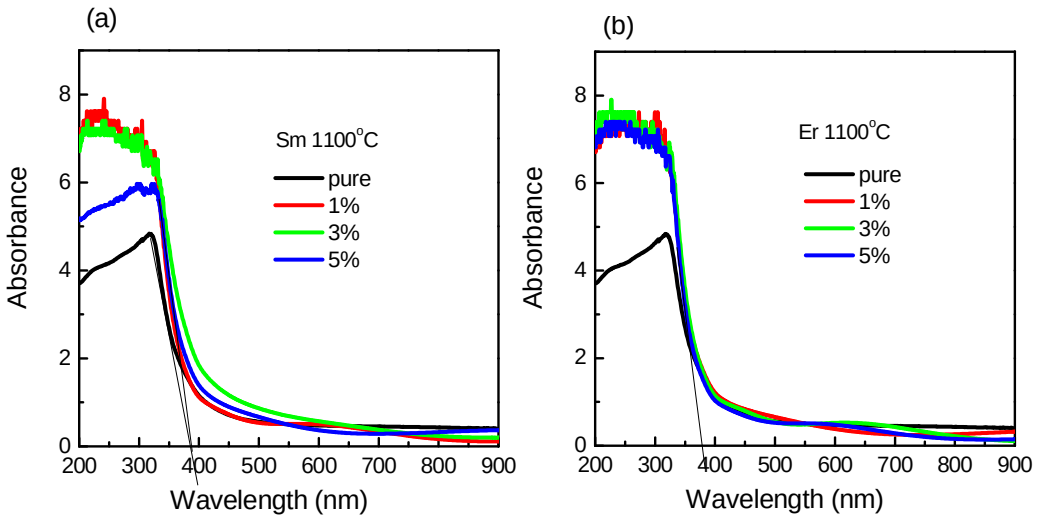

Figure 4.3.2 Optical absorption spectra of Sm-TiO_2 films annealed at 1100°C; (b) Er-TiO_2 films annealed at 1100°C.

4.3.3 Conclusions

TiO_2 thin films doped by rare earth metal Gd, Sm and Er were prepared by PLD method respectively. No obvious red shift can be seen from the optical absorption spectra in spite the annealing temperature was as high as 1100°C, suggesting it was hard to replace Ti atoms in TiO_2 matrix by rare earth atoms via this method.

4.4 V-Ga co-doped TiO_2 thin films by PLD

4.4.1 Ga doped TiO_2 thin films

Theoretical modelling shows substitution of Ti by trivalent elements will induce a p-type TiO_2 via introducing acceptor states located above valence band of TiO_2 from hybridization between X p and O 2p orbits, being certainly responsible for the band gap narrowing. Among all trivalent elements, Ga is the most promising ion that can insert into TiO_2 lattice easily by substitution because the ionic radius of Ga^{3+} (0.62 Å) is comparable to Ti^{4+} (0.605 Å). The lattice distortion caused by doping could be efficient inhibited because of similar ionic radius, which thereby retains intrinsic integrality of TiO_2 crystal lattice and decreases defects introduced by impurity.

4.4.1.1 Methods

Ga doped TiO_2 thin films were fabricated by employing the same parameters used for pure TiO_2 by adding Ga_2O_3 into TiO_2 powder before pressed into targets, with weight concentration of Ga_2O_3 in range of 1% to 15%. The oxygen partial pressure was set as 1 Pa during PLD process and a tube furnace was used to post anneal samples at different temperatures.

Theoretical calculation of electronic structures of the material phases was carried out on the basis of the density functional theory (DFT) with Hubbard U correction to account for the non-local effect owing to Coulomb interaction in the correlated oxide structures (DFT+U). The calculations were performed using the Vienna *Ab initio* Simulation Package (VASP) [31,32]. Here, the projector augmented wave (PAW) pseudopotentials [33,34] and the generalized gradient approximation (GGA) within the PAW-PBE framework [35] were used to expressing the exchange correlation. The energy cutoff for the plane wave basis set was 400 eV, and the Brillouin zones were sampled using the Monkhorst-Pack scheme [36]. Before the calculation of electronic structures, the model supercells were geometrically relaxed until the total forces on each ion were converged to 0.01 eV/Å.

4.4.1.2 Results and discussion

A. Microstructures and optical properties

From the optical absorption spectra we can see that all as-deposited samples had exactly same absorption edge located at 350 nm as described in Fig. 4.4.1(a). The non-crystalline structure of the as-deposited films, attributable to high cooling rates involved in such a physical vapour deposition process as mentioned before, undoubtedly restrained doping effect as well as band gap changing.

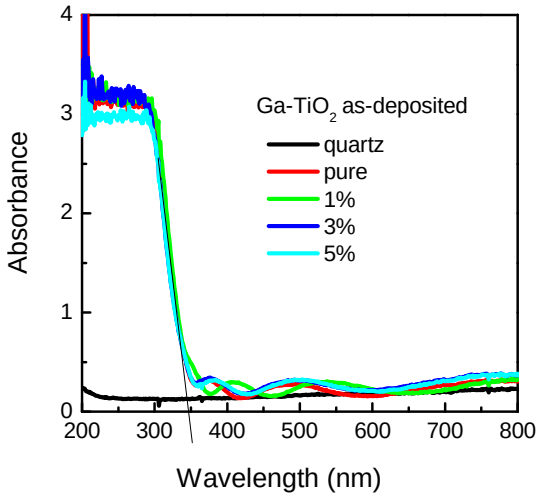

Figure 4.4.1 Optical absorption spectra of as-deposited Ga-TiO_2 thin films.

After annealing at 1000°C, the optical absorption spectra of thin films are illustrated in Fig. 4.4.2(a). It is interesting that the intrinsic absorption edges of thin films were firstly shifted to longer wavelength region when doping concentration was lower than 5%, and then shifted back into UV region when the concentration was over 10%, implying the hybridization of intermediate levels with intrinsic energy bands happens and thereby altered the band structure of TiO_2. Furthermore, 10% and 15% doped TiO_2 thin films had same absorption edge, meaning the actual doping concentrations in TiO_2 of two samples were the same while the additive dopants probably aggregated as gallium oxide on the surface. Apart from these, a secondary shoulder amazingly appeared when the doping concentration was 1%, in addition to the intrinsic absorption edge at shorter wavelength attributable to intrinsic excitation of electrons from the valence band to the conduction band, extending absorption spectrum well into visible light region with absorption edge located at around 480 nm. This obviously suggests modified energetic properties of 1% Gd-TiO_2 via forming impurity energy levels in the forbidden gap of TiO_2. It is therefore deduced that appropriate low doping with Ga could effectively narrow the band gap of TiO_2 and thus red shift its absorption edge to a longer wavelength range. This effective doping in TiO_2 matrix happened during post annealing process at high temperature as the crystallization of TiO_2.

The surface morphology of the typical 1% Ga-TiO_2 thin film was measured by SEM, as shown in Fig. 4.4.2(b). In comparison with pure TiO_2 surface, as shown previously, the doped thin film was made up of dispersive particles with hundreds nanometres in diameter, suggesting this thin film was well crystallized. Being conceivably attributed to Ga doping, the growing up of grains in Ga-TiO_2 thin film led to extremely coarse surface, different from the dense thin film observed in pure TiO_2 thin film. It is worth stressing that this kind of coarse surface would have a bigger specific surface area, making Ga-TiO_2 more efficient as photocatalyst.

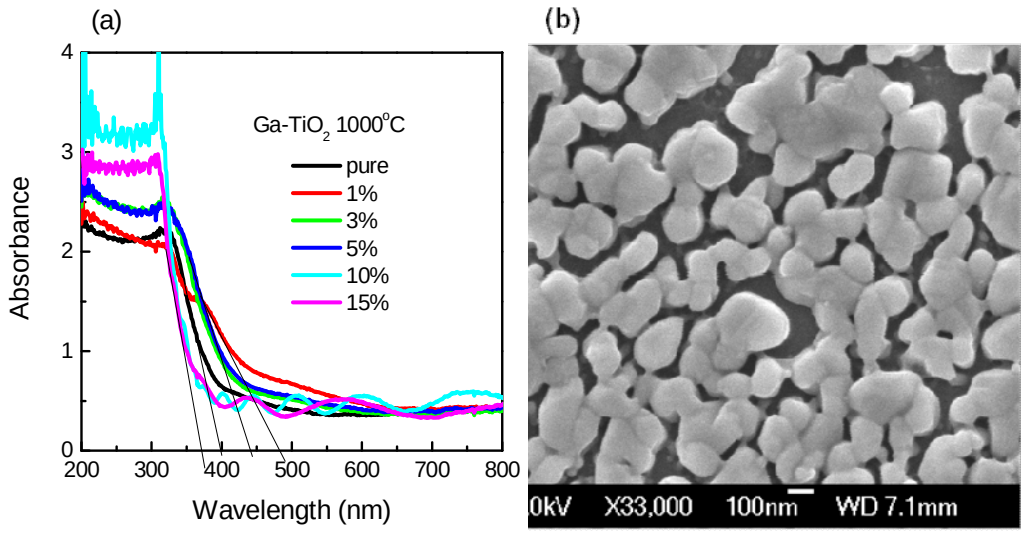

Figure 4.4.2 (a) Optical absorption spectra of Ga doped TiO_2 thin films annealed at 1000°C; (b) SEM of 1% Ga-TiO_2 annealed at 1000°C.

Optical absorption spectra of 1% Ga-TiO_2 thin films annealed at different temperatures are shown in Fig. 4.4.3, where intrinsic band gap was slightly shifted towards longer wavelength when the annealing temperature was elevated up to 900°C. This slight difference was largely due to the improvement of crystallization degree and growing up of grains along with the increased annealing temperature, since the most stable rutile phase has a relative smaller band gap compared with anatase phase and, the widen of band gap caused by small size effect was effectively restrained. The secondary absorption edge only happened when annealing

temperature was as high as 1000°C, it is therefore deduced that band gap narrowing effect of TiO_2 upon Ga doping happened following crystallization process.

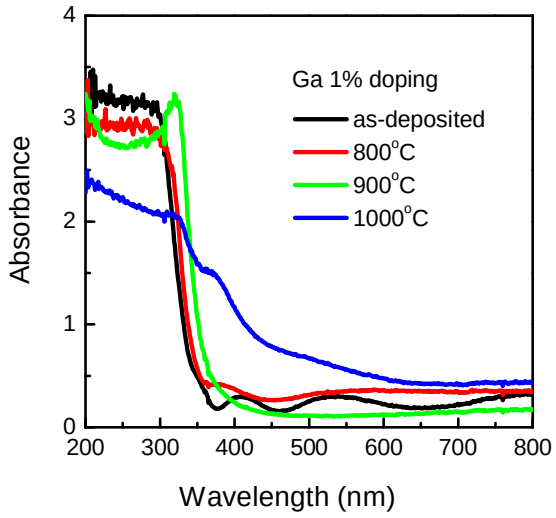

Figure 4.4.3 Optical absorption of 1% Ga-TiO_2 under different annealing temperatures.

B. Theoretical modelling

The theoretical approach in the framework of DFT follows the methodology which has been established recently through extensive testing on modelling parameters, superlattice sizes for the doped structures and the treatment of possible non-local contribution to the exchange-correlation functional by the Hubbard U correction. For the DFT+U calculations in this work, the effective Hubbard U value of 7 eV was applied to d electrons of the transition metals.

The level of doping of interest to this work can be treated by introducing doping atoms in a 2×2×2 supercell of rutile TiO_2. We investigated the effect by replacing a Ti atom by a Ga atom in the supercell, giving a doping concentration of 6.25%. The calculated band structure and density of states (DOS) are shown in Figs. 4.4.4 (a) and (b), where the calculated band gap (2.71eV) of virgin TiO_2 is marked by green vertical bar for comparison. Comparing to the band structure of pure TiO_2, Ga doping raises the valence band maximum (VBM) with respect to the Fermi level thus turning the intrinsic virgin phase into a p-type semiconductor. The band gap of Ga-doped phase is 2.41 eV, which is 0.3 eV or about 11% narrower than that of pure

TiO_2. The experimentally observed red shift of absorption edge is thus attributed to doping of Ga.

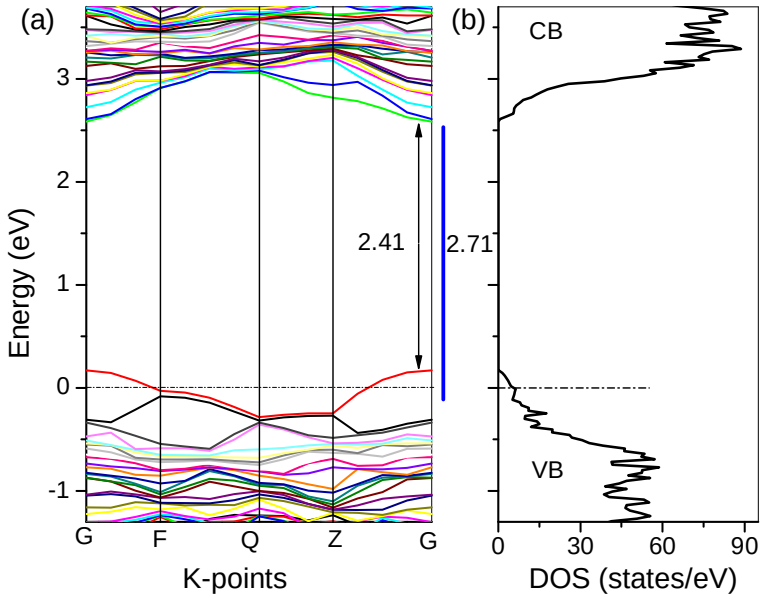

Figure 4.4.4 Band structures (a) and DOS (b) of Ga doped TiO_2.

4.4.1.3 Conclusions

Ga-TiO_2 thin films with different doping levels were fabricated by PLD method. The optical absorption spectra suggested the prime doping concentration for extending absorption range was 1% Ga, which red shifted absorption edge into visible region via introducing secondary absorption shoulder. Theoretical modelling showed Ga doping raises the valence band maximum (VBM) with respect to the Fermi level, giving rise to band gap narrowing.

4.4.2 V-Ga co-doped TiO_2 thin films by PLD

Vanadium and Gallium metal ions were chosen to co-dope into TiO_2 films and expected to narrow the band energy and improve the surface area ratio in this work.

4.4.2.1 Methods

The target for doped materials was made by adding 1% V_2O_5 and 0.5% Ga_2O_3 in weight into the pure TiO_2 powder before pressing into a pellet. The deposition duration was 1-hour with laser energy of 200~250 mJ per pulse and frequency of 5 Hz. After deposition, samples were annealed at 1000^{o}C or 1100^{o}C for 10-minutes, or 700^{o}C for 30-minutes in ambient atmosphere.

Theoretically calculation of electronic structures of the material phases were carried out by using the same method as described in the previous section.

4.4.2.2 Results and discussion

A. Microstructures

The XRD patterns of TiO_2 thin films are shown in Fig. 4.4.5, with peaks identified according to the standard JCPDS cards for powdered materials. None of the as-deposited and 700^{o}C annealed films showed any diffraction peaks in the XRD patterns. It is clear that both V-Ga co-doped and pure TiO_2 thin films crystallized into the rutile phase after annealing at temperatures higher than 1000^{o}C, with the XRD pattern from both annealed films showing only one characteristic peak corresponding to the (110) plane. Apparently, the non-crystalline structure of the as-deposited films was attributable to high cooling rates involved in such a physical vapour deposition process. It has been generally recognized that crystallization of the amorphous pure TiO_2 undergoes anatase to rutile transition, at least at intermediate temperatures [37]. Although prolonged annealing at 700^{o}C was sufficient to transfer anatase into rutile, the 30-minuters annealing in this work was inadequate to complete the phase transition and the thin film was still largely amorphous (see Fig. 4.4.5). The fact that rutile peaks were detected in the samples annealed at high temperatures offers confirmation that the featureless diffraction pattern from the as-deposited films was not due to the limitation of sample quantity. A striking feature is that both annealed films only had the (110) diffraction peak, which is owing to the formation of fibrous texture in the thin films. Considering that the fused quartz glass substrate is amorphous and the as-deposited films were non-crystalline, this was unlikely to be due to seeding effect.

According to the theoretical predictions using DFT modelling [38] the (110) plane corresponds to the lattice planes of the lowest surface energies for the pure rutile phase [39]. On the basis of energy minimization, during crystal growth the high-energy surface tends to decrease its surface area while the low-energy surface will increase its surface area, so as to decrease the total surface energy per crystal. Therefore, the {110) surface is supposed to grow fastest and has the biggest surface area, while the surface (001), being perpendicular to {110), tends to be small or even disappear. Thus, TiO_2 nanograins grow into energetically favourable rod like structures along [001] direction lying on quartz substrate. This also well explains the unique (110) diffraction peak detected by XRD, where nearly all exposed surfaces of nanorods are (001) surfaces.

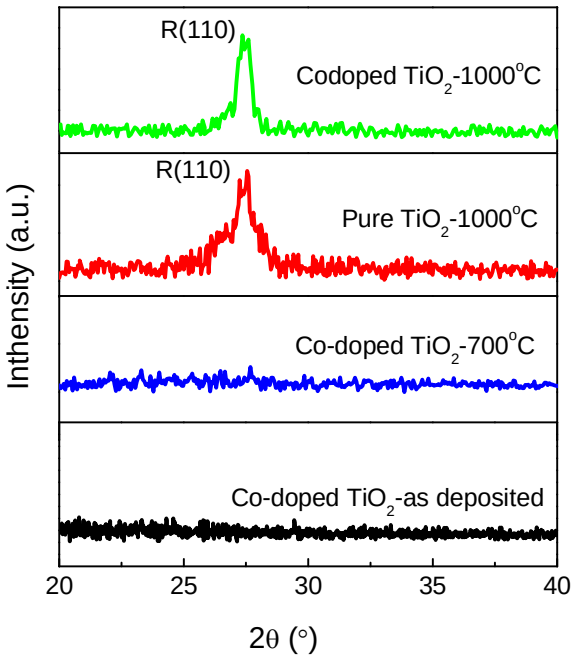

Figure 4.4.5 XRD patterns of V-Ga co-doped and pure TiO_2 thin films annealed at 1000°C.

The formation, therefore, of [110] texture in the annealed films was attributable to minimization of surface energy during crystallization. The small thickness of the thin film was obviously advantageous for the nucleation at the surface which then grew through the whole thickness. Indeed, surface energy has been found to play an important role on crystal orientations in thin films, as long as surface nucleation was

kinetically favoured [40,41]. Because of the evident anisotropic surface energies of the tetragonal lattices of the rutile phase, minimization of overall surface energy has been found to be pivotal for the realization of self-assembling of nanorods during the hydrothermal growth of TiO_2 films [42]. Fig. 4.4.6 shows the surface morphologies of the pure and V-Ga co-doped TiO_2 thin films (annealed at 1000^{o}C for 10-minutes), respectively. One can see that the pure TiO_2 film demonstrates a fine and dense granular surface, while the V-Ga co-doped film is composed of coarser nanorods lying on the substrates. The cross sectional (Fig. 4.4.6(c)) TEM image of the doped film show neat correspondence of the annealed film thickness and the aspect size of a nanorod. Comparing to the top surface morphology in Fig. 4.4.6(b), one concludes that the substrate is not fully covered by rutile TiO_2 nanorods after annealing. This was caused by the coarsening process of the ruitle phase and the small prior film thickness of the as-deposited film. Each nanorod is a single rutile crystal, which is encased in the low-surface-energy (110) planes to deliver a typical rectangular columnar morphology [42,43]. An example of SAED pattern from the rutile nanorod is shown in Fig. 4.4.6(d), which is typical for a single crystal.

The different phases sizes in the annealed samples of the pure and doped films is suggestive that the incorporation of the co-doping species promoted the rutile phase stability with respect to the anatase phase, so that direct crystallization of the rutile crystals occurred in the doped film during annealing. On the other hand, the crystallization in the pure film may have gone through the process of amorphous to anatase followed by anatase to rutile, so that there was shorter time for the lastly formed rutile crystals to grow. Such anatase to rutile transition has been widely reported to occur in pure TiO_2 films [44,45].

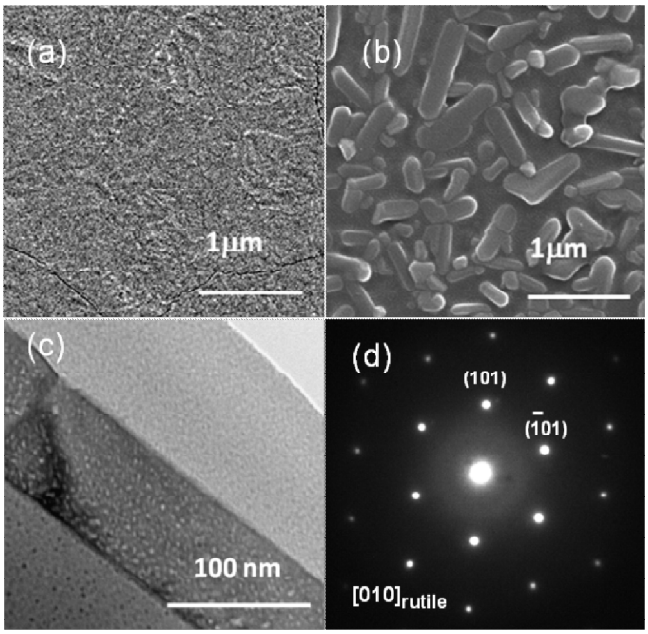

Figure 4.4.6 STM micrographs of (a) pure TiO_2 thin film, (b) V-Ga co-doped TiO_2 thin film, (c) TEM cross section image of V-Ga co-doped TiO_2 thin film, and (d) a SAED patten from a single nanorod of V-Ga co-doped TiO_2 thin film.

EDX analysis was carried out to study the distribution of doping elements in the thin films. Average composition was obtained from a real EDX quantification under SEM for good statistics over larger field of views, showing that the total atomic ratio for Ti: V: Ga through the 1000^{o}C annealed sample was 92.9: 4.8: 2.3. Point analysis was also obtained from various morphological features under TEM to limit beam spreading. As shown in the inset of Fig. 4.4.7(a), in addition to TiO_2 nanorods, TEM resolved significantly finer particles. The rutile nanorods contained all the metal elements, as shown Fig. 4.4.7(b). The inset, of Fig. 4.4.7(b) is the elemental map of Ti, showing uniform distribution of Ti through the nanorod. This is also indicative that other elements such as O, V and remaining Ga, if any due to the weak signal, are also evenly distributed throughout the nanorods. In contrast, EDX spectra from the fine particles such as the indicated ones in the inset of Fig. 4.4.7(a) only showed characteristic peaks from oxygen and Ga, indicating they were precipitates of gallium oxide. Therefore, in the annealed film, so that some supersaturated Ga was

rejected from the TiO_2 phase. From the EDX spectrum from the rutile nanorod, one noted the evidence for remaining Ga in the TiO_2 is rather weak after annealing.

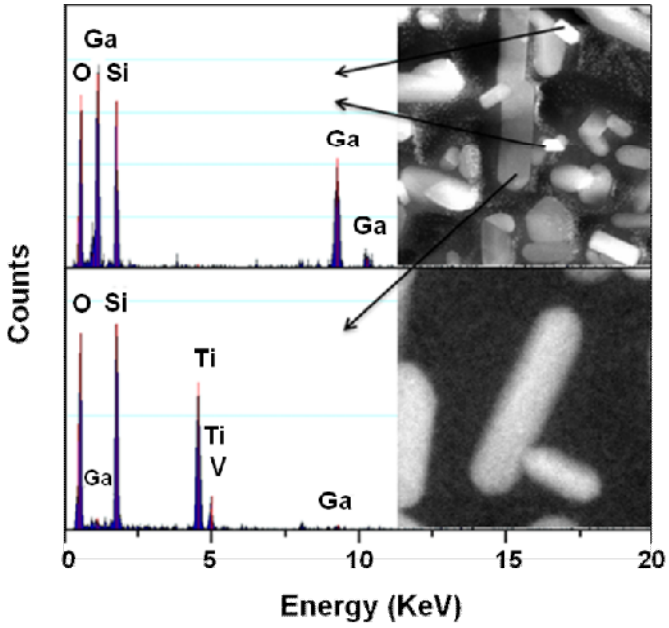

Figure 4.4.7 EDX spectra on different nanoparticles of the TiO_2 thin film with V-Ga co-doping (inset is the Ti mapping image of some nanorods).

B. XPS analysis

In order to obtain information on the chemical states of each element in the thin films, we also carried out high resolution XPS analysis. In addition to the two samples annealed at 1000°C, the doped sample was also annealed at 1100°C to offer additional information. Fig. 4.4.8 shows the high resolution Ti 2p core level spectra from all three samples, wherein each core level spectrum contains a set of conjugated spin orbital peaks attributed to Ti 2p3/2 and Ti 2p1/2. It can be seen that each Ti 2p peak can be decomposed into two sets of Gaussian peaks after deconvolution. According to the reported data from the literature, the first set of conjugated peaks at lower binding energy are assigned to Ti^{3+} state and the second set at higher binding energy correspond to Ti^{4+} oxidation state [46,47]. The relative percentages of Ti^{3+} and Ti^{4+} can be calculated from the integrated area under the resolved peaks and the result is presented in Table 4.1 with EDX data. From data shown in Table 4.1, the

pure TiO_2 contained 22.3 at% Ti^{3+}. To compare, 32.6 at% Ti^{3+} were present in V-Ga co-doped TiO_2 thin film annealed at 1000°C. This indicates that V-Ga co-doping led to increased content of Ti^{3+} in TiO_2 thin films. As the annealing was carried out in ambient atmosphere, the annealed thin films could pick oxygen from the environment to make up any oxygen deficiency during annealing. Therefore, it is more likely that increased percentage of 3+ Ti states was owing to charge transferring to Ti from the doped system. In addition, the content of Ti^{3+} increased from 32.6 at% to 41.7 at% when the annealing temperature was raised from 1000°C to 1100°C, indicating that annealing at high temperature also contributed to increasing the percentage of Ti^{3+}.

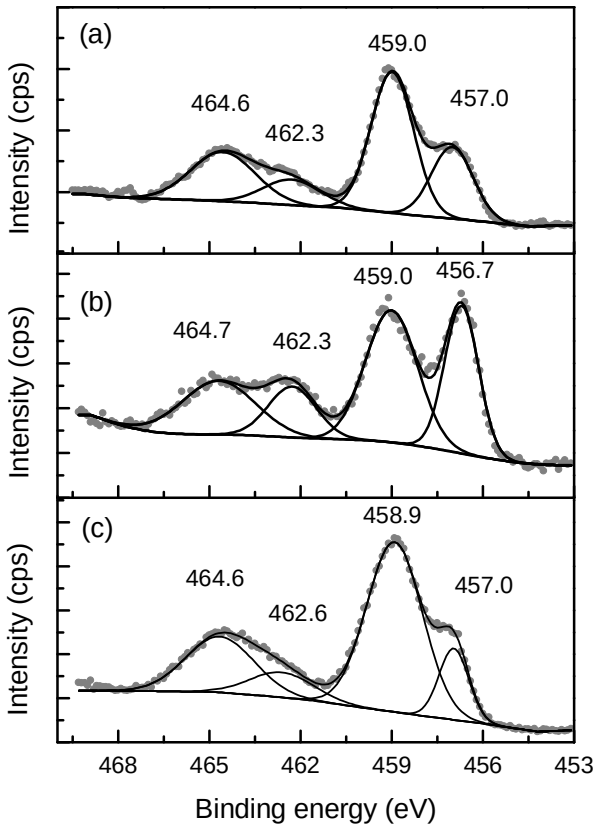

Figure 4.4.8 XPS spectra of Ti-2p in V-Ga co-doped TiO_2 annealed at 1000°C (a) and 1100°C (b), and pure TiO_2 thin film annealed at 1000°C (c).

The V 2p3/2 core levels of the co-doped samples annealed at 1000 and 1100°C are shown in Fig. 4.4.9, with data summarized in Table 4.1. We can see from Fig. 4.4.9(a) that the peak of the sample annealed under 1000°C was also fitted into two sets of Gaussian peaks. The two V 2p1/2 peaks from these two sets are located at 515.8 eV and 517.6 eV respectively and they are attributed to V^{4+} and V^{5+}, respectively, according to the XPS database. Interestingly, the presence of two valency states for V ions corresponds well with the two states of Ti ions. Overall, the valency for V ions is higher than 4+, and that for Ti ions is lower than 4+. This offers a self-consistent conclusion that charge was transferred from V to Ti. This is not shocking, considering that V does tend to have higher valency due to its higher oxygen affinity than Ti. This is in agreement with the proposition of Klosek and Raftery that the presence of V^{4+} is owing to the reduction of V^{5+} by Ti ions to reach charge equilibrium [48]. The signal of V^{5+} can be attributed to the local charge state in the doped rutile lattices. It is interesting to note that with reference to the 1000°C sample, the overall valence of V and Ti ions decreased in the 1100°C annealed thin film. This could be owing to increased levels of vacancies in the thin film due to the higher annealing temperature.

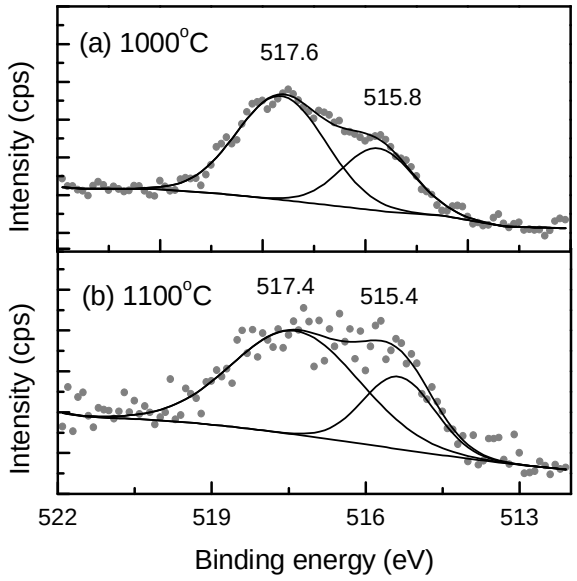

Figure 4.4.9 XPS spectra of V-2p3/2 in V-Ga co-doped TiO_2 annealed at 1000°C (a) and 1100°C (b).

Similarly, the Ga $2p_{3/2}$ peaks of two co-doped samples are presented in Fig. 4.4.10, in which the two Gaussian peaks located at 1116.8 and 1118.7 eV correspond to the Ga^{3+} and Ga^{4+} states respectively [49]. The presence of Ga^{3+} is consistent with the TEM observation that Ga oxide was precipitated after annealing at high temperatures. For the XPS results, one can conclude that the Ga oxide was in the form of stable Ga_2O_3. Apparently, the 4+ state of Ga ions were those that were retained in the host TiO_2 lattice to replace the Ti^{4+} ions. From the results summarized in Table 4.1, one notices that about half of the Ga was retained in the valency 4+ state as dopant in the TiO_2 phase in the 1000°C annealed sample, while the doping Ga ions reduced to about a quarter of the total amount in the 1100°C annealed.

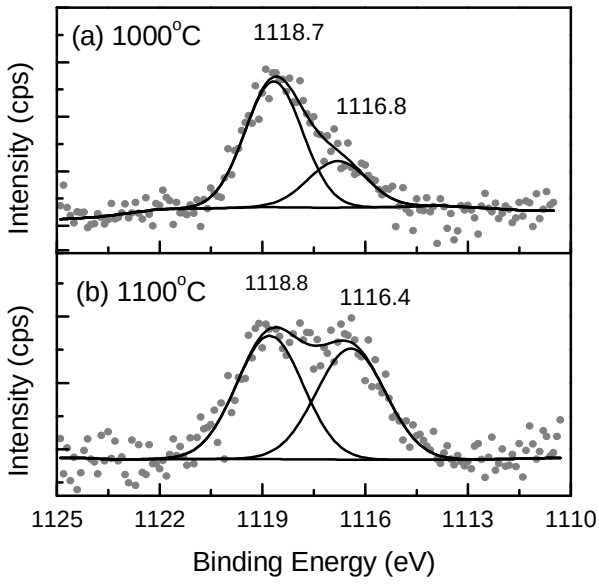

Figure 4.4.10 XPS spectra of Ga-2p3/2 in V-Ga co-doped TiO_2 annealed at 1000°C (a) and 1100°C (b).

Table 4.1 Integral area according different XPS peaks

	Doped TiO_2 1000°C	Doped TiO_2 1100°C	Pure TiO_2 1000°C
Ti^{4+}	62.6 at%	54.2 at%	77.7 at%
Ti^{3+}	30.3 at%	38.7 at%	22.3 at%
V^{5+}	3.2 at%	3.4 at%	
V^{4+}	1.6 at%	1.4 at%	
Ga^{4+}	1.1 at%	0.5 at%	
Ga^{3+}	1.2 at%	1.8 at%	

C. Optical absorption properties

The optical absorption properties were studied by transmission UV-visible-Infrared spectrometry. The results from doped and pure thin films are summarized in Fig. 4.4.11. The absorption coefficient of pure TiO_2 thin film in the UV region is around 4.5×10^5 cm^{-1}, being consistent with the value reported [50]. The absorption edge is about 400 nm, which corresponds to the band gap 3.0 eV of pure rutile TiO_2.

Remarkable red shifts were achieved in doped thin films. The extent of the absorption edge was observed to depend on the annealing temperature. The primary absorption edge for the 700°C annealed thin film located at around 650 nm, well into the red light region. After being annealed at 1000°C, the edge was shifted up to about 1000 nm, in the infrared region. For the 1100°C annealed thin film, the edge was at about 800 nm in the near-infrared region. It is amazing that the absorption spectrum of the high temperature annealed samples cover the full visible light region and part of the infrared or near-infrared region, with well defined primary absorption edges and high absorption coefficient over 10^5 cm^{-1}. Considering that only a few percentage of doping atoms were incorporated in the host lattice, such a co-doping effect is indeed shocking to compare the doping effect owing to single metal dopant, wherein rather high content of doping/alloying elements were necessary to induce significant redshift [51]. It is worth stressing that the high absorption coefficient and well defined edge are desirable for an efficient optical absorber for efficient utilization of solar energy, and the present discovery provides a new material system for absorption of a wide range of solar irradiance for energy harvest or photocatalytic applications. An absorption coefficient of more than 10^5 cm^{-1} over the full visible light region suggests that over 90% of the day light can be absorbed by a film of 230 nm in thickness. As TiO_2 is a cheap material system with enormous natural resources, the present discovery offers a new class of materials for the fabrication of low-cost thin film solar cells with the potential for sustainable long-term application. Such a solar cell technology is yet lacking.

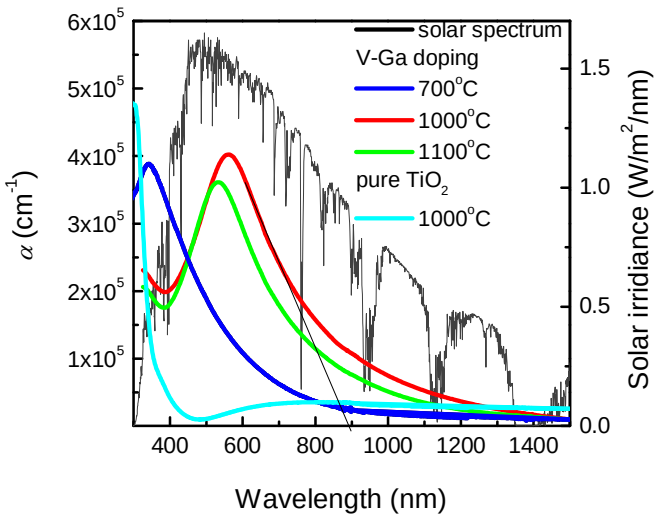

Figure 4.4.11 UV-visible optical absorption spectra of V-Ga co-doped and pure TiO_2 thin films under different annealing temperature.

Fig. 4.4.12 presents the square of the absorption coefficient against the photon energy. The intersections of the tangents correspond to the optical gaps of the direct gap material. One notes that the optical gap for pure rutile is larger than that for the bulk material, indicating some effect due to quantum confinement from the nanocrystals. Apparently, the optical gap is remarkably reduced for 2.0 eV due to co-doping, making the material effective in absorbing a wide range of light from the infrared up to the near-ultraviolet.

The origin of the enhanced optical absorption is apparently due to the doping of the TiO_2 phase, as the experimentally measured band gap for the Ga_2O_3 phase was reported to be between 4.4 and 5.1 eV [52,53]. There is no microstructural evidence of V_2O_5 precipitates in the annealed films. Even if one attributes the V^{5+} from the XPS analysis to the V_2O_5 phase, the relative amount was extremely low (see Table 4.1), so that it would not have induced the remarkable red shift in the primary absorption edge. Furthermore, the reported band gap for V_2O_5 is 2.2-2.5 eV, which corresponds to absorption edge located at between 496 - 564 nm [54,55,56] and thus its presence would have not induced the remarkable red shift well beyond the visible light region.

One notices from Fig. 4.4.11 and Fig. 4.4.12 that the extent of red shift was smallest in the 700°C annealed sample, it reached maximum in the 1000°C annealed sample, and decreased somewhat in the 1100°C annealed sample. Even though the 700°C annealed sample is expected to contain all the doping elements, the atomic disorder evidenced by XRD would reduce the doping effect considerably. This has been observed in Mn-doped TiO_2, wherein structural defects were found to have significant effect on reducing the doping effect [51]. Indeed, by comparing the 1100°C and 1000°C annealed samples, one realizes that the lower dopant contents in the former led to reduced effect on redshift.

It is worth pointing out that V doping of TiO_2 has been experimentally investigated, and the best reported red shift corresponded to an absorption edge about 600 nm [57]. The co-doping with both V and Ga is therefore behind the enormous red shift achieved in the thin film samples of this work. Obviously, an in-depth understanding about the co-doping effect necessitates theoretical modelling.

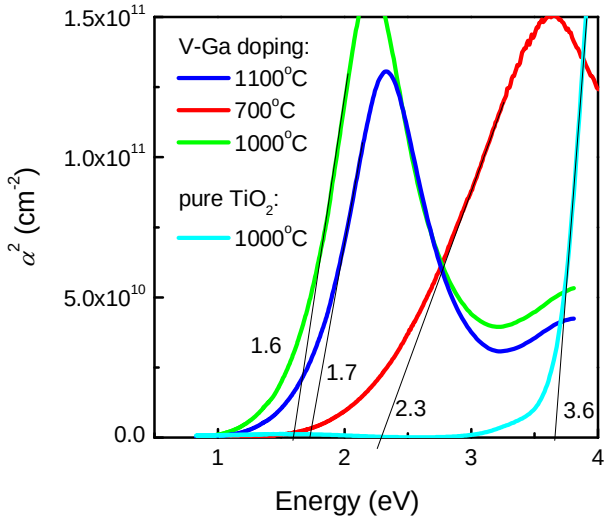

Figure 4.4.12 α^2 against the photon energy of V-Ga co-doped and pure TiO_2 thin films under different annealing temperature.

D. Theoretical modelling

Obviously, the simulated reduction of the band gap caused by solely Ga doping in last section is far from what was co-doping achieved experimentally. In the same way as Ga doping, the effect of V doping was investigated by studying the electronic structure of the 2×2×2 supercell with one Ti atom being replaced by V. The band structure and DOS for the V doped phase is shown in Figs. 4.4.13 (a) and (b) respectively, showing that V induces gap states in the form of a donor-like band below the conduction band minimum (CBM). The overall band gap of the doped phase is 2.36 eV, about 13% narrower than that of the corresponding virgin phase. As the energy gap between the top of the donor-like band and the CBM is rather small, the excitation of valence electrons to the conduction band is effectively dictated by the energy gap below the donor-like band. Such an effective band gap is 2.02 eV (Fig. 4.4.13(a)), which corresponds to about 25% reduction of the band gap with respect to that for the virgin phase. Although V doping is more effective than Ga in gap narrowing, it alone is yet inadequate to account for the enormous red shift in the experimental work.

The V and Ga co-doping was studied through substituting two Ti atoms, one by V atom and another by Ga. Several distinctive ways of distributing V and Ga atoms were attempted, with V atom being placed at Ti site as nearest, second nearest to Ga or far away from it. Total energy calculations on these configurations showed that the nearest V and Ga configuration is most stable. This is not difficult to understand since a substitutional Ga induces one hole and a substitutional V introduces one electron, thus achieving charge neutrality. This suggests that the coexistence of V and Ga is compensating electron charges to form a stable state. Therefore, in the following the nearest V and Ga configuration will be used to study the co-doping effect on rutile TiO_2.

The calculated band structure and DOS of V-Ga co-doped TiO_2 are plotted in Fig. 4.4.13(c) and (d). It is apparent that VBM is lowered down so that the material recovers the intrinsic nature for perfect crystals, Fig. 4.4.13(c). This is consistent with the charge compensation mechanism so that donor-acceptor annihilation occurs. The resultant band gap due to co-doping is 1.81 eV (Fig. 4.4.13(d)), being about one

third narrower than that of pure rutile. Compared to the band structure of pure TiO_2, we can see that the co-doping induces several energy bands next to the CBM and their considerable band width and curvatures result in overlapping of the conduction band. The appearance of these doping induced bands results in significant reduction of the band gap. Clearly, compared to Ga or V doping alone, V-Ga co-doping is significantly more effective in narrowing the band gap and thus improving the efficiency of optical absorption. It is should be pointed out that the one third gap reduction due to such co-doping only shift the absorption edge up to 620 nm, which is still far smaller than the 1000 nm absorption edge achieved in the experimental work. We notice that the equal amount of Ga and V doping in the model supercell for calculation is not the same as that in the experimental work. The latter had a V to Ga ratio about 5 to 1. Such a doping composition requires a much larger supercell to accommodate the right amount of dopants, and would be too costing for practical computation with the non-local effect considered. The observed gigantic extent of red shift is thus likely attributed to optimized combination of the co-dopants.

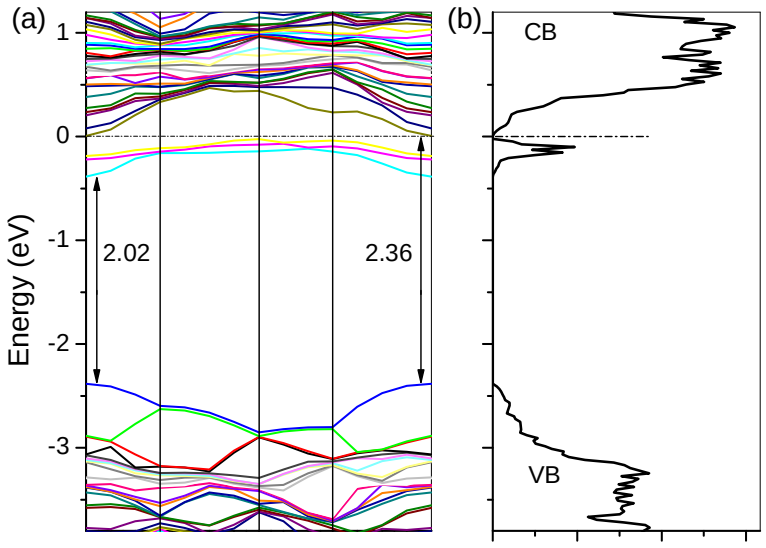

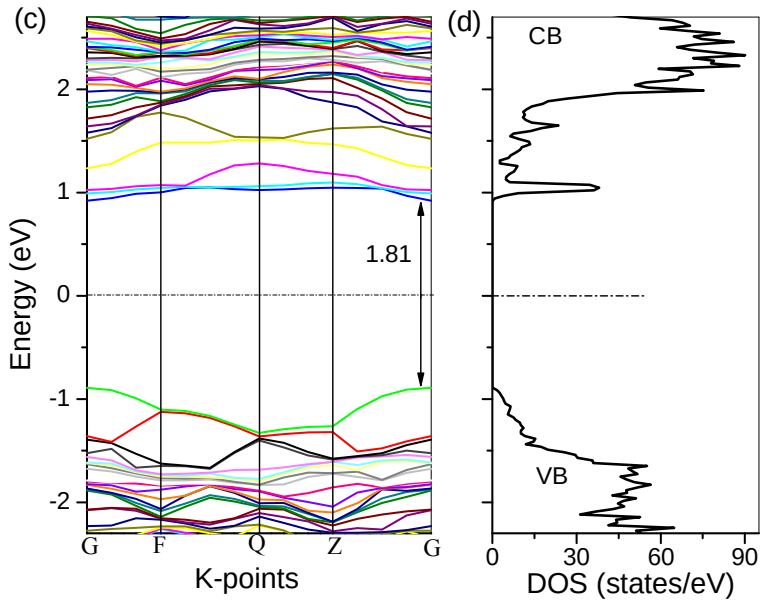

Figure 4.4.13 Band structures and DOS of V doped TiO_2 (a, b), and V-Ga co-doped TiO_2 (c, d). The dot lines at the energy zero represent the Fermi levels.

4.4.2.3 Conclusions

V-Ga co-doped TiO_2 films composed of rutile nanograins were fabricated on fused quartz substrates by pulsed laser ablation. The doped thin film exhibited remarkable red shifts in the optical absorption edges, from UV to infrared region. The absorption edges of the doped materials were well defined and the optical absorption coefficients were very high, in the order of 10^5 cm^{-1}, which makes TiO_2 extremely effective in absorbing a wide range of solar spectral radiation and thus highly desirable for a wide range of photo-based devices including novel low cost solar cells.

Theoretical calculation of electronic structures showed that Ga alone has little effect for the reduction of the band gap of TiO_2, while V-Ga co-doping induces additional energy bands to overlap with the conduction band minimum and leads to significant reduction of the band gap. The enormous red shift observed in this work is likely owing to optimised combination of co-dopants.

References

[1]H. U. Habermeier. Pulsed laser deposition–a versatile technique only for high-temperature superconductor thin-film deposition? Applied Surface Science 69 (1993) 204–211.

[2]N. Stankova, I. Dimitrov, T. Stoyanchov, P. Atanasov, D. Kovacheva. Structure and optical anisotropy of pulsed-laser deposited TiO_2 films for optical applications. Applied Surface Science 255 (2009) 5275–5279.

[3]G. Shukla, P. K. Mishra, A. Khare. Effect of annealing and O_2 pressure on structural and optical properties of pulsed laser deposited TiO_2 thin films. Journal of Alloys and Compounds 489 (2010) 246–251.

[4]M. Walczak, E. Papadopoulou, M. Sanz, A. Manousaki, J. Marco, M. Castillejo. Structural and morphological characterization of TiO_2 nanostructured films grown by nanosecond pulsed laser deposition. Applied Surface Science 255 (2009) 5267–5270.

[5]D. A. H. Hanaor, C. C. Sorrell. Review of the anatase to rutile phase transformation. Journal of Materials Science 46 (2010) 855-874.

[6]N. T. Nolan, M. K. Seery,and S. C. Pillai. Spectroscopic investigation of the anatase-to-rutile transformation of sol−gel-synthesized TiO_2 photocatalysts. The Journal of Physical Chemistry C 113 (2009) 16151-16157.

[7] H. Zhang , J. F. Banfield. Phase transformation of nanocrystalline anatase-to-rutile via combined interface and surface nucleation. Journal of Materials Research 15 (2000) 437-448.

[8]J. Yu, H. Yu, B. Cheng, X. Zhao, J. Yu, W. Ho. The effect of calcination temperature on the surface microstructure and photocatalytic activity of TiO_2 thin films prepared by liquid phase deposition. The Journal of Physical chemistry B 107 (2003) 13871-13879.

[9]L. Gomathi Devi, S. Girish Kumar, B. Narasimha Murthy, Nagaraju Kottam. Influence of Mn^{2+} and Mo^{6+} dopants on the phase transformation of TiO_2 lattice and its photocatalytic activity under solar illumination. Catalysis Communication 10 (2009) 794–798.

[10]C. Sima, C. Grigoriu. Study on TiO_2 thin films grown by advanced pulsed laser deposition on ITO. Thin Solid Films 518 (2009) 1314–1317.

[11]M. Walczak, E. Papadopoulou, M. Sanz, A. Manousaki, J. Marco, M. Castillejo. Structural and morphological characterization of TiO_2 nanostructured films grown by nanosecond pulsed laser deposition. Applied Surface Science 255 (2009) 5267–5270.

[12]N. T. Nolan, M. K. Seery, S. C. Pillai. Spectroscopic investigation of the anatase-to-rutile transformation of sol–gel-synthesized TiO_2 photocatalysts. The Journal of Physical Chemistry C 113, (2009) 16151-16157.

[13]H. Zhang, J. F. Banfield. Phase transformation of nanocrystalline anatase-to-rutile via combined interface and surface nucleation. Journal of Material Research 15 (2000) 437-448.

[14] N. Mathews, E. Morales, M. Cortes-Jacome, J. Toledo Antonio. TiO_2 thin films – Influence of annealing temperature on structural, optical and photocatalytic properties. Solar Energy 83 (2009) 1499–1508.

[15] D. D. Claudio, A. R. Phani, S. Santucci. Enhanced optical properties of sol–gel derived TiO_2 films using microwave irradiation. Optical Materials 30 (2007) 279–284.

[16] T. Umebayashi, T. Yamaki, H. Itoh, K. Asai. Analysis of electronic structures of 3d transition metal-doped TiO_2 based on band calculations. Journal of Physics and Chemistry of Solids 63 (2002) 1909-1920.

[17] K. Iijima, M. Goto, S. Enomoto, H. Kunugita, K. Ema, M. Tsukamoto, N. Ichikawa, H. Sakama. Influence of oxygen vacancies on optical properties of anatase TiO_2 thin films. Journal of Luminescence 128 (2008) 911–913.

[18] Y. Wang, D. Doren. First-principles calculations on TiO_2 doped by N, Nd, and vacancy. Solid State Communications 136 (2005) 186–189.

[19] G. Shao. Red shift in Mn- and Fe-doped TiO_2: a DFT+U analysis. The Journal of Physical Chemistry C 113 (2009) 6800-6808.

[20] R. S. Sonawane, B. B. Kale, M. K. Dongare. Preparation and photo-catalytic activity of Fe-TiO_2 thin films prepared by sol–gel dip coating. Materials Chemistry and Physics 85 (2004) 52-57.

[21] B. Xin, Z. Ren, P. Wang, J. Liu, L. Jing, H. Fu. Study on the mechanisms of photoinduced carriers separation and recombination for Fe^{3+}-TiO_2 photocatalysts. Applied Surface Science 253 (2007) 4390–4395.

[22] Z. Li, W. Shen, W. He, X. Zu. Effect of Fe-doped TiO_2 nanoparticle derived from modified hydrothermal process on the photocatalytic degradation performance on methylene blue. Journal of Hazardous Materials 155 (2008) 590–594.

[23] M. C. Wang, H. J. Lin, T. S. Yang. Characteristics and optical properties of iron ion (Fe^{3+})-doped titanium oxide thin films prepared by a sol–gel spin coating. Journal of Alloys and Compounds 473 (2009) 394–400.

[24] G. Shao. Electronic structures of manganese-doped rutile TiO_2. The Journal of Physical Chemistry C 112 (2008) 18677-18685.

[25] G. Shao. Electronic structures of manganese-doped rutile TiO_2 from first principles. The Journal of Physical Chemistry C 112 (2008) 18677-18685.

[26] J. I. Pankove. Optical Processes in Semiconductors. Courier Dover Publications (1971).

[27] L. Bian, M. Song T. Zhou, X. Zhao, Q. Dai. Band gap calculation and photo catalytic activity of rare earths doped rutile TiO_2. Journal of Rare Earths 27 (2009) 461-468.

[28] M. Brik, I. Sildos, V. Kiisk. First-principles calculations of optical and electronic properties of pure and Sm^{3+}-doped TiO_2. Physica B: Condensed matter 405 (2010) 2450–2456.

[29]E. Setiawati, K. Kawano. Stabilization of anatase phase in the rare earth; Eu and Sm ion doped nanoparticle TiO_2. Journal of Alloys and Compounds 451 (2008) 293-296.

[30] C. Liang, F. Li, C. Liu, J. Liu, X. Wang. The enhancement of adsorption and photocatalytic activity of rare earth ions doped TiO_2 for the degradation of Orange I. Dyes and Pigments 76 (2008) 477-484.

[31]G. Kresse, J. Hafner. Ab initio molecular dynamics for liquid metals. Physical Review B 47 (1993) 558-561.

[32] G. Kresse, J. Hafner. Ab initio molecular-dynamics simulation of the liquid-metal–amorphous-semiconductor transition in germanium. Physical Review B 49 (1994) 14251-14269.

[33]P. E. Blochl. Projector augmented-wave method. Physical Review B 50 (1994) 17953-17979.

[34]G. Kresse, D. Joubert. From ultrasoft pseudopotentials to the projector augmented-wave method. Physical Review B 59 (1999) 1758-1775.

[35]J. P. Perdew, K. Burke, M. Ernzerhof. Generalized gradient approximation made simple. Physical Review Letter 77 (1996) 3865-3868.

[36]H. J. Monkhorst, J. D. Pack. "Special points for Brillouin-zone integrations"—a reply. Physical Review B (1977) 1748-1749.

[37]J. Yu, H. Yu, B. Cheng, X. Zhao, J. C. Yu, W. K. Ho. The effect of calcination temperature on the surface microstructure and photocatalytic activity of TiO_2 thin Films prepared by liquid phase deposition. The Journal of Physical Chemistry B 107 (2003) 13871-13879.

[38]P. M. Oliver, G. W. Watson, E. T. Kelsey, S. C. Parker. Atomistic simulation of the surface structure of the TiO_2 polymorphs rutileand anatase. Journal of materials Chemistry 7 (1997) 563-568.

[39]A. S. Barnard, P. Zapol. Effects of particle morphology and surface hydrogenation on the phase stability of TiO_2. Physical Review B 70 (2004) 235403.

[40]G. Shao, P. Tsakiropoulos. On the structural evolution of Fe-Al laminates obtained by physical vapour deposition. Philosophical Magazine A 80 (2000) 693-710.

[41]S. Z. Wang, G. Shao, P. Tsakiropoulos, F. Wang. Phaseselection in magnetron sputter-deposited TiAl alloy Materials Science and Engineering: A 140 (2002) 329-331.

[42]M. Guo, X. Xia, Y. Gao, G. Jiang, Q. Deng, G. Shao. Self-aligned TiO_2 thin films with remarkable hydrogen sensing functionality. Sensors and Actuators B: Chemical (2012) In Press.

[43]L. Li, C. Y. Liu, Y. Liu. Study on activities of vanadium (IV/V) doped TiO_2 (R) nanorods induced by UV and visible light. Materials Chemistry and Physics 113 (2009) 551-557.

[44]N. T. Nolan, M. K. Seery, S. C. Pillai. Spectroscopic investigation of the anatase-to-rutile transformation of sol−gel-synthesized TiO_2 photocatalysts. The Journal of Physical Chemistry C 113 (2009) 16151-16157.

[45]H. Zhang, J. F. Banfield. Phase transformation of nanocrystalline anatase-to-rutile via combined interface and surface nucleation. Journal of Materials Research 15 (2000) 437-448.

[46]J. Wang, X. Ni. Interfacial structure of poly(methyl methacrylate)/TiO_2 nanocomposites prepared through photocatalytic polymerization. Journal of Applied Polymer Science 108 (2008) 3552-3558.

[47]J. Pouilleau, D. Devilliers, H. Groult, P. Marcus. Surface of a titanium-based ceramic electrode material by X-ray photoelectron spectroscopy. Journal of Materials Science 32 (1997) 5645-5651.

[48] S. Klosek, D. Raftery. Visible light driven V-doped TiO_2 photocatalyst and its photooxidation of ethanol. The Journal of Physical Chemistry B 105 (2001) 2815-2819.

[49] D. Briggs, M. P. Seah. Practical surface analysis by auger and X-ray photoelectron spectroscopy. Wiley (1990).

[50]M. Perego, G. Seguini, G. Scarel, M. Fanciulli, F. Wallrapp. Energy band alignment at TiO_2/Si interface with various interlayers. Journal of Applied Physics 103 (2008) 043509.

[51]X. Xia, L. Lu, A. Walton, M. Ward, X. Han, R. Brydson, J. Luo, G. Shao. Origin of significant visible-light absorption properties of Mn-doped TiO_2 thin films. Acta Materialia 60 (2012) 1974-1985.

[52]M. Passlack, E. F. Schubert, W. S. Hobson, M. Hong, N. Moriya, S. N. G. Chu, K. Konstadinidis, J. P. Mannaerts, M. L. Schnoes, G. J. Zydzik. Ga_2O_3 films for electronic and optoelectronic application. Journal of Applied Physics 77 (1995) 686-693.

[53]H. H. Tippins. Optical absorption and photoconductivity in the band edge of β-Ga_2O_3. Physical Review A 140 (1965) 316-319.

[54]A. Chakrabarti, K. Hermann, R. Druzinic, M. Witko, F. Wagner, M. Petersen. Geometric and electronic structure of vanadium pentoxide: A density functional bulk and surface study. Physical Review B 59 (1999) 10583-10590.

[55]Z. S. E. Mandouh, M. S. Selim. Physical properties of vanadium pentoxide sol gel films. Thin Solid Films 371 (2000) 259-263.

[56] P. Singh, D. Kaur. The inset shows the variation of ex- cess free volume of grain boundaries with crystallite size. Journal Applied physics 103 (2008) 043507.

[57]K. Melghit, O. S. Al-Shukeili, I. Al-Amri. Effect of M-doping (M = Fe, V) on the photocatalytic activity of nanorod rutile TiO_2 for Congo red degradation under the sunlight. Ceramics International 35 (2009) 433-439.

Chapter 5 Fe and Mn doped TiO_2 powders as visible light photocatalyst

5.1 Fe doped TiO_2 nanopowders by hydrothermal method

5.1.1 Experimental details

Fe doped TiO_2 (Fe-TiO_2) samples were synthesized by a hydrothermal method. In a typical procedure, a precursor of acidic aqueous solution was prepared by mixing a certain amount of acid (HCl or H_2SO_4, or both) with 135 ml of distilled water. Then 10 ml tetrabutyl titanate, $Ti(OC_4H_9)_4$ or $Ti(OBu)_4$, was added into the acidic precursor, whilst stirring, drop by drop. A certain amount of $Fe(NO_3)_3 \cdot 9H_2O$, according to the required Fe/Ti atom ratio, was dissolved into the mixture of precursor. Thus a transparent yellow solution was obtained and transferred into an autoclave. The autoclave was then kept in an oven at 80°C for 10-hours. After being cooled down to room temperature, the precipitates were washed with de-ionized water under centrifugation till the pH of the solution reached about 7. The precipitates were then dried in air at 50°C for about 12-hours, followed by thermal annealing, at different temperatures, for an hour in air. A number of powder samples with the Fe/Ti ratio ranging from 0 at% to 1.8 at% were obtained.

The photocatalytic activity of the Fe-TiO_2 samples was studied by measuring the degradation of aqueous MB solution under visible light radiation. The solution for photo-degradation measurement was prepared by adding an amount of 0.1 g of pure or doped TiO_2 powder to 50 ml of aqueous solution of methylene blue (MB, 4 mg/l). The suspension was magnetically stirred in the dark for 20-minutes to ensure the establishment of an adsorption/desorption equilibrium and then transferred into a cylindrical beaker surrounded by a circulating water jacket for cooling. A 300 W halide lamp was used as the light source, which was positioned above the cylindrical beaker. A cut-off filter was placed between the lamp and beaker to remove the radiation below 400 nm and ensure visible light illumination. At given time intervals, about 4-5 ml of samples was taken from the beaker, which was then centrifuged for 5-minutes to separate the catalyst particles. The concentration of MB in the solutions

was ascertained by referring to an absorption–concentration standard curve that was established by measuring the optical absorption of MB at 665 nm.

5.1.2 Results and discussion

5.1.2.1 Microstructures

A. The effect of the annealing temperature on phase structures

Pure and Fe-TiO_2 samples were synthesized using mixtures of H_2SO_4 and HCl (H_2SO_4: HCl = 3: 4) for the acidic precursor. TiO_2 powders were doped to different Fe/Ti ratios (nominal Fe/Ti ratios: 1, 1.5 and 1.8 at%), and they were then subjected to annealing for an hour at different temperatures. Fig. 5.1.1 shows the XRD patterns of the pure and the 1.8 at% Fe doped TiO_2 samples. Only the anatase phase was present in the pure sample, even after it was annealed at 700°C, as shown in Fig. 5.1.1(a). As for the doped samples, the anatase phase was retained as the annealing temperature increased up to 500°C and then some extra peaks owing to the rutile phase occurred when the temperature reached 700°C. Applying the Scherrer's equation to the major (101) diffraction peak, the sizes of the pure TiO_2 crystals were estimated to be 5.19, 6.30, 8.04 and 17.74 nm, and the sizes of the doped samples were about 4.70, 5.73, 8.05, and 20.43 nm, for the as-synthesized powder and samples annealed at 400°C, 500°C, 700°C. The intensity of the diffraction peaks in both Fig. 5.1.1(a) and (b) increased slightly and the full width at half maximum (FWHM) of diffraction peaks decreased as the annealing temperature increased, indicating improved crystallinity and enlarged crystal grain size of the annealed samples. It is interesting to note that the growth of the particles was restrained by Fe doping, with the sizes of the doped samples being smaller than the pure ones (with/without annealing at 400°C). As the annealing temperature increased to 500°C, the sizes of the doped and pure samples were similar. The grain size increased dramatically when the phase transformation from anatase to rutile occurred in the doped samples at 700°C.

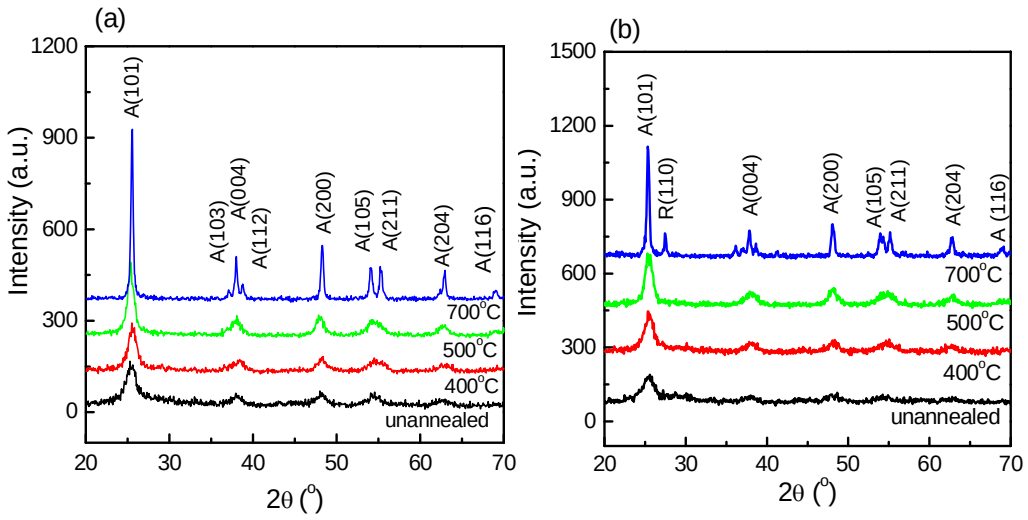

Figure 5.1.1 XRD patterns of the pure (a) and 1.8 at% Fe-TiO_2 (b) samples annealed at different temperatures (400°C, 500°C and 700°C). The acidic precursor was a mixture of H_2SO_4 and HCl (H_2SO_4: HCl = 3: 4).

TEM was used to examine the microstructures of the prepared powder samples using mixtures of H_2SO_4 and HCl (H_2SO_4: HCl = 3: 4) for the acidic precursor. For example, the TEM images for the pure TiO_2 and 1.8 at% Fe TiO_2 nanopowders annealed at 400°C are shown in Fig. 5.1.2(a) and (b) respectively. The average particle size was about 6.5 nm for the pure TiO_2 and 5.5 nm for the 1.8 at% Fe-TiO_2 nanoparticles. As for the 1.8% Fe-TiO_2 annealed at 700°C shown in Fig. 5.1.2(c), nanoparticles grew significantly to about 20 nm. The TEM measured grain sizes were in excellent agreement with XRD data using the Scherrer's equation. Energy dispersive X-ray (EDX) analysis under TEM showed that the Fe/Ti ratios corresponding to the nominal Fe concentrations of 1.0 at%, 1.5 at%, and 1.8 at% were about 2.1 at%, 2.45 at%, and 3.25 at%. Such deviations from nominal contents are due to incomplete reaction. The presence of SO_4^{2-} offset the H^+ effect on hydrolysis and promoted the formation of anatase over rutile, leading to enhanced capacity for the incorporation of Fe dopant in the metastable anatase lattice. This will be discussed in detail in following sections (Sections 3.3 and 3.4).

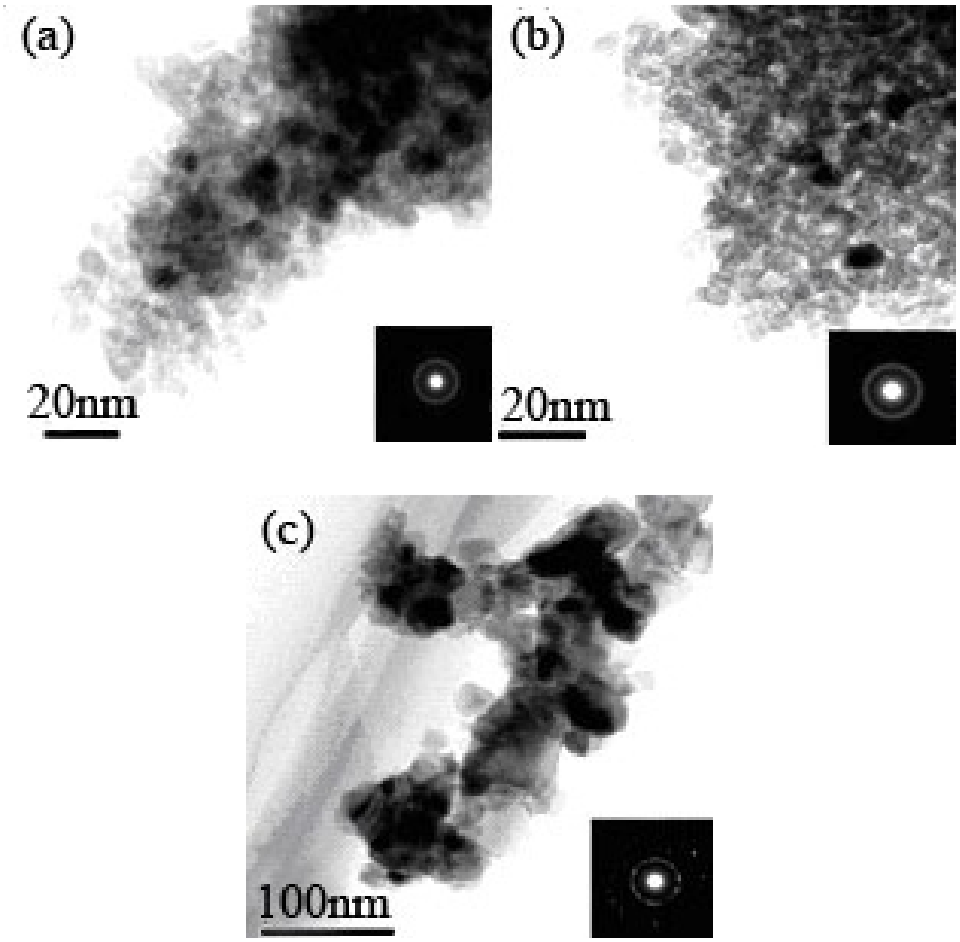

Figure 5.1.2 TEM image of the samples using mixtures of H_2SO_4 and HCl (H_2SO_4: HCl = 3: 4) for the acidic solvent: (a) pure TiO_2 powder annealed at 400°C, (b) 1.8 at% Fe-TiO_2 annealed at 400°C, and (c) 1.8 at% Fe-TiO_2 annealed at 700°C.

B. Doping effect on phase formation

Fig. 5.1.3 shows the XRD patterns for the pure and Fe-TiO_2 nanopowders annealed at 700°C for an hour, the acidic precursor was instead by a H_2SO_4 solution. For the pure powder, annealing at 700°C for an hour did not trigger the phase transformation to the stable rutile structure. On the other hand, minor peaks owing to a small proportion of rutile TiO_2 were observed to co-exist with anatase in the doped samples. This suggests that Fe doping tends to lower the transformation temperature to turn the metastable anatase TiO_2 into the stable rutile phase. The crystal sizes in the TiO_2 samples were estimated from the FWHM of the major (1 0 1) peaks, giving

22.1, 21.1, 20.8, and 20.4 nm for pure, 1.0 at%, 1.5 at% and 1.8 at% Fe-TiO_2. It shows again that the crystal sizes in the nanopowders could be reduced via Fe doping.

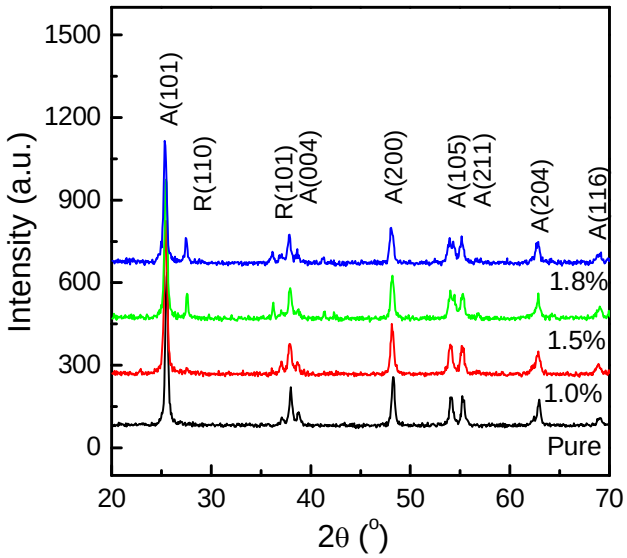

Figure 5.1.3 XRD patterns of the samples with various Fe/Ti ratios, annealed at 700°C for an hour. The acidic precursor was H_2SO_4 solution.

C. The pH value effect on phase formation

Fig. 5.1.4 shows the XRD patterns of 1.8 at% Fe-TiO_2 samples synthesized at different H^+ concentrations and annealed at 600°C, using only HCl solution as precursor. It is interesting to observe that pure anatase was obtained when no acid was introduced into the precursor. However, mixed phases with both anatase and rutile occurred when H^+ concentration was 0.1 mol/L. With increasing H^+ concentration, the proportion of anatase gradually reduced and that of the rutile phase increased. When the H^+ concentration reached 2.94 mol/L, the products were completely made of the rutile phase, suggesting that the pH value could greatly affect the phase formation of Fe-doped TiO_2.

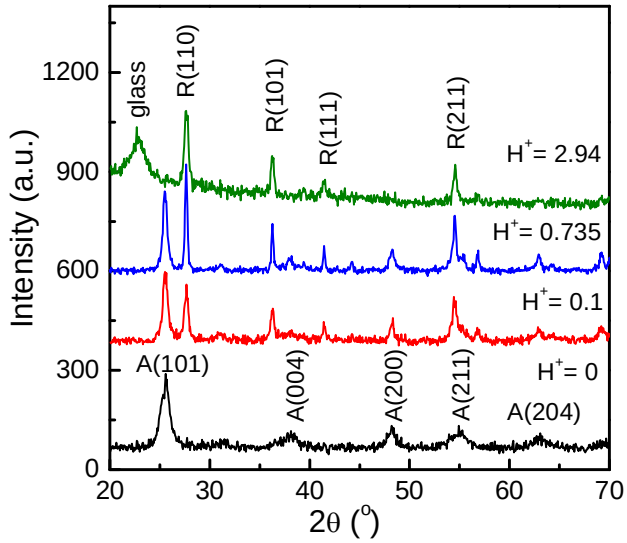

Figure 5.1.4 XRD patterns of the samples prepared at different pH values (H^+ = 0, 0.1, 0.735 and 2.94 mol/L) and annealed at 600°C, using HCl to adjust the acidity of the precursor solution.

The chemical process for the synthesis of TiO_2 is by a hydrolysis-condensation process of the titanium alkoxides $Ti(OR)_4$. The hydrolysis process can be fulfilled via the following reaction:

$$Ti(OR)_4 + H_2O \rightarrow Ti(OH)_4 + 4ROH \qquad (5.1)$$

wherein H^+ was proven to offer effective catalysis for hydrolysis. Under acidic conditions, an alkoxide group is protonated in a rapid first step, making it more electrophilic and thus more susceptible to attack from water [1].

The condensation process occurs via:

$$2Ti(OH)_4 \rightarrow (OH)_3Ti - O - Ti(OH)_3 + H_2O \qquad (5.2)$$

The condensation process is carried out by the loss of water to form linear −[Ti − O − Ti] − chains in a way similar to the gelation process in a sol-gel process. Further cross-linking of these linear chains delivers the crystalline structure during the hydrothermal process. On the basis of crystallographic characteristics, vertical cross-

linking of longer chains is considered to favour the formation of the rutile structure, while anatase is related to lower symmetry bridging between shorter chains. The slow condensation process in a strongly acidic solution provides adequate time to allow the formation of longer chains to deliver the rutile structure. This is consistent with Gopal [2] who observed that increased H^+ concentration benefited the formation of rutile phase, and suggested that the presence of H^+ lowered the activation energy for rutile formation.

D. Effect of acidic anions on phase formation

It is noted that in addition to the H^+ ions, acidic anions such as Cl^- and SO_4^{2-} may also affect the above hydrolysis-condensation process. Here we compare the results owing to the Cl^- and SO_4^{2-} anions, using the same acidity (H^+ = 1 mol/L).

Fig. 5.1.5 shows the XRD patterns of the 0.8 at% Fe-TiO_2 samples, which were fabricated with the HCl solution as the acidic precursor and the pH value of the precursor is H^+ = 1 mol/L. The as-synthesized powders were then annealed at various temperatures. All the diffraction peaks in Fig. 5.1.5 were attributed to the rutile phase in both the as-synthesized and annealed samples.

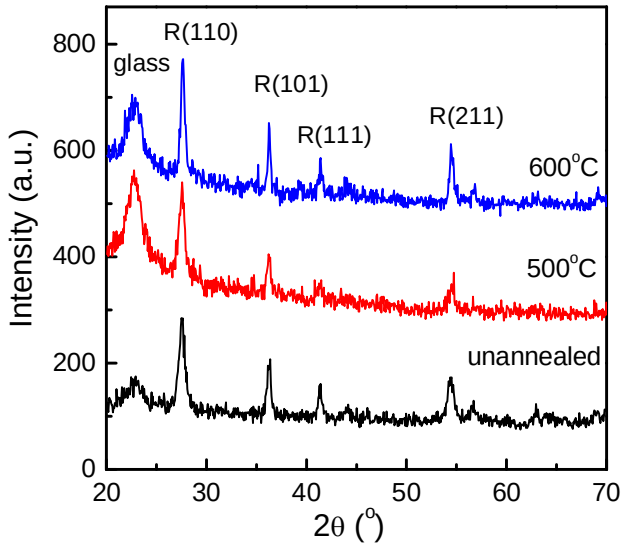

Figure 5.1.5 XRD patterns of the samples obtained using HCl solution as precursor annealed at different temperatures (unannealed, 500°C and 600°C). The peaks located at about 23° were attributed to the glass sample holder.

Fig. 5.1.6 shows the XRD patterns of as-synthesized 1.5 at% Fe- TiO_2 samples obtained using only HCl, only H_2SO_4 and mixed acids (H_2SO_4: HCl = 3: 4) with the same pH value (H^+ = 1 mol/L), for the acidic precursor. Unlike the above case of HCl precursor, it was found that pure anatase phase was formed when H_2SO_4 or mixed acid was used. This indicates that the presence of SO_4^{2-} anions could strongly retard the formation of rutile and favour the formation of the anatase phase. These results were consistent with previous studies [3]. It was postulated that SO_4^{2-} ions would form complexes with titanium ions, which could partially substitute the hydrated or aqueous solution of titanium hydroxyl ion ligands, resulting in the formation of lower symmetry of ligand ions. These low symmetry ligand ions could be conducive to the formation of anatase titanium dioxide.

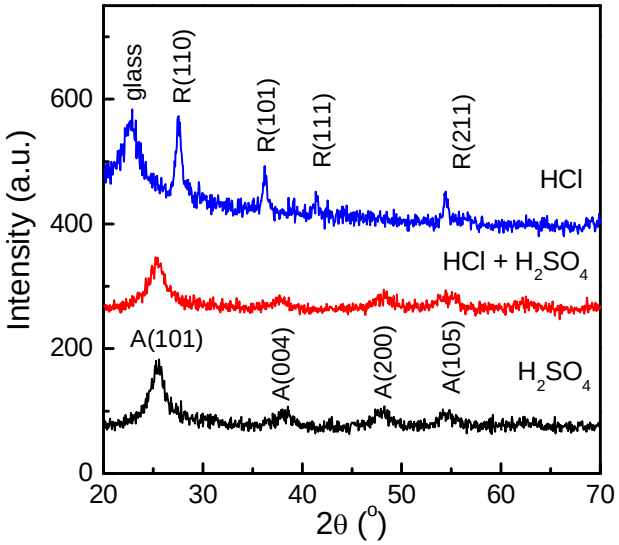

Figure 5.1.6 XRD patterns of the as-synthesized samples by using different acidic solutions as precursors (HCl, H_2SO_4 and mixed acid).

5.1.2.2 XPS analysis

The chemical states of doped Fe have been studied using XPS. Fig. 5.1.7 shows the high resolution XPS spectra of Fe 2p region taken on the surface of the 1.5 at% Fe-TiO_2 sample. It is seen that the two peaks of Fe 2p are not symmetrical, and each of them could be fitted into two peaks. As is well known, peak deconvolution for XPS

analysis can be rather uncertain, and great care has been taken to achieve convincing peak fitting in our work for which we have used FWHM comparable to the instrumental resolution for all fitted peaks. The dominant peaks located at 710.8 eV and 724.2 eV are in excellent agreement with the accepted binding energies of Fe^{3+} 2p3/2 and 2p1/2 respectively [4] while the other two peaks located at 713.2 eV and 725.6 eV have higher binding energy than Fe^{3+}, suggesting the existence of another higher oxidation state. While it is different from the earlier reports on Fe doped TiO_2 wherein Fe^{3+} and Fe^{2+} oxidation states were postulated [5], the present observation is consistent with the fact that Ti has a higher oxygen affinity than Fe, leading to charge transfer from Ti to Fe to induce lowered valence of Fe in an otherwise 4+ metallic site in the host of TiO_2. The charge transfer can be theoretically correlated to the lowered Mulliken charge of the substitutional Fe atom at the Ti site in TiO_2 than Fe in the hypothetical FeO_2 phase (4+ state), which predicts a calibrated valence of 3.13 for Fe at the Ti site in TiO_2. From our XPS measurement, the dominant Fe 2p peaks are indeed attributed to the Fe^{3+} state and the higher oxidation state of Fe^{4+} corresponds to minor peaks.

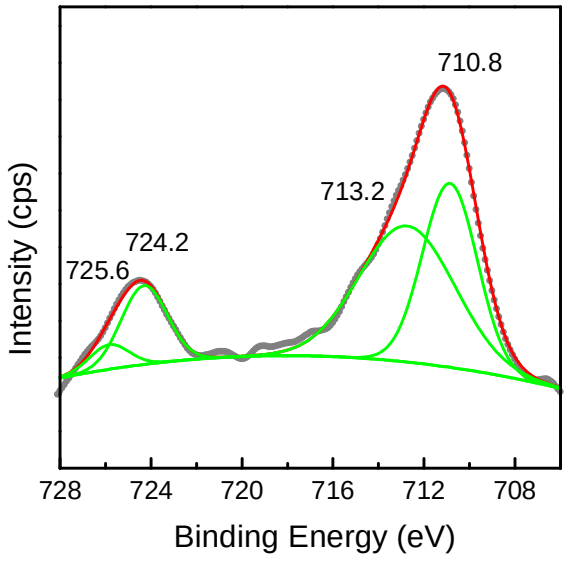

Figure 5.1.7 High resolution XPS spectra of Fe 2p region taken on the surface of the 1.5 at% Fe-TiO_2 sample.

5.1.2.3 Optical absorption properties

Fig. 5.1.8 shows the UV–visible absorption spectra of the Fe-TiO_2 powders with different iron concentrations using the mixed H_2SO_4 and HCl acidic solvent (H_2SO_4: HCl = 3: 4). It is noticed that there is a slight shift of the absorption edge of pure anatase powder to about 400 nm, this is likely to be attributed to the effect of surface scattering of the nanoparticles which induced certain degree of optical trapping. With respect to the pure sample, red shift of the optical absorption edge was observed in all Fe doped samples. Also, comparing with that of as-synthesized samples, significantly enhanced red shift was observed from the samples annealed at 700°C. The red shift increased with increasing Fe concentration. The maximum red shift to about 700 nm was obtained with 1.8 at% Fe doping.

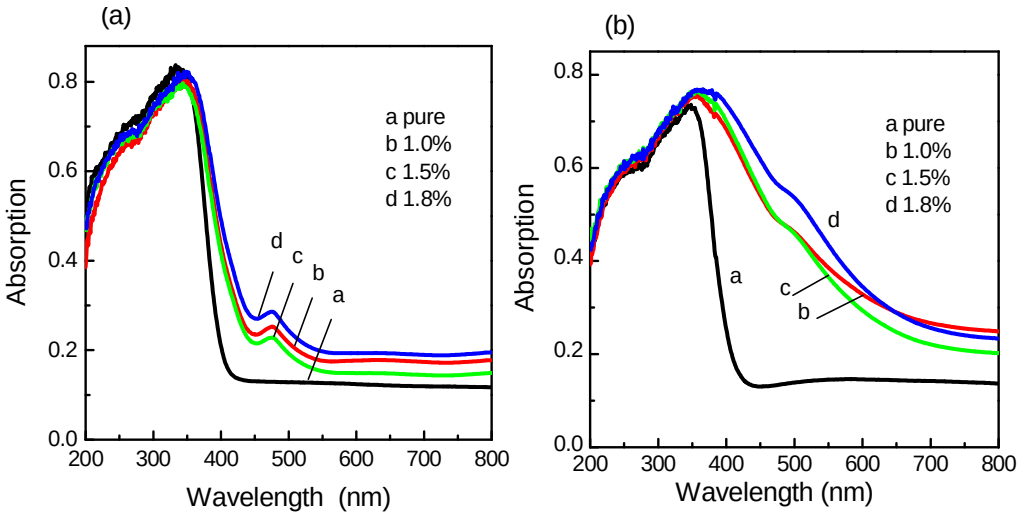

Figure 5.1.8 UV–visible absorption spectra of the Fe-TiO_2 samples: (a) as-synthesized, (b) annealed at 700°C for an hour.

Theoretical modelling showed that the origin of red shift in 3d metal doped TiO_2 is the doping induced intermediate bands/states in the forbidden gap together with gap narrowing, which were attributed to the hybridization of the dopant 3d and the oxygen 2p orbitals [3,6]. In the case of Fe-TiO_2, in addition to significant band gap reduction, a number of intermediate states are also induced through Fe substitution of the Ti sublattice [3]. The redshift in the principal optical absorption edge in Fig. 5.1.8 is attributed to the narrowed band gap, and the secondary absorption edge

corresponds to the Fe induced intermediate states/bands. Defects in the form of interstitial occupancy or oxygen vacancies only lead to localized defect states without reducing the forbidden gap, making the doping less effective for red shift. Annealing is thus very useful in reducing the crystalline defects to cause more effective optical absorption.

5.1.2.4 Visible light photocatalytic activity

The photocatalytic results for the degradation of MB under visible light are shown in Fig. 5.1.9, using the photocatalysts synthesized with the mixed H_2SO_4 and HCl acidic (H_2SO_4: HCl = 3: 4) solvent and annealed at 700°C. The degradation of MB with pure TiO_2 as catalyst is similar to the photosensitized degradation of MB. The Fe-TiO_2 samples showed remarkably enhanced photocatalytic activity with respect to that of the pure TiO_2. The photocatalytic activity of TiO_2 increased gradually with the increasing Fe/Ti ratio up to 1.5 at%. Further increase of iron concentration did not induce enhanced photocatalytic activity for the catalyst. This may be due to the difficulty in eliminating interstitial Fe atoms in highly doped materials. The introduction of excessive Fe ions into TiO_2 powder and the associated difficulty in removing doping induced crystalline defects would offer recombination centres to shorten the life time of the photo activated charge carriers and harm the photocatalytic activity of the catalysts.

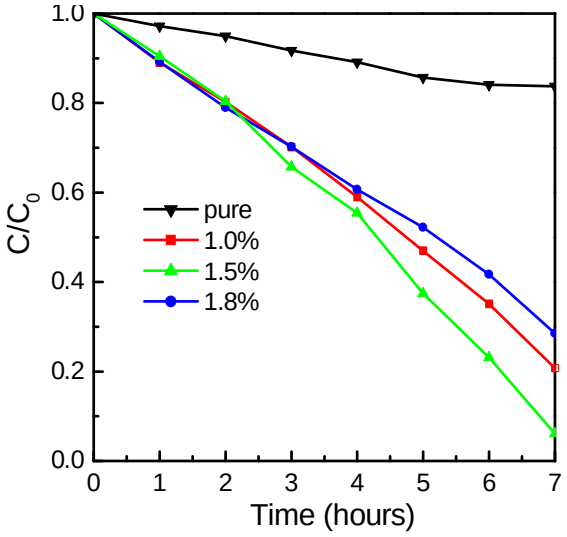

Figure 5.1.9 Photocatalytic degradation curves of MB under visible light, without catalyst, using pure and doped TiO_2 as photocatalysts. The TiO_2 powders were annealed at 700°C.

5.1.3 Conclusions

Fe doped TiO_2 nanopowders were prepared using a hydrothermal method at low temperature. Doping Fe into TiO_2 tended to restrict the grain growth of TiO_2 during synthesis and annealing, leading to finer TiO_2 grains.

Low solution acidity favoured the formation of anatase TiO_2 and high H^+ concentration resulted in the formation of rutile TiO_2. The presence of SO_4^{2-} ions in the acidic precursor solution was propitious for the formation of anatase TiO_2.

Fe doping induced significant red shift in the optical absorption edge of TiO_2 into the visible light region. The presence of secondary absorption edge was attributed to doping induced intermediate states.

The photocatalytic activity of TiO_2 increased gradually with increasing Fe/Ti ratio up to 1.5 at%, beyond which, photocatalytic activity began to lose.

5.2 Mn doped TiO_2 nanopowders by sol-gel method

5.2.1 Experimental details

Pure and Mn doped TiO_2 (Mn-TiO_2) nanoparticles were synthesized using a sol–gel technique. Initially, 5 ml of tetrabutyl titanate ($Ti(OBu)_4$), was dissolved in 15.4 ml of ethanol in a beaker at room temperature under vigorous magnetic stirring, wherein 0.85 ml glacial acetic acid and 0.65 ml deionised water were sequentially introduced to form the precursor solution. The pH of the solution was adjusted to 2 by adding nitric acid (HNO_3), which was subjected to vigorous stirring for 2-hours and aged for 24-hours at room temperature to form the TiO_2 sol. The obtained sol was a transparent solution of light yellow color. The resultant sol was then dried at 85°C in a water thermal bath to obtain a xerogel. For the preparation of Mn doped TiO_2, pre-determined amounts of the manganese nitrate were added in the ethanol first, and the subsequent processes were the same as the method described above. The obtained pure and Mn doped xerogel were calcinated at 400°C or 800°C for 3-hours to remove residual organic compounds.

The photocatalytic activity of the samples was studied by means of degrading MB under visible light as that described in Fe doped TiO_2 materials. Herein, in order to study the initial adsorption ability of dye on different TiO_2 samples and reach the establishment of an adsorption/desorption equilibrium, the mixture was initially treated with ultrasonic stirring for 10-minute, followed by continuous stirring in the dark for an hour. Then about 3 ml of the mixture of catalyst and MB solution was sampled before light illumination. After that, the lamp was turned on and about 3 ml of the mixture of catalyst and MB solution was sampled from the beaker every 30-minutes. At the same time, one MB solution without any photocatalyst was also illuminated under light for reference in view of the light induced self degradation of MB solution. The concentration of MB in the solutions was ascertained by referring to an absorption–concentration standard curve that was established by measuring the optical absorption of MB at 665 nm.

5.2.2 Results and discussion

5.2.2.1 Microstructures

X-ray diffraction was used to determine the phase structure of pure and Mn-TiO_2 powders post annealed at 400^{o}C. As can be seen in Fig. 5.2.1, all diffraction peaks for both pure and doped powders were attributed to the anatase phase by comparing them with JCPDS cards. Apparently, with the increase of Mn concentration (Mn/Ti atomic ratio from 0.1 at% to 12.0 at%), the peak width of the (101) plane ($2\theta = 25.4°$) broadened slightly. By employing the Scherrer's equation with the strongest (101) peak, the sizes of the nanocrystals were calculated to be about 7 nm in all the samples. In addition, the anatase grain size decreased slightly with increasing Mn doping level, from 7.5 nm for pure TiO_2 down to 6.8 nm for 12 at% Mn doped powder. It is worth mentioning that although the doping concentration was as high as 12 at%, no manganese rich oxides or $MnTiO_x$ phases presented in the XRD patterns, being possibly attributed to the sensitivity of XRD technology.

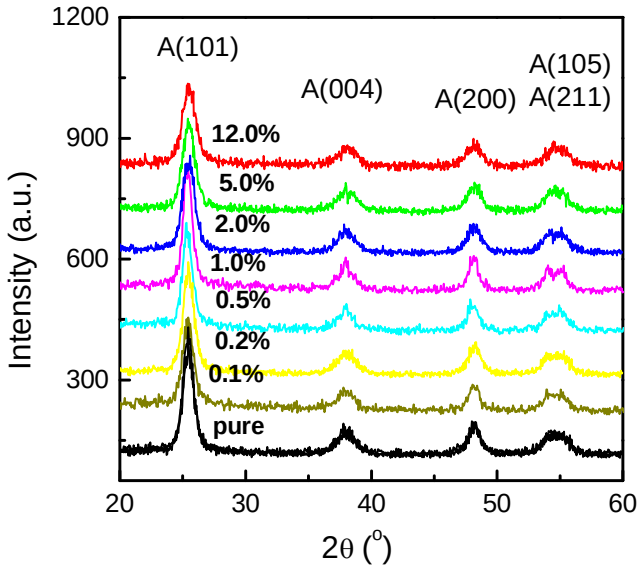

Figure 5.2.1 XRD patterns of sol-gel synthesized pure and Mn-TiO_2 post annealed at 400°C.

The XRD patterns of Mn doped TiO_2 powders annealed at 800°C are shown in Fig. 5.2.2, with peaks identified and marked on. It is obvious that all of these powders were transformed into rutile phase upon high temperature annealing. In addition to peaks attributed to the rutile phase, an extra peak at 32.9° appeared in the XRD profiles when the doping concentration was over 5 at%, with the peak intensity being increased as the increasing of doping concentration. To clarify the impurity phase, a typical Mn over-doped sample with designed Mn: Ti ratio of 1: 1 was prepared in the same way, with corresponding XRD spectrum shown in Fig. 5.2.2(b). One set of diffraction peaks attributed to α-Mn_2O_3 was identified in this Mn over doped samples, suggesting those additional peaks in high Mn doped samples were attributed to the Mn_2O_3, which has body centred cubic structure with lattice parameter a=9.43 Å (space group). The results revealed that the equilibrium Mn solubility in rutile TiO_2 was not as high as Mn in metastable anatase lattice.

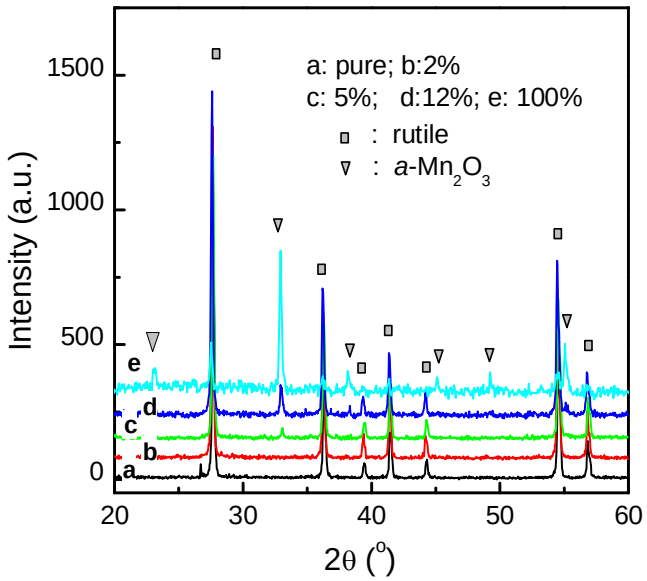

Figure 5.2.2 XRD patterns of sol-gel synthesized pure and Mn-TiO_2 post annealed at 800°C.

The morphologies of the pure and Mn doped TiO_2 nanocrystals were examined under TEM. Images from both pure and doped powder samples exhibited highly uniform nanocrystalline microstructures. Fig. 5.2.3(a) shows a typical bright field (BF) image of 12 at% Mn doped TiO_2 powder which annealed at 400°C. The relative selected area electron diffraction (SAED) pattern of this sample is shown as Fig. 5.2.3(b), in which the dark rings on the right are the standard polycrystalline diffraction rings for the anatase phase (indexed). As it can be seen, the obtained SAED diffraction rings on Mn-TiO_2 particles match the standard anatase rings very well. No sign of rings or spot related to other phases can be seen in spite of great care, though the electron diffraction under TEM is expected more sensitive to minor phases than XRD due to the strong dynamic effects under the illumination of energetic electrons. This implies that all doped samples were solely made of the anatase phase after annealing, being consistent with the XRD results. Fig. 5.2.3(c) shows the central dark field (CDF) image of this sample obtained by selecting the diffraction beam from the encircled part of the (101) diffraction ring. Nanoparticles with grain size of several nanometres are clearly seen in this dark field image, also agreeing with that determined by XRD. In addition, the atomic Mn percentages of all

Mn doped TiO_2 powders were determined by quantitative EDX analysis and summarized in Fig. 5.2.3(d), in which the actual Mn to Ti ratios were slightly lower than the nominal doses in the sol.

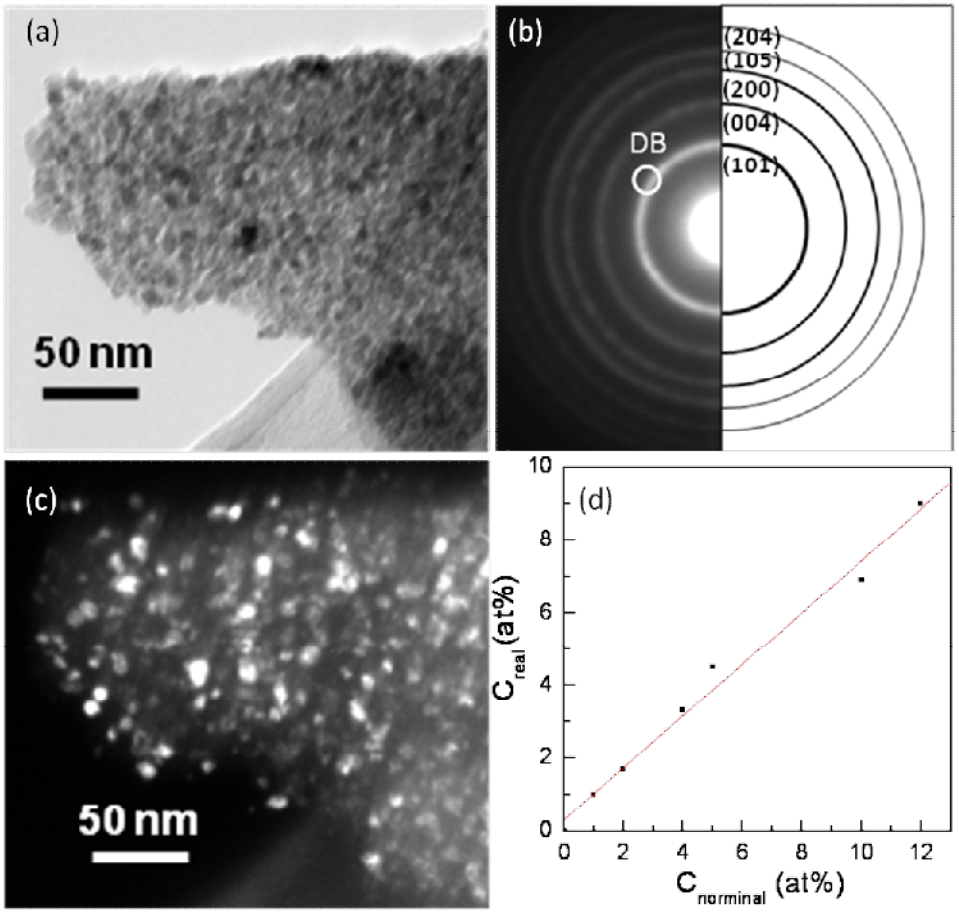

Figure 5.2.3 (a) Bright field TEM image, (b) SAED pattern (left half) matching standard ring pattern of the anatase phase (right half), (c) dark field image of 12 at% Mn-TiO_2 powder; (d) EDX measured Mn-Ti ratio v.s. nominal ratio.

Fig. 5.2.4 shows TEM image of 12 at% Mn doped TiO_2 particles that annealed at 800^{o}C. As it is shown, most of nanoparticles had grown up to hundreds nanometres with some small particles decorating around. The relative SAED pattern of this sample is shown as Fig. 5.2.4(b), in which the bright rings are the standard polycrystalline diffraction rings for the rutile phase. It is apparent that most of diffraction spots are located on the standard rings attributed to rutile TiO_2 while

several individual spots belong to Mn_2O_3, which completely consent to XRD result that rutile TiO_2 was formed with Mn_2O_3 participated out upon 800°C annealing.

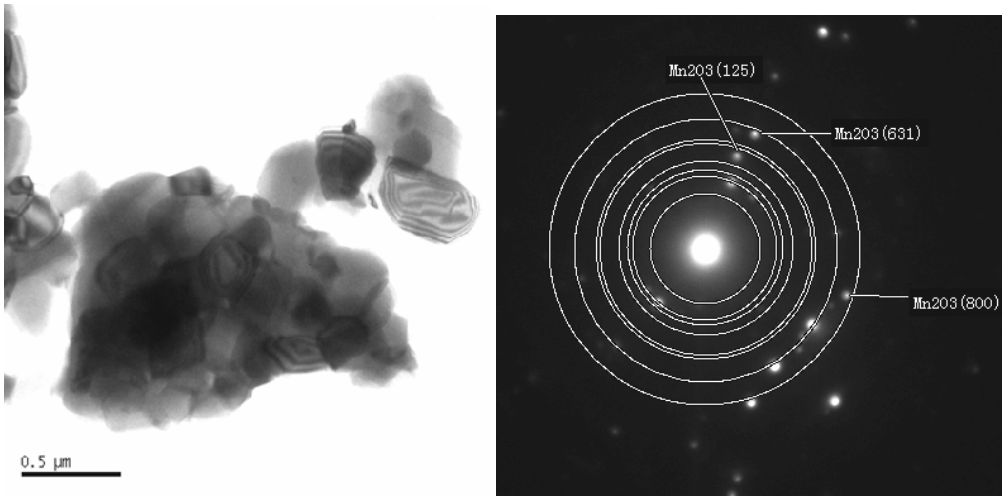

Figure 5.2.4 (a) Bright field TEM image, (b) SAED pattern of 12 at% Mn-TiO_2 powder and standard ring pattern of the rutile phase.

5.2.2.2 XPS analysis

To further clarify the location of dopants in the TiO_2 matrix, high resolution XPS analysis has been carried out on 2 at% and 12 at% Mn doped TiO_2 samples, as well as the relative pure one. Fig. 5.2.5(a) and (b) show the XPS core level spectra of Ti 2p and Mn 2p for Mn-TiO_2 powders annealed at 400°C. As it can be seen in Fig. 5.2.5(a), each Ti 2p core level spectrum had one set of conjugated symmetric peaks located at 458.6 eV and 464.3 eV, corresponding to the Ti 2p3/2 and Ti 2p1/2 spin orbit peaks of Ti^{4+} oxidation state with reference to literature [7]. Apart from this, no other multiple Ti components or chemical shift occurred here, suggesting that Mn doping could hardly influence the local chemistry of the host Ti atoms in the TiO_2 phase.

Fig. 5.2.5(b) shows the characteristic core level spectra of Mn 2p from 2 at% and 12 at% Mn-TiO_2 powders, wherein each Mn 2p core level spectrum had one set of conjugated peaks corresponding to the Mn 2p3/2 and Mn 2p1/2 spin orbit peaks. It can be seen that each Mn 2p peak can be decomposed into two Gaussian lines after

deconvolution. For 2 at% Mn-TiO_2, the first set of conjugated peaks located at 641.4 eV and 652.8 eV are reasonably ascribed to Mn^{3+} with reference to literature data from 641.3 eV to 641.9 eV [8, 9, 10], and the other set of conjugated peaks with higher binding energy of 643.6 eV and 654.4 eV is thereby assigned to an higher oxidation state Mn^{4+}. On the basis of the peak areas, the percentage of Mn^{4+} is about 45%. This is consistent with theoretical prediction, which showed that charge transfer occurs between substitutional Mn and the host Ti atoms, which lowers the oxidation state of the Mn atom from a 4+ environment to slightly above 3+. Similarly, two sets of conjugated spin orbit peaks were discernibly observed in 12 at% Mn-TiO_2 powder, suggesting both Mn^{3+} and Mn^{4+} ions (47.3 at%) also existed in this sample. It is worth to mention that atomic disorder associated with the high level of doping gave rise to a satellite peak (Plasmon peak) in addition to conjugated Mn peaks. The little and unavailable fluctuation in the value of peaks is considered to originate from apparatus error and Gauss fitting.

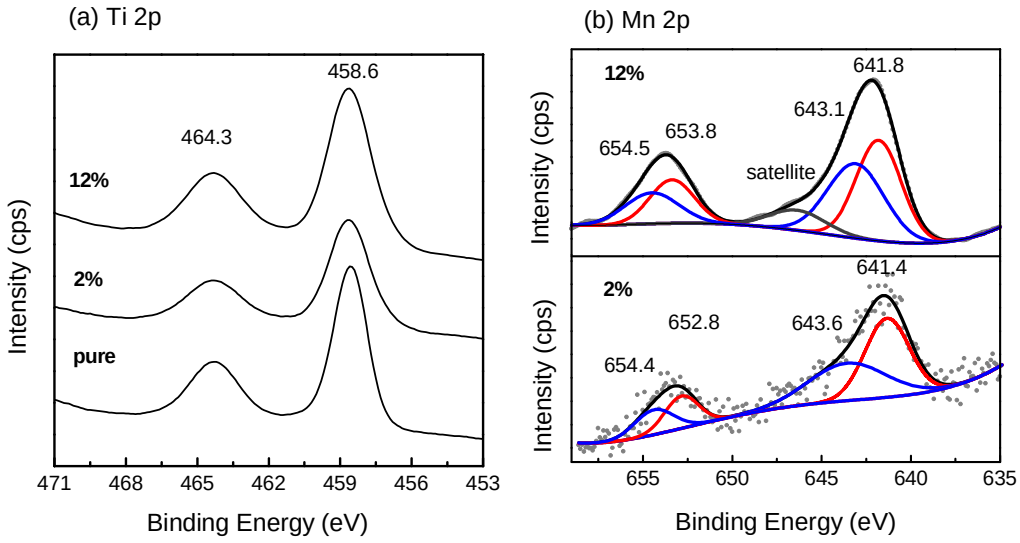

Figure 5.2.5 XPS patterns of (a) Ti 2p for Mn doped and pure TiO_2; (b) Mn 2p for 2 at% and 12 at% Mn-TiO_2 powders.

Fig. 5.2.6 shows the 12 at% Mn-TiO_2 annealed at 800°C, in which (a) is the Ti 2p core level spectrum and (b) is the Mn 2p core level spectrum. Discernibly, there was

only Ti^{4+} existing in Ti host due to the extremely symmetric conjugated peaks. Moreover, in addition to the satellite peak, each Mn 2p core spectrum could be fitted into two Gaussian peaks after deconvolution, originated from Mn^{3+} and substantial Mn in TiO_2 matrix. By comparing it with the sample annealed at 400°C, we find the content of Mn^{3+} increased when the annealing temperature is raised from 400°C to 800°C, being in good agreement with XRD result that partial Mn was precipitated out to form Mn_2O_3 as the transformation from anatase to rutile phase. As a result, the content of substantial Mn in rutile TiO_2 is lower than that in anatase even though the total concentrations of Mn in two samples are the same.

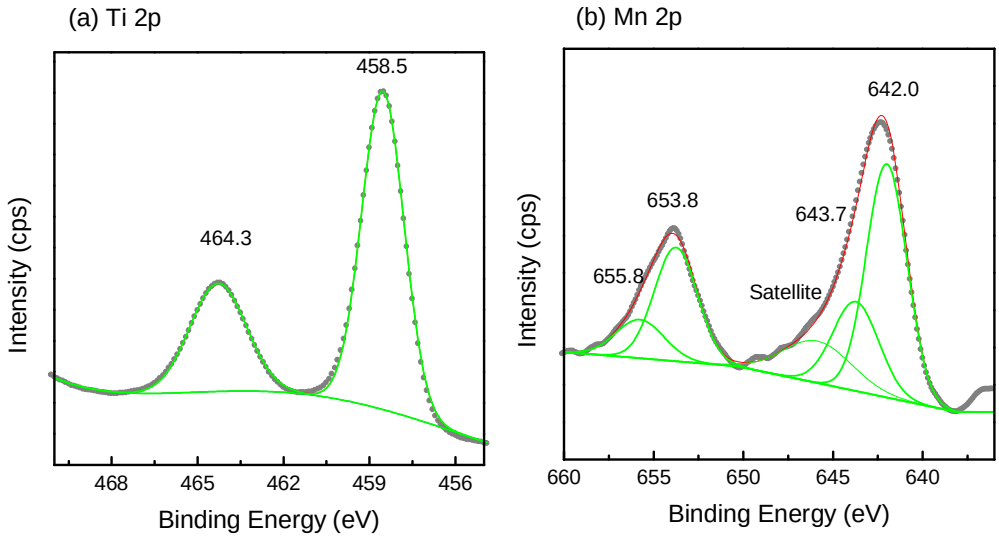

Figure 5.2.6 XPS patterns of (a) Ti 2p; (b) Mn 2p for 2 at% and 12 at% Mn-TiO_2.

5.2.2.3 Optical absorption properties

All doped samples exhibited pale grey color after being annealed at 400°C, with the color gradually deepening as the concentration of dopant Mn increases. Fig. 5.2.7, illustrates the UV–visible absorption spectra as a function of wavelength, measured by a Lambda UV–Vis diffuse reflection spectrometer, for Mn-TiO_2 samples together with pure phase. The absorption spectrum for the pure TiO_2 powder demonstrated a typical sharp edge at around 400 nm, which corresponded to the intrinsic electron excitation from the valence to the conduction band of semiconductor. The relative

band gap value was calculated to be 3 eV for pure anatase, being smaller than the reported experimental value of 3.2 eV, possibly due to the surface scattering induced optical trapping. Compared with the optical absorption edge pure TiO_2, significant optical absorption beyond the visible spectral region was observed from the Mn doped samples, since a secondary absorption shoulder was present and located around 580 nm in the absorbance spectra of all of the Mn doped samples in addition to the primary absorption edge at shorter wavelength. This is consistent with the recent theoretical study which showed that substitution of Ti ions by Mn ions into the TiO_2 matrix leads to remarkable red shift of the optical absorption edges by not only reducing the overall of band gap but also introducing curvy intermediate bands into the forbidden gap [3]. By increasing Mn doping level, the intensity of the secondary shoulder was enhanced, and thereby the absorption edge was shifted to longer wavelength together, being consistent with the theoretical prediction that band gap is reduced as increasing of Mn doping concentration via introducing intermediate bands into the virgin forbidden gap of rutle TiO_2 [3,6]. When the doping level reached 12 at%, optical absorption was extended obviously into the infrared spectral range. This leads to the observed red shift of principle absorption edge and the appearance of secondary absorption shoulder, extending absorption range well into the visible and even infrared spectral regions.

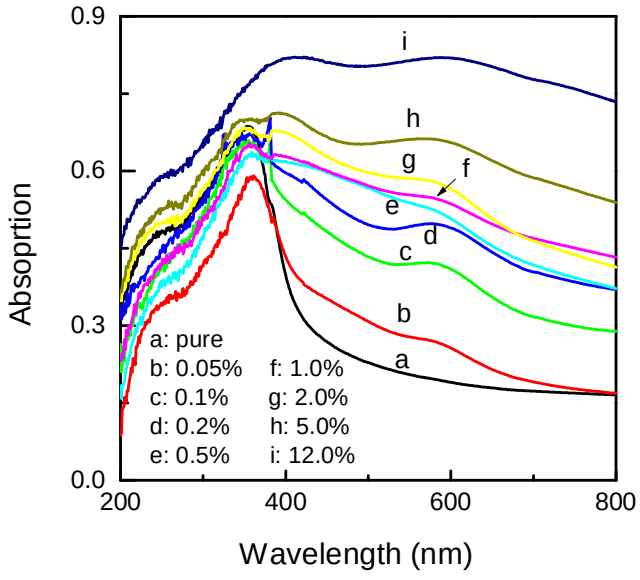

Figure 5.2.7 UV–visible absorption spectra of pure and Mn-TiO_2 powders.

Fig. 5.2.8 presents optical absorption spectra, measured by another apparatus with bigger test coverage, of the Mn-TiO_2 powders post annealed at 400°C and 800°C. It is seen from Fig. 5.2.8(b) that Mn doping also gave rise to significant affection on the absorption region of rutile TiO_2 with respect to that of pure one, extending absorbance over a large range of the spectral radiation from UV well into the infrared region. Albeit Mn was precipitated out as Mn_2O_3 in the samples with Mn content higher than 5 at%, the experimentally measured band gap of α-Mn_2O_3 was reported to be between 2.5~2.6 eV [11, 12], which hardly had influence on the long wavelength part of the absorption spectra. Therefore, it is also evidently concluded that Mn doping in rutile TiO_2 led to remarkable red shift in the band gap. In addition, it is worth mentioning that the secondary absorption shoulder disappeared in rutile Mn-TiO_2, being speculated to come from the mixing of interstitial levels with intrinsic bands.

Moreover, through comparing the optical spectra of the Mn-TiO_2 powders annealed at different temperature, we find rutile Mn-TiO_2 powders showed much stronger absorption intensity in the visible region, even though the substantial Mn in rutile Mn-TiO_2 was lower than that on anatase phase as mentioned in XPS analysis. This conceivably suggests Mn doping has much higher affection on the band gap narrowing of rutile phase than anatase phase TiO_2.

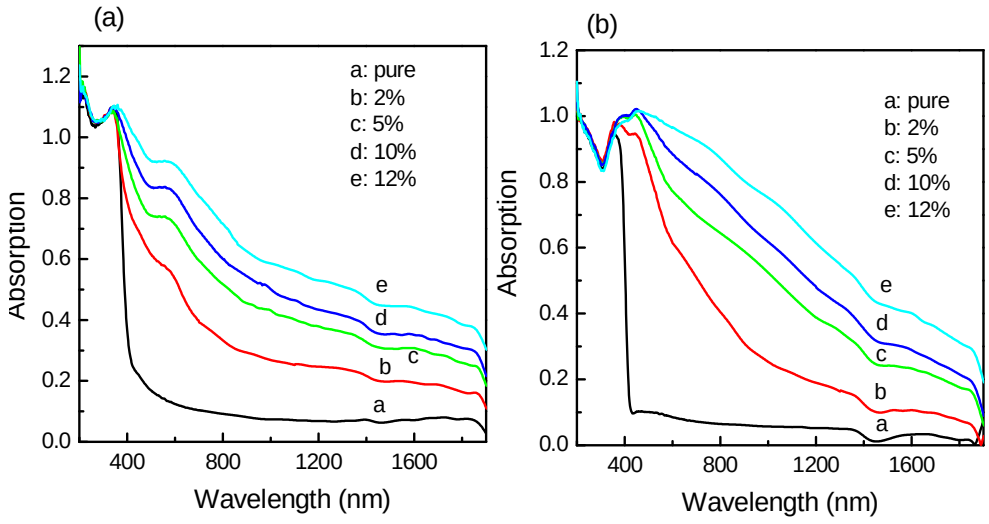

Figure 5.2.8 UV–visible absorption spectra of pure and Mn-TiO_2 powder annealed at 400°C (a) and 800°C (b).

5.2.2.4 Visible light photocatalytic activity

Although rutile Mn-TiO_2 powders show better optical absorption ability, the extremely large size makes them unsuitable for photocatalysis as the result of their small specific surface area. Accordingly, visible light photocatalytic activity of anatase Mn-TiO_2 powders by means of measuring the degradation of MB solution, as shown in Fig. 5.2.9. Generally speaking, the higher affinity of the dye to the surface of the catalyst particles gives rise to higher initial adsorption, leading to the initial adsorption of MB is different from one another [13]. Except for the adsorption of dye molecules on catalyst surfaces, visible light photocatalytic degradation rate of MB solution by pure TiO_2 material almost equals to the self degradation rate of MB under light illumination, owing to its poor absorption in the corresponding light region since the activity of a semiconductor photocatalyst is strongly influenced by its optical absorption. On the other hand, Mn-TiO_2 catalysts exhibited intensively improved visible light photocatalytic activity with respect to that of the pure TiO_2 powder. When the doping concentration was 0.2 at%, the photocatalytic activity reached a maximum value. Apparently, the highly improved photocatalytic activity of doped TiO_2 catalysts is attributed firstly to the narrower band gap of Mn doped TiO_2 powders, which permits enhanced photoelectric effect to generate charge carriers to assist photocatalytic reactions. Secondly, the smaller average grain sizes of the Mn-TiO_2 nanoparticles offer higher specific surface areas for the catalytic reactions, which are indicated by the discrepant adsorption efficiency of MB before radiation. Thirdly, an appropriate amount of Mn incorporation in TiO_2 on the Ti lattice sites induces intermediate bands as stepping stones for the generation of electrons and holes under photons of varied wavelengths [3,6], and the curvy nature, with associated high carrier mobility, of these intermediate bands helps excited carriers in them to reach the catalyst surfaces, therefore increasing the life time of charge carriers and yields a higher photocatalytic activity [6].

Similar to references that the photocatalytic activity of doped TiO_2 was strongly dependent on the dopant concentration [14,15,16], herein when the Mn doping level was beyond 0.2 at%, the gained photocatalytic activity began to disappear even though the optical absorption was further enhanced. This is because when the doping concentration becomes too high, a great many crystal defects could be induced,

which may serve as recombination centres to reduce photocatalytic activity. Fundamentally, these defect levels in TiO_2 are too localized to allow trapped carriers to migrate to the catalyst surface to take part in photocatalysis.

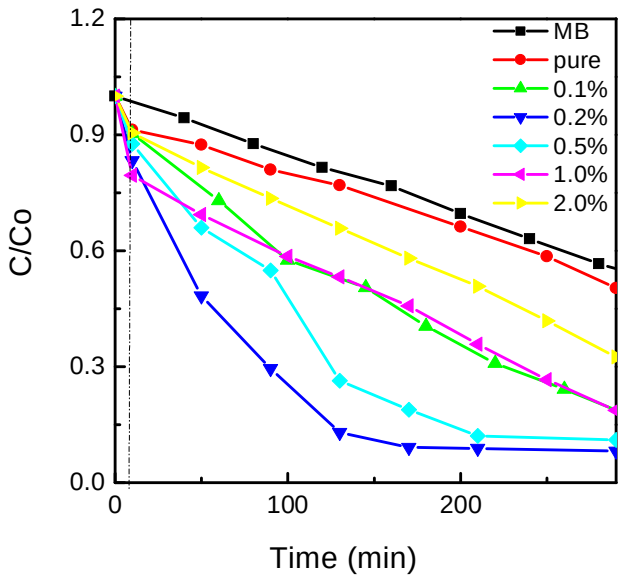

Figure 5.2.9 Photodegradation of methylene blue by TiO_2 powder under visible light.

5.2.3 Conclusions

In this work, Mn doped TiO_2 nanopowders have successfully prepared by means of a sol–gel method using ethanol–water as solvent. A remarkable red shift of the absorption edge was achievable through Mn doping, giving rise to gigantically narrowed energy gap to permit absorption well into the infrared spectral region. The Mn doped anatase TiO_2 powders exhibited considerable visible-light photocatalytic activity, leading to enhanced degradation rate of MB under visible light irradiance.

References

[1] Z. Wang, D. Xia, G. Chen, T. Yang, Y. Chen. The effects of different acids on the preparation of TiO_2 nanostructure in liquid media at low temperature. Materials Chemistry and Physics 111 (2008) 313-316.

[2] M. Gopal, W. J. M. Chan, L. C. D. Jonghe. Room temperature synthesis of crystalline metal oxides. Journal of Materials Science 32 (1997) 6001-6008.

[3] G. Shao. Red shift in manganese- and iron-doped TiO_2: a DFT+U analysis. The Journal of Physical Chemistry C 113 (2009) 6800–6808.

[4] T. K. Ghorai, S. K. Biswas, P. Pramanik. Photooxidation of different organic dyes (RB, MO, TB, and BG) using Fe(III)-doped TiO_2 nanophotocatalyst prepared by novel chemical method. Applied Surface Science 254 (2008) 7498-7504.

[5] J. Yu, M. Zhou, H. Yu, Q. Zhang and Y. Yu. Enhanced photoinduced super-hydrophilicity of the sol–gel-derived TiO_2 thin films by Fe-doping. Materials Chemistry and Physics 95 (2006) 193–196.

[6] G. Shao. Electronic structures of manganese-doped rutile TiO_2. The Journal of Physical Chemistry C 112 (2008) 18677-18685.

[7] J. Xie, D. Jiang, M. Chen, D. Li, J. Zhu, X. Lu, C. Yan. Preparation and characterization of monodisperse Ce-doped TiO_2 microspheres with visible light photocatalytic activity. Colloids and Surfaces A: Physicochemical and Engineering Aspects 372 (2010) 107-114.

[8] B. Murugan, A. V. Ramaswamy. Chemical states and redox properties of Mn/CeO_2-TiO_2 nanocomposites prepared by solution combustion route. Journal of Physical Chemistry C 112 (2008) 20429-20442.

[9] C. Lee, B. Nam, W. Choi, J. Lee, D. Choi, Y. Oh. Mn: SnO_2 ceramics as p-type oxide semiconductor. Materials Letters 65 (2011) 722–725.

[10] M. A. Kostowskyj, D. W. Kirk, S. J. Thorpe. Ag and Ag–Mn nanowire catalysts for alkaline fuel cells. International Journal of Hydrogen Energy 35 (2010) 5666–5672.

[11] H. Minoura, M. Nasu, Y. Takahashi. Comparative studies of photoelectrochemical behaviours of rutile and anatase electrodes prepared by OMCVD technique. Berichte der Bunsengesellschaft für physikalische Chemie 89: 1064–1069.

[12] K. J. Kim, Y. R. Park. Sol–gel growth and structural and optical investigation of manganese-oxide thin films: structural transformation by Zn doping. Journal of Crystal Growth 270 (2004) 162-167.

[13] K. Sopajaree, S. A. Qasim, S. Basak, K. Rajeshwar. An integrated flow reactor-membrane filtration system for heterogeneous photocatalysis. Part I: Experiments and modelling of a batch-recirculated photoreactor. Journal of Applied Electrochemistry 29 (1999) 533-539.

[14] A. Fujishima, T. N. Rao, D. A. Tryk. Titanium dioxide photocatalysis. Journal of Photochemistry and Photobiology C: Photochemistry Reviews 1(2000) 1–21.

[15] M. Zhou, J. Yu, B. Cheng. Effects of Fe-doping on the photocatalytic activity of mesoporous TiO_2 powders prepared by an ultrasonic method. Journal of Hazardous Materials 137 (2006) 1838–1847.

[16]P. R. Ettireddya, N. Ettireddya, S. Mamedovb, P. Boolchandc, P. G. Smirniotis. Surface characterization studies of TiO_2 supported manganese oxide catalysts for low temperature SCR of NO with NH_3. Applied Catalysis B: Environmental 76 (2007) 123–134.

Chapter 6 Structural engineering of vertically aligned TiO_2 nanorod thin films

6.1 Experimental details

The material synthesis procedure began at cleaning the substrates of the FTO coated glass with acetone, absolute ethanol and deionised water in sequence. The substrates were then dried under ambient condition. The chemical precursor solutions were obtained by dissolving 30 ml of concentrated hydrochloric acid (36.5%–38% by weight) in a 30 ml solution of mixed deionised water and absolute ethanol with various volumetric ethanol/water ratios. The chosen HCl concentration was based on previous work of Liu for optimum restraint of oxide precipitation and solution stability [1]. The mixture was stirred at ambient condition for 5-minutes before adding a specified volume of $Ti(OBu)_4$. After stirring for another 5-minutes, two pieces of substrates were placed at an angle against the wall of a Teflon lined steel autoclave (180 ml volume) with the conducting side of the FTO facing downward. The hydrothermal synthesis was conducted at 150°C-180°C for several hours. After synthesis, the autoclaves were cooled to room temperature under running water for about 15-minutes. The samples were then taken out and immersed into deionised water for 3-hours, and then rinsed extensively and dried in ambient air.

6.2 Results and discussion

6.2.1 Microstructures of TiO_2 nanorod thin films

Fig. 6.1(a) presents the high magnified surface SEM images of the samples synthesized for 20-hours by using H_2O, HCl and $Ti(OBu)_4$ as the starting material. Apparently, the FTO substrates were covered by the uniform porous network structures formed by a large amount of nanorods regardless the reaction time. Being consistent with Liu and Aydil [1], the separately grown nanorods were loosely populated on the FTO substrate, and the macroscopic morphology of the nanorod was characteristic of a tetragonal compound phase such as the rutile TiO_2. Viewing closer, as shown as inset in Fig. 6.1(a), it was observed that each nanorod was

tetragonal in shape with square to surface and comprised of ten to tens of neighboring nanofibres, with diameter approximately 10 nm. Fig 6.1(b) shows the relative cross sectional SEM image of the sample, in which the film was largely made of aligned nanorods, being nearly perpendicular to the surface of substrate, together with some mis-aligned rods. The longitudinal length of the nanorod was measured to be around 2.7 μm, suggesting the longitudinal growth speed of nanorod was at least one order faster than lateral growth. Moreover, it was found that partial initially formed nanorods, close to FTO surface, stopped growing cross the whole thin film, due to the fact that the nanorods in the upper of thin film was not as dense as those at the bottom.

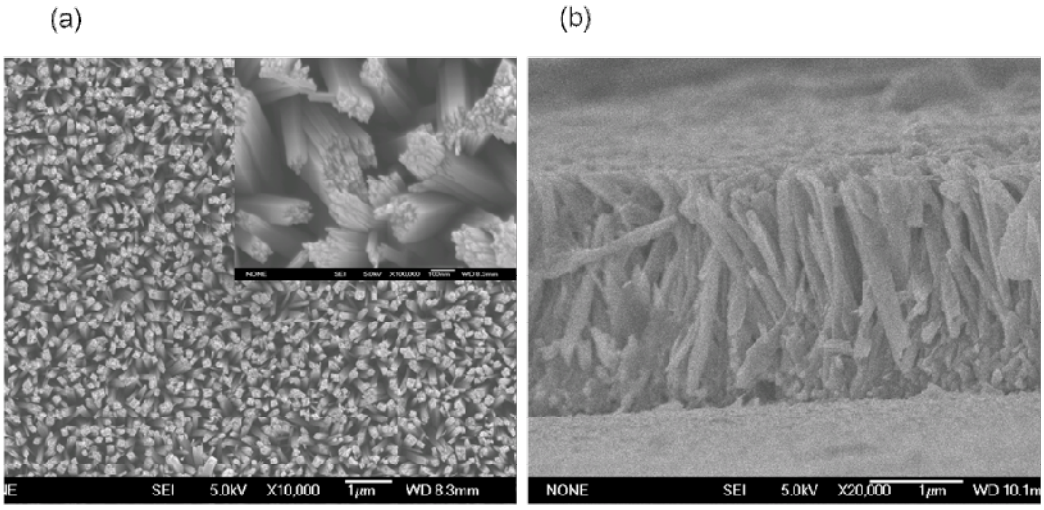

Figure 6.1 (a) surface SEM image, (b) cross section SEM image of the sample prepared with pure water as solvent for 20h.

In order to confirm the crystal structure of this TiO_2 thin film, X-ray diffraction (XRD) pattern of the as-prepared TiO_2 thin film was measured as shown in Fig. 6.2(a). To assign all diffraction peaks, the XRD pattern of FTO substrate was also shown as reference. By identifying diffraction peaks, except for those from substrate, the nanorods can be classified as having a standard tetragonal rutile structure. As marked on, only two peaks owing to R (101) and R (002) planes were observed, except for the diffraction peaks coming from FTO substrate, and all other diffraction peaks were missing. The missing of (110) diffraction peak, which is the predominant

diffraction peak of TiO_2 polycrystalline powders, indicates the as synthesized TiO_2 film had preferred growth orientation even though the oriented direction can hardly be identified by the observed XRD diffraction pattern. This agreed well with the observed rod-like column structure in the SEM image.

The optical absorption property of this film was also measured and shown in Fig. 6.2(b), wherein the longitudinal coordinates α^2 was plotted as the function of photon energy hv to determine the direct band gap of rutile TiO_2. By extrapolating the liner part of plotted line to the photon energy axis, the band gap of the sample was estimated to be 3.0 eV, being consistent well with the band gap of bulk rutile TiO_2. In the range of photo energy lower than 3.0 eV, the thin film maintained the low absorption coefficient of bulk TiO_2 materials.

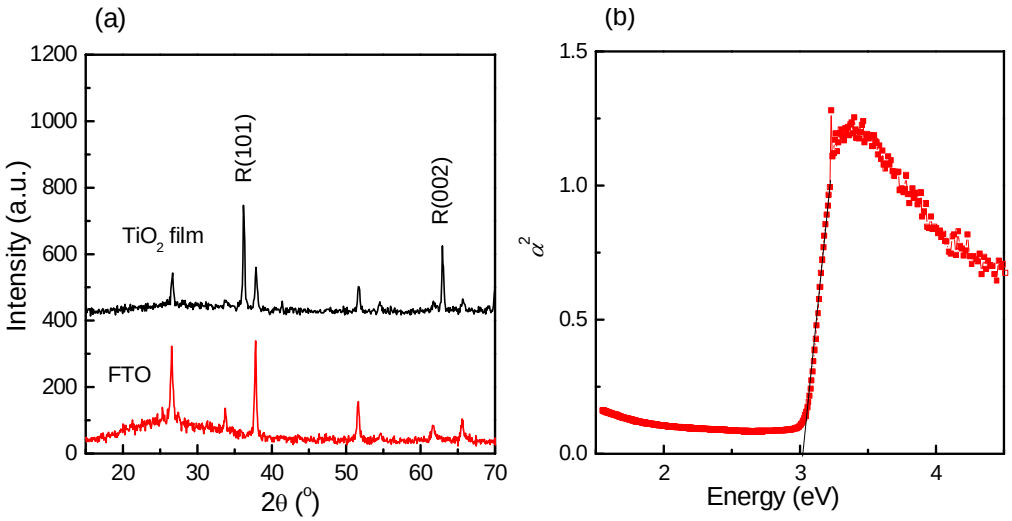

Figure 6.2 (a) XRD pattern and (b) α^2 versus hv plot of the thin film prepared with pure water as solvent for 20-hours.

TEM was employed to reveal the fine structure within each nanorod by peeling off the nanorods from FTO substrate. As depicted in Fig. 6.3(a), a single nanorod with neat and sharp edges was clearly seen. The corresponding SAED pattern from the rod measured along [110] zone axis was shown in Fig. 6.3(b), in which a symmetric diffraction pattern corresponding to a single rutile crystal diffraction pattern was identified and marked on. Through comparing the diffraction pattern with the TEM

image, one can see the longitudinal growth direction of the nanorod was [001] and the [110] axis was perpendicular to the nanorod side wall, suggesting that the [001] direction was the preferred growth direction which was nearly perpendicular to the substrate plane. This understandably explained the appearance of R(002) and R(101) peaks in XRD pattern, wherein R(101) originating from the small deviation of rod axis from the normal of substrate.

Fig. 6.3(c) is a corresponding high resolution TEM (HRTEM) image to show the refined structural features between the nanofibres. Discernibly, each nanorod was indeed made of oriented nanofibres parallel to each other, with an average fibre diameter of about 5 nm to form a collective columnar nanorod. It is obvious from Fig. 6.3(d) that individual nanofibre was completely crystallized as single crystal without grain boundary along their whole length. Inter planar spacing along growth direction was measured to be 2.9±0.5 Å, being in good agreement with (001) spacing of rutile phase according to the standard JCPDS card. In spite of great care, only one set of diffraction pattern was seen from the corresponding fast Fourier transformation (FFT) image of a nanofibre, as inset in Fig. 6.3(d), demonstrating the nanofibre was a single rutile crystal growing along [001] direction.

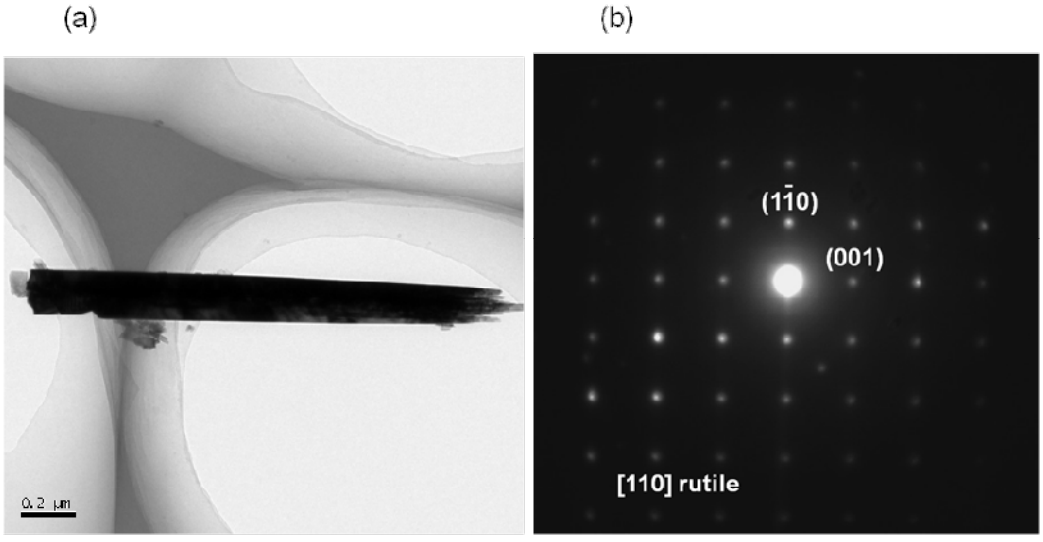

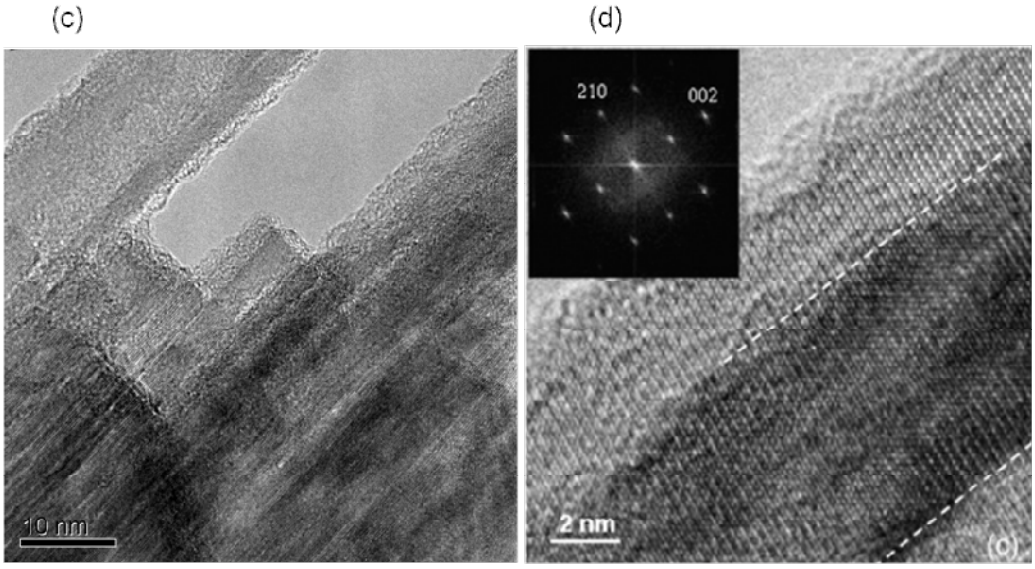

Figure 6.3 (a) TEM image, (b) SAED pattern of one typical nanorod; (c) and (d) high resolution TEM of nanofibres, with inset being the corresponding fast Fourier transformation (FFT) image.

Several reasons are contributable to the formation of oriented single crystalline rutile TiO_2 nanorod thin film along [001] direction by using hydrothermal method. At first, high concentration of H^+ in solution significantly slowed the condensation process with respect to the enhanced hydrolysis process, resulting in a repulsive charge and limited the size of formed precipitates, leading to the presence of free TiO_2 growth units in solution [2,3,4]. These octahedrons can move freely and then link together to give crystalline TiO_2 phases, being advantageous for uniform nucleation on top of FTO surface and crystal growth of TiO_2 through the whole thickness. On the other hand, it has been reported that high concentration of H^+ in solution also provides slow kinetic condition for the formation of long –Ti-O-Ti chains essential for the formation of rutile phase [5,6].

Besides, the growth of TiO_2 nanorod arrays on glass substrate was unsuccessful, suggesting the FTO substrate was also central to the growth of TiO_2 owing to its similar tetragonal rutile structure. The small lattice mismatch of rutile TiO_2

(a=b=0.4594 nm) [7] and FTO (a=b=0.4687 nm) [8] along c-axis promoted the epitaxial nucleation and growth rutile TiO_2 thin film on top of FTO.

Moreover, the (110) plane corresponds to the lattice planes of the lowest surface energies for the pure rutile phase on the basis of the theoretical predictions using DFT modelling [9,10]. According to the energy minimization principle, during crystal growth the high-energy surface tends to decrease its surface area while the low-energy surface will increase its surface area, so as to decrease the total surface energy per crystal. Thus the (110) surface is supposed to grow fastest and has the biggest surface area, while the surface (001), being perpendicular to (110), tends to be small or even disappear. Because of the evident anisotropic surface energies of the tetragonal lattices of the rutile phase, during hydrothermal process, minimization of overall surface energy was pivotal for the realization of self-assembling of nanorods along [001].

Furthermore, the connecting manner of TiO_6^+ units determines the final crystal phase and structure [6]. In this work, the presence of Cl^- could preferentially adsorb on rutile (110) surface and retarded the contact of TiO_2 growth units onto (110) surface and thus extensively limited the lateral growth [11], which in turn promoted TiO_2 crystal growth into rod instead of particle.

6.2.2 Effect of hydrothermal reaction time

To study the growth mechanism, the morphologies of TiO_2 nanorod thin films synthesized under different hydrothermal reaction time were measured by SEM. Fig. 6.4 presents the high magnification SEM images of the samples synthesized for hydrothermal reaction time of 3-hours (a), 8-hours (b), and 20-hours (c) using H_2O, HCl and $Ti(OBu)_4$ as the starting material. When the reaction time was 3-hours, isolated nanorods are randomly distributed on the FTO surface with rod axis at certain angles with respect to the substrate. This was mainly owing to the rough surface of random oriented polycrystalline FTO substrate, even though the nanorods nucleated and grew epitaxially on FTO grains. The nanorod was measured to have 400 nm in length and about 20 nm in diameter, indicating the longitudinal growth speed was approximately 20 times bigger than lateral growth. As the extending of reaction time, it was found that the diameter of the nanorod increased to about 100

nm when the growth time was 20-hours, accompanied by the increasing of longitudinal length to 2.7 μm, due to 3-dimensional crystal growth. On the other hand, the nanorods shown in Fig. 6.4(c) were better aligned than those synthesized for shorter time, since some of those initially unoriented nanorods, shown in Fig. 6.4(a), eventually run into a neighbouring nanorod and stopped growing, leaving well aligned nanorods to keep growing and leading to the reduced number of nanorods in a specific area.

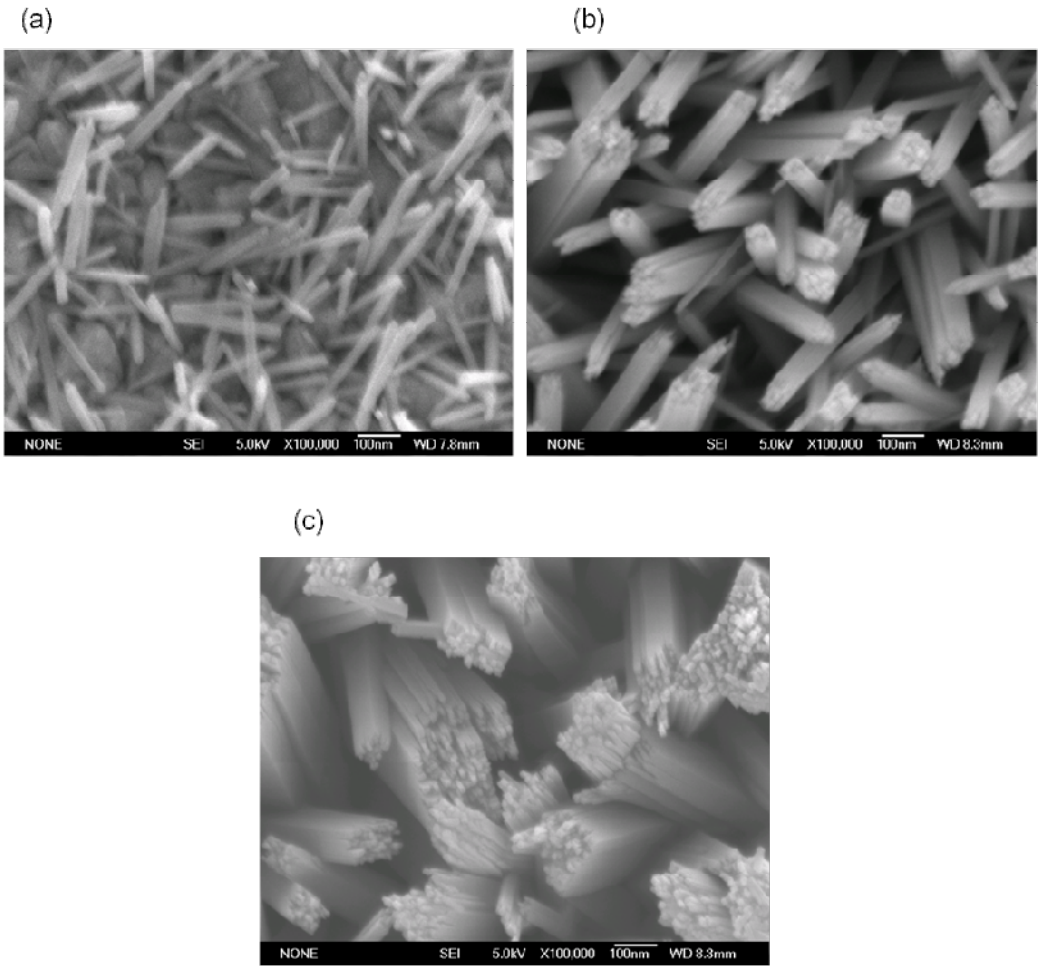

Figure 6.4 Surface SEM images of the samples prepared at 150°C for (a) 3-hours, (b) 8-hours, and (c) 20-hours.

X-ray diffraction (XRD) pattern of as-prepared TiO_2 films were measured to clarify the orientation of thin films as shown in Fig. 6.5, with the XRD pattern of FTO

substrate shown as reference. However, no other diffractive peak can be seen when the hydrothermal growth time was 3-hours, being conceivably attributed to the fact that the nanorods were sparse and unoriented with respect to substrate normal evidenced by the SEM image. Moreover, only single TiO_2 (101) diffraction peak at ~36.1° appeared except for the peaks form FTO substrate when the reaction time was 8-hours. It was corroborated before that the growth orientation of nanorod was [001], with the appearance of (101) diffraction peak coming from the disorder of nanorods. Therefore, the appearance of R(101) together with the absence of R(002) suggested the nanorods were not well oriented along the normal direction of substrate plane, being in line with SEM image that nanorods were standing obliquely on the FTO surface. When the hydrothermal reaction time was prolonged to 20-hours, R(002) diffraction peak appeared apart from the R (101) peak, indicating these nanorods were better oriented with rod axis having smaller deviation from the normal direction of substrate plane compared with the nanorods in thin film synthesized under shorter reaction time.

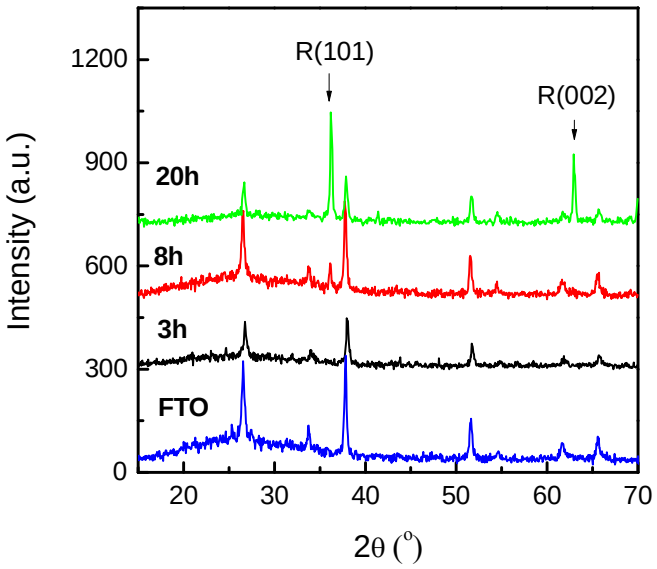

Figure 6.5 XRD of the samples prepared at 150°C volume ratios of (a) 3-hours, (b) 8-hours and (c) 12-hours.

Based on the results obtained above, it is concluded that the diameter and relative longitudinal length can be adjusted by controlling the hydrothermal reaction time, resulting in that thicker thin film has higher packing density of nanorod with smaller angle of rod axis to the normal of FTO surface. However it is worth mentioning that the increase of packing density was always accompanied by the increasing of longitudinal length; and one can hardly get a dense nanorod film with thin thickness by prolonging reaction time. Therefore, the initial nucleation density on the surface of FTO, being influenced by various parameters, including concentration $Ti(OBu)_4$, the reaction temperature and the pressure in autoclave, is expected to play key role on the packing density of final nanorod thin film.

6.2.3 Effect of precursors: type of alcohol

We have discovered for the first time in this work that the introduction of alcohol into the precursor solution has remarkable effect on the structural evolution of the TiO_2 nanorods. Here we demonstrate the alcohol effect, using alcohol to substitute some water in the solvent and allowing the reaction for a specific period of time (8-hours). To reveal the influence mechanism of alcohol on the properties of structured TiO_2 thin film, with increased molecular sizes, several kinds of alcohols including methanol, ethanol and butanol, were studied by using 5 ml alcohol to substitute same volume of water in the solvent.

The surface morphologies were measured by SEM as presented in Fig. 6.6, in which all graphs are under same magnification. As presented in Fig. 6.6(d), thin film synthesized in pure water solvent was composed of isolated nanorods uniformly distributed on the FTO surface, with respect to the substrate, with rod axis at certain angles. However, it is striking to discover that the packing density was significant promoted by replacing 5 ml water solvent with alcohols even though the morphologies were similar. It was seen that the introduction of methanol had the most significant effect on preparing dense nanorods thin film, followed by ethanol and butanol. The relative thickness of thin films with methanol, ethanol or butanol in solvent were measured by cross sectional SEM to be 2.7 um, 1.9 um and 1.0 um, respectively.

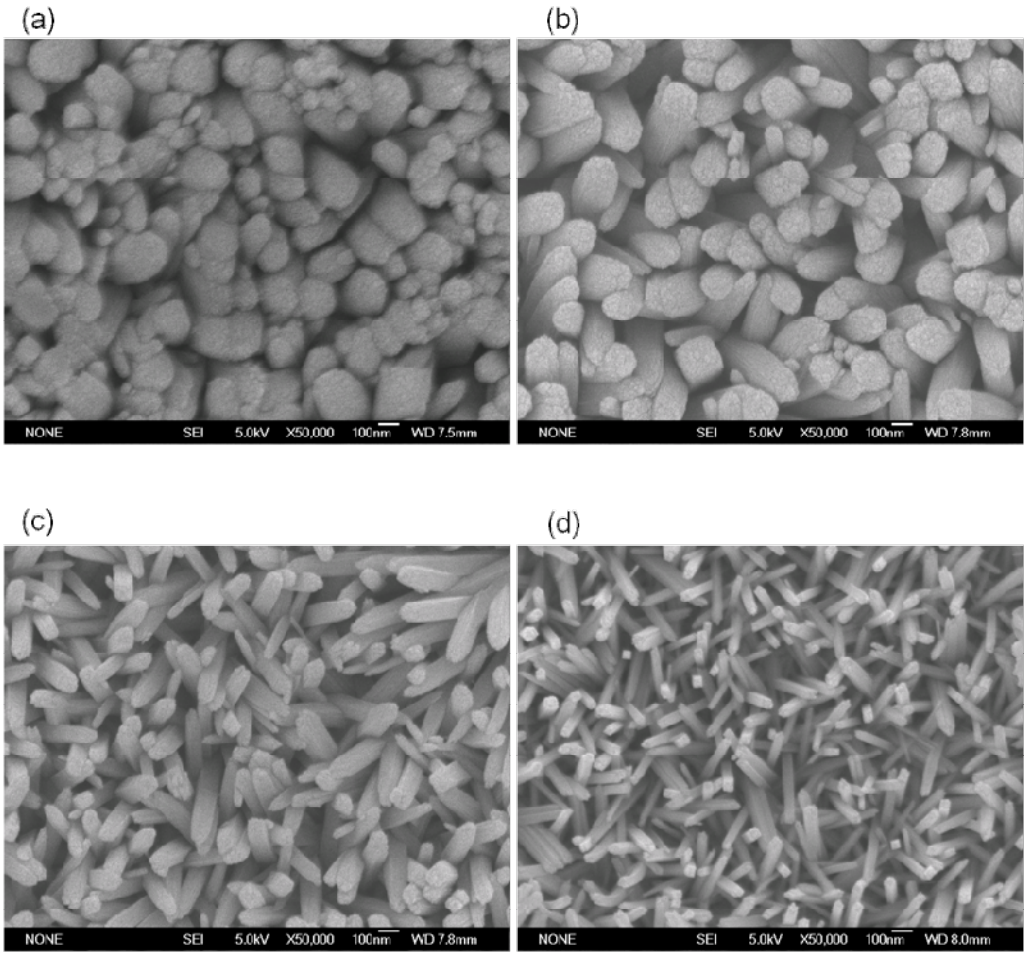

Figure 6.6 Surface SEM images of the films synthesized by replacing 5 ml water by (a) methanol, (b) ethanol, (c) butanol, (d) water.

The corresponding XRD patterns of these thin films are presented in Fig. 6.7, wherein R (101) and R (002) peaks were identified except for peaks from FTO substrate. Obviously, only R (101) instead of R (002) peak appeared in the film synthesized in pure water solvent and slight R(002) appeared in thin film with butanol. Compared to these, the relative ratio of R(002) peak to R (101) was increased in thin film with ethanol, and further increased in thin film with methanol, which suggests that thin film with alcohol of smaller molecular size was better aligned along the normal of substrate, being consistent with SEM images.

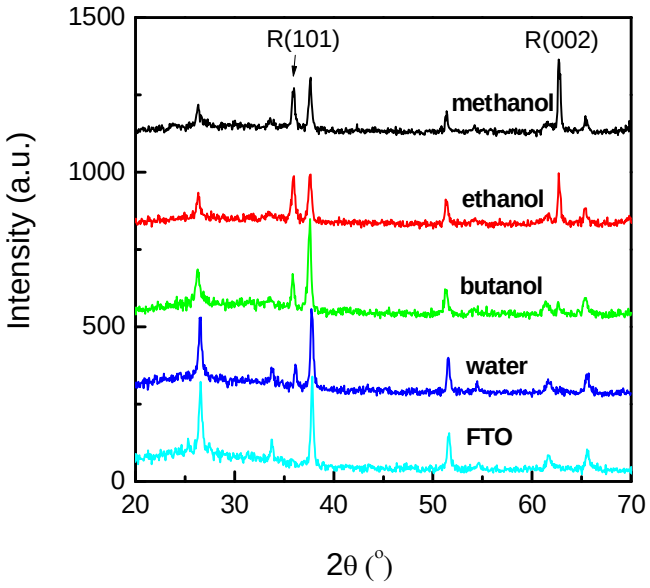

Figure 6.7 XRD patterns of the films synthesized by replacing 5 ml water by different alcohol.

The molecular sizes of the alcohols are important to the formation kinetics of TiO_2 films. The synthesis of TiO_2 is through a two-stage hydrolysis-condensation process [12,13]. The hydrolysis process for a titanium tetraalkoxide, the $Ti(OB)_4$ in this work, is fulfilled through either of the following reactions:

$$Ti(OB)_4 + H_2O \rightarrow Ti(OH)_4 + 4BOH \quad (6.1)$$

$$Ti(OB)_4 + ROH \rightarrow Ti(OH)_4 + 4BOR \quad (6.2)$$

wherein R represents an alkoxyl group, and B is the butoxyl group. While both alcohol and water can provide the (OH) needed for the hydrolysis process, alcohols are less effective due to their larger molar volumes than water. Therefore, the volumetric alcoholic substitution of water as solvent would weaken the hydrolysis reaction, and bigger alcohol molecules (with bigger alkoxyl group sizes) can thus be envisaged to promote the condensation through weakened hydrolysis via enhanced solution disability. The condensation process occurs via dehydration:

$$2Ti(OH)_4 \rightarrow (OH)_3Ti\text{-}O\text{-}Ti(OH)_3 + H_2O \quad (6.3)$$

which is carried out by losing water to provide the –[Ti–O–Ti]– chains to construct the TiO_2 crystal structures. On the other hand, it has been discovered that the alkoxyl group in a metal alkoxide such as $Ti(OBu)_4$ tends to be partially replaced by smaller alkoxyl groups in the solvent [14]:

$$Ti(OBu)_4 + ROH \rightarrow Ti(OBu_{1-x}R_x)_4 + 4Bu_xR_{1-x}OH \quad (6.4)$$

The partially replaced titanium tetraalkoxide is expected to help the hydrolysis kinetics, due to the weaker bond dissociation energy, while the lowered OH concentration due to alcohol replacement of water offers kinetic advantage to dehydration. Although the film growth is largely owing to condensation (dehydration), adequate hydrolysis is key to safeguard the maximized use of the titanium tetraalkoxide for film growth. Overall, the balanced effect on the two stages of synthesis could make ethanol the most effective in promoting the condensation process for thin film growth.

6.2.4 Effect of precursors: ratios of water and ethanol

Fig. 6.8(a)-(d) give SEM morphologies of the films formed with different volumetric ethanol/water ratios. As it is shown in Fig. 6.8(a), the film, with thickness measured to be 500 nm, were composed of isolated nanorods uniformly distributed on the FTO surface with rod axis at certain angles with respect to the substrate. With a moderate 5 ml ethanol substitution of water as solvent, the morphology of the thin film was similar to that synthesized using only water as solvent, with nanorods being roughly perpendicular to the substrate as shown in Fig. 6.8(b). It is disturbing to notice that the total length of the nanorods reached 1.9 μm within only 4-hours, suggesting that the average growth rate was nearly five times of those grown using pure water as solvent. As the ethanol volume was increased to 10 ml (30% of solvent volume), it was clearly observed in Fig. 6.8(c) that the gaps between nanorods were disappearing as the packing density of the nanorods was further increased, resulting in densely packed thin film made up of homogeneously distributed and well-aligned nanofibres. Moreover, completely dense and smooth thin films were achieved when the ethanol volume reaches 15 ml (50% replacement of water), with the longitudinal growth rate being enhanced further to result in an average nanofibre length of 3.8 μm in 4 h. The corresponding thickness versus ethanol volume was plotted in Fig. 6.8(f),

in which the thickness of synthesized thin film was eminently increased by increasing ethanol volume in solvent. However, some cracks occur in dense packed nanofibre thin film because of the coarse surface of FTO substrate. Fig. 6.8(e) shows a tilted view from the one crack, wherein well aligned fine nanofibres were discernibly seen, suggesting the observed dense thin films were made up of vertical aligned nanofibres with respect to substrate.

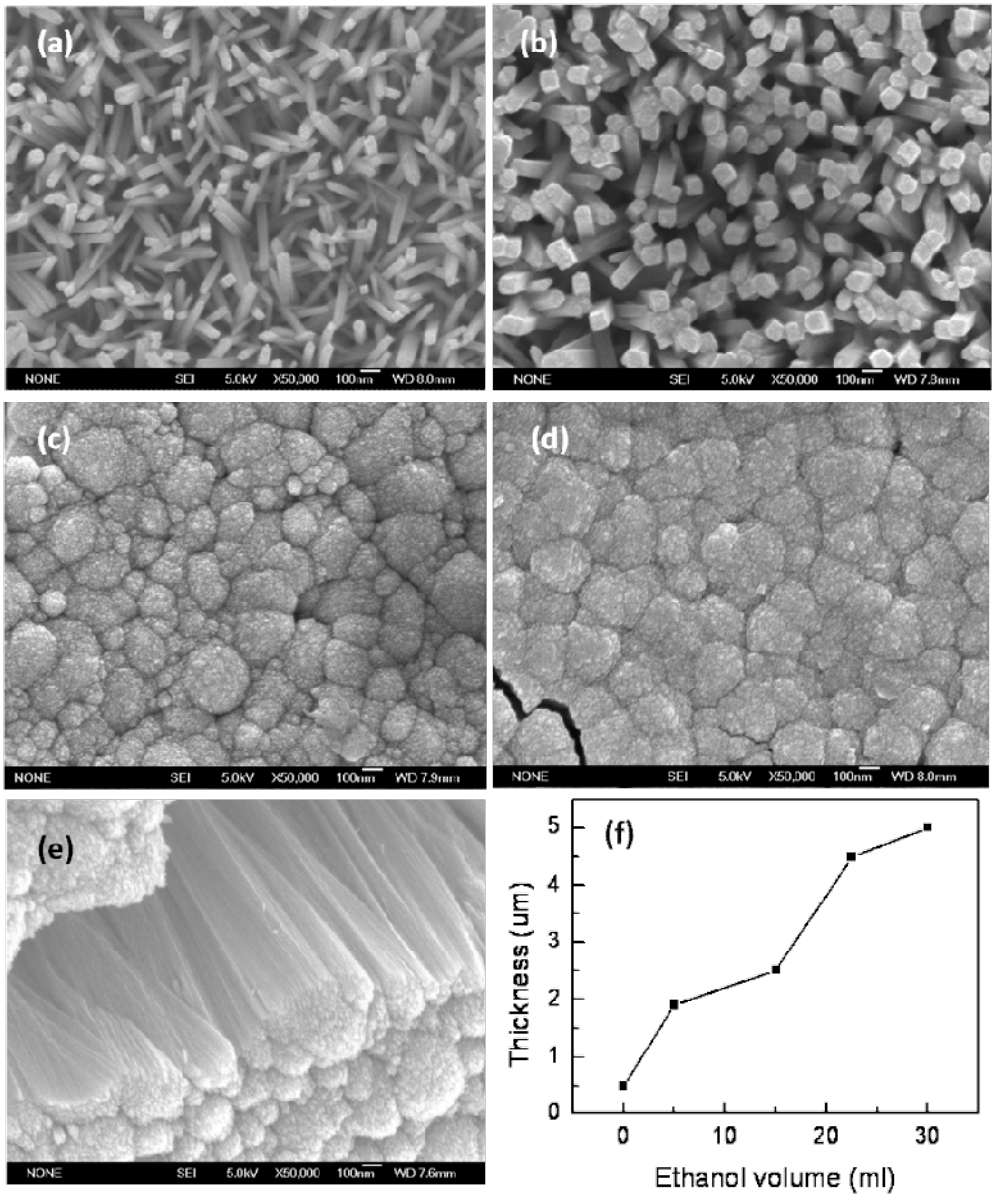

Figure 6.8 Surface SEM images of the samples prepared at 150°C for 4-hours with ethanol/water volume ratios of (a) 0:30, (b) 5:25, (c) 10:20, (d)15:15, (e) tilted view from one crack, (f) the thickness of thin films versus ethanol volume in solvent.

Fig. 6.9(a) presents the relative XRD patterns of thin films formed with different volumetric ethanol/water ratios, together with the spectrum of the FTO substrate as a reference. There were only two peaks owing to the (101) and (002) planes of rutile TiO_2 and all other diffraction peaks of TiO_2 were missing. In addition, the intensity of the FTO peaks decreased with respect to increased amount of ethanol substitution of water, conceivably owing to the ethanol induced enlargement of the film thickness. Apparently, the intensity of the rutile (002) diffraction peak, R(002), increased with increasing ethanol concentration, in contrast to reduced intensities for the (101) peak of rutile TiO_2, suggesting the presence of ethanol in the solvent enhanced the preferential growth in the [002] direction.

The ratio of the peak intensity between the R(002) and R(101) peaks was derived from Fig. 6.9(a) and shown in Fig. 6.9(b). It is worth mentioning that the ratio was drastically decreased with increasing ethanol substitution of water in the solvent, revealing the orientation of TiO_2 nanofibres (or nanorods) was promoted by the introduction of ethanol. The existence of the diffraction peak R(101) indicated the occurrence of some degree of random growth off the [002] normal growth direction. Such random growth mainly occurred at the initial stage of nucleation, and the relative nucleation density was the main factor to affect the population of random crystals [1]. The observed reduction of peak ratio suggests that the random growth was suppressed as the ethanol concentration increased, since the ethanol induced higher nucleation rate being advantageous to offer adequate population of the preferred [002] growth direction.

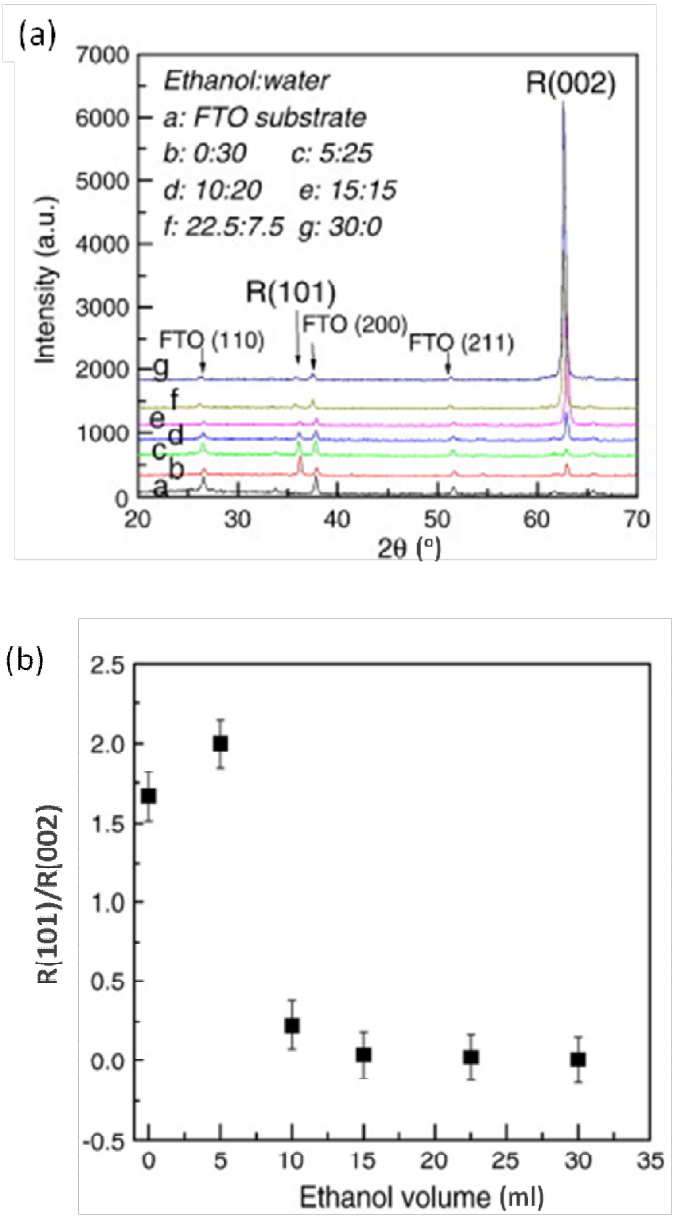

Figure 6.9 (a) XRD diffraction patterns of samples prepared at 150°C for 4-hous with different ethanol/water volume ratios, (b) the ratio of R(101)/R(002) versus ethanol volume in solvent.

6.2.5 Effect of reaction temperature

Evidently, hydrothermal temperature also had an effect on the structure of TiO_2 thin films as shown in Fig. 6.10, which were synthesized at 130°C, 150°C and 180°C for

4-hours, with 15 ml ethanol and 15 ml water as solvent. It was seen that the packing density was increased from rod like film to dense self assembled nanofibres films when the reaction temperature elevated from 130°C to temperature higher than 150°C. The corresponding XRD patterns in Fig. 6.10(d) shows that the R(002) peak was enhanced eminently in contrast to the same intensity of R (101) by elevating hydrothermal temperature, indicating the longitudinal orientation R (001) of nanofibres were better along the substrate normal. On the other hand, in spite of same reaction time of 4-hours, 130°C resulted in thin film of 950 nm in thickness while the thickness for thin films under 150°C and 180°C were 2.3 μm and 4.1 μm, respectively. This is not hard to understand, as higher temperature gave rise to faster crystallization kinetic via promoting nucleation and growth owing to higher diffusion coefficient. Under fast crystallization process, nanofibre of certain angle with respect to substrate would easily come into contact with others and thus stop growing, leading to well aligned nanofibre TiO_2 thin film.

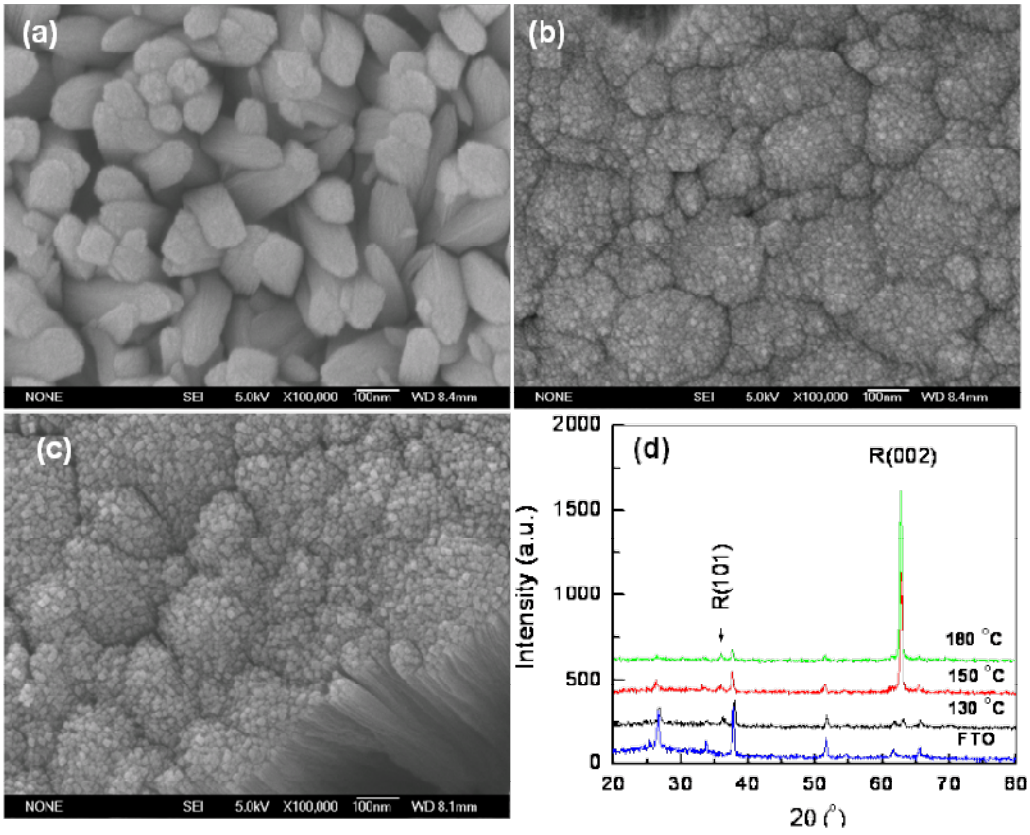

Figure 6.10 SEM images of thin films synthesized at (a) 130°C, (b) 150°C, (c) 180°C, (d) XRD diffraction patterns of thin films synthesized at different temperatures.

6.2.6 Effect of $Ti(OBu)_4$ concentration

We further investigated the effect of $Ti(OBu)_4$ on the formation of the TiO_2 nanorods structures in 30 ml absolute ethanol for 4-hours at 180°C. Fig. 6.11 presents the SEM images of the three thin films synthesized using 2 ml, 6 ml or 8 ml $Ti(OBu)_4$. Apparently, only particle like dots can be seen from surface view of all three thin films. From the cross section view presented as insets, we found thin films were obviously composed of self aligned nanorods, suggesting the observed dots in surface SEM images were the tips of nanorods. For different $Ti(OBu)_4$ volume of 2 ml, 4 ml and 8 ml, the thickness of thin films were measured to be 5.4 um, 6.9 um and 12.2 um respectively, since the increase of $Ti(OBu)_4$ volume promoted hydrolysis speed giving rise to higher nucleation density and growth speed.

It is worth to point out the white aligned nanorod thin film began to peel off when the $Ti(OBu)_4$ volume was more than 4 ml, as seen from Fig. 6.11(b) and (c). The substrate conductivities remained after the removal of TiO_2 nanorod thin film, revealing the peeling off occurs at the FTO-TiO_2 interface. Internal mechanical stress exists in all materials due to lattice mismatch and different thermal expansion between thin films and substrate, due to stress, leading to elastic energy stored in the thin film [15]. The stored elastic energy per unit area of thin film, μ_s, is expressed by

$$\mu_s = \frac{\sigma^2 d}{2Y} \ (J/m^2) \qquad (6.5)$$

Where σ is the internal stress, Y is Young's modulus of thin film and d is the thickness of the thin film. Thus thicker thin film is corresponding to lager μ_s. When the μ_s is higher than the adhesive energy of a film to substrate, which is strongly dependent on the chemical nature, cleanliness and the micro topography of substrate surface, the film will peel off. On the other hand, the crystal growth and dissolution processes coexist in hydrothermal reaction. In the process of synthesizing TiO_2 thin film on FTO substrate, the precursor in autoclave was firstly heated up, leading to fast diffusion and intensive hydrolysis of titanium precursor and in solvent, thus nanorods grew. Then after a period of reaction time, the autoclave was cooled down and crystal growth started to decrease as the system approached equilibrium.

Simultaneously, crystal dissolution on high energy FTO-TiO_2 surface became dominant, resulting in the peeling of TiO_2 thin films.

From the XRD pattern presented in Fig. 6.11(d), we can see the R(001) orientation was promoted as only R(101) peaks of TiO_2 can be seen with some tiny peaks from FTO substrates. The absence of R (101) suggests all nanorods were well aligned and perpendicular to substrate because the starting nucleation density was too high the nanorods had no space to go, with respect to substrate, except for growing perpendicularly.

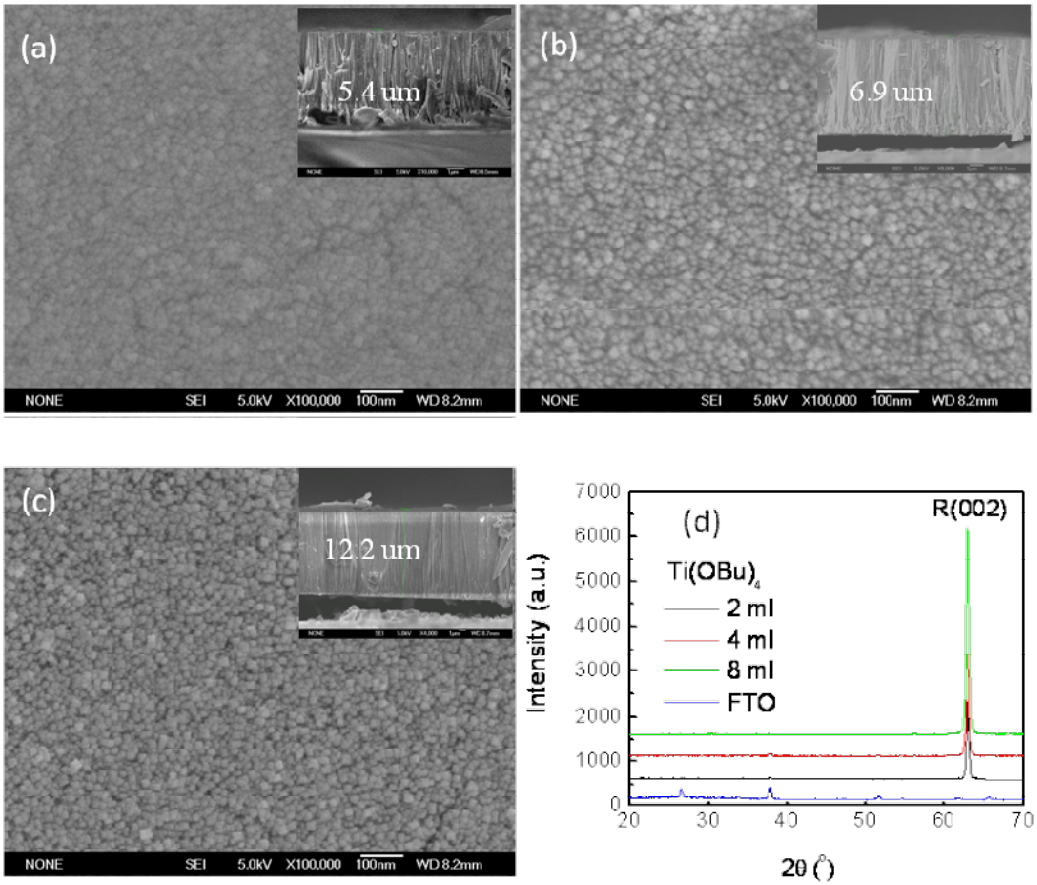

Figure 6.11 SEM images of TiO_2 thin films synthesized with different amount of $Ti(OBu)_4$ (a) 2 ml, (b) 4ml, (c) 8 ml and (d) XRD patterns of TiO_2 thin films synthesized with different amount.

6.3 Conclusions

In this part of work, single rutile TiO_2 nanorod and nanofibre thin films, with preferred [002] orientation, were successfully synthesized on FTO substrate. Through adjusting the reaction duration, alcohol substitution of water as solvent, reaction temperature, and $Ti(OBu)_4$ concentration TiO_2 thin films of different packing density and thickness were well controlled for various potential applications.

References

[1] B. Liu, E. S. Aydil. Growth of oriented single-crystalline rutile TiO_2 nanorods on transparent conducting substrates for dye-sensitized solar cells. Journal of the American Chemical Society 131 (2009) 3985-3990.

[2] D. A. H. Hanaor, C. C. Sorrell. Review of the anatase to rutile phase transformation. Journal of Materials Science 46 (2010) 855-874.

[3] S. T. Aruna, S. Tirosh, A. Zaban. Nanosize rutile titania particle synthesis via a hydrothermal method without mineralizers. Journal of Materials Chemistry 10 (2000) 2388-2391.

[4] M. Gopal, W. J. Moberly Chan, L. C. D. Jonghe. Room temperature synthesis of crystalline metal oxides. Materials Science 2 (1997) 6001-6008.

[5] C. C. Wang, J. Y. Ying. Sol-gel synthesis and hydrothermal processing of anatase and rutile titania nanocrystals. Chemistry of Materials 11 (1999) 3113-3120.

[6] B. Tian, F. Chen, J. Zhang, M. Anpo. Influences of acids and salts on the crystalline phase and morphology of TiO_2 prepared under ultrasound irradiation. Journal of Colloid and Interface Science 303 (2006) 142–148.

[7] J. K. Burdett, T. Hughbanks, G. J. Miller, J. W. Richardson, J. V. Smith. Structural-electronic relationships in inorganic solids: powder neutron diffraction studies of the rutile and anatase polymorphs of titanium dioxide at 15 and 295 K. Journal of the American Chemical Society 109 (1987) 3639-3646.

[8] M. Abd-Lefdil, R. Diaz, H. Bihri, M. A. Aouaj, F. Rueda. Preparation and characterization of sprayed FTO thin films. The European Physical Journal - Applied Physics 38 (2007) 217–219

[9]P. M. Oliver, G. W. E. Watson, T. Kelsey, S. C. Parker. Atomistic simulation of the surface structure of the TiO_2 polymorphs rutileand anatase. Journal of Materials Chemistry 7 (1997) 563-568.

[10]A. S. Barnard, P. Zapol. Effects of particle morphology and surface hydrogenation on the phase stability of TiO_2. Physical Review B 70 (2004) 235403 1-10.

[11]Y. Li, M. Guo, M. Zhang, X. Wang. Hydrothermal synthesis and characterization of TiO_2 nanorod arrays on glass substrates. Materials Research Bulletin 44 (2009) 1232–1237.

[12] H. Choi, E. Stathatos, D. D. Dionysiou. Sol–gel preparation of mesoporous photocatalytic TiO_2 films and TiO_2/Al_2O_3 composite membranes for environmental applications. Applied Catalysis B: Environmental 63 (2006) 60–67.

[13]C. Lu, M. Wen. Synthesis of nanosized TiO_2 powders via a hydrothermal microemulsion process. Journal of Alloys and Compounds 448 (2008) 153–158.

[14]C. Sanchez, J. Livage, M. Henry, F. Babonneau. Chemical modification of alkoxide precursors. Journal of Non-Crystalline Solids 100 (1988) 65-76.

[15]K. Wasa, M. Kitabatake, H. Adachi. Thin film materials technology: sputtering of compound materials. William Andrew (2005).

Chapter 7 Hybrid solar cells with TiO_2 nanorod thin films

7.1 TiO_2/P3HT solar cells with electrolyte

7.1.1 Experimental details

This experiment started with synthesizing TiO_2 nanorod of fibre thin films on FTO substrate as the process described in Chapter 6. Herein, in order to obtain a dense and thin nanorod film on FTO substrate, hydrothermal reaction was implemented at 150^{o}C for 0.5-hours by using 5 ml $Ti(OBu)_4$ and 30 ml HCl, 30 ml H_2O as precursor. After fabrication, the as-prepared TiO_2 thin films were immersed into100 ml of $TiCl_4$ solution, which was prepared by mixing $TiCl_4$ and ice water with different concentration of $TiCl_4$ (0.5 M-2 M), at 50^{o}C for 1-hour. Then $TiCl_4$ treated films were rinsed by ethanol followed by annealing at 450^{o}C for 2- hours inside a tube furnace. For comparison, thin ZnO by atomic layer deposition was alternatively deposited on top of TiO_2 to replace $TiCl_4$ treatment. P3HT was chosen as absorption layer by dissolving it in chlorobenzene to a concentration of 5 mg/ml and then spin coated in ambient atmosphere on top of TiO_2 layer. Thermal annealing was carried out in tube furnace at different temperature under N_2 atmosphere. Then the P3HT coated TiO_2 electrode was clamped firmly together with a FTO counter electrode covered with graphite. A drop of redox $I^-/I3^-$ electrolyte solution was introduced into the space between two electrodes. Therefore, the photovoltaic devices had a structure of FTO/TiO_2/buffer layer/P3HT/electroyte /FTO (graphite). Except for the annealing process, the entire synthesis process and measurement were conducted in ambient atmosphere.

7.1.2 Results and discussion

Fig. 7.1 shows schematic structure of the hybrid solar cell and its relative aligned energy band diagram. Under light illumination, electron and hole pairs generate in P3HT. Then photogenerated electrons transfer to TiO_2 owing to discrepancy electron affinity between TiO_2 and P3HT, and at the same time, transfer of holes are refused

by the valence band of TiO_2. Holes in HOMO band of P3HT are transferred to counter electrode by electrolyte. The voltage generated under illumination is similar to that of DSSC, corresponding to the difference between the Fermi level of the electron in TiO_2 and the redox potential of the electrolyte [1], and only partially dependent on the difference in work functions of two electrodes [2]. Therefore the maximum voltage is speculated to be approximately 900 mV.

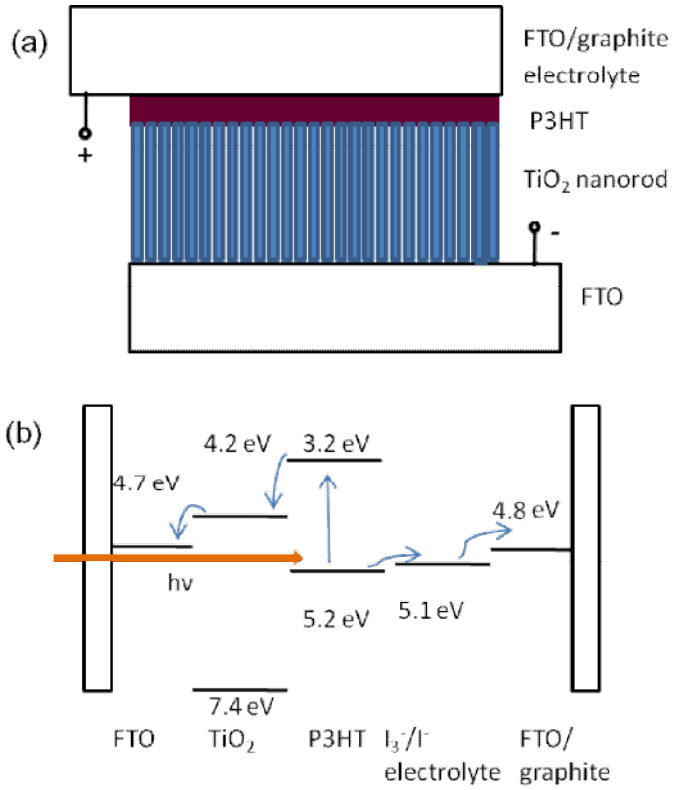

Figure 7.1 (a) Schematic structure and (b) energy band diagram of TiO_2 hybrid solar cell.

Fig. 7.2 shows the top surface SEM image of as synthesized TiO_2 thin film, in which a rough but dense surface with particle like dots can be seen clearly. The thickness of this thin film was measured by cross sectional SEM, showing a thickness around 300 nm. Even though the cross sectional image did not clearly show the fine structure of thin film, owing to the resolution of equipment, the thin film was conceivably composed of nanorods on account of the results discussed in last chapter. Therefore, the observed superficial dots were reasonably attributed to the tips of nanorods and

the rough surface was conceivably resulted from the rough FTO surface. This rough surface can be helpful to increase the contact area between P3HT and TiO_2 thin film, which is expected to promote charge separation.

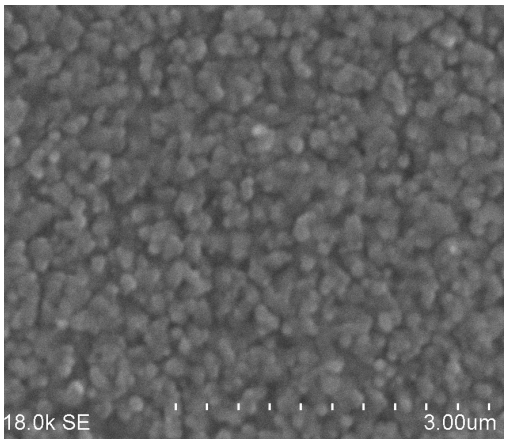

Figure 7.2 Top surface SEM image of as synthesized TiO_2 nanorod thin film.

As it can be seen from the dark curve, the current started to increase intensively when the forward voltage was more than 735 mV, making solar cell forward biased, as seen from Fig 7.3. For an ideal solar cell, the reverse break down voltage, over which the current begins to intensively increase, should be far larger than forward biased voltage. However, the break down voltage was estimated to be about 330 mV, since electrolyte may directly contact with TiO_2 or conductive FTO electrodes in this kind of structure due to electrolyte penetration, leading to current leaking which generally happens in dye sensitized solar cells [3]. Under illumination, this solar cell gave out V_{oc} of 550 mV, which was lower than the speculated maximum voltage, J_{sc} of 0.88 mA, and η of 0.191 %.

The lower V_{oc} was mainly attributed to the existence of dark current at V_{oc}, implying that tri-iodide (I_3^-) reduction happened at surfaces of TiO_2 thin film where P3HT did not completely cover, as well as at FTO/electrolyte interface where both TiO_2 thin film and P3HT did not fully cover [4,5].

The practical V_{oc}, under illumination, is expected to obtain in accordance with DSSC as presented as following equation:

$$V_{oc} = \frac{kT}{q} ln\ (\frac{I_{inj}}{I_0} + 1) \qquad (7.1)$$

Where k is the Boltzmann constant, T is the absolute temperature, q is the magnitude of the electron charge, I_{inj} is injection current and I_0 is the dark current. The injection current and dark current are determined by following equations:

$$I_{inj} = q\eta\Phi_0 \qquad (7.2)$$

$$I_0 = qn_0k_{et}C_{[I_3^-]} \qquad (7.3)$$

where η is the quantum yield for photogenerated electrons, Φ_0 is the incident photon flux, n_0 is the electron density on the conduction band of the semiconductor in the dark, k_{et} is the recombination rate of injected electrons with tri-iodides (I_3^-) on TiO_2 surface or FTO surface, and $C_{[I_3^-]}$ is the concentration of I_3^- in the electrolyte [6].

The short circuit current density is dependent on the generation and the collection of light generated carriers approximately as:

$$J_{sc} = qG(L_n + L_p) \qquad (7.4)$$

G is the generation rate, L_n and L_p are the electron and hole diffusion length respectively [7].

Therefore, the lower V_{oc} was mainly attributed to the existence of dark current at V_{oc}, implying that tri-iodide (I_3^-) reduction happened at surfaces of TiO_2 thin film where P3HT did not completely cover, as well as at FTO/electrolyte interface where both TiO_2 thin film and P3HT did not fully cover [8,5].

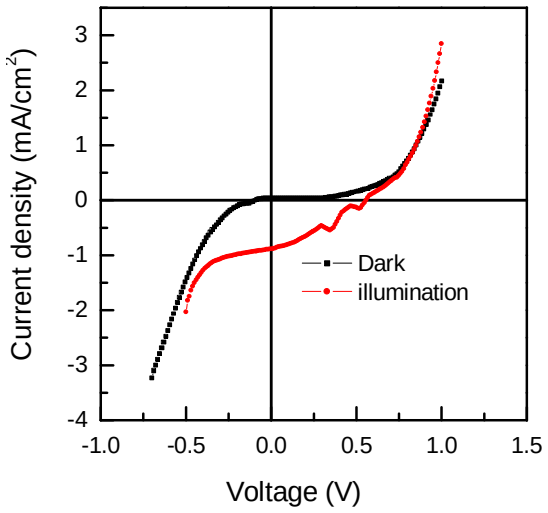

Figure 7.3 Dark and illuminated J-V curves of P3HT/dense TiO_2 nanorod thin film.

Considering that the thickness and carrier conductivity of P3HT layer may have significant influence on the performance of solar cells, different spin coating speed and annealing temperature were studied. Firstly, P3HT of all solar cells were spin coated on to $TiCl_4$ treated TiO_2 nanorod thin films at speed of 1000 rpm, 1500 rpm and 3000 rpm respectively, and then annealed at 80^{o}C. Lower spin coating speed was expected to result in thicker P3HT layer, so as to enhance carrier generation under illumination. The optical absorbance spectra of P3HT/TiO_2 films on FTO are shown in Fig. 7.4(a), in which the absorption edges located at around 400 nm were conceivably attributed to TiO_2 thin films and the board absorption in range from 400 nm to 650 nm were caused by π-π^* transition of P3HT. Apparently, 1000 rmp resulted in the strongest absorbance intensity owing to thickest P3HT layer. Then increasing spin coating speed gave rise to reduction of absorbance intensity, being consistent with the fact that higher spin coating speed is conceivably corresponding to thinner P3HT layer.

The illuminated J-V characteristics of solar cells are exhibited in Fig. 7.4(b), with relative parameters listed in Table 7.1. It is mentioned before that the voltage generated under illumination corresponds to the difference between the Fermi level of the electron in TiO_2 and the redox potential of the electrolyte. However, in comparison with the V_{oc} of 550 mV obtained by 3000 rmp, lower spin coating speed

was associated with slight lower V_{oc}. Moreover, the J_{sc} decreases significantly as the reduction of spin coating speed, to 0.27 mA when the spin coating speed was 1000 rmp. Generally, carrier dissociation occurs on the interface of TiO_2 and P3HT, thus to reach electrolyte holes must go through the whole P3HT layer, in where the diffusion length is merely a few nanometres to allow efficient carrier transport [9,10], leading to a much stronger carrier recombination. Therefore, although light absorption was enhanced, photogenerated carriers hardly contributed to photocurrent, which also increased series resistance of the solar cell, resulting in evident reduction of J_{sc} shown in Table 7.1.

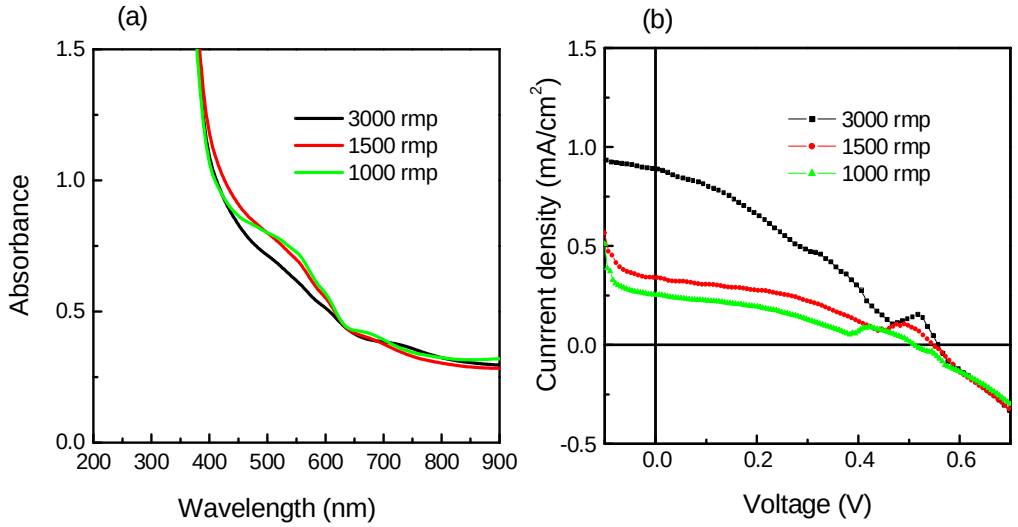

Figure 7.4 J-V curves of (a) solar cells with different P3HT thickness, (b) solar cells with different spin coating speed.

Fig. 7.5 shows J-V curves of solar cells spin coated at a speed of 3000 rmp, but annealed at 60°C, 80°C and 100°C, respectively. Evidently, annealing temperature hardly affected the V_{oc}, since the same thickness of P3HT layer undoubtedly led to same carrier generation which kept the same recombination on TiO_2 or FTO surface. However, both 60°C and 100°C caused lower J_{sc}, which were reasonably attributed to different series resistance. When the annealing temperature was 100°C, the J_{sc} of 0.48 mA was merely half of the value of solar cell annealed at 80°C. This implies P3HT had the highest carrier mobility when the annealing temperature was 80°C.

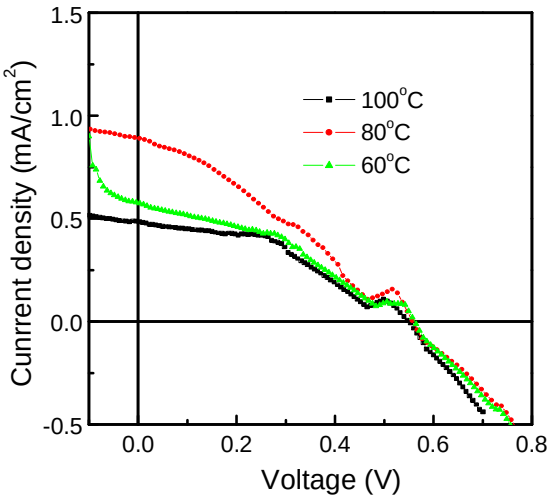

Figure 7.5 J-V curves of solar cells annealed at 60°C, 80°C and 100°C.

Table 7.1 Photovoltaic parameters of solar cells with different P3HT layer.

Annealing temperature (°C)	Spin coating speed (rmp)	A(cm^2)	V_{oc} (mV)	J_{sc} (mA)	Ff (%)	η (%)
100	3000	0.2375	551	0.48	47.4	0.123
80	3000	0.2375	550	0.88	39.4	0.191
60	3000	0.2375	557	0.60	42.1	0.140
80	3000	0.2375	550	0.88	39.4	0.191
80	1500 (thicker)	0.2375	548	0.36	34.2	0.067
80	1000 (thickest)	0.2375	517	0.27	29.8	0.041

In view of low break down voltage partially caused by structural defects, different treatment methods on top of TiO_2 surface were employed for the purpose of blocking reverse current penetration. Replacing $TiCl_4$ treatment by ZnO buffer layer deposited by atomic layer deposition (ALD), the forward current under dark nearly remained the same as before, whereas as depicted in Fig 7.6 (a), reverser break down voltage was increased. This means ZnO blocking layer deposited by ALD was structural better than TiO_2 formed by $TiCl_4$ solution treatment. Unfortunately, it is interesting to see that the illuminated J-V curve revealed a lower J_{sc} of 0.4 mA with ZnO

blocking layer, even though merely a small decrease existed in V_{oc}. In comparison with the forward dark characteristic, discrepancy occurring under illumination indicated the charge separation on ZnO/P3HT interface was practically worse than TiO_2/P3HT interface, though they have similar band gaps and ZnO has higher carrier mobility [11,12]. This was also demonstrated elsewhere that introduction of TiO_2 thin shells on top of ZnO nanorod significantly promoted the open voltage and fill factor as well as efficiency [13].

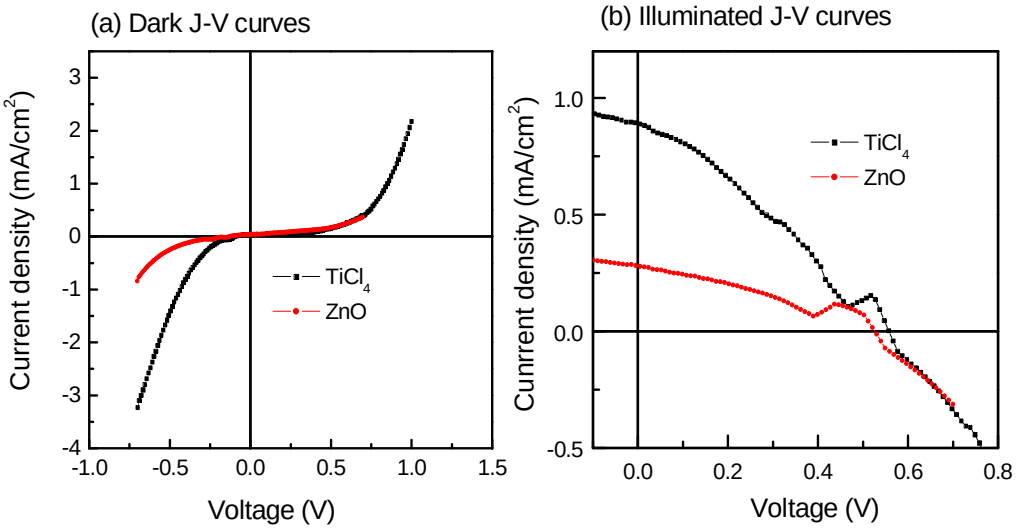

Figure 7.6 (a) Dark J-V curves and (b) illuminated J-V curves of solar cells treated with $TiCl_4$ or ZnO.

The requirement of liquid electrolytes in dye sensitized solar cell is still a very challenging issue to be resolved for commercial applications, due to slow dissolve of P3HT by liquid electrolyte and the temperature stability problems [14], at high temperature the electrolyte could expand, making sealing the panels a serious problem while lower temperature cause the liquid to freeze, ending power production and potentially leading to physical damage. Therefore, based on the optimized synthesis conditions, the performance of solar cells without electrolyte was studied.

7.2 TiO_2/P3HT solar cells without electrolyte

7.2.1 Experimental details

As it is know that the diffusion length of carriers in P3HT is less than 20 nm and thus only carriers generate near the electrodes can be collected and give rise to photocurrent. Therefore sparse nanorod thin films were expected to improve solar cell performance by providing bigger TiO_2/P3HT interface area compared with dense nanorod thin film, so as to improve charge separation. Thus, the structures of TiO_2 nanorod thin film on solar cell performance were studied by adjusting hydrothermal parameters. Before hydrothermal process, a thin but dense TiO_2 layer was deposited on FTO substrate by using magnetron sputtering, for the purpose of forming a dense blocking layer and acting as seed layer for the uniform growth of TiO_2 nanorods. Hydrothermal reaction was implemented at 150^{o}C for different time by using 1 ml $Ti(OBu)_4$ and 30 ml HCl, 30 ml H_2O as precursor. After fabrication, the as prepared TiO_2 thin films were treated by $TiCl_4$ 0.5 M solution. P3HT was spin coated in ambient atmosphere on top of TiO_2 layer with speed of 3000 rpm and then annealed at 80^{o}C in N_2 atmosphere. Then thick Cu dot electrodes were deposited on top of P3HT layer by evaporation in vacuum chamber.

7.2.2 Results and discussion

Fig. 7.7 shows schematic structure of the hybrid solar cell composed of sparse TiO_2 nanorods. These kind of solar cells had a structure of FTO/TiO_2(dense particle)/TiO_2 (nanorod)/$TiCl_4$(treated)/P3HT/Cu, referred to be P_nR_m, in which P_n means TiO_2 particle layer by using sputtering for n hours and R_m means TiO_2 rod layer by employing hydrothermal for m hours.

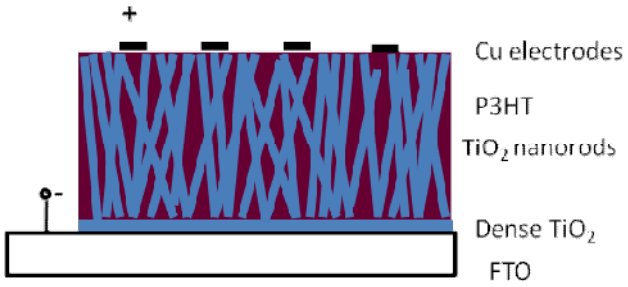

Figure7.7 Schematic structure of the hybrid solar cell composed of sparse TiO_2 nanorods.

Firstly, the J-V curves of solar cells made up by dense TiO_2 nanorod thin film depicted in last section were plotted in Fig. 7.8. In comparison with dark curve of solar cell with electrolyte, both forward biased current and reverse biased current were reduced due to increased series resistance. This suggests electrolyte indeed promoted solar cell performance by improving electric conduction. Herein, the dark current was mainly caused by the direct contact of metal electrode with TiO_2 thin film or counter FTO electrode. Under illumination, increased series resistance gave rise to significant reduction of J_{sc} and V_{oc}, from 0.88 mA cm^{-2} and 550 mV to 0.18 mA cm^{-2} and 480 mV, resulting in an efficiency of 0.03%. Besides the dark current, increased series resistance also contributed to the lower J_{sc}, V_{oc} as well as η.

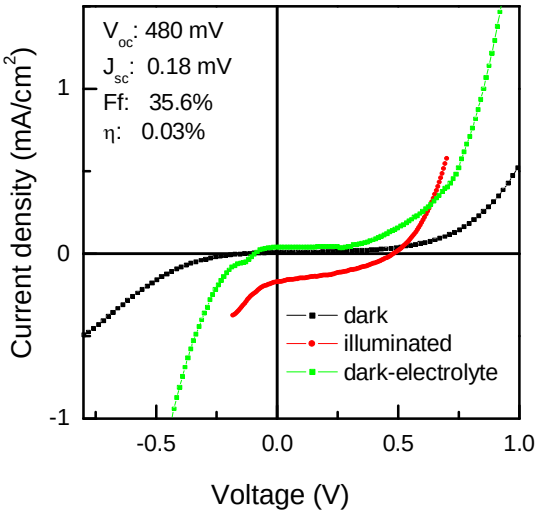

Figure 7.8 J-V curves of solar cells composed of dense TiO_2 nanorod thin film and treated with or without electrolyte.

J-V characteristics of solar cells composed of sparse nanorod thin films were systematically studied. Solar cells composed of merely TiO_2 particle layer, referred as P_1-P_4 according to deposition duration, were all short circuited, though the S_4 had thickness of about 120 nm since the speed of sputtering deposition of TiO_2 thin film here was measured to be 30 nm per hour. On the other hand, solar cells made up by TiO_2 nanorod thin film without bottom particle layer, referred as R_1-R_4 were also short circuited. This suggests that neither sputtering deposited particle thin films nor

hydrothermal synthesized sparse nanorod thin films were not dense enough to avoid direct contact of two electrodes.

The J-V curves of solar cells P_mR_n are plotted in Fig. 7.9, with corresponding parameters listed in Table 7.2. Through comparing P_1R_2 and P_2R_2, it is apparently seen that these solar cells composed of thicker TiO_2 particle layer gave out higher V_{oc} but lower J_{sc}, since the thicker TiO_2 particle layer not only refrained current leaking but also increased series resistance. Therefore, the effect of this layer was conflicting and optimized thickness was deduced to be between 30-50 nm. On the other hand, the influence of TiO_2 nanorod layer on J-V performance is complicated, since both packing density and length of nanorods were altered as after distinct fabrication duration. The optimized reaction time for hydrothermal is 2-hours, leading to the hybridized solar cell had V_{oc} of 255 mV, J_{sc} of 1.00 mA and η of 0.07% under AM 1.5. The geometrical structure of solar cells composed of TiO_2 nanorod thin films are expected to be adjusted furthermore so as to achieve a better cell performance.

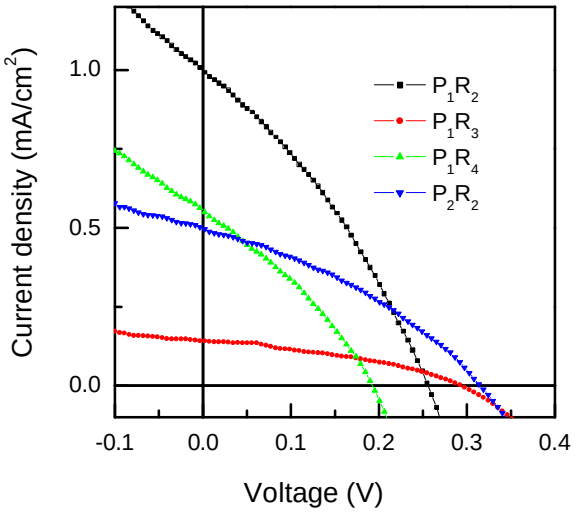

Figure 7.9 Illuminated J-V curves of solar cells composed of P_mR_n.

Table 7.2 Photovoltaic parameters of solar cells solar cells composed of P_mR_n

samples	A(cm^2)	V_{oc} (mV)	J_{sc} (mA)	Ff (%)	η (%)
P_1R_2	0.0078	255	1.00	47.4	0.07
P_1R_3	0.0078	292	0.15	39.4	0.02
P_1R_4	0.0078	198	0.54	42.1	0.04
P_2R_2	0.0078	315	0.50	35.0	0.06

7.3 Conclusions

Hybrid solar cells composed of TiO_2 nanorod thin films with or without electrolyte were, the first time, successfully synthesized and studied. TiO_2 nanorod/P3HT with electrolyte gave out an efficiency of 0.191% while TiO_2 nanorod/P3HT, without electrolyte, showed the highest efficiency of 0.07%.

References

[1]M. Gratzel. Conversion of sunlight to electric power by nanocrystalline dye-sensitized solar cells. Journal of Photochemistry and Photobiology A: Chemistry 164 (2004) 3–14.

[2] T. Ishwara, D. D. C. Bradley, D. Vanderzande, L. Lutsen, J. Nelson,S. Tierney, P. Ravirajan, M. Heeney, I. Vanseveren, I. McCulloch. Influence of polymer ionization potential on the open-circuit voltage of hybrid polymer/TiO_2 solar cells. Applied Physics letters 92 (2008) 053308.

[3]J. Bandara, H. C. Weerasinghe. Enhancement of photovoltage of dye-sensitized solid-state solar cells by introducing high-band-gap oxide layers. Solar Energy Materials and Solar Cells 88 (2005) 341–350.

[4]K. H. Ko, Y. C. Lee, Y. J. Jung. Enhanced efficiency of dye sensitized TiO_2 solar cells (DSSC) by doping of metal ions. Journal of Colloid and Interface Science 283 (2005) 482–487.

[5] M. Gratzel. Mesoscopic Solar Cells. 15th international photovoltaic science and engineering conference (PVSEC-15), Shanghai China (2005).

[6] A. Luque, S. Hegedus, K. Hara, H. Arakawa. Handbook of photovoltaic science and engineering. John Wiley and Sons (2003)

[7]http://pveducation.org/pvcdrom/solar-cell-operation/short-circuit-current.

[8]K. H. Ko, Y. C. Lee, Y. J. Jung. Enhanced efficiency of dye sensitized TiO_2 solar cells (DSSC) by doping of metal ions. Journal of Colloid and Interface Science 283 (2005) 482–487.

[9]H. Hoppe, N. S. Sariciftci. Polymer solar cells. Advances in Polymer Science 214 (2008) 1–86.

[10]W. Cai, X. Gong, Y. Cao. Polymer solar cells: Recent development and possible routes for improvement in the performance. Solar Energy Materials and Solar Cells 94 (2010) 114–127.

[11]M. Law, L. E. Greene, J. C Johnson, R. Saykally, P. D. Yang. Nanowire dye-sensitized solar cells. Nature Materials 4 (2005) 455-459.

[12]M. Law, L. E. Greene, A. Radenovic, T. Kuykendall, J. Liphardt, P. D. Yang. ZnO-Al_2O_3 and ZnO-TiO_2 core-shell nanowire dye-sensitized solar cells. The Journal of Physical Chemistry B 110 (2006) 22652-22663.

[13]L. E. Greene, M. Law, B. D. Yuhas, P. Yang. ZnO-TiO_2 core-shell nanorod/P3HT solar cells. The Journal of Physical Chemistry C 111 (2007) 18451-18456.

[14]H. Tributsch. Dye sensitization solar cells: a critical assessment of the learning curve. Coordination Chemistry Reviews 248 (2004) 1511-1530.

Chapter 8 Conclusions and future work

8.1 Major findings

Two important aspects of TiO_2 materials have been studied in this work, including band gap narrowing through ions doping and structural engineering of TiO_2 thin film for the application of organic-inorganic hybrid solar cells. The most important findings are as follows:

1. Pure TiO_2 thin films under different oxygen partial pressure were successfully fabricated by PLD method. It was demonstrated that lower oxygen partial pressure, during deposition, were responsible for facilitating phase transformation of anatase to rutile in post annealing process. Annealing manners also played important roles on the properties of TiO_2 thin film, in which lacking of oxygen, during annealing, gave rise to plenty of oxygen deficiency in thin film while introduction of oxygen, again during annealing, compensated oxygen deficiency, leading to distinctive optical absorption properties.

2. Fe doped TiO_2 thin films with different doping levels were successfully fabricated by PLD method at room temperature. Higher post annealing temperature gave rise to bigger red shift of absorption edge. It was shown that the optimized Fe doping concentration for band gap narrowing was 2%, with absorption edge red shifted to 550 nm, under the preparation parameters used in this work. Substrate temperature of 700^{o}C, during deposition process, showed no difference with respect to microstructure and optical absorption properties of Fe doped TiO_2 thin films compared with room temperature.

3. Mn doping gigantically narrowed the band gap TiO_2 thin films fabricated by using PLD method. 1% Mn doping significantly shifted the absorption edge from 360 nm to 1200 nm after post annealed at 1000^{o}C, corresponding to the band gap of 1.2 eV, making TiO_2 is extremely sensible to visible light even infrared region. Through comparing the optical absorption properties of Mn doped TiO_2 thin films with that of Fe doped ones, we found the Mn doping effect on band gap narrowing was stronger than Fe doping, agreeing well theoretical calculation results.

4. No obvious red shift can be seen from the optical absorption spectra of rare earth doped TiO_2 thin films by utilizing PLD, in spite of the post annealing temperature was as high as 1100^oC, suggesting it was hard to replace Ti atoms in TiO_2 matrix by rare earth atoms via this method owing to the their big ionic sizes, e.g. Gd^{3+} (0.938 Å), Sm^{3+} (0.964 Å) and Er^{3+} (0.881 Å).

5. Ga doped TiO_2 thin films with different doping levels were fabricated by PLD method. The optical absorption spectra suggested the prime doping concentration for extending absorption range was 1% Ga, which red shifted absorption edge to around 480 nm in visible region via introducing secondary absorption shoulder. Theoretical modelling showed the red shift of absorption edge was mainly caused by the raising-up of valence band maximum (VBM) with respect to the Fermi level on account of Ga doping.

6. V-Ga co-doped TiO_2 films composed of rutile nanograins were fabricated by PLD. The doped thin film exhibited remarkable red shifts in the optical absorption edges, from UV to infrared region with the biggest absorption edge located at 900 nm. The optical absorption coefficients of the doped materials were very high, in the order of 10^5 cm^{-1}, which makes TiO_2 extremely effective in absorbing a wide range of solar spectral radiation and thus highly desirable for a wide range of photo-based devices including novel low-cost solar cells. Theoretical calculation of electronic structures showed that Ga alone has little effect for the reduction of the band gap of TiO_2, while V-Ga co-doping induces additional energy bands to overlap with the conduction band minimum and leads to significant reduction of the band gap. The enormous red shift, observed in this work, is likely owing to optimised combination of co-dopants.

7. Fe doped TiO_2 nanopowders were prepared using a hydrothermal method at low temperature. Doping Fe into TiO_2 tended to restrict the grain growth of TiO_2 during synthesis and annealing, leading to finer TiO_2 grains. Low solution acidity favoured the formation of anatase TiO_2 and high H^+ concentration resulted in the formation of rutile TiO_2. The presence of SO_4^{2-} ions in the acidic precursor solution was propitious for the formation of anatase TiO_2. Fe doping induced significant red shift in the optical absorption edge of TiO_2 into the visible light region. The presence of secondary absorption edge was attributed to doping induced intermediate states.

Accordingly the visible light photocatalytic activity of TiO_2 increased on account of visible light absorption by Fe doped TiO_2, resulting in improved degradation rate of MB under visible light irradiance. The photocatalytic activity of TiO_2 increased gradually with increasing Fe/Ti ratio up to 1.5 at%, beyond which, photocatalytic activity began to lose.

8. Mn doped TiO_2 nanopowders have successfully prepared by means of a sol–gel method using ethanol–water as solvent. A remarkable red shift of the absorption edge was achievable through Mn doping, giving rise to gigantically narrowed energy gap to permit absorption well into the infrared spectral region. The Mn doped anatase TiO_2 powders exhibited considerable visible-light photocatalytic activity, leading to enhanced degradation rate of MB under visible light irradiance. It was striking to find that both band gap narrowing and relative visible light photocatalytic activity of optimized Mn doped TiO_2 nanopowder were higher compared with optimized Fe doped TiO_2 nanopowder, being consistent with theoretical prediction.

9. Single rutile TiO_2 nanorod and nanofibre thin films, with preferred [002] orientation, were successfully synthesized on FTO substrate by utilizing hydrothermal method. The growth mechanisms were studied, which gave fundamental guidance to fabricate controllable structured TiO_2 nanorod thin films. Through adjusting the reaction duration, alcohol substitution of water as solvent, reaction temperature, and $Ti(OBu)_4$ concentration TiO_2 thin films of different packing density and thickness were well controlled for various potential applications. The oriented single TiO_2 nanorod/nanofibre thin films are expected to offer improved properties in thin-film PV cells, owing to the longer electron diffusion lengths through their one dimensional channel for carrier transportation, unique electric properties and low recombination rate of carriers.

10. Hybrid solar cells composed of TiO_2 nanorod thin films with or without electrolyte were the first time synthesized and studied. TiO_2 nanorod/P3HT with electrolyte gave out an efficiency of 0.191% while TiO_2 nanorod/P3HT without electrolyte showed the highest efficiency of 0.07%.

8.2 Future work

Concerning the findings presented in this thesis, future efforts are suggested as follows:

The band gaps of TiO_2 materials, including thin films and nanopowders, can be effectively narrowed by Fe or Mn doping, leading to beneficial visible light absorption. Also, through measuring the degradation speed of MB under visible light, the photocatalytic activities of doped nanopowders were found to be significantly promoted. Therefore, the practical applications of Fe or Mn doped TiO_2 materials under solar light should be pursued, e.g. photocatalysis, self cleaning and water splitting for H_2 production.

V-Ga co-doping can give rise to gigantic band gap narrowing of TiO_2 through introducing several energy levels/bands next to the CBM with their considerable band width and curvatures result in overlapping of the conduction band. The main absorption of V-Ga co-doped TiO_2 materials covers the full visible light region and part of the infrared or near-infrared region, with well defined primary absorption edges and high absorption coefficient over 10^5 cm^{-1}. It is worth stressing that the high absorption coefficient and well defined edge are desirable for an efficient optical absorber for efficient utilization of solar energy; the present discovery provides a new material system for absorption of a wide range of solar irradiance for energy harvest or photocatalytic applications. Hence, the testing of visible light activity of V-Ga doped TiO_2 materials is demanded.

Single rutile TiO_2 nanorod and nanofibre thin films with preferred [002] orientation with controllable length and packing density have merit in the potential to be used in sensors, solar cells on account of their unique pathways for charge carriers and relative higher carrier mobility compared with polycrystalline materials. Although we have implemented these structural engineered thin films in organic-inorganic hybrid solar cells, the achieved efficiencies are still far from expected. The detailed geometry structures TiO_2/polymer solar cells should be studied and required to be optimized furthermore to improve the energy conversation efficiency. Besides, literatures suggested that hole conductor such as PEDOT: PSS, MoO_3, NiO, WO_3 are

helpful for hybrid solar cell, through serving as electron blocking and hole conducting material. It is therefore suggested that a thin layer of hole conductor should be employed between P3HT and metal electrode.

List of publications

- Q. Deng, X. Han, Y. Gao, G. Shao. Remarkable optical red shift and extremely high optical absorption coefficient of V-Ga co-doped TiO_2. Journal of Applied Physics. 112 (2012) 013523.
- M. Guo, X. Xia, Y. Gao, G. Jiang, Q. Deng, G, Shao. Self-aligned TiO_2 thin films with remarkable hydrogen sensing functionality. Sensor and Actuators B: Chemical http://dx.doi.org/10.1016/j.snb.2012.02.072.
- Q. Deng, X. Xia, M. Guo, Y. Gao, G. Shao. Mn doped TiO_2 nanopowders with remarkable visible light photocatalytic activity. Materials Letters 65 (2011) 2051-2054.
- L. Wan, Y. Gao, X. Xia, Q. Deng, G. Shao. Phase selection and visible light photocatalytic activity of Fe-doped TiO_2 prepared by the hydrothermal method. Materials Research Bulletin 46 (2011) 442-446.
- Y. Zhang, Y. Gao, X. Xia, Q. Deng, M. Guo, L. Wan, G. Shao. Structural engineering of thin films of vertically aligned TiO_2 nanorods. Materials Letters 64 (2010) 1614-1617.
- G. Shao, Q. Deng, L. Wan, M. Guo, X. Xia, and Y. Gao. Molecular design of TiO_2 for gigantic red shift via sublattice substitution. Journal of Nanoscience and Nanotechnology 10 (2010) 1–5.
- Q. Deng, Y. Gao, X. Xia, R. Chen, L. Wan, G. Shao. V and Ga Co-doping effect on optical absorption properties of TiO_2 thin films. Journal of Physics: Conference Series 152 (2009) 012073.